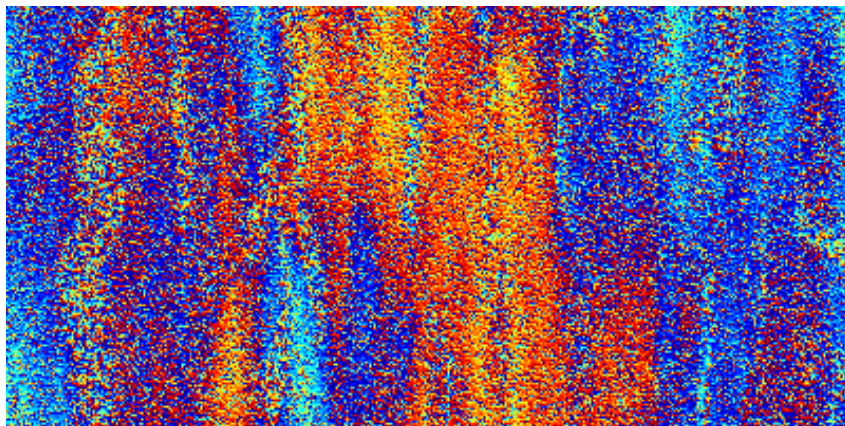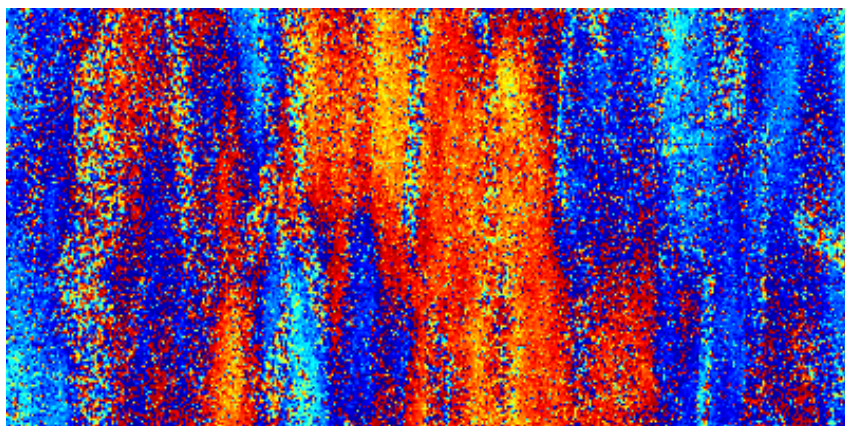# Spectral filtering

and oversampling

for radar interferometry

L.M.Th. Swart

Spectral filtering
and oversampling
for radar interferometry

L.M.Th. Swart

Thesis for the master's degree in geodetic engineering
Supervisors: R.F. Hanssen and S. Usai
Professor: R.A.P. Klees

Faculteit Civiele Techniek en Geowetenschappen – Afdeling Geodesie
Technische Universiteit Delft

Alphen aan den Rijn – Nederland
November 2000

Front page: interferometric phase images of the tandem pair 21410 and 1737 before and after spectral filtering in azimuth and range. See page 89.

Preface

This is the report of the research done for my master's degree in geodetic engineering. The research was performed at the department of Geodesy of the Faculty of Civil Engineering and Geosciences of the University of Technology in Delft, the Netherlands.

The fascinating subject of radar interferometry kept me busy for more than a year. I liked to try to achieve a thorough understanding of the subjects that deal with the master's research and had the opportunity to combine the work on the theory of spectral filtering for radar interferometry with its implementation. This was nice, although programming is the weird kind of stuff where you think something can be done in an hour or two but after all it turns out to have kept you busy two weeks. Beyond this I liked to spend time at other subjects that interest me, like our Rover 3500 Vanden Plas, the organ and my work for the *Cuypersgenootschap*, society for the conservation of nineteenth- and twentieth-century cultural heritage. Why are there only twenty-four hours in a day? And why do I have only one processor? It was intensive, but it was quite a nice year. And probably this was the last opportunity to do things this way.

I would like to thank Stefania Usai and Ramon Hanssen for guiding me and learning me how to do scientific research and how to write it down. Bert Kampes was always ready for discussion. They inspired me and I'm looking forward to extend my skills in the field of SAR interferometry at Delft. Dirk Geudtner answered all my questions on subjects that where not clear to me after reading his thesis. The ESA helpdesk provided me with valuable information. Thank you all. And last, but certainly not least, I would like to thank my wife, Sabine Broekhoven, who made this all possible.

Rens Swart

Alphen aan den Rijn, November 2000

Contents

Summary

Two of the fields of interest to geodesy are the determination of the shape of the earth's surface and the analysis of its deformation. The shape of the surface can be modelled using a digital elevation model. In the past few years, a newly developed remote sensing technique for the determination of an elevation or deformation model became operational: radar interferometry or interferometric synthetic aperture radar (InSAR). This technique uses images obtained by a radar instrument on board of a satellite or aeroplane. From two images interferograms can be calculated, which essentially are phase difference images.

Because the phase of an interferogram has a relation with the path length difference between the two imaging positions, a digital elevation model can be extracted from an interferogram. If in the time-span between the acquisition of two images from the same position a deformation took place, the resulting path length change is visible in the phase of the interferogram, making interferometry a suitable technique for deformation measurements. In particular the ERS-missions resulted in making radar interferometry an important subject of geodetic research.

To obtain an interferogram of a quality high enough to derive a digital elevation model or a deformation model, the radar backscattering properties during the acquisition of both SAR images must be as similar as possible. Only then the images show enough correlation to be able to calculate the phase difference accurately. One cause of decorrelation between SAR images is the imaging geometry. Because the imaged scene is viewed from two positions separated by a certain distance (the baseline) and the incidence angles are different, the backscattering properties change. This leads to a deterioration of the similarity of the spectra in range (the viewing direction of the radar): the spectra are shifted with respect to each other. In the flight or azimuth direction a spectral shift can take place due to the difference in Doppler centroid frequency, related to the antenna pointing direction.

The decorrelation caused by range and azimuth spectral shifts can be reduced by filtering: removing the spectral bands that are not common to both images. The central research question for this thesis is how the interferogram can be improved by spectral filtering in range and azimuth.

The calculation of an interferogram is a complex multiplication of two images, with a resulting doubled bandwidth. To prevent aliasing from deteriorating the interferogram, oversampling may be necessary. This is another subject of the research in this thesis.

A quantitative description of the quality of an interferogram is provided by the coherence, which can be estimated with a coherent sum over a window of the interferogram. With the coherence, the improvement achieved by SAR-processing methods can be described.

The coherence estimator is biased. The higher the coherence and the greater the number of independent pixels in the estimator window, the smaller the bias. Choosing a large coherence estimator window decreases the bias, but the influence of local topography increases, reducing the estimated coherence.

The bias of the coherence estimator can be removed to a great extent. From the estimation, the bias for that particular estimated coherence is subtracted. Because the standard deviation for smaller numbers of independent pixels in the estimation window is higher, the distribution of the biased coherence is broader; the bias correction algorithm cannot correct for this. The mean (corrected) coherence of an interferogram is a suitable interferogram quality measure to assess the effectiveness of interferogram improvement algorithms, like spectral filtering.

The net result of the angle the antenna beam makes with respect to the direction perpendicular to the flight direction, the inclination of the orbit and the rotation of the earth causes the azimuth spectrum to show a shift with respect to zero-frequency. This is the Doppler centroid frequency. It depends on the geographic latitude. Within one image, the Doppler centroid frequency depends on range, due to the variation of the incidence angle over range.

The azimuth spectra of master and slave image are misaligned because in general they have a different Doppler centroid frequency. The shift of the azimuth spectra with respect to each other is equal to the Doppler centroid frequency difference. The envelopes of the range spectra of master and slave are not misaligned; however, the ground range or object spectra (in which the characteristics of the terrain are reflected) are misaligned due to the different incidence angle from either side of the baseline. The shift of the object spectrum features in the range spectrum is equal to the fringe frequency, which is linearly dependent on the perpendicular component of the baseline. It decreases with the incidence angle. The spectral misalignment in azimuth and range can be removed by filtering the spectra in order to achieve a common system transfer function.

The spectral filtering in azimuth is performed by multiplying the spectrum of master and slave with a filter that is the geometrical mean between the theoretical spectrum with the respective Doppler centroids of the master and slave. The bandwidth of master and slave is limited to the overlap of the original spectra; it decreases with the Doppler centroid frequency difference. Because of the range dependency, the Doppler centroid must be determined for the azimuth spectrum of each range line. Because the spectra show fluctuations, several azimuth spectra must be averaged. After the blockwise determination of the Doppler centroid, it can be smoothed with a cubic spline. The Doppler centroid can be determined from the location of the maximum of the spectrum by fitting a parabola through an interval of averaged spectra. Alternatively, the Doppler centroid can be determined from the location of the empty band, which is supposed to differ half the sampling frequency from the Doppler centroid. For this, the autoconvolution may be used.

The range filtering is performed by removing the original Hamming weighting of the spectra and reweighting the spectra with a Hamming function over the new bandwidth, which is equal to the original bandwidth minus the fringe frequency. In the master spectrum, a spectral band is removed from the side opposite to the band removed from the slave spectrum. The fringe frequency is the dominant frequency in the spectrum of the interferogram. It can be determined from the spectrum of a patch of the interferogram. This patch must be as small as possible to account for the variation in the fringe frequency due to topography. If the interferogram shows a very low correlation, due to

a long baseline or a bad coregistration, the fringe frequency cannot be determined from the interferogram spectrum. The fringe frequency must then be determined from the perpendicular component of the baseline and the incidence angle, as if the terrain would be flat or ellipsoidal. Alternatively, the fringe frequency can be determined from the orbits and a digital elevation model.

The theoretical decorrelation due to spectral misalignment for spectra with a rectangular envelope can be converted to the theoretical decorrelation for (Hamming) weighted spectra. The experimental improvement of the estimated coherence after filtering in azimuth and range agrees very well with the predicted improvement. The decorrelation due to spectral misalignment in azimuth and range and other sources is theoretically multiplicative. The experimental decorrelation and coherence factor can be derived from the estimated coherence before and after filtering.

The coherence of three interferometric pairs with very long baseline was extremely bad, due to baseline decorrelation, a bad coregistration and temporal decorrelation. Determination of the fringe frequency from the interferogram spectrum was not possible. Range filtering improved the coherence considerably. The interferometric phase images show that spectral filtering reduces the resolution in range or azimuth.

For ERS pairs, range filtering is necessary depending on the baseline. For ERS-1 pairs, azimuth filtering is in general not necessary, but often profitable. For tandem ERS-1-ERS-2 pairs, azimuth filtering is often advantageous. For ERS-2 pairs, azimuth filtering is in general not necessary, but often profitable. Since the operation of ERS-2 with one gyroscope, azimuth filtering is more often necessary.

For exact azimuth and range filtering, the shift of the slave with respect to the master image must be known. In general, coarse and fine coregistration is therefore performed before spectral filtering. If the interferogram shows a very low correlation, the fine coregistration can be bad or impossible. The coherence can be improved by prefiltering the images, after which the coregistration parameters are determined. The original unfiltered images are then coregistered and filtered. However, because the prefiltering reduces the bandwidth and hence the resolution, it does not always result in a better coregistration. If it is better, the increase of the coherence of the coregistered images is only moderate.

If the spectra of master and slave are not oversampled before calculating the interferogram, the spectrum of the interferogram may show aliasing because its sampling frequency is too small to fulfil the Nyquist criterion. This increases the noise in the interferogram. To oversample, the spectra are split at the empty band and zeros are inserted to double the number of samples. If the interferogram must be restricted to the number of samples of the original images, lowpass filtering is performed by removing the high-frequency bands. Oversampling is not necessary if the spectra have a maximum bandwidth equal to half the sampling frequency, for example after spectral filtering. Because the limited bandwidth after spectral filtering and the application of multilooking after the calculation of the interferogram, the noise due to aliasing will be very limited, making oversampling in general not necessary.

Samenvatting

Twee van de aandachtsgebieden van de geodesie zijn de bepaling van de vorm van het aardoppervlak en de analyse van zijn deformatie. De vorm van het oppervlak kan worden gemodelleerd met een digitaal hoogtemodel. In de afgelopen jaren is een nieuwe remote-sensingtechniek voor de bepaling van een hoogte- of deformatiemodel operationeel geworden: radarinterferometrie of interferometrische apertuursyntheseradar (InSAR). Deze techniek gebruikt beelden gemaakt met een radarinstrument aan boord van een satelliet of vliegtuig. Uit twee beelden kunnen interferogrammen worden berekend, wat feitelijk faseverschilbeelden zijn.

Omdat de fase van een interferogram in relatie staat tot het weglengteverschil tussen de twee opnameposities, kan een digitaal hoogtemodel uit het interferogram worden afgeleid. Als in de tijd tussen de opname van twee beelden vanaf dezelfde positie een deformatie heeft plaatsgevonden, is de resulterende weglengteverandering zichtbaar in de fase van het interferogram. Daardoor is interferometrie een geschikte techniek voor deformatiemetingen. Met name de ERS-missies maakten radarinterferometrie een belangrijk geodetisch onderzoeksonderwerp.

Om een interferogram te verkrijgen met een kwaliteit die hoog genoeg is om er een digitaal hoogte- of deformatiemodel uit te kunnen afleiden, moeten de eigenschappen van de terugverstrooiing van het radarsignaal gedurende de opname van beide SAR-beelden zo vergelijkbaar mogelijk zijn. Alleen dan bezitten de beelden genoeg correlatie om in staat te zijn het faseverschil nauwkeurig te berekenen. Eén oorzaak van decorrelatie tussen SAR-beelden is de opnamegeometrie. Doordat het opgenomen stuk terrein wordt waargenomen vanaf twee posities gescheiden door een zekere afstand (de basislijn) en de invalshoeken verschillend zijn, veranderen de terugverstrooiingseigenschappen. Dit tast de vergelijkbaarheid van de spectra in range (de kijkrichting van de radar) aan: de spectra zijn ten opzichte van elkaar verschoven. In de vlieg- of azimuthrichting kan een spectrale verschuiving plaatsvinden door een verschil in Dopplercentroïdefrequentie, gerelateerd aan de richting waarin de antenne wijst.

De decorrelatie die wordt veroorzaakt door de spectrale verschuiving in range en azimuth kan worden gereduceerd door filtering: verwijdering van de spectrale band die beide beelden niet gemeenschappelijk hebben. De centrale onderzoeksvraag voor deze doctoraalscriptie is hoe het interferogram kan worden verbeterd door spectrale filtering in range en azimuth.

De berekening van een interferogram is een complexe vermenigvuldiging van twee beelden, waardoor de bandbreedte verdubbelt. Om te voorkomen dat het vouweffect (aliasing) het interferogram vervormt, kan overbemonsteren noodzakelijk zijn. Dit is een

ander onderzoeksonderwerp in deze scriptie.

Een kwantitatieve beschrijving van de kwaliteit van een interferogram wordt gegeven door de coherentie, die kan worden geschat door een coherente som over een venster van het interferogram. Met de coherentie kan de verbetering door SAR-bewerkingsprocessen worden beschreven.

De coherentieschatter is onzuiver. Hoe hoger de coherentie en hoe groter het aantal onafhankelijke pixels in het schattingsvenster, hoe kleiner de onzuiverheid. Door een groot coherentieschattingsvenster te kiezen neemt de onzuiverheid af, maar de invloed van de lokale topografie neemt toe waardoor de coherentieschatting afneemt.

De onzuiverheid van de coherentieschatter kan voor een groot deel worden verwijderd. Van een schatting wordt de onzuiverheid voor die schatting afgetrokken. Omdat de standaardafwijking voor vensters met een kleiner aantal onafhankelijke pixels groter is, is de verdeling van de onzuivere coherentie breder; het onzuiverheidscorrectiealgoritme kan hiervoor niet corrigeren. De gemiddelde (gecorrigeerde) coherentie van een interferogram is een geschikte kwaliteitsmaat om de effectiviteit van interferogramverbeteringsalgoritmen zoals spectrale filtering te kunnen beoordelen.

Het netto resultaat van de hoek die de antennebundel maakt ten opzichte van de richting loodrecht op de vliegrichting, de inclinatie van de baan en de rotatie van de aarde veroorzaakt een verschuiving in het azimuthspectrum ten opzichte van de nulfrequentie. Dit is de Dopplercentroïdefrequentie. Deze hangt af van de geografische breedte. Binnen een beeld hangt de Dopplercentroïdefrequentie af van de range als gevolg van de variatie van de invalshoek over range.

De posities van de azimuthspectra van het meester- en slaafbeeld komen niet overeen doordat ze in het algemeen een verschillende Dopplercentroïdefrequentie hebben. De onderlinge verschuiving van de azimuthspectra is gelijk aan het verschil in Dopplercentroïdefrequentie. De omhullenden van de rangespectra van meester en slaaf zijn onderling niet verschoven; de grond- of objectspectra (waarin de karakteristieken van het terrein zijn besloten) zijn echter wel verschoven als gevolg van de verschillende invalshoek van beide einden van de basislijn. De verschuiving van de objectspectrumkarakteristieken in het rangespectrum is gelijk aan de fringefrequentie, die lineair afhankelijk is van de loodrechte component van de basislijn en afneemt met de invalshoek. De spectrale ongelijkvormigheid in azimuth en range kan worden verwijderd door de spectra zo te filteren dat een gemeenschappelijke systeemoverdrachtsfunctie wordt bereikt.

De spectrale filtering in azimuth wordt uitgevoerd door de spectra van meester en slaaf met een filter te vermenigvuldigen dat het geometrisch gemiddelde is van de theoretische spectra met de respectievelijke Dopplercentroïde van meester en slaaf. De bandbreedte van meester en slaaf wordt beperkt tot de overlap van de originele spectra; hij neemt af met het verschil van de Dopplercentroïdefrequenties. Vanwege de rangeafhankelijkheid moet de Dopplercentroïde worden bepaald voor het azimuthspectrum van elke rangelijn. Omdat de spectra fluctueren moeten enige azimuthspectra worden gemiddeld. Na de bloksgewijze bepaling van de Dopplercentroïde kan deze worden versmeerd met een kubische spline. De Dopplercentroïde kan worden bepaald uit de positie van het maximum van het spectrum door een parabool te passen aan een interval van gemiddelde spectra. Ook kan de Dopplercentroïde worden bepaald uit de ligging van de lege band, die wordt verondersteld de halve bemonsteringsfrequentie te verschillen van de Dopplercentroïde. Hiervoor kan de autoconvolutie worden gebruikt.

De rangefiltering wordt uitgevoerd door de originele Hammingweging van de spectra te verwijderen en de spectra opnieuw te wegen met een Hammingfunctie ter breedte van de nieuwe bandbreedte, die gelijk is aan de originele bandbreedte minus de fringefrequentie. Uit het meesterspectrum wordt een spectrale band verwijderd aan de tegenovergestelde kant ten opzichte van de band die uit het slaafspectrum wordt verwijderd. De fringefrequentie is de dominante frequentie in het spectrum van het interferogram. Deze kan worden bepaald uit het spectrum van een gebiedje van het interferogram. Dit gebiedje moet zo klein mogelijk zijn om rekening te kunnen houden met de variatie in fringefrequentie als gevolg van de topografie. Als het interferogram een zeer lage coherentie heeft, bijvoorbeeld door een lange basislijn of een slecht bepaalde coregistratie, kan de fringefrequentie niet uit het interferogramspectrum worden bepaald. De fringefrequentie kan dan worden bepaald uit de loodrechte component van de basislijn en de invalshoek, alsof het terrein vlak of ellipsoïdisch zou zijn. Ook kan de fringefrequentie dan worden bepaald uit de banen en een digitaal hoogtemodel.

De theoretische decorrelatie als gevolg van spectrale ongelijkvormigheid voor spectra met een rechthoekige omhullende kan worden omgerekend in de theoretische decorrelatie voor (Hamming) gewogen spectra. De experimentele verbetering in de coherentieschatting na filtering in azimuth en range komt zeer goed overeen met de voorspelde verbetering. De decorrelatie als gevolg van spectrale ongelijkvormigheid in azimuth en range en andere oorzaken is theoretisch multiplicatief. De experimentele decorrelatie en coherentiefactor kan worden berekend uit de geschatte coherentie voor en na filtering.

De coherentie van drie interferometrische beeldparen met een zeer lange basislijn was zeer slecht, als gevolg van basislijndecorrelatie, een slechte coregistratie en temporele decorrelatie. Bepaling van de fringefrequentie uit het interferogramspectrum was onmogelijk. Rangefiltering verbeterde de coherentie aanzienlijk. De interferometrische fasebeelden toonden de vermindering van de resolutie in range of azimuth.

Voor ERS-paren is rangefiltering is noodzakelijk afhankelijk van de basislijn. Voor ERS-1-paren is azimuthfiltering in het algemeen niet noodzakelijk, maar vaak gunstig. Voor ERS-1-ERS-2-tandemparen is azimuthfiltering vaak nuttig. Voor ERS-2-paren is azimuthfiltering in het algemeen niet noodzakelijk, maar vaak gunstig. Sinds ERS-2 met één gyroscoop functioneert is azimuthfiltering vaker noodzakelijk.

Voor exacte azimuth- en rangefiltering moet de verschuiving van de slaaf ten opzichte van de meester bekend zijn. In het algemeen wordt daardoor de grove en fijne coregistratie uitgevoerd vóór spectrale filtering. Als het interferogram een zeer lage coherentie vertoont kan de fijnregistratie slecht bepaald of onmogelijk zijn. De coherentie kan dan worden verbeterd door voorfiltering op de beelden toe te passen, waarna de coregistratieparameters worden bepaald. De originele ongefilterde beelden worden dan gecoregistreerd en gefilterd. Doordat de voorfiltering de bandbreedte en daardoor de resolutie verkleint, levert dit echter niet altijd een betere coregistratie op. Als er al een verbetering is, is de verbetering in coherentie van de gecoregistreerde beelden slechts matig.

Als de spectra van meester en slaaf niet worden overbemonsterd vóór het interferogram wordt berekend, kan het vouweffect (aliasing) in het spectrum van het interferogram optreden doordat de bemonsteringsfrequentie te klein is om te voldoen aan het Nyquistcriterium. Dit verhoogt de ruis in het interferogram. De overbemonstering bestaat uit het splitsen van de spectra op de lege band en het toevoegen van nullen zodat het aantal monsters verdubbelt. Als het interferogram moet worden beperkt tot het aantal monsters van de originele beelden, wordt laagdoorlaatfiltering uitgevoerd door de hoogfrequente

banden te verwijderen. Overbemonsteren is niet nodig als de spectra een maximale band-
breedte hebben ter grootte van de helft van de bemonsteringsfrequentie, bijvoorbeeld na
spectrale filtering. Vanwege de beperkte bandbreedte na spectrale filtering en de toepas-
sing van middeling (multilooking) na de berekening van het interferogram, zal de ruis
door het vouweffect zeer beperkt zijn, waardoor overbemonstering in het algemeen niet
noodzakelijk is.

1 Introduction

Background: radar interferometry as a geodetic technique

Two of the fields of interest to geodesy are the determination of the shape of the earth's surface and the analysis of its deformation. The shape of the surface can be digitally modelled using a digital elevation model. In the past decades elevation models were produced with aerial photogrammetry; with digital techniques the efficiency of the production of these semi-continuous elevation models have been improved. Since a few years also airborne laser scanning became an operational technique to produce a semi-continuous elevation model.

For pointwise height measurements the classic geodetic technique of levelling is employed. Since the past few years, the global positioning system GPS can serve as a cost-effective alternative to levelling, provided that the geoid is well-known and that it is used differentially. Because these discrete techniques generally yield a higher height accuracy compared to the semi-continuous techniques just mentioned, they are often applied if a deformation of the earth's surface must be analysed.

In the past few years, a newly developed remote sensing technique became operational: *radar interferometry* or interferometric synthetic aperture radar (InSAR). Remote sensing using an active microwave instrument on board of aeroplanes and satellites is applied since the 1970's, using the *synthetic aperture radar* (SAR) image formation technique. Various applications have been developed. In the 1980's the use of two radar instruments – simultaneously or in repeat-pass – have been investigated to form *interferograms*, which essentially are phase difference images.

Because the phase of an interferogram has a relation with the path length difference between the two imaging positions, a digital elevation model can be extracted from an interferogram. If in the time-span between the acquisition of two images from the same position a deformation took place, the resulting path length change is visible in the phase of the interferogram, making interferometry a suitable technique for deformation measurements.

With the launch of the European Remote Sensing satellite ERS-1 in 1991, radar interferometry became a widespread subject of intensive study. ERS-1 has covered almost the entire earth repeatedly during a time-span of almost a decade, the orbit is known very accurately and the orbit geometry is favourable to interferometry, in particular during the tandem phase with ERS-2 (Bamler and Hartl, 1998). In particular the ERS-missions resulted in making radar interferometry an important subject of geodetic research.

Problem description

To obtain an interferogram of a quality high enough to derive a digital elevation model or a deformation model, the radar backscattering properties during the acquisition of both SAR images must be as similar as possible. Only then the images show enough *correlation* to be able to calculate the phase difference accurately. If the time interval between the acquisitions is more than a few days, *temporal decorrelation* can seriously diminish the similarity of the two images. Especially in these cases the decorrelation from other sources must be minimized in order to obtain a high quality interferogram.

One cause of decorrelation between SAR images is the imaging geometry. Here a distinction is made between the flight or *azimuth* direction of the space vehicle and the radar looking direction, perpendicular to the flight track, the *range*. Because the imaged scene is viewed with different incidence angles, the backscattering properties change, leading to a deterioration of the similarity of the spectra in range: the spectra are shifted with respect to each other. In the azimuth direction a spectral shift can take place due to the difference in Doppler centroid frequency. This is the Doppler frequency of the direction in which the antenna points, which can be different for the two images.

The decorrelation caused by range and azimuth spectral shifts can be reduced by *filtering*: removing the spectral bands that are not common to both images. The development of these filters and the study of their effectivity is the goal of this thesis. Furthermore the *coherence*, a quality measure for interferograms, is studied.

The calculation of an interferogram is a complex multiplication of two images, with a resulting doubled bandwidth. To prevent aliasing from deteriorating the interferogram, *oversampling* seems to be necessary. This is another subject of our research.

Research questions

The subjects of this thesis can be summarized with the following central research question:

How can the interferogram be improved by spectral filtering in range and azimuth and by oversampling?

This question can be specified by the following questions.

On coherence:
- how can the coherence of an interferogram be calculated?
- how can it be used to estimate the quality of the interferogram?

On spectral parameters:
- what are the properties of the spectra in range and azimuth and how do they relate to the radar image processing parameters?

On filtering in azimuth:
- how can filtering in azimuth best be performed?
- what parameters does it depend on?
- under what circumstances is it necessary?
- what improvement of the coherence of the interferogram can be achieved with azimuth filtering?

On filtering in range:
- how can filtering in range best be performed?
- what parameters does it depend on?
- under what circumstances is it necessary?

- can range filtering be optimized for the slope of the terrain?
- what improvement of the coherence of the interferogram can be achieved with range filtering?

On oversampling:
- is oversampling in the filtering process necessary?
- how can oversampling best be performed?

Research approach

The research begun by collecting and studying literature as recent as possible. From the theory, algorithms have been developed and implemented, not only as a possible practical application of the work, but also to make an assessment of the improvement that can be achieved with data filtering.

Structure of this thesis

In chapter 2 of this thesis the principles of radar, the image formation technique with a synthetic aperture, and interferometry are discussed, as well as the derivation of a digital elevation model and a deformation model. A quantitative description of the quality of an interferogram is provided by the coherence. This notion, its relation with the interferometric phase and the way it can be estimated from the interferogram and used to assess the improvement achieved by SAR-processing methods is discussed in chapter 3. Because the filtering takes place in the spectral domain, the properties of the spectra in range and azimuth and the relation with the radar image processing parameters are discussed in chapter 4.

In chapter 5 the filtering in azimuth and range is discussed. The need for filtering is discussed and the filter parameters are derived. From these parameters and knowledge of the spectra, the theoretical improvement due to filtering can be derived. After this, issues on the implementation of filtering are discussed and the results of the filtering experiments are presented. In chapter 6 the need for oversampling is discussed. In chapter 7 conclusions are given. The thesis is concluded with a list of references and some appendices.

2 **Principles of radar interferometry**

In this chapter, we will discuss a selection of the principles of radar interferometry, in particular those that are needed to understand the properties of spectra described in chapter 4 and the spectral filtering treated in chapter 5.

In § 2.1, we start with radar itself; in § 2.2 we describe the way a radar is able to form an image in the range direction and in § 2.3 the image formation in azimuth direction with aperture synthesis is explained. After treating interferometry with radar in § 2.4, we describe the way to establish a digital height model in § 2.5. The ability to measure deformations with radar interferometry is described in in § 2.6. We conclude with an overview of radar interferometry processing steps in § 2.7.

2.1 **Radar and imaging**

If we generate microwave radiation – with wavelengths in the order of centimeters – and transmit it to the ground, the signal will be reflected, absorbed and scattered. By employing an antenna, we can record the amount of returning microwave radiation. Specular reflection of a transmitted pulse will occur if the material has a high dielectric constant, because of its high water content or metallic nature. If we emit a pulse of short duration, we can measure the time between the emission and the reception of an echo of the pulse. By multiplying the time difference with the speed of light, we are able to calculate the distance to the reflecting object. Here we see the origin of the term *radar*: it is an acronym for *radio detection and ranging* and this stems from military use about half a century ago.

If we measure the shift in frequency of the reflected signal due to movement of the target, we are able to measure its speed relative to the antenna. This application of radar is called *Doppler radar* because it resembles the Doppler frequency shift.

Microwave radiation has properties very different from light. Because the wavelength of radar is about ten thousand times longer than that of visible light, the interaction with the atmosphere is totally different. Radar is to a great extent independent of clouds, not very sensitive to rain and snow and because of its long wavelength it does not 'feel' microscopic particles as are present in smoke. Also its interaction with the free electron content in the ionosphere differs from that of light. Radar systems provide their own source of illumination and are to be called *active* systems, as opposed to *passive* systems that make use of reflected sunlight. A mayor distinction therefore is that radar systems can be operated during night.

The influence of the atmosphere and the echo characteristics of the terrain are

Band	Wavelength (cm)	Frequency (GHz)
K_α	0.75–1.1	40–26.5
K	1.1–1.67	26.5–18
K_u	1.67–2.4	18–12.5
X	2.4–3.75	12.5–8
C	3.75–7.5	8–4
S	7.5–15	4–2
L	15–30	2–1
P	30–100	1–0.3

Table 2.1   The microwave bands used for radar remote sensing with their name, wavelength and frequency (from Lillesand and Kiefer, 1994)

dependent of the wavelength of the radar radiation. The wavelength bands used for radar are listed in table 2.1. In this thesis, we concentrate on the European Remote Sensing satellites ERS, which employ C-band radar with a frequency of 5.3 GHz and a wavelength of 5.66 cm.

If a surface that is illuminated by the radar is not perpendicular to the transmitting direction, as is the most common geometry for reasons we will see in the next paragraph, reflection will not take place towards the receiver. If the surface material has a high dielectric constant, e.g., because of its high water content, mainly specular reflection occurs and this type of surface will appear dark in microwave images, like calm water surfaces generally are. If however the surface is rough, there are always patches that are perpendicular to the transmitted pulse and some reflection towards the receiver occurs. Generally, the rougher the surface, the higher the intensity of the received radiation. Different from specular reflection is the *scattering* mechanism, which backscatters incident energy in different directions with different intensity, dependent on the surface material, roughness and wavelength. Vegetation usually has a high water content and leaves are reflecting radar radiation well, but in general only a small part will be reflected into the direction of the receiver. However, because multiple reflections occur, eventually enough radiation is backscattered towards the receiver to show vegetation with a certain intensity in a radar image. This process is called *volumetric scattering*, as opposed to *surface scattering*, and it also occurs on a smaller scale within soil. For short radar wavelengths, almost no backscattering originates from the soil under vegetation, whereas for long wavelengths the radiation penetrates the canopy. Generally, rough surfaces appear smoother as the wavelength becomes longer. The Rayleigh criterion states that if the surface height variation is less than one eighth of the wavelength, the surface appears perfectly smooth (Lillesand and Kiefer, 1994; Zebker et al., 1994; ASF, 1998; Bamler and Hartl, 1998).

Apart from being an active system and utilizing far longer wavelengths, radar systems also operate different from optical remote sensing systems in their way of imaging. Optical images of the earth's surface can be made by registration of the sunlight the surface reflects. Different parts of the surface scatter the sunlight with different intensities and coming from slightly different directions; if this is focussed with a lens and a sheet of photographic paper is exposed, we obtain an image. We could also use a video camera or semiconductor technique, like the charge coupled device (CCD). However,
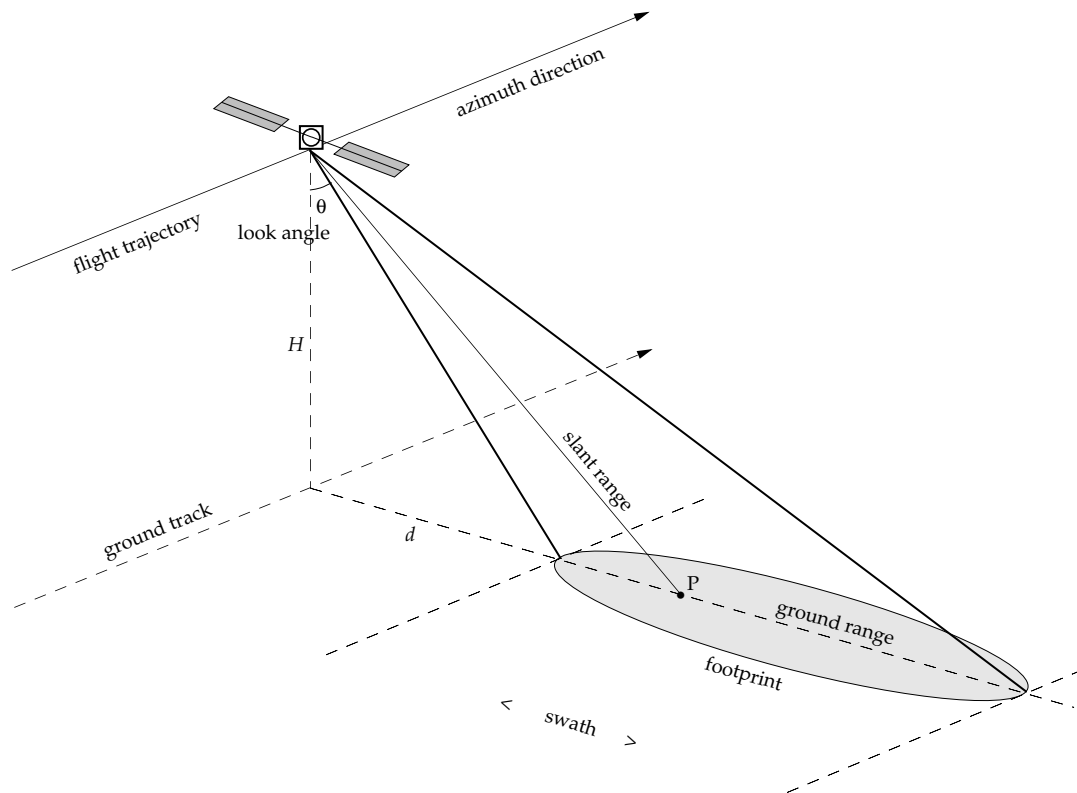
Figure 2.1   The geometry of a side-looking radar remote sensing satellite.

radar systems do not have an imaging device that distinguishes between backscattering from different directions. Only the total intensity (and phase) of the backscattered beam is recorded. The next two sections are devoted to techniques to obtain an image in both image coordinate directions.

2.2   Radar imaging in range direction: pulse compression

In this thesis, radar systems are restricted to airborne and spaceborne systems, like ERS. The direction in which the platform moves is called the *azimuth* direction. The direction in which the radar transmits and receives radiation is called *range*. This term relates directly to the ranging ability of a radar described in § 2.1. Most remote sensing radar systems are looking to one side and thus the range direction is perpendicular to the flight track and azimuth direction. In this section, the imaging mechanism in the range direction is described for an airborne or spaceborne system that is *side-looking*.

The geometry of such a side-looking radar satellite is shown in figure 2.1. The projection of the flight track onto the ground is called *ground track*. The radar looks with the *look angle* θ to the strip the radar beam illuminates. The area that is illuminated is called *footprint* and the strip is called *swath*. The look direction is the *slant range* and its projection onto the surface is the *ground range*. For the European Remote Sensing satellites ERS-1 and ERS-2, the height H is 785 km and for the Active Microwave Instrument (AMI) in image mode onboard ERS, the footprint is 100 km long and 4.8 km wide, beginning $d = 250$ km to the right of the ground track. The look angle of the microwave
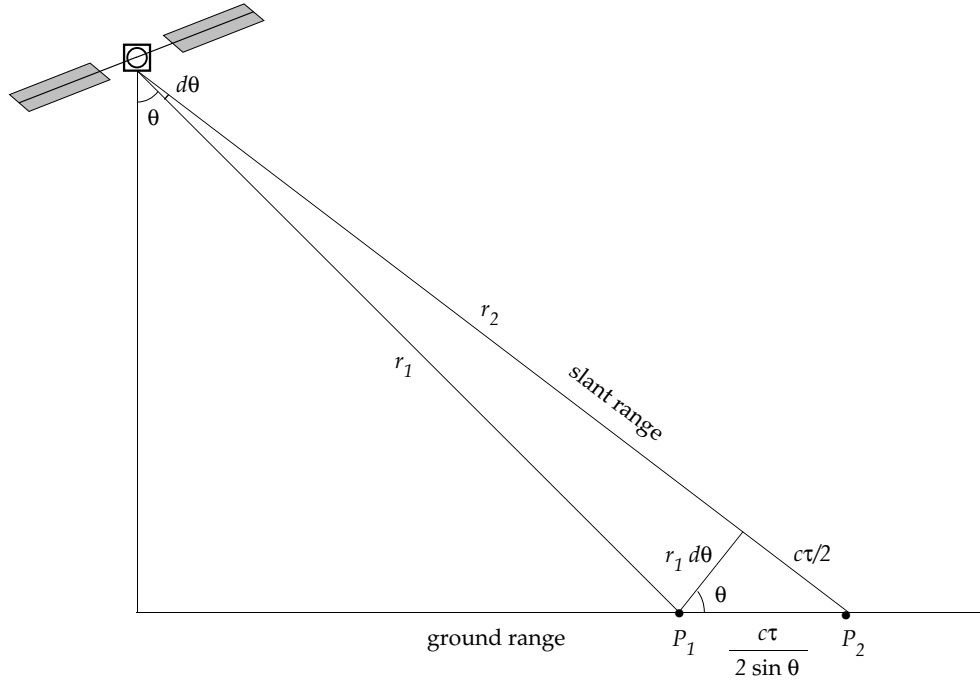
Figure 2.2   Because the round trip distance of the signal backscattered by features P_1 and P_2 is different, the radar is able to distinguish them by their different echo delay times. If P_1 is at the leading edge and P_2 at the trailing edge of a pulse with duration τ, the difference in slant range distance is $c\tau/2$. Projection onto the ground range yields a resolution of $c\tau/2\sin\theta$.

instrument is $20.355°$. Because of the ellipsoidal shape of the earth, the incidence angle at the centre of the swath is approximately $23°$ and that of the edges of the footprint are $19.35°$ to $26.50°$, if there would be no topography (ESA, 1997; ASF, 1995b). In the sequel θ will be used for the incidence angle. For simplicity the figures are drawn as if the earth were flat and without topography; only in that case the look angle equals the incidence angle.

As stated in the previous section, a radar system is not able to distinguish between reflections coming from different directions and thus is not able to establish a focused image. However, it can record the delay time differences of pulses reflected by objects with different ranges. This is illustrated in figure 2.2. A pulse is emitted to the ground. Because both features P_1 and P_2 fall within the swath and are illuminated, they both scatter part of the incident energy towards the radar antenna. Because the radar signal travels two times the distance r_1 or r_2, the delay time of the received echoes of the pulses is

$$t_1 = \frac{2r_1}{c}; \qquad t_2 = \frac{2r_2}{c}. \qquad (2.1)$$

Recording of the time delay therefore makes it possible to establish an image in the range direction.

We now see why remote sensing radar systems are *side-looking*: if they would see points on either side of the ground track, the radar would not be able to distinguish them, because they have the same range.

The radar emits pulses of radiation of duration τ; in order to separate features on the ground, the pulse length must be as short as possible. This is illustrated in figure 2.3.
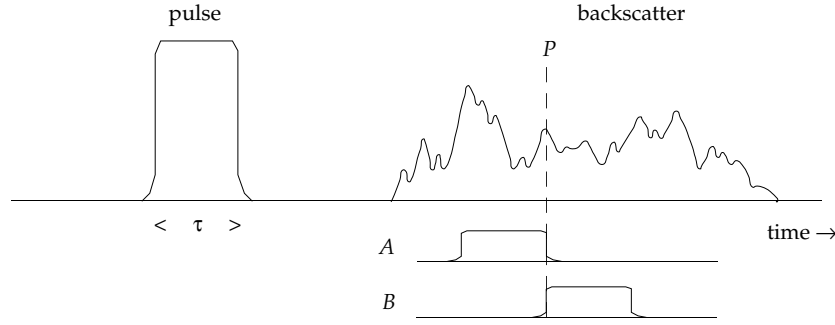
Figure 2.3   The feature P in the backscattered signal can be due to a ground feature at the trailing edge of pulse A or at the leading edge of pulse B. The resolution – the ability to resolve certain ground features – is thus determined by the pulse length τ.

The feature P in the backscattered signal can be due to a ground feature at the trailing edge of pulse A or at the leading edge of pulse B. The resolution – the ability to resolve certain ground features – is determined by the pulse length τ. The spatial separation in slant range between the edges of the pulse is $c\tau$, with c the speed of light. In figure 2.2, the slant range difference between P_1 and P_2 is $c\tau/2$ and because the reflected pulse travelled this distance twice, this is the spatial separation between reflections of the leading and trailing edges of the pulse. The resolution in slant range is therefore

$$\Delta r_{\text{slant range}} = \frac{c\tau}{2}. \tag{2.2}$$

If we project this onto the ground with incidence angle θ, we get the (ground) range resolution

$$\Delta r_{\text{range}} = \frac{c\tau}{2\sin\theta}. \tag{2.3}$$

In order to obtain a resolution as high as possible, the pulse length must be a short as possible. However, in particular for radar satellites only a very weak backscatter is received and because there is a limit to the power of the pulse, the pulse must be made longer to transmit sufficient energy to be able to receive a certain backscattered energy. So, a trade-off has to be made between resolution and signal-to-noise-ratio.

If we would be able to change the nature of the pulse by modulating it during its transmission, we would receive backscatter that reflects that modulation. We could then distinguish features smaller than the pulse length. The other way around, we could increase the pulse length and the signal-to-noise-ratio without decreasing the range resolution (Fitch, 1988). We will treat this, because then we are able to make the link with the range spectrum, which plays a mayor role in range filtering and is described in chapter 4.

Our goal is to design a pulse $u(t)$ long enough to contain a high energy but with a shape that enables us to distinguish backscattered pulses from objects with a small separation. A measure for the similarity of the two backscattered signals is the correlation. Because the signals are alike, this is the autocorrelation,

$$A(\tau_1, \tau_2) = \int u(t - \tau_1)u(t - \tau_2)\, dt, \tag{2.4}$$

which is, with a change of variables $t := t + \tau_1$ and $\tau := \tau_1 - \tau_2$,

$$A(\tau) = \int u(t)u(t+\tau)\,dt. \tag{2.5}$$

In order to obtain a high resolution, the autocorrelation should be small everywhere except where the time difference of the two signals is zero.

    In figure 2.4, the autocorrelation of different pulse shapes is shown. The classical representation of a pulse is a rectangular shape, as in figure 2.4a, or a triangular shape, as in 2.4b. According to the Maxwell laws only alternating currents are emitting an electromagnetic field and are able to propagate (Feynman et al., 1963). We must therefore modulate the pulse with a sine, as shown in 2.4c. Its autocorrelation has the same envelope as the autocorrelation of the dc (direct current, not alternating) pulse. The modulation of the pulse during its transmission we mentioned before, can be realized by linearly increasing the frequency f, as in 2.4d:

$$u(t) = \cos\left(2\pi(ft + \tfrac{1}{2}at^2)\right), \tag{2.6}$$

or in complex form,

$$u(t) = \exp\left(2\pi i(ft + \tfrac{1}{2}at^2)\right). \tag{2.7}$$

The derivative of the phase is

$$\frac{\partial\phi}{\partial t} = 2\pi(f + at), \tag{2.8}$$

which shows the linear increase of the frequency. This is a linearly frequency modulated (FM) pulse, that is called a *chirp*. As is illustrated in figure 2.4d, the autocorrelation of a chirp indeed is short: if the pulse has a duration T and starts at T_0 with frequency $f + aT_0$,

$$A(\tau) = \int u^*(t)u(t+\tau)\,dt \tag{2.9}$$

$$= \exp\left(2\pi i(f\tau + \tfrac{1}{2}a\tau^2)\right) \int \exp(2\pi i\,a\tau t)\,dt$$

$$= \Phi \cdot (T - |\tau|) \cdot \frac{\sin\left(\pi a\tau(T - |\tau|)\right)}{\pi a\tau(T - |\tau|)}, \tag{2.10}$$

where Φ is the phase factor. We recognize the sinus cardinalis, sinc $x = \sin\pi x/\pi x$, and its character is also recognizable in figure 2.4d (Fitch, 1988; ASF, 1995c; ASF, 1998).

    Using a linear FM chirp, the pulse, with a duration long enough to contain sufficient energy, can be made effectively short enough to obtain a high resolution. This is why this technique is called *pulse compression*. The width of the main lobe of the autocorrelation – and therefore the resolution – is approximately $2/aT$ and thus inversely proportional to the length of the pulse T and the increase of the chirp frequency a. As equation (2.8) shows, the bandwidth of the chirp is

$$B_{\text{chirp}} = aT \tag{2.11}$$

and therefore the resolution is improving proportional to the bandwidth of the chirp.

    However, the length of the pulse is limited by the speed of the satellite. During its

Pulse   Autocorrelation
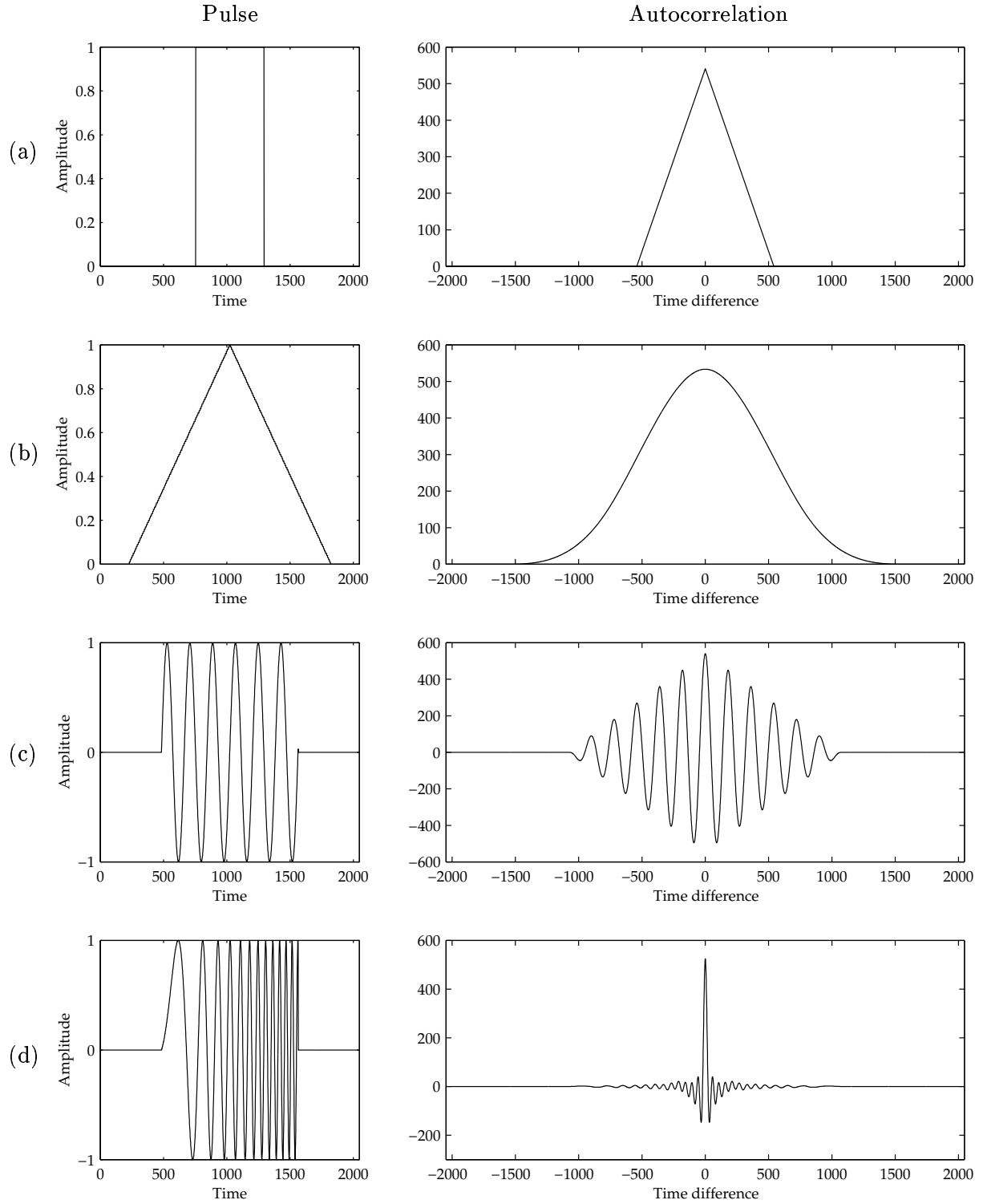
Figure 2.4   The correlation of the pulse with the backscattered signal is used to retrieve the ranges of the backscat-tering objects. The width of the autocorrelation of the applied pulse determines the possible resolution. In figure (a), a classical rectangular pulse is shown; in (b) the triangular pulse. Because only alternating currents are emitting an electromagnetic field, a rectangular pulse must be modulated with a sine (c). Its autocorrelation has the same envelope as the autocorrelation of the dc (direct current, not alternating) pulse (a). The narrowest autocorrelation and therefore the highest resolution is obtained when using a linear frequency modulated pulse or *chirp* (d).

flight, the satellite emits pulses with the *pulse repetition frequency* (PRF), each of which is used to obtain one range line in the radar image. Because of the height of the satellite, the microwave instrument records the backscatter of a certain pulse after the next several pulses have been emitted. The time between pulses must be large enough to record the reflection of a certain pulse from the near end of the swath as well as the reflection from the far end of the swath, before the next pulse is emitted.

The sinc in the autocorrelation has sidelobes, as figure 2.4d shows, which can disturb the retrieval of the features in the terrain we want to separate. By tapering the spectrum of the chirp, this can be improved. This is discussed in § 4.1.2.

This correlation can also be used to retrieve the time delays of backscattering objects. As we saw, the time delay is proportional to the range and in this way an range line image can be made. If all backscattered signal is correlated with the pulse, then – because the autocorrelation of the pulse has a narrow peak – we obtain peaks for all reflecting objects. This correlation can most efficiently be performed in the frequency domain, where a correlation becomes a multiplication. The process can be described by multiplication with a *matched filter*. This frequency domain filter is called 'matched', because essentially a replica of the transmitted pulse is compared to the received signal (Fitch, 1988; Otten, 1998; Curlander and McDonough, 1991; Jakowatz et al., 1996).

With this *pulse compression* technique, for the ERS satellites a resolution in ground range can be obtained of 25 meter. Because the signal is slightly oversampled, the 'single look complex' (SLC) SAR images supplied by the Processing and Archiving Facilities (PAFs) have a slant range pixel spacing of 7.905 meter, which is with equation (2.3) a ground range pixel spacing of 20.23 meter.

2.3   Radar imaging in azimuth direction: aperture synthesis

In this section, the formation of an image in azimuth direction is discussed. Normally, the resolution of an instrument depends on the wavelength and antenna size. In the optical case, the diameter of the lens is of interest. The angular resolution is

$$\Delta\theta = 1.22\frac{\lambda}{L} \approx \frac{\lambda}{L}, \qquad (2.12)$$

with λ the wavelength and L the antenna size or lens diameter. The factor depends on the definition of separation; 1.22 originates from the first minimum of the Airy disk: the ring pattern resulting from light falling through a circular aperture (Hecht and Zajac, 1974). By multiplying with the slant range r, we get the resolution (Curlander and McDonough, 1991),

$$\Delta r_a \approx \frac{r\lambda}{L}. \qquad (2.13)$$

For ERS, with $\lambda = 5.66$ cm, $L = 10$ m and $r = 785$ km$/\cos 23° = 853$ km, $\Delta r_a \approx 4.8$ km, the width of the footprint. To obtain a ground azimuth resolution of 26 m, like with pulse compression in the range direction, ERS would require an antenna of 1.9 kilometer. In 1951 a technique was discovered to obtain a higher resolution with moderate antenna sizes that utilizes the Doppler shift.

In § 2.2, resolution in range was achieved by discriminating backscatter by its round trip delay. As figure 2.5 shows, in this way objects in the footprint that have the same range cannot be separated. However, because the component of the satellite's velocity in the look directions is different, the frequency of the backscattered signal has a Doppler
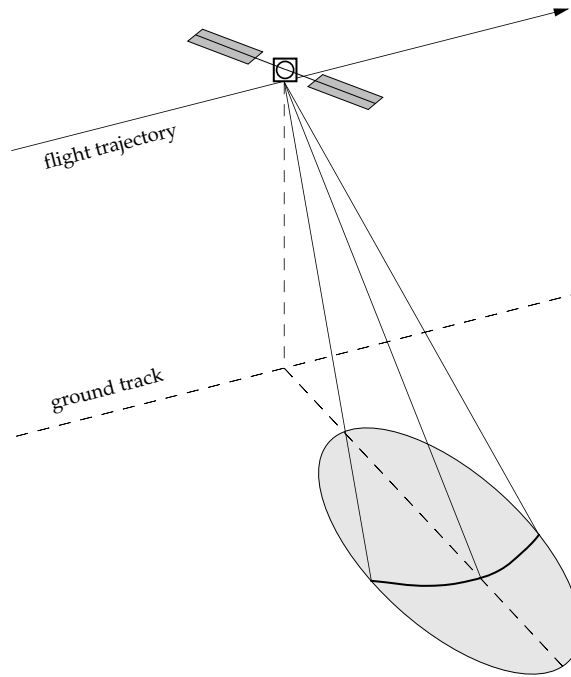
Figure 2.5   Objects in the footprint lying on the thick circle segment have the same range and cannot be separated with their round trip delay. However, because the component of the satellite's velocity in the look directions is different for those objects, they can be separated utilizing their Doppler shift.

shift depending on whether the object is ahead of the satellite or not. This Doppler shift thus can be used to separate the echoes of the objects with the same range in the beam.

A certain object can be traced in the recorded received radar signal on the basis of the expected Doppler shift, as figure 2.6 shows. If the satellite is at position a, object P is ahead of the satellite and the received frequency has a positive Doppler shift. If the satellite arrives at position b, the look direction to P is perpendicular to the satellite's flight trajectory and the Doppler shift is zero. At position c, the Doppler shift of radiation backscattered by P is negative. Each object that was in the footprint during adjacent pulses, therefore has a 'Doppler history' that can be used to extract its backscatter from the raw data. But because of the effect illustrated in figure 2.5, the range of an object varies during the passage of the footprint. This is called *range migration*. The surface of the earth meanwhile is moving due to the earth's rotation, adding a further Doppler effect.

To resolve the features on the surface from this complicated signal, the backscattered signal can be correlated in a way similar to the correlation in range, shown in § 2.2. If the signal is correlated with the expected Doppler shifted response, the position of the objects in azimuth can be obtained. Like in range, this matched filter processing in azimuth can best be done in the frequency domain (ASF, 1995c; ASF, 1998; Fitch, 1988; Curlander and McDonough, 1991; Otten, 1998).

The influences of the range response and the azimuth response are not separable. This complicates the processing of SAR data to a great extent. Otten (1998) gives a concise overview of several techniques that have been developed to approach this problem.

The operation of the matched filter in azimuth to obtain a resolution can be compared to the operation of a lens in optics. The signals from different parts of the beam
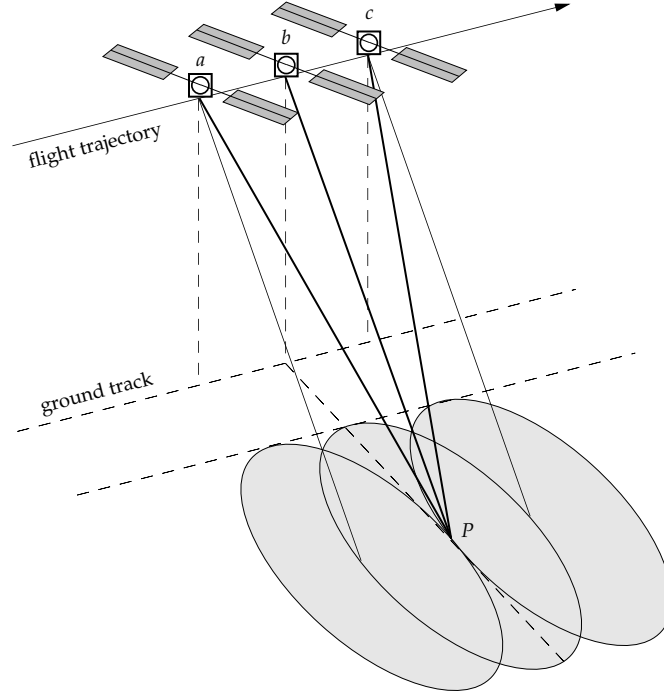
Figure 2.6   An object P can be traced in the recorded radar signal on the basis of the expected Doppler shift. If the satellite is at position a, object P is ahead of the satellite and the received frequency has a positive Doppler shift. If the satellite arrives at position b, the look direction to P is perpendicular to the satellite's flight trajectory and the Doppler shift is zero. At position c, the Doppler shift of radiation backscattered by P is negative.

are delayed due to the refractive index of the glass of the lens, the most where the lens is the thickest. The effect is that all signals arrive at the same time. This operates as a coherent summation of the signal (Hartl et al., 1996). In a similar way the signals the satellite received while moving in its orbit are processed. Because the backscattering of an object is recorded by the satellite as long as the object is in the footprint, the antenna of the satellite is effectively extended to a section of the track equal to the width of the footprint. In fact use have been made of a synthetic antenna, hence the name *synthetic aperture radar* or SAR (Fitch, 1988).

The resolution that can be achieved in azimuth with this synthetic aperture technique can be shown to be

$$\Delta r_a \approx \frac{L}{2}. \tag{2.14}$$

Compare this with equation (2.13) (Curlander and McDonough, 1991). For ERS, with its antenna size of 10 m, the resolution achieved is approximately 5 m. Because of the sampling characteristics the pixel – or azimuth line – spacing in the single look complex images provided by the PAFs is approximately 3.97 meter (ASF, 1995b; ESA, 1997).

Equation (2.14) suggest that a higher resolution could be obtained by decreasing the antenna size, the opposite of the requirement discussed before. However, decreasing the antenna in size results in the received power to decrease. The bandwidth of the Doppler signal relates to the swath width and must be smaller than the pulse repetition frequency. Curlander and McDonough (1991) show that this implies that the radar must transmit at least one pulse each time the satellite travels a distance equal to half the antenna length.
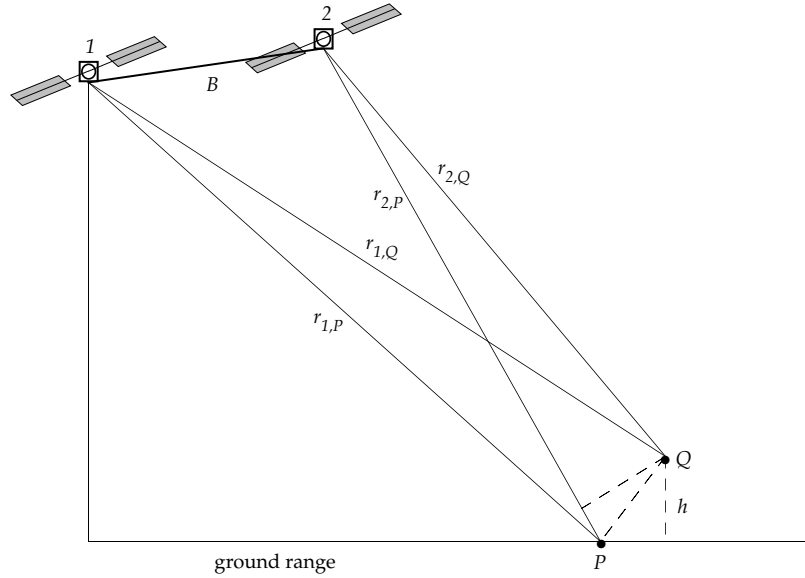
Figure 2.7   An object Q having a different ground range from object P cannot be separated from P on the basis of its round trip delay to satellite position 1, because due to its height h, it has the same range: $r_{1,Q} = r_{1,P}$. From position 2, Q can be separated from P, because $r_{2,P} \neq r_{2,Q}$. Interferometry utilizes path length differences like this to resolve height ambiguities.

2.4   Interferometry

If objects in the terrain do not have the same ground range, this does not imply that they can always be separated on the basis of their different round trip delay, as described in § 2.2. The height of an object can cause the range to the satellite to be the same, as figure 2.7 illustrates. Adding information by measuring the range difference from an other viewpoint can resolve this problem.

Interferometry is a technique that utilizes the path length difference induced by a separation between the two imaging viewpoints. This separation is called the *baseline B*. The path length difference induces a phase difference. For SAR interferometry, not only the amplitude A but also the phase ϕ of the received signal should be recorded:

$$c_1 = A_1 e^{i\phi_1}; \qquad c_2 = A_2 e^{i\phi_2}. \tag{2.15}$$

For interferometry it is essential that the imaging and processing process is *coherent*, i.e., the phase of the signal is preserved. In general, the SAR-processing does not cause phase errors (Geudtner, 1995; Zebker et al., 1994).

A configuration of two antennae or image forming devices is called an *interferometer*. Different configurations exist. In a *single-pass* configuration, an airborne or spaceborne platform carries two antennae, acquiring images at the same time. The separation between the antennae is small, but the relative positions of the antennae are fixed and very well known. If a high sensitivity to path length differences is necessary, the separation between the two antennae sould be high and they can no longer be mounted on the same platform. Then a *repeat-pass* configuration is used, where the same or a similar platform realizes a second pass with a certain separation to the first pass. The separation can be in the flight direction (*along-track*) or in the direction perpendicular on the flight trajectory (*across-track*). For ERS, the used technique is repeat-pass, across-track

interferometry.

The most important interferometric image product is the *interferogram*. An interferogram consists, for each pixel, of the product of the complex response of the first (or *master*) image c_1 and the complex conjugate of the response of the second (or *slave*) image c_2,

$$I = c_1 \cdot c_2^* = A_1 A_2 e^{i(\phi_1 - \phi_2)}. \tag{2.16}$$

The *interferometric phase* is the phase of the complex interferogram,

$$\phi = \arctan\left(\frac{\mathrm{Im}(I)}{\mathrm{Re}(I)}\right) = \phi_1 - \phi_2. \tag{2.17}$$

Because a path length difference is equivalent to a phase difference, we see that the interferometric phase reflects path length differences due to the imaging geometry.

The way the interferometer geometry yields an interferometric phase is illustrated in figure 2.8, where the satellite acquired SAR images on position 1 and 2 of a scene on the flat earth. The distance B between those positions is called the *baseline*. The slant range from satellite position 1 to point P is $r_{1,P}$ and the phase of the radar signal over this round trip distance is

$$\phi_{1,P} = -\frac{4\pi}{\lambda} r_{1,P}. \tag{2.18}$$

The minus sign is due to the SAR processing and we use it by definition (Bamler and Hartl, 1998). The phase recorded by satellite 2 from point P is

$$\phi_{2,P} = -\frac{4\pi}{\lambda} r_{2,P}. \tag{2.19}$$

The interferometric phase is the phase difference $\phi_1 - \phi_2$ from (2.17),

$$\phi_P := \phi_{1,P} - \phi_{2,P} = -\frac{4\pi}{\lambda} \Delta r_P. \tag{2.20}$$

The range difference of P as seen from both satellites is Δr_P. The thick circle segment between satellite 2 and q_2 in figure 2.8 denotes the curve where the range is equal to $r_{2,P}$. The distance d from q_2 to 1 is thus Δr_P. Now, if

$$d(1, q_2) = \Delta r_P = \frac{n}{2}\lambda, \qquad n \in \mathbb{Z}, \tag{2.21}$$

the round trip range difference is exactly an integer number times the wavelength and the signals received at 1 and 2 are in phase. Thus, the interferometric phase is zero. If we now shift from point P to a point Q, the location of point q_2 shifts into the direction of q_1 and the range difference Δr_P decreases. If we reach point Q,

$$d(1, q_1) = \Delta r_Q = \frac{n-1}{2}\lambda, \qquad n \in \mathbb{Z}, \tag{2.22}$$

and the round trip range difference again is an integer number times the wavelength, the number now being one lower. We thus showed that the interferometric phase over the ground range from P to Q drops from zero to -2π and, wrapped to the interval $(-\pi, \pi]$,
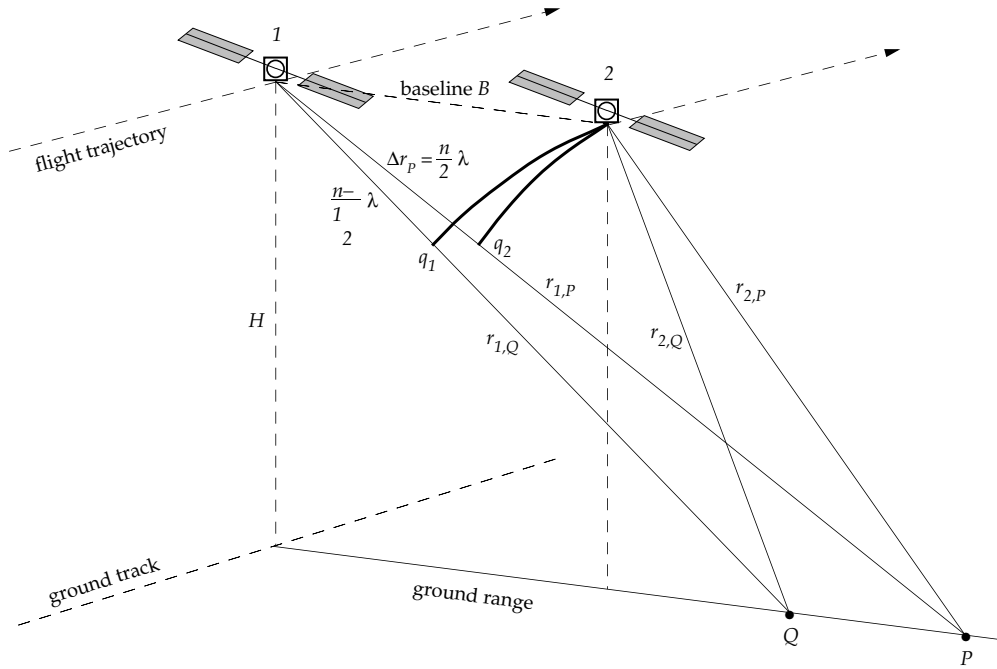
Figure 2.8   Satellites 1 and 2 form an interferometer with baseline B. If the range distance difference to point P is $\Delta r_P = r_{1,P} - r_{2,P} = \frac{n}{2}\lambda$, $n \in \mathbb{Z}$, the interferometric phase of P is zero. If we shift from P to Q so that $\Delta r_Q = r_{1,Q} - r_{2,Q} = \frac{n-1}{2}\lambda$, the signals at 1 and 2 are again in phase and the interferometric phase decreases to -2π and, wrapped to the interval $(-\pi, \pi]$, that is again zero. With this figure we are able to derive the pattern of the interferometric phase for this interferometer geometry.
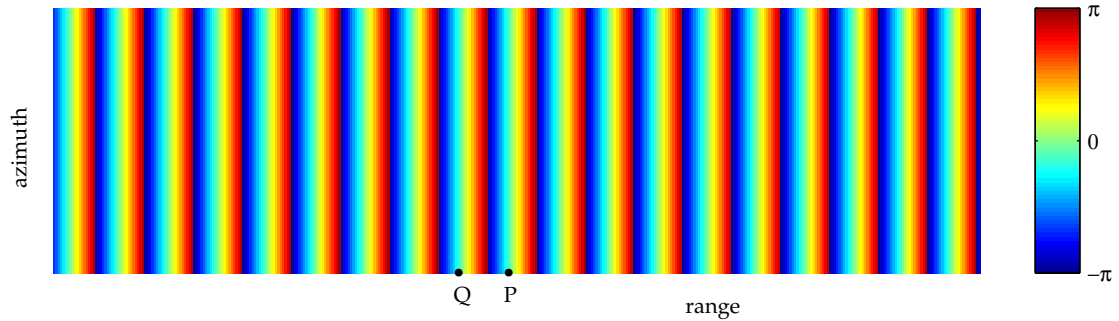
Figure 2.9   The interferometric phase pattern viewed by the interferometer of figure 2.8, if the earth's surface would be flat. Each band or *fringe* denotes a phase range from $-\pi$ to π.

that is again zero.

If we would extend this to the whole footprint of the interferometer and the surface would be flat, an interferometric phase pattern develops like the one shown in figure 2.9. The coloured iso-phase bands used to denote the interferometric phase are called *fringes* and are – if the orbits are parallel – perpendicular to the range direction and parallel to the flight trajectory. If the orbits are not exactly parallel, the fringe rate alters slightly depending on azimuth (Geudtner, 1995; Schwäbisch, 1995); because the footprint is usually far from the ground track, the fringes viewed in the interferogram are

approximately parallel but show an angle with the azimuth direction. An example of a
fringe pattern from ERS-data is shown in figure 2.11 of the Canary Island Fuerteventura;
because it is not flat, the fringes are not straight and parallel, as will be discussed in § 2.5.

The distance between the fringes decreases – and the *fringe frequency* increases –
if the baseline gets longer. This can be concluded from figure 2.8 but can also be derived
in a more mathematical way, using figure 2.10. We will consider a flat earth, where the
look angle θ equals the incidence angle. With this angle θ and a baseline B that shows a
slope angle of ξ, the length of the baseline component perpendicular to the look direction
and that parallel to it are

$$B_\perp = B \cos(\theta - \xi) \qquad (2.23)$$

$$B_\parallel = B \sin(\theta - \xi) \qquad (2.24)$$

The path length difference between both ends 1 and 2 of the baseline is Δr. As we saw
before, and illustrated in figure 2.8, if the look direction is rotated so that the path length
difference increases with half the wavelength, the round trip distance increases with a
wavelength and the phase with 2π, causing one fringe. Let us call the angle over which
the perpendicular baseline is rotated $\Delta\theta$, then the distance over which the range r_0 is
rotated is $g_\perp$,

$$\Delta\theta \approx \frac{\lambda/2}{B_\perp} = \frac{g_\perp}{r_0} \qquad (2.25)$$

$$\Leftrightarrow \quad g_\perp = \frac{\lambda r_0}{2 B_\perp}. \qquad (2.26)$$

If we project $g_\perp$ onto the ground, which is assumed to be flat, we have the fringe distance
g_{fringe},

$$g_{\text{fringe}} = \frac{g_\perp}{\cos\theta} = \frac{\lambda r_0}{2 B_\perp \cos\theta}. \qquad (2.27)$$

The fringe distance decreases linearly with the increase of the perpendicular baseline $B_\perp$
and decreases with the cosine of the look angle θ and the distance to the ground track.
For example, for a perpendicular baseline of 300 meter of ERS, the distance between
fringes for a flat earth is

$$g_{\text{fringe}} = \frac{\lambda H}{2 B_\perp \cos^2\theta} = \frac{0.0566 \cdot 785000}{2 \cdot 300 \cdot \cos^2 23°} = 87 \text{ meter.} \qquad (2.28)$$

With a ground range pixel spacing of 20.23 meter, this is equivalent with 4.3 range pixels.

We could interpret the fringe distance g_{fringe} as a 'ground fringe wavelength' and
translate it into a 'ground (or object) fringe frequency' $f_{\text{fringe},g}$,

$$f_{\text{fringe},g} = \frac{c}{g_{\text{fringe}}}. \qquad (2.29)$$

This ground fringe frequency is often expressed in cycles per pixel. It can be projected
onto the viewing direction, like the pulse length $c\tau$ in equation (2.3), where the factor 2
accounts for the round trip,

$$f_{\text{fringe}} = \frac{f_{\text{fringe},g}}{2 \sin\theta} = \Delta f_r. \qquad (2.30)$$

This fringe frequency is denoted with Δf_r, because it turns out to be the range frequency
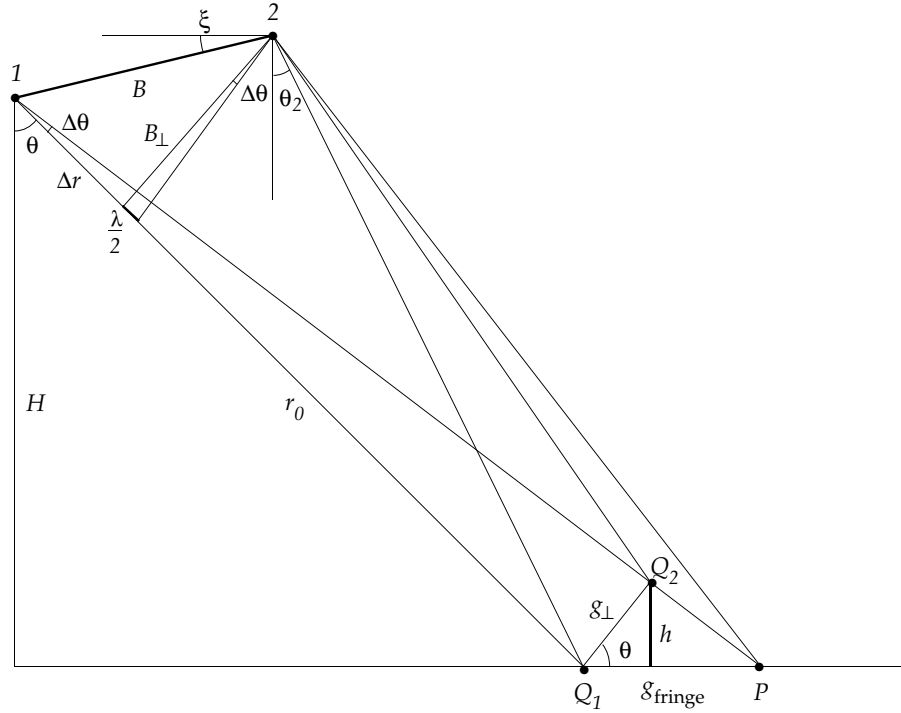
Figure 2.10 The separation on the (flat) ground of two points P and Q_1 that are exactly one fringe of the interferogram apart, can be calculated by rotating the view direction over an angle $\Delta\theta$, so that the perpendicular component $B_\perp$ of the baseline B of the interferometer that 1 and 2 form, spans a range distance difference of $\lambda/2$. An object Q_2 with the same range as Q_1 but at a height h causes also exactly one fringe.

shift in the section on spectral filtering, § 5.2.2. In this way, the fringe frequency has been projected in the dimensions of the SAR image. With equations (2.27) and (2.30),

$$\Delta f_r = \frac{2cB_\perp \cos\theta}{2\sin\theta\,\lambda r_0} = \frac{cB_\perp}{\lambda r_0 \tan\theta} = \frac{cB_\perp \cos\theta}{\lambda H \tan\theta}. \tag{2.31}$$

For the example presented in equation (2.28), the fringe frequency in the SAR data will be $\Delta f_r = 4.4$ MHz. The expression of the fringe frequency in megaHertz is common for spectral filtering; however, it is also often expressed in fringe cycles per pixel. For this example, with equation (2.28) and a ground range pixel spacing of 20.23 meter, this is equivalent with 0.23 fringe cycles per pixel.

Derivations different from the one presented here can be found in the literature, where a minus sign can be present (Hartl et al., 1996; Gatelli et al., 1994; Geudtner, 1995); alternative derivations will be presented in § 5.2.2 and in appendix B. The fringe frequency is the central parameter to spectral filtering in range.

In this section, we derived the interferometric phase and the fringe pattern of the earth if it would be flat. This phase image is called *flat-earth correction* or – also in the case of the ellipsoidal surface – *reference phase*. What happens if the surface is not flat will be discussed in the next section.

azimuth
↓

← range

Figure 2.11   The interference
pattern of the interferometric
phase of the Canary Island
Fuerteventura. The differences
with the straight fringe pattern
like that in figure 2.9 are mainly
due to the topography. The sea
shows noise because the surface
has changed and hence the phase
shows no correlation. The range
direction is horizontally; the
ground track is to the right of
the image, as can be seen from
the *layover* of the mountain tops.
That the fringes are not perpen-
dicular to the range direction is
caused by the orbits being not
exactly parallel.
(Figure from Schwäbisch, 1995.)

azimuth
↓

← range

Figure 2.12   The interference
pattern of the interferometric
phase of the Canary Island
Fuerteventura after the fringes
due to the 'flat earth' have been
removed. Compare with figure
2.11. The fringe pattern bears re-
semblance with a iso-height
contour map. (Figure from
Schwäbisch, 1995.)

2.5   Derivation of an elevation model with interferometry

In this section, the derivation of an elevation model from an interferogram is discussed. For the subject of this thesis – spectral filtering of the SAR images – we do not need to know much about it; the discussion will be concise.
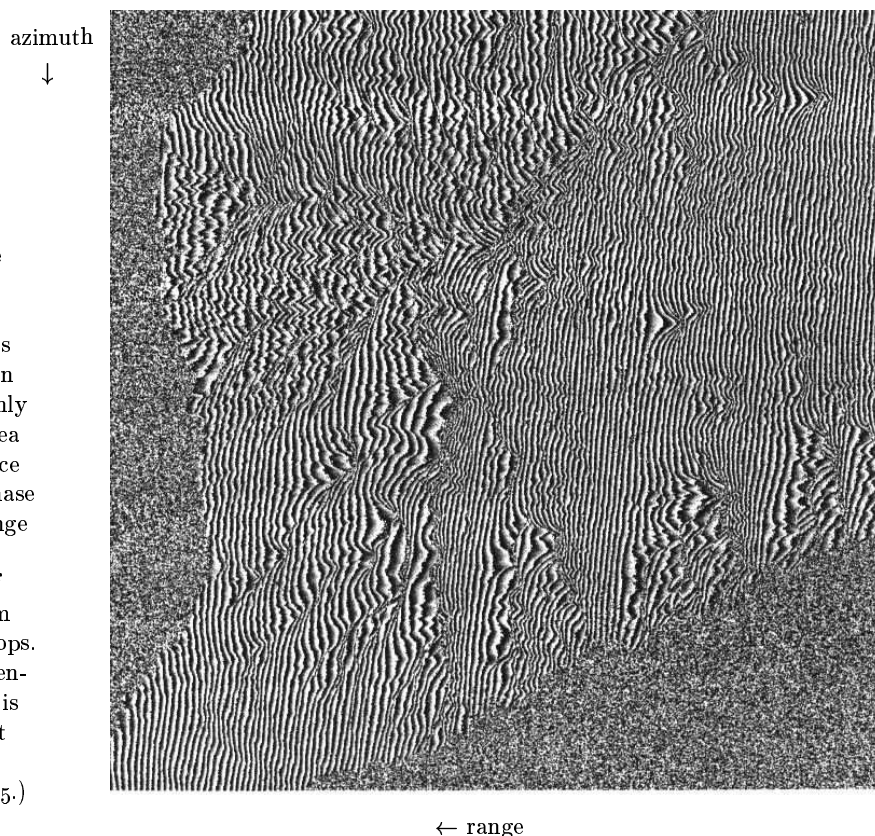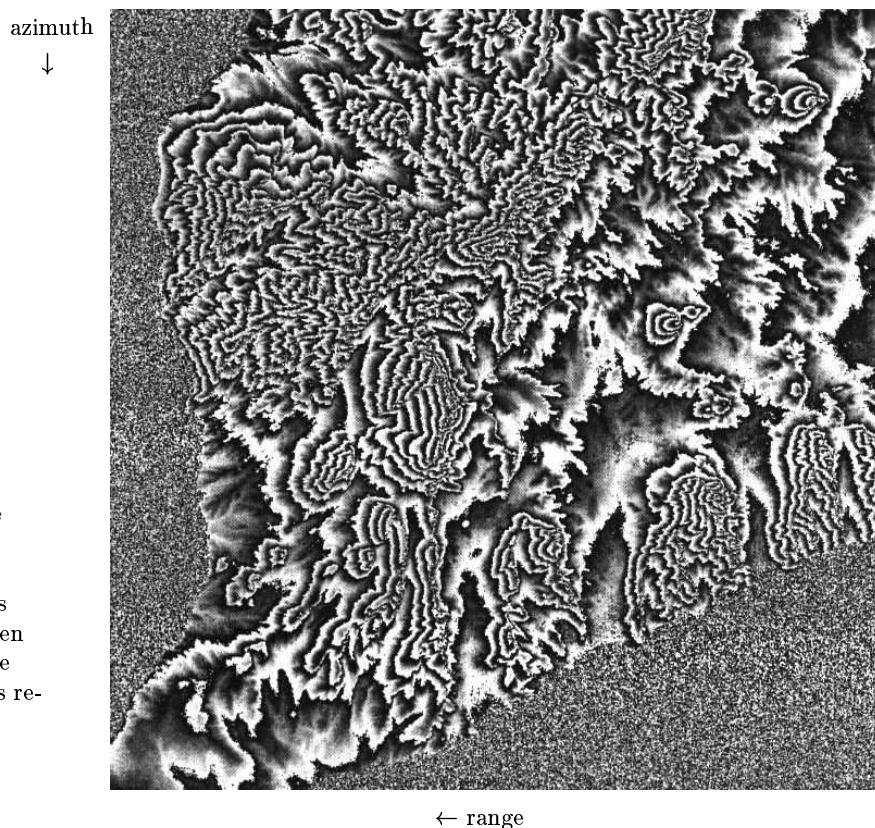
The topography of the earth induces ranges different from that of the 'flat earth', which cause the interferometric phase to show a different fringe pattern. In figure 2.11 of the Canary Island Fuerteventura, the excursions from the straight fringe pattern due to mountains are clearly visible. The sea shows noise because the surface has changed and hence the phase shows no correlation. Because the mountain tops have a range less than a flat surface, they move into the direction of the ground track, an effect known as *foreshortening*.

We can extend the treatment of the fringe pattern in § 2.4 to fringes induced by height differences. In figure 2.10, point Q_2 has the same range as Q_1 because it has height h, but it is shifted over angle $\Delta\theta$ and distance $g_\perp$. A height h thus causes exactly one fringe. This height, known as *ambiguity height $h_{2\pi}$*, is, with equation (2.26), (Bamler and Hartl, 1998; Hanssen and Klees, 1998)

$$h_{2\pi} = g_\perp \sin\theta = \frac{\lambda r_0 \sin\theta}{2B_\perp}.$$

(2.32)

With the example equation (2.28) for ERS from the previous section,

$$h_{2\pi}(B_\perp = 300 \text{ m}) = 31 \text{ meter}.$$

As is clear from equation (2.32) and is shown in figure 2.13, the longer the baseline of the interferometer, the higher the sensitivity to height variations. However, a limit on the effective baseline length exists; for ERS, this is 1060 meter (see § 5.2.2).

The interferometer measures the interferometric phase (equation 2.17). If the geometry of the interferometer is known, i.e., its height H, look angle θ and baseline length B and slope angle ξ, heights can be calculated from the phase. In figure 2.10, the path length difference is

$$\Delta r = B \sin(\theta - \xi).$$

(2.33)

In the interferogram, a relation between the look angle θ of a certain detail, its range r_0 and its height h exists,

$$\theta(h) = \arccos\left(\frac{H-h}{r}\right) = \arccos\left(\cos\theta_0 - \frac{h}{r}\right), \qquad \theta_0 = \theta(h=0).$$

(2.34)

Now we can substitute this into equation (2.33) and expand it in a Taylor series around $h = 0$ up to and including second order,

$$\Delta r(h) \approx B\sin(\theta_0 - \xi) + \frac{B\cos(\theta_0 - \xi)}{r_0 \sin\theta_0}h - \frac{B\cos\xi}{2r_0^2 \sin^3\theta_0}h^2.$$

(2.35)

Instead of using this Taylor series, equation (2.34) can also be linearized, after which the equation can be solved by iteration.

By using equation (2.20), we can translate equation (2.35) into the interferometric phase,

$$\phi(h) = -\frac{4\pi B}{\lambda}\left(\sin(\theta_0 - \xi) + \frac{\cos(\theta_0 - \xi)}{r_0 \sin\theta_0}h - \frac{\cos\xi}{2r_0^2 \sin^3\theta_0}h^2\right).$$

(2.36)

The first term is that for $h = 0$, which is the phase due to the 'flat earth'. The second-order term is small compared to the linear term; iteration would therefore also yield the solution efficiently (Schwäbisch, 1995). By using the interferometric phase, we are now in principle able to establish a digital elevation model (DEM).

If the phase due to the 'flat earth' is subtracted, i.e., the first term in equation (2.36), a fringe pattern results that bears resemblance with a iso-height contour map (Bamler and Hartl, 1998). In figure 2.12, this is shown for Fuerteventura; compare this with figure 2.11. If the geometry of the interferometer is known, the ambiguity height $h_{2\pi}$ between two fringes is known and a digital elevation image can in principle be calculated by counting the fringes and multiplying with $h_{2\pi}$.

The first step in the derivation of an elevation model is to calculate the reference phase: the phase of the 'flat earth' or the ellipsoid. This can be done by fitting the fringes of a plane in range and azimuth to the interferometric fringes, but mostly, the orbital parameters are calculated or acquired, after which the geometry of the interferometer is known. The orbits can be calculated by using corner reflectors and/or terrain reference points, but they are in general not available. An estimation in a process mixed with the geolocation has been developed by Schwäbisch (1995). Geudtner (1995) also developed a method. An alternative is to calculate the expected phase from a digital elevation model, which then must be available (Massonnet and Feigl, 1998); in this case the reference phase is not that of the 'flat earth' or earth ellipsoid. However, usually precise orbits are used, as published by research institutes like DEOS of Delft University of Technology.

If the reference phase ϕ_{ref} is subtracted, the interferogram equation (2.16) becomes

$$I = c_1 \cdot c_2^* \cdot e^{-i\phi_{\mathrm{ref}}} = A_1 A_2 e^{i(\phi_1 - \phi_2 - \phi_{\mathrm{ref}})}. \tag{2.37}$$

As fringe images already show, in an interferogram and also in the reference-phase-corrected interferogram, the interferometric phase is only known modulo 2π. The second step in the derivation of an elevation model is to correct this *phase ambiguity*. This is done in an integration process known as *phase unwrapping*. If the height of a certain point is known, its phase is the starting point for the integration of the phase with multiples of 2π and thus integration of the height with the ambiguity height $h_{2\pi}$. Because of noise in the interferogram, this is one of the most challenging tasks in radar interferometry. Different integration paths can yield different multiples of 2π, in which case *residues* remain (Goldstein et al., 1988; Geudtner, 1995; Schwäbisch, 1995; Bamler and Hartl, 1998; Massonnet and Feigl, 1998; Davidson and Bamler, 1999; Xu and Cumming, 1999).

The number of fringes must be high to be able to estimate the phase accurately, but a fringe rate too high can cause the fringes to become indistinguishable, especially if the terrain topography shows variations. The subtraction of the reference phase is a favourable first step to decrease the fringe rate, without losing the height information (Schwäbisch, 1995). The *layover* effect mentioned before and visible in figure 2.11 causes the fringes to be compressed at the slopes of mountains directed towards the viewing position. As long as the slope of the hill, denoted by α, is less than the incidence angle for a flat earth θ, the fringes can still be distinguished. Because the active microwave instrument on board of ERS was designed primarily to monitor ocean phenomena, its look angle is relatively small ($20.355°$), resulting in an incidence angle of approximately $23°$ if the surface would be flat (ASF, 1999). For the establishment of elevation models in mountainous areas, this is not favourable. Althought RADARSAT has some other draw-backs, its look angle of $45°$ makes it useful for radar interferometry and the calculation

Ambiguity height for ERS
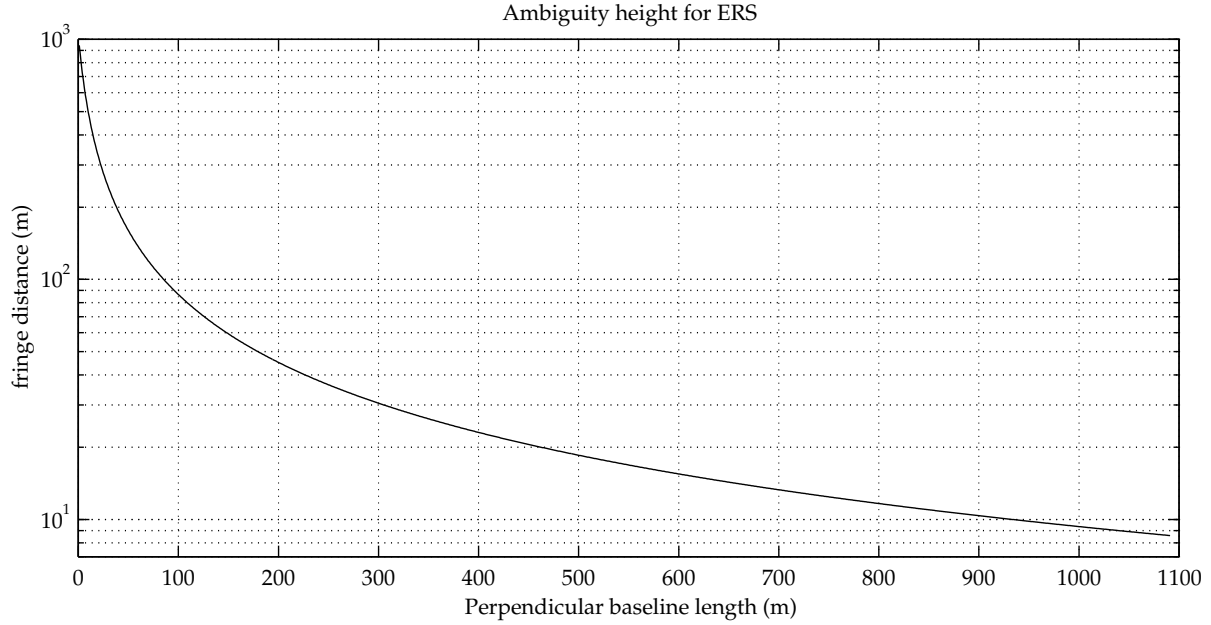
Figure 2.13   For ERS, the height ambiguity is shown, i.e. the height causing an interferometric phase change of 2π. The longer the effective baseline $B_\perp$ of the interferometer, the higher the sensitivity to height variations.

of elevation models (Geudtner et al., 1998; Gens and Van Genderen, 1996b).

The calculation of a digital elevation model relies on the interferometric phase (equation 2.36). In order to be able to derive a digital elevation model with an error as small as possible, the only difference between both SAR images should be the phase difference induced by the different viewpoints of the satellites. Other phase components can cause errors. The realisation of the phase of the interferogram is discussed in § 3.1; sources of decorrelation are described in § 3.2. One source of decorrelation is the spectral misalignment between the master and slave image, discussed in chapter 5.

The noise in the interferogram that is corrected for the reference phase can be decreased by *filtering*. Mostly this is a smoothing operation along the fringes. Because it depends on the fringe frequency and the orientation of the fringes, it is called *adaptive*. These adaptive filtering methods are totally different from the spectral filtering in this thesis, that in range can also be adaptive; see § 5.2.5.

2.6   Derivation of deformation with differential interferometry

If an interferogram is calculated from two SAR images taken from the same position but at different time instants, a change in path length during the time interval between the image acquisitions will cause a change in interferometric phase. A deformation with a component δr in the satellite viewing direction, for example due to land subsidence, will cause a differential interferometric phase

$$\delta\phi = -\frac{4\pi}{\lambda}\delta r.\tag{2.38}$$

In this way deformations in the order of a small fraction of the wavelength are distinguishable (Bamler and Hartl, 1998). However, in general the baseline does not equal zero and an additional phase difference due to topography and the imaging geometry occurs. This

geometry-induced interferometric phase can be calculated from a topography-pair as in § 2.5 or from an existing digital elevation model. From the phase of a second interferometric pair, this topography-induced phase can be subtracted. In the remaining phase, only phase differences due to deformation are present, except for additional phase delays caused by atmospheric phenomena. This is called *differential interferometry* (Hanssen and Klees, 1998).

The determination of deformation with differential interferometry is only possible if the properties of the scatterers remain the same during the temporal separation between the acquisitions. This requirement is often difficult to fulfil. As treated in § 3.2, often *temporal decorrelation* deteriorates the coherence between parts of the two interferograms and the determination of the deformation is hampered (Bamler and Hartl, 1998). However, use can be made of man-made features like buildings, which better preserve their backscattering characteristics (Usai and Klees, 1999).

Because of the high sensitivity of differential interferometry, atmospheric effects can pose major problems (Massonnet and Feigl, 1998). This is illustrated by the phase variations in figure 5.31, where the topographic phase is known to be limited and no deformation took place.

If high-coherence features are used, like corner reflectors, deformations of 2 mm can be detected with ERS, depending on the distance between points and the present atmosphere delays. For less coherent surfaces, the accuracy can be in the order of centimeters (Schwäbisch, 1995).

Not only height differences due to for example subsidence can be measured, also horizontal shifts, as long as the deformation has a component in the viewing direction. In this way earthquakes and glacier movements can be monitored. SAR differential interferometry thus can serve as an important geophysical measuring tool (Massonnet and Feigl, 1998).

2.7   Interferometric processing steps

In this section, the processing steps typical for interferometry are listed. This concise treatment is not only presented to get an idea of the process, but will also serve as the framework in which in chapter 5 the spectral filtering will be positioned. In figure 2.14 this is illustrated; the processing steps discussed in this thesis are outlined in grey.

The process starts with the selection of a suitable (i.e., with respect to decorrelation, § 3.2) master and slave single look complex SAR image pair. Also the precise orbits are acquired or calculated.

The images of the same scene must be aligned exactly in order to be able to calculate the interferogram (2.16). In the first step, called *coarse coregistration*, the offset of the slave image with respect to the master image in integer pixels is determined. Knowledge of the orbits can be of help. After this, during *fine coregistration* a subpixel transformation – including stretch, shear, etc. – is determined so that all parts of the images coincide as good as possible. This fine registration is determined with a correlation or coherence estimation of patches regularly distributed over the images.

If the Doppler centroid frequency of the master and slave image is different, the azimuth spectra of the master and slave are misaligned (§ 5.2.1). For high differences this can result in a serious coherence and interferogram quality reduction. In order to improve this, spectral filtering in azimuth of the single look complex images can be performed before the interferogram is calculated (§ 5.4). If the perpendicular component
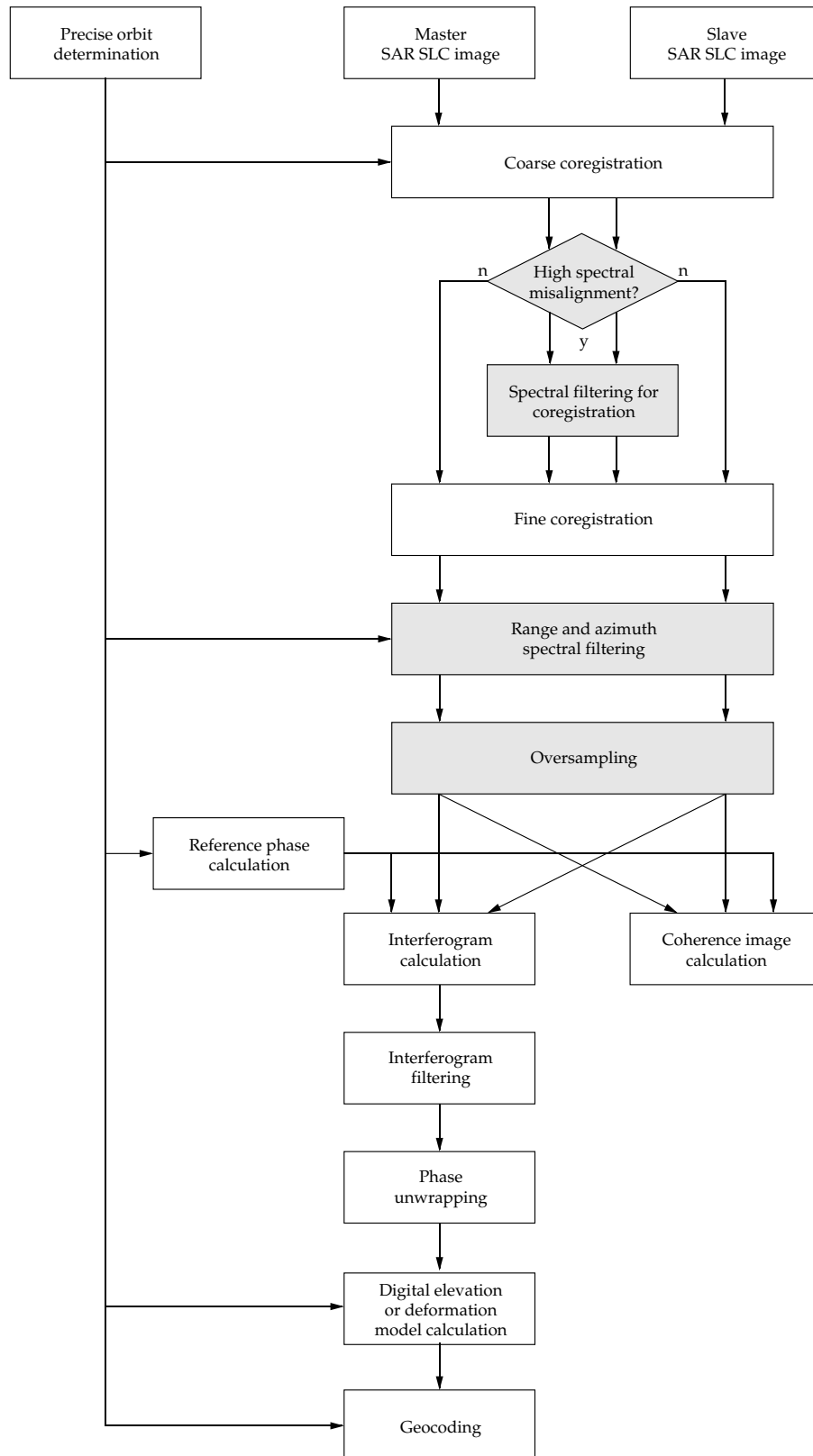
Figure 2.14 Overview of the interferometric processing steps. The grey steps are discussed in this thesis.

of the baseline is long, the range spectra of master and slave are misaligned (§ 5.2.2). To improve the interferogram quality, in a similar way spectral filtering in range of the single look complex images can be performed (§ 5.6). If the baseline is very long, determination of the fringe frequency from the images can be difficult and the orbit parameters are used instead.

Because the fine registration utilizes the correlation between master and slave, it suffers from spectral misalignment in range or azimuth. The fine registration and all consecutive steps can be improved by determination of the registration parameters from spectral filtered SLC images (Geudtner, 1995). After determination of the registration parameters, the next processing step uses the original, unfiltered images (§ 5.9).

From the orbits or an existing digital elevation model, the reference phase is determined: the phase of the flat or ellipsoidal earth or existing coarse elevation model (§ 2.4).

To prevent aliasing from deteriorating the interferogram, the master and slave image are oversampled before the interferogram is calculated, if the bandwidth of the interferogram would otherwise be greater than the Nyquist frequency (§ 6.1). Now the interferogram, corrected for the reference phase, can be calculated. Also interferometric products like the coherence image can be calculated. The coherence can be used to estimate the quality of the interferogram (§ 3.3).

The ambiguities in the phase of this interferogram are solved. This *phase unwrapping* is sometimes improved by smoothing or adaptive filtering the interferogram. From the resulting absolute phase, a digital elevation model or a deformation model can be derived (§ 2.5 and § 2.6). Finally, the calculated model is *geocoded*: it is connected with an earth reference system (Geudtner, 1995; Schwäbisch, 1995; Massonnet and Feigl, 1998).

3 Quality of interferograms

The quality of the geodetic results of measurements in SAR-interferograms depends on the quality of the interferograms, which in turn depends on properties of the SAR-images. As the phase of the interferometric signal is directly related to the path length difference, the phase is the key interferometric measure. In § 3.1 properties of the phase are described. The phase of the SAR-images and the interferogram is influenced by several processes, which could cause decorrelation and affect the quality of the interferogram. Sources of decorrelation are described in § 3.2. A quantitative description of the quality of an interferogram is provided by the coherence. This notion, its relation with other quality measures and the way it can be used to assess the improvement achieved by SAR-processing methods is treated in § 3.3. Subjects concerning the implementation of coherence estimation are discussed in § 3.4.

3.1 Realisation of the phase of the interferogram

As pointed out in § 2.5, the phase of the interferogram is the key measure to interferometry. It has a direct relation to the path length difference of the backscattered radar signal as seen from both ends of the baseline. If the slant range distance from one end of the baseline to a resolution element in the scene is r_1, the phase of the backscattered signal can be described as

$$\phi_1(r_1) = -\frac{4\pi}{\lambda}r_1, \tag{3.1}$$

with the wavelength $\lambda = 5.66$ cm for ERS. According to equation (2.17), the phase of the interferogram is the phase difference

$$\phi = \phi_1 - \phi_2. \tag{3.2}$$

As the distance to the resolution element from the other side of the baseline is usually different, the phase difference between the signals received at the ends of the baseline is

$$\phi = -\frac{4\pi}{\lambda}\Delta r, \tag{3.3}$$

where $\Delta r = r_1 - r_2$ is the path length difference and the sign is negative by definition. This is the *geometric phase difference*.

Because the bandwidth of the SAR-signal is less than 0.4 per cent of the frequency of the carrier, the signal can be assumed to be monochromatic and the phase can be electronically measured with an accuracy of a fraction of a wavelength (Schwäbisch, 1995;

Geudtner, 1995; Prati and Rocca, 1994). This means that, once the phase ambiguity has been solved, the path length difference can be measured to the level of a few millimetres.

This assumes that no phase shift occurs during the backscattering of the signal by the resolution element, which in general is not true. If we denote this phase shift as seen from side 1 of the baseline with the object phase $\phi_{\mathrm{obj},1}$, the total phase due to the two-way travel time of the radar signal for baseline side 1 and the object phase is (see also Geudtner, 1995 and Schwäbisch, 1995)

$$\phi_1(r_1) = -\frac{4\pi}{\lambda}r_1 + \phi_{\mathrm{obj},1}, \tag{3.4}$$

whereas the signal received by side 2 of the baseline has a travel path that differs from that of side 1 by Δr, yielding a total phase

$$\phi_2(r_2) = -\frac{4\pi}{\lambda}(r_1 - \Delta r) + \phi_{\mathrm{obj},2}. \tag{3.5}$$

If the backscattering characteristics of the resolution cell did not change in the period between the moments the SAR-images were acquired and if they are not too sensitive to the slightly different incidence angles from the radar signals from both ends of the baseline,

$$\phi_{\mathrm{obj},1} = \phi_{\mathrm{obj},2} \tag{3.6}$$

and thus

$$\phi = \phi_1 - \phi_2 = -\frac{4\pi}{\lambda}\Delta r. \tag{3.7}$$

Apart from the object scattering characteristics, several other processes (§ 3.2) could also introduce a phase shift different at either side of the baseline, so that equations (3.6) and (3.7) do not hold any more. It is particularly important that the SAR-processing is phase-preserving and that the active microwave instrument itself also has a well-known phase behaviour (Geudtner, 1995).

A single resolution element in the SAR-image causes an average phase shift $\phi_{\mathrm{obj},i}$ (equation 3.4) that is composed of the backscattering properties of a finite number of elementary scatterers in the resolution cell. Because the signal can be considered as monochromatic, the resultant phase of the resolution cell can be regarded as the phase of the *coherent sum c* of individual elementary scatterers c_i,

$$c = \sum_i c_i = \sum_i A_i e^{i\phi_{\mathrm{obj}}}, \tag{3.8}$$

with

$$\phi_{\mathrm{obj}} = \arctan\left(\frac{\mathrm{Im}(c)}{\mathrm{Re}(c)}\right). \tag{3.9}$$

In a coherent sum the addition is performed with the phase of the terms taken into account. This is sketched in the complex plane in figure 3.1, where the amplitude of the elementary scatterers is denoted by the length of the arrow and the phase by the angle with respect to the real axis (Schwäbisch, 1995). This is also known as *phasor addition*
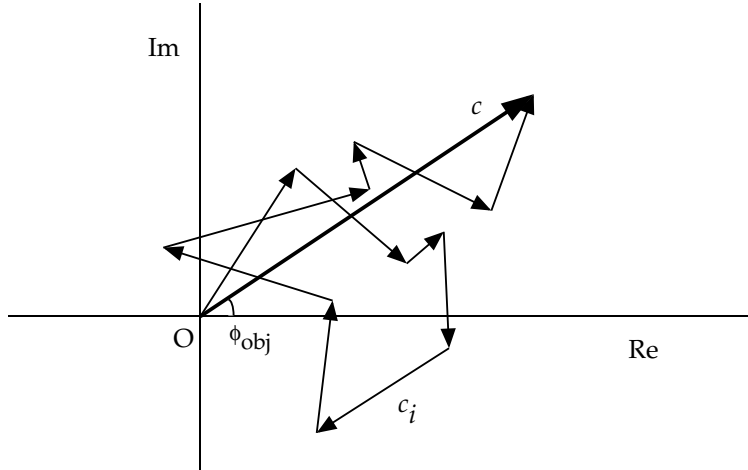
Figure 3.1 Because the radar signal can be considered as monochromatic, the resultant complex response c of one resolution cell can be obtained as the coherent sum of the individual elementary scatterers c_i. The amplitude and phase are denoted in the complex plane by the length of the signal vector and its angle with the real axis, respectively. The amplitude of the resulting backscatter of the resolution element is the length of the thick vector, its phase is ϕ_{obj}.

(Hecht and Zajac, 1974).

Zebker and Villasenor (1992) describe the *speckle* nature of the elementary scattering centres, of which at least several will be present in one resolution cell. If the elementary scatterers are randomly distributed in each resolution cell of the radar image and one cell is assumed to have a dimension of many wavelengths in size, the phase of each scatterer will be random and the coherent sum over the resolution cell will be well characterized by a complex number with a Gaussian distribution with a zero mean and a variance proportional to the average radar cross section of the surface. This only applies if the scattering of a resolution cell is Gaussian distributed scattering and composed of a number of random scatterers; if one scatterer dominates, the response is that of a point scatterer (Bamler and Hartl, 1998).

Although the response of the resolution cell is complex circular Gaussian distributed and hence has a stochastic nature, a fixed relation between the response at two different times can exist: if the backscatter is not changed by a change in position or cross-section of the elementary scatterers, and the resolution cell is viewed with the same geometry, the response will be identical for different time instants (Zebker and Villasenor, 1992). Two electromagnetic waves are *coherent* if there exists a fixed relation between the phase of each of them (Hecht and Zajac, 1974); interferometry is a coherent imaging technique because both amplitude and phase are measured. If the response of the resolution cell is similar at different time instants and hence coherent, the radar backscatter received at those instants will thus be *correlated*.

This is an important condition in repeat-pass interferometry, where the interferometric phase is calculated from the phase response of a resolution cell recorded at different times. The notion of correlation is also of importance to understand how an interferometric phase related to the path length difference can be obtained from scatterers that show a stochastic behaviour.

3.2 Sources of decorrelation

From the complex response of a certain resolution cell as recorded at a certain time from either side of the baseline, it is always possible to calculate the interferometric phase. A condition for calculating a high-quality interferogram is that the interferometric phase is well-defined and a result of only the path length difference. As Zebker and Villasenor (1992) state, coherent radar echoes will be correlated with each other if each represents nearly the same interaction with a scatterer or a set of scatterers. If the amplitude of imaging radars is considered, this means that the observed speckle patterns are similar. The complex response of a resolution cell can differ due to several processes, causing *decorrelation*. This deteriorates the interferogram. Sources of decorrelation are:

- Thermal noise of the instruments.

- Phase errors due to the acquisition or interferometric processing, in particular the registration of the single look complex images. The decorrelation caused by different interpolation schemes applied in the image registration is discussed by Hanssen and Bamler (1999). Zebker et al. (1994) mention processing phase noise due to sidelobes and defocusing.

- Temporal decorrelation. If the interferogram is acquired in a repeat-pass configuration, changes in the object phase between the data acquisition of the first SAR-image and the second will induce phase errors, leading to a decrease of the coherence. This can be caused by, for example, changes in the vegetation due to the seasons, different contents of moisture due to rain or flooding, snowfall, freezing of the surface or by mechanical changes like ploughing and building. Water surfaces show an extreme decorrelation (Zebker and Villasenor, 1992; Massonnet and Feigl, 1998; Gens and Van Genderen, 1996b). The 35-day repeat orbit of the most important of the ERS-1 observation phases turns out to yield a considerable decorrelation for many scenes, where the 1-day separation orbits of the tandem pair ERS-1 and ERS-2 yield interferograms that show much less decorrelation (Bamler and Hartl, 1998). Usai and Klees (1999) give an example of the dramatic difference in temporal decorrelation between an acquisition interval of one day and 3.5 year.
  Decorrelation caused by movement of parts of the scene, can be considered as temporal. The movements of the scene can, for example, be caused by land slides, glacier movements, earthquakes and other geophysical processes. However, if this movement is piecewise continuous, correlation between the pieces is conserved and interferometry can be used to measure the movement (Massonnet and Feigl, 1998).

- Geometric decorrelation, caused by different viewing positions. In general, the complex response depends on the incidence angle, especially if it regards volume scattering instead of surface scattering, as Bamler and Hartl (1998) and Cattabeni et al. (1994) show (see also Zebker and Villasenor (1992) and Li and Goldstein (1990)). Because the projection of the radar signal, that in fact samples the terrain, is shifted in wavelength as seen from either side of the baseline, the spectra are misaligned. This is called *baseline decorrelation* discussed in § 5.2 (Bamler and Just, 1993; Gatelli et al., 1994; Zebker et al, 1994). Different antenna pointing has a similar effect and is the reason for azimuth filtering, the main subject of this thesis. Zebker and Villasenor (1992) treat the decorrelation occurring due to rotation of the scene, in particular if the SAR images have been acquired from crossed orbits, but this is of limited importance for ERS. Another cause of decorrelation is the occurrence of layover and shadowing,

where strips of the scene are hidden behind mountains due to the incidence angle.

3.3   Coherence as a measure for interferogram quality

Often we are interested in the quality of the interferogram, especially if the improvement of the accuracy of the phase has to be measured after a processing step, like in this thesis. If the interferometric phase difference is calculated for any resolution element, it is not clear whether this difference is the result of the path length difference only, or that decorrelation sources also have contributed. The phase of a cell could be compared with the phase of neighbouring cells, which have about the same path length difference. If the phase ramp due to the incidence angle from baseline to the 'flat' earth surface is removed, neighbouring cells would have even better comparable phase differences. This can be used to estimate the similarity between neighbouring resolution cells and hence the phase noise.

3.3.1   Coherence

Two electromagnetic signals are *coherent* if there exists a fixed relation between the phase of each of them (Hecht and Zajac, 1974). The *normalized complex coherence* for two zero-mean, complex circular Gaussian random variates c_1 and c_2 is defined as

$$\gamma_{12} = \frac{E\{c_1 \cdot c_2^*\}}{\sqrt{E\{|c_1|^2\} \cdot E\{|c_2|^2\}}}, \tag{3.10}$$

where $E\{\cdot\}$ denotes the expectation. The two complex SAR image pixels have a *coherence* $|\gamma_{12}|$ that can be

$$\begin{cases} |\gamma_{12}| = 1 & \text{completely coherent,} \\ |\gamma_{12}| = 0 & \text{completely incoherent,} \\ 0 < |\gamma_{12}| < 1 & \text{partial coherence.} \end{cases} \tag{3.11}$$

In radar interferometry, the coherence is related to the standard deviation of the phase and the signal-to-noise ratio (SNR) (Just and Bamler, 1994). The phase of the normalized complex coherence (3.10) in this case is the expected interferometric phase ϕ (equation 3.2) of the pixel.

Zebker and Villasenor (1992) show that, if the received signals s_1 and s_2 are composed of the noise-free part c and the noise n and n_2,

$$s_1 = c + n_1 \tag{3.12}$$

$$s_2 = c + n_2$$

the correlation between the signals that form the interferogram is, calculated with the coherence formula (3.10),

$$\gamma = \frac{E\{s_1 s_2^*\}}{\sqrt{E\{s_1 s_1^*\} E\{s_2 s_2^*\}}} = \frac{|c|^2}{|c|^2 + |n|^2}, \tag{3.13}$$

since noise and signal are uncorrelated. Now, because the signal-to-noise ratio SNR is $|c|^2/|n|^2$, equation (3.13) can be written as

$$\gamma = \frac{\text{SNR}}{\text{SNR} + 1} = \frac{1}{1 + \text{SNR}^{-1}}. \qquad (3.14)$$

Extending equation (3.12) with other sources of decorrelation, Zebker and Villasenor (1992) show that, via a similar derivation as above, the correlation coefficients of different decorrelating origins can be written as a product,

$$\gamma_{\text{total}} = \gamma_{\text{thermal}} \cdot \gamma_{\text{processing}} \cdot \gamma_{\text{temporal}} \cdot \gamma_{\text{geometric}}, \qquad (3.15)$$

where the product is extended with all sources of decorrelation listed in § 3.2.

In the case of ERS-1 and ERS-2, because the satellites show a somewhat different SNR, γ_{thermal} can be written as (Askne et al., 1996; Bamler and Hartl, 1998)

$$\gamma_{\text{thermal}} = \frac{1}{\sqrt{\left(1 + \text{SNR}_1^{-1}\right)\left(1 + \text{SNR}_2^{-1}\right)}}. \qquad (3.16)$$

3.3.2 Estimation of the coherence

The expectation in equation (3.10) is a theoretical quantity for a stochastic process, that asks for a realisation in practice. As stated in the introduction of § 3.3, the realisation of the phase in one resolution cell could be compared with that of its neighbours, which will have about the same phase. Better would be if we had realisations of the phase of one resolution cell for several time instants. If a process is *ergodic*, it has a stochastical nature that allows to interchange time and space (Touzi et al., 1999).

For a stationary, ergodic process, the expectation in equation (3.10) can be calculated by averaging over N neighbouring image cells. The estimator for the coherence then becomes (Touzi et al., 1999; Schwäbisch, 1995)

$$\hat{\gamma} = \frac{\sum\limits_{n=1}^{N} c_{1n} \cdot c_{2n}^*}{\sqrt{\sum\limits_{n=1}^{N} \left|c_{1n}\right|^2 \cdot \sum\limits_{n=1}^{N} \left|c_{2n}\right|^2}}. \qquad (3.17)$$

Equation (3.17) shows in the nominator the sum over N cells of the complex interferogram. This is a coherent sum because the phase of the image elements is taken into account. The argument of the nominator of this equation is the resultant phase of N phasors. The more the phases of the individual interferogram cells are comparable, the larger the sum becomes, as figure 3.1 shows. The denominator serves to normalise the estimator, although it is not exactly the same as the modulus of the nominator, apparently because of its optical origin. The modulus of the estimator $\hat{\gamma}$ is therefore a measure for the coherence based on several image cells of the interferogram.

If the phase ϕ_{topogr} induced by the topography and the earth ellipsoid shows a considerable increase over the estimator window, the imaging process can no longer be considered as stationary (Touzi et al., 1999). Adjacent image cells of the interferogram then can be expected to have a different phase due to the imaging geometry and topography. For example, if an interferogram is made from ERS-images with a baseline of

350 metre, the path length difference increment per range line induces a phase difference increment of one third of a cycle; the fringes due to the 'flat earth' will have a cycle of 3 range pixels. If the coherence estimator equation (3.17) would be applied to an estimator window over several range pixels, the nominator will be less than expected because of the coherent summation. This is demonstrated in figure 3.2. If the imaging geometry induces a fringe pattern of 5 range pixels – corresponding with an ERS baseline of about 200 metre – the complex sum of 5 pixels in range direction with only the noise-free (in this case unit) signal of the 'flat earth' yields zero (figure 3.17a). The coherent sum over 10 pixels in range of a simulated interferogram is small compared to the sum of the amplitudes (3.17b). However, if the phase due to the earth ellipsoid (3.17a) is subtracted from the phase of each pixel, then the phases are similar and the coherent sum yields the result needed for the estimation of the signal coherence (3.17c).

If the coherence should be estimated without the influence of the imaging geometry, for example if the noise in the interferometric phase corrected for the geometry-induced fringes is considered, the source of the signal non-stationarity might be removed. The phase of each term in the sum of the nominator of equation (3.17) is corrected for the deterministic phase due to the geometry and becomes

$$\phi_n = \phi_{1n} - \phi_{2n} - \phi_{\mathrm{geometry},n}, \qquad n = 1, \ldots, N. \tag{3.18}$$

The coherence can then be estimated with (Touzi et al., 1999; Monti Guarnieri and Prati, 1997)

$$\hat{\gamma} = \frac{\sum\limits_{n=1}^{N} c_{1n} \cdot c_{2n}^* \cdot \exp(-i\phi_{\mathrm{geometry},n})}{\sqrt{\sum\limits_{n=1}^{N} \left|c_{1n}\right|^2 \cdot \sum\limits_{n=1}^{N} \left|c_{2n}\right|^2}}. \tag{3.19}$$

3.3.3 Bias of the coherence estimator

The coherence estimator $\hat{\gamma}$ (3.17) is biased. Touzi et al. (1999) show that the coherence sample magnitude $d = |\hat{\gamma}|$ differs from the coherence magnitude $D = |\gamma|$: it is biased towards higher values. The lower the coherence magnitude, the greater the bias of the estimator. The bias decreases with increasing number of independent samples L; the maximum likelihood estimate is asymptotically unbiased.

The expectation of the coherence sample magnitude d is

$$E\{d\} = E\{|\hat{\gamma}|\} = \frac{\Gamma(L)\Gamma(1 + \frac{1}{2})}{\Gamma(L + \frac{1}{2})} \cdot {}_3F_2(\tfrac{3}{2}, L, L; L + \tfrac{1}{2}, 1; D^2) \cdot (1 - D^2)^L, \tag{3.20}$$

with Γ the Gamma function and ${}_qF_p$ the generalized hypergeometric function.

The number of independent samples L is lower than the number of cells N in the estimator window in equations (3.17) and (3.19), because due to oversampling the pixel spacing in SLC-images is smaller than the resolution. For an ERS SLC image, the pixel size in ground range is approximately 20.23 m (7.905 m in slant range) and in azimuth approximately 3.97 m; the size of the resolution cell can be calculated by multiplying these figures with the oversampling factors. For the unweighted spectrum these are ratio of the sampling frequency and the bandwidth, which is for range $18.96/15.55 = 1.219$ and for azimuth $1679/1379 = 1.218$. For the weighted spectrum (§ 4.1) these figures are
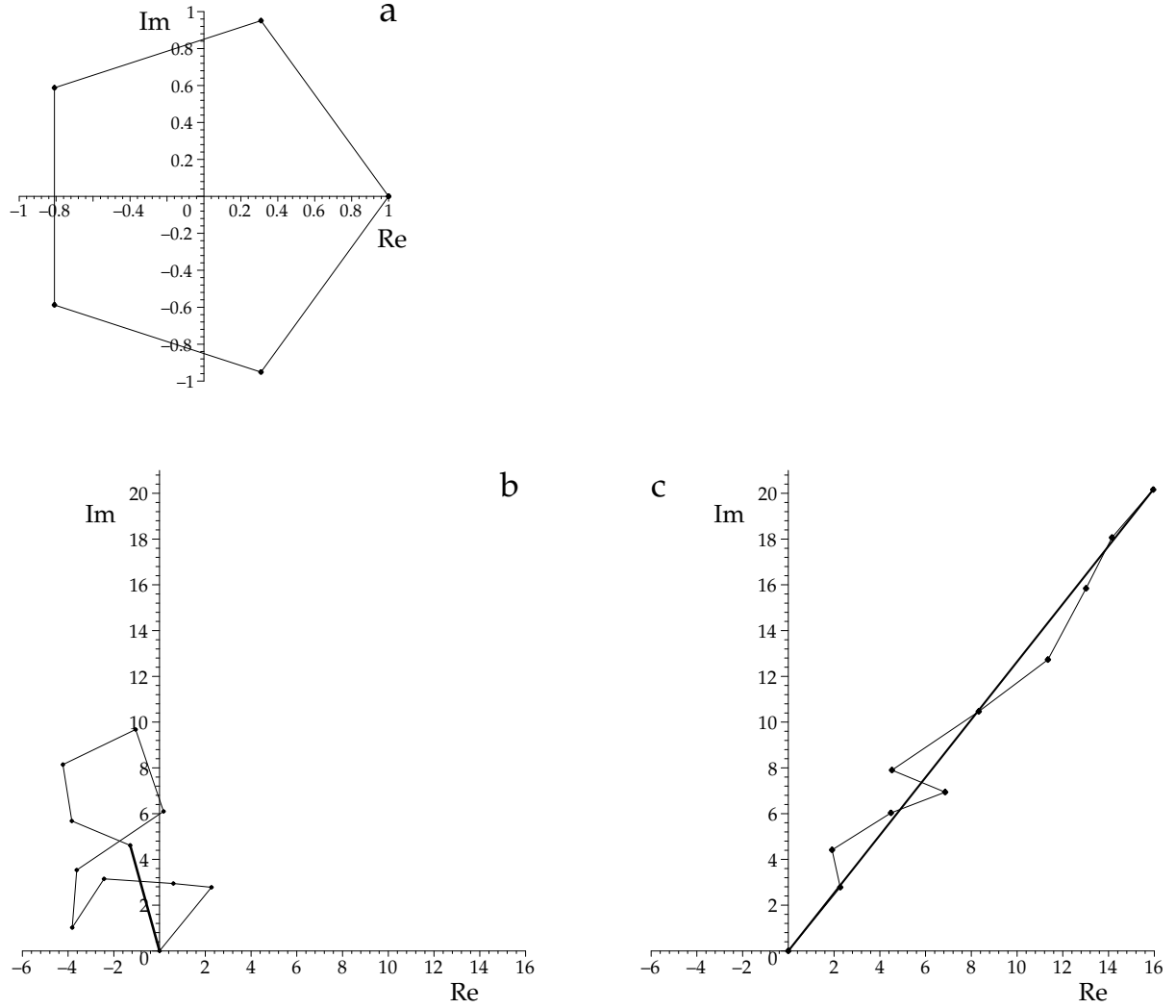
Figure 3.2 The coherent sum of 5 pixels in range direction with only the noise-free unit signal of the 'flat earth' yields zero if the cycle of the fringes is 5 pixels (a). The sum over 10 pixels in range of a simulated interferogram without correction for the phase of the flat earth is small (thick line in b). If the correction is applied, the phases of the pixels are about the same and the coherence estimator will yield a higher value (c).

slightly higher. For this moment, we continue with the calculated ratios. The dimension of the resolution cell for ERS is thus 24.7 m in ground range and 4.83 m in azimuth. Thus for ERS, we will use as straightforward approximation

$$N = 1.485L \approx 1.5L. \tag{3.21}$$

In figure 3.3 the bias in the coherence estimator for several values of the independent sample number L and estimator window size N is shown. As for ERS the pixels of the single look complex SAR images are not square, estimator windows of $N = 2 \times 11$, 3×15 and 6×30 are frequently used to obtain coherence images with square pixels; therefore the expectation of the coherence of equation (3.20) was drawn for $N = 22$ ($L = 14.8$), $N = 45$ ($L = 30.3$) and $N = 180$ ($L = 121$) as well. In experiments, reported in § 5.9, we used $N = 720$ ($L = 485$).
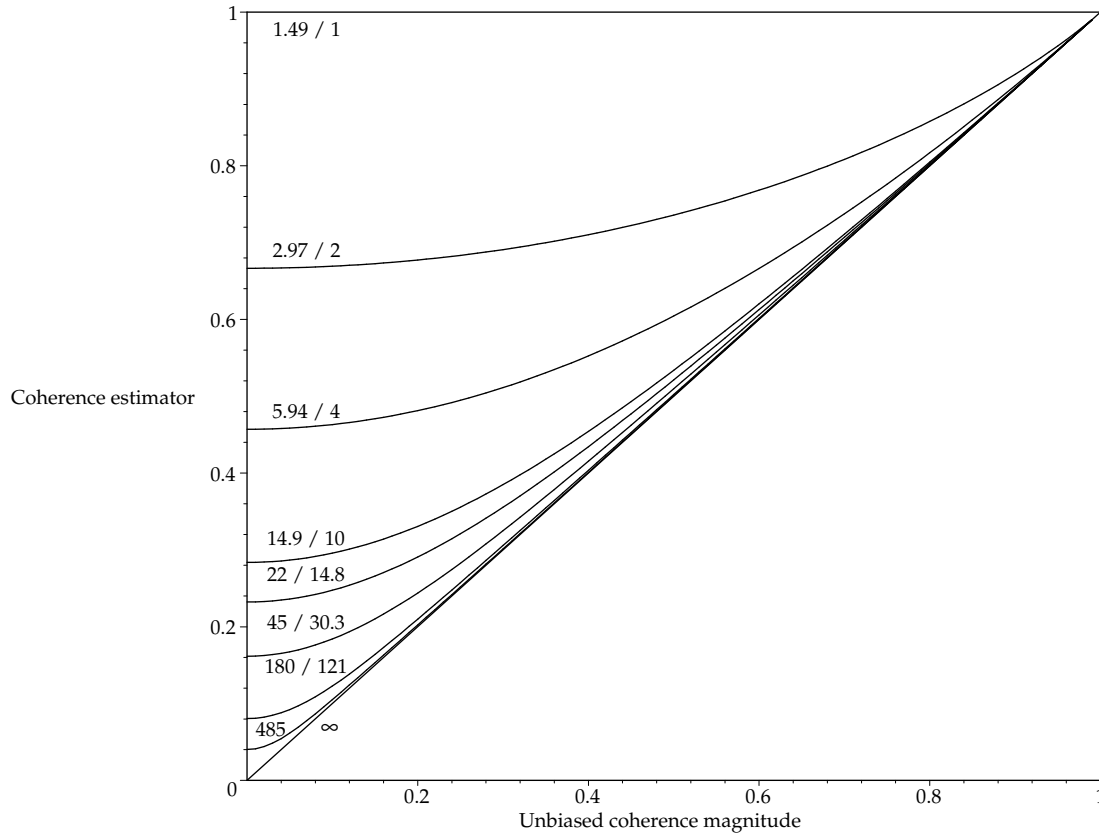
Figure 3.3   The bias of the coherence estimator for several window sizes as a function of the unbiased coherence. The smaller the estimator window and the lower the coherence, the greater the bias. The annotated numbers N/L are the number of pixels N in the estimator window and the number of independent resolution cells L in equation (3.20) in the estimator window; $N = 1.485L$ is assumed for ERS. Because of the approximately square window, the window size is often chosen $N = 22$ ($L = 14.8$), $N = 45$ ($L = 30.3$), $N = 180$ ($L = 121$) and $N = 720$ ($L = 485$).

Because the estimation of the coherence is a stochastic process, in practice coherence estimations below the lower limit of the bias equation (3.20) for a particular L will occur. Furthermore, the lower L and N, the higher the standard deviation of the estimate. This is illustrated in figure 3.4, where histograms of the coherence estimations of an interferogram with different window sizes N are shown.

One could easily work around the bias in the coherence estimator by choosing an estimator window which is very large. However, for the application of coherence as a classification tool (see § 3.3.5), the resulting reduction in resolution is not always acceptable. Furthermore, the assumption of ergodicity will be less viable. Another problem that can occur as a result of using a larger estimator window is a deterioration caused by the phase due to topography different from the earth ellipsoid.

Touzi et al. (1999) show that an unbiased estimator $G(d)$ which is a function of the sample coherence magnitude d cannot be found. The only way to correct for the bias is to numerically invert equation (3.20), as we did in our implementation (see § 3.4.4).

3.3.4   Another way to measure interferogram improvement: residues

The calculation of the coherence estimator is not the only way to measure interferogram quality. Another method utilizes the *number of residues*. To assess the improvement in the interferogram due to a processing step, the number of residues before and after the step can be determined.

       The removal of the phase ambiguity from the interferometric phase is the most important step to be able to calculate a digital elevation model or deformation pattern from the interferogram. In the imaging process, the recorded phase lies within the limits $-\pi$ and π. If this 'wrapped' phase along a certain path in the interferogram transits to the other end of the wrapped phase scale, resulting in a fringe in the interferogram, 2π can be added or subtracted to remove the ambiguity. Due to phase noise in the interferogram (and also because of layover and shadowing), other paths can yield other multiples of 2π. This leads to an inconsistency. The *phase residue* is such an inconsistency for a path over 2×2 pixels. The percentage of residues can be used to measure the interferogram quality improvement (Geudtner, 1995). We do not use residues in this thesis.

3.3.5   Coherence as classification measure

Not always the goal of the calculation of the coherence is measuring the quality of the interferogram or discriminating between parts of the scene with different phase noise. For remote sensing, a coherence image can give a considerable amount of information about the soil, crop, vegetation or other remote sensing objects. The coherence value can be used for the calculation of the vegetation index (Lillesand and Kiefer, 1994) or for other classifications (Zebker and Villasenor, 1992; Geudtner, 1995; Askne et al., 1996).

3.4   Implementation of the coherence estimation

In this section, some subjects concerning the implementation of coherence estimation will be discussed.

3.4.1   Choice of windows for coherence estimation

In equation (3.17) or with the correction for the phase of the ellipsoid equation (3.19), the summation over the N pixels of the estimation window yields one number, the correlation. To obtain the coherence over the complete image, there are two approaches.

Overlapping windows

The first approach assumes that the coherence image should be the same number of rows and columns as both SAR images. In this way for example a database can have the same properties for all types of images, what can be an advantage. Each image pixel has a coherence value and for example colour-lookup-table-coded images of the SAR, intensity and coherence images can be made. In this way it is also possible to classify an image per pixel.

       Because the coherence estimation window extends over N pixels – for example over 6 pixels in range and 30 lines in azimuth – and is shifted only by one pixel or line each time, the sum for adjacent coherence image pixels will have most of the summation terms in common. This will lead to a coherence image that looks rather smoothed: the information added by shifting the window with one pixel or line is limited.

       The efficiency of the implementation of this method will take advantage of an

approach in which the nominator and denominator of the coherence estimator are kept and only the new terms in the sum are added and the old terms are dropped. This holds in particular for the calculation of the correction for the ellipsoidal reference phase, which can be numerically intensive.

For the border of the coherence image, the estimator window is extending over the SAR image borders. The algorithm can assume the pixels outside the images to be zero, the borders can be replicated or the estimator can be kept zero as long as it is not entirely inside the image. In the implementation we had at our disposal, the COHRNC module of the PCIworks package (PCI, 1997), the latter approach is followed. The module works in two inseparable stages: in the first stage, a coherence image is calculated using an estimator window of size N_1, shifting one pixel at a time. In the second stage, the sum is calculated over N_2 pixels of the first stage. In this second stage, the sum is incorporating the zeros at the borders, yielding a coherence estimation that is too low. If the module is used with $N_1 = N_2$, a small image results, but the result is different from the estimation over adjacent windows, as described below. The result will be smoothed, because if the window is n pixels in range and m lines in azimuth, the result will be the average over $(2n - 1)(2m - 1)$ pixels.

The only advantage of the approach of estimating the coherence over overlapping windows is that it yields images of the same size as the original SAR images. It is smoothed, there are problems on the edges and it is time consuming. Moreover, it is not yielding substantial additional information over the approach we followed, if no information on the pixel level is needed: the use of adjacent windows.

Adjacent windows

The second approach to choosing windows for estimating the coherence is taking windows that are adjacent to each other. A sum is calculated over any pixel only once, which makes it very efficient. No smoothing results from shifting the window. The resulting coherence image is smaller than the original SAR images. The estimates at the borders are of the same quality as the other estimates, as long as the size of the window fills the interferogram completely.

If only one coherence value is needed for the quality estimation of the interferogram, the window can even be taken equal to the whole SAR image. Note that this is not possible with the approach discussed before, unless the coherence estimator window is chosen considerably smaller than the averaging window; even then the result is biased due to the zeros at the edges.

It is advisable to choose a smaller window than the whole image, because the phase over the image can contain systematic effects due to an inaccurate description of the subtracted reference phase, due to the phase induced by the topography or due to atmospheric phase delays, violating the stationarity condition. In these cases, the coherent sum shown in figure 3.2 can result in the coherence estimation to be too low.

In the experiments in § 5.9, we used a coherence estimator window of 12 pixels in range and 60 lines in azimuth, hence $N = 720$ and $L \approx 485$.

3.4.2 Subtraction of the reference phase

As discussed in § 3.3.2 and shown in figure 3.2, a coherence estimation over N adjacent pixels can yield too small values because over the estimation window the phase due to the 'flat earth' or ellipsoidal surface is not constant. The coherence estimation of equation (3.17) can be corrected for this reference phase as in equation (3.19), if the geometry-induced non-stationarity should be removed.

We used the reference phase calculated with module REFPHA of the PCIworks package, with the Delft precise orbits. The phase is described as a fifth-order two-dimensional polynomial, which has 21 coefficients (PCI, 1997).

3.4.3 Use of one coherence value and use of histograms

For some applications only one quality number for an interferogram suffices. For example, with one quality number estimated from the interferogram, it is possible to judge whether the algorithms for spectral filtering, discussed in chapter 5, result in the expected improvement of the interferogram.

The *mean coherence* can be used as such a number. We calculate the mean of the coherence image calculated from the original SAR images with the adjacent estimator window technique described in § 3.4.1. Then we apply the filtering and again calculate the mean coherence. The improvement can then be characterized by the ratio of both mean coherence values (see equation (5.50) in § 5.9) and compared with the predicted improvement.

To get a spatial impression of the coherence and its improvement, we could use a coherence image. This is done in § 5.9; because no detail is needed, the estimator window size $N = 720$ suffices. An other way to present the coherence is to draw *histograms* of it, like in figure 3.4. From histograms we cannot get spatial information, but the distribution of the coherence becomes very clear. Histograms show clearly the improvement of processing steps like spectral filtering (Gatelli et al., 1994).

3.4.4 Correction of the bias

The coherence estimation of equation (3.17) is biased; an unbiased estimator cannot be found. The estimation could be made unbiased by multiplication with the inverse of the bias equation (3.20). However, a inverse of this equation does not exist. In our implementation of the coherence estimation, we inverted equation (3.20) numerically. The goal was to obtain one unbiased coherence estimation for the interferogram and corrected histograms; the coherence images itself were not corrected for the bias.

We calculated lists of the estimated coherence magnitude $E\{d\}$ with equation (3.20) for $D = 0 \dots 0.99$ with a step size of 0.01. We added $E\{d\} = 1$ for $D = 1$ by hand, because (3.20) is singular there. After calculating the coherence estimation for the interferogram with equation (3.19) and making a histogram with 50 bins of the coherence estimation distribution, the coherence value of the centre of each of the bins is searched in the unbiased coherence list. From the listed values nearest to this, the unbiased coherence is determined by linear interpolation.

In this way the location of each bin of the histogram is shifted to a lower coherence. The bias-corrected histograms can be drawn and compared with the biased histograms, as is done in figure 3.4 for different values of N. The figure shows that the smaller the estimator window and the lower the coherence, the greater the bias.

After this, the *bias-corrected mean coherence* can be calculated by multiplication
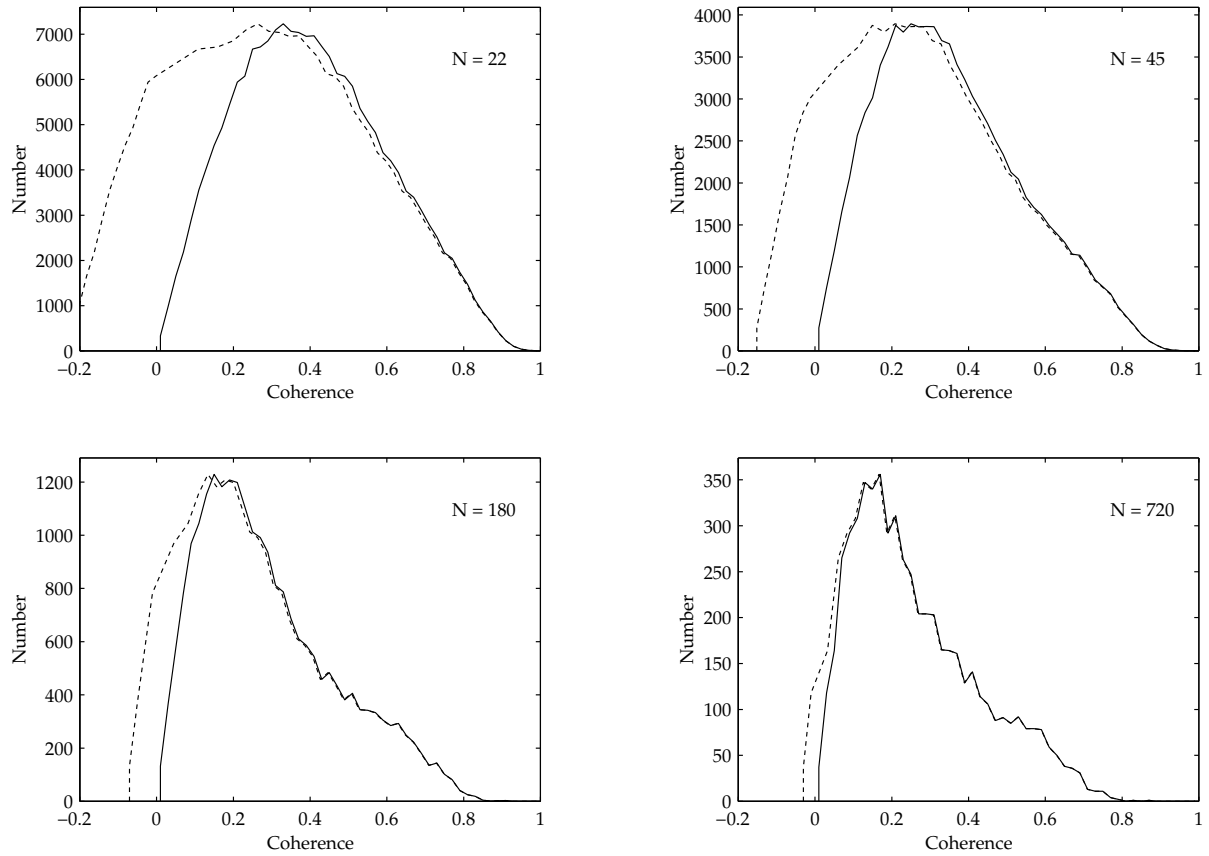
Figure 3.4   Coherence histograms are shown for several window sizes N of the coherence estimator (solid lines). This estimator is biased; the smaller the estimator window and the lower the coherence, the greater the bias. The bias can be removed to a great extent by correcting the locations of the histogram bins by numerically inverting the bias equation (3.20). This results in coherence estimates that can be less than zero (dashed lines). Furthermore, due to the larger standard deviation in the coherence estimation for small windows, high estimates occur that are only marginally corrected. As a result, the bias-corrected coherence histograms are not similar for all window sizes.

of the histogram frequencies with the corrected centres of their bins, summation and division by the total number of coherence values.

Although this algorithm removes the bias to a great extent, the result is not completely free of bias. In the first place, because the coherence estimation is a result of a stochastic process, the histogram bins for coherences lower than the value of $E\{d\}$ in equation (3.20) for $D = 0$ are not empty. In our algorithm all estimates less than $E\{d\}$ for $D = 0$ are corrected by subtracting $E\{d\}$. This is visible in figure 3.4. This is probably not the right correction because the correction of $E\{d\}$ for $D > 0$ is increasing for $D \downarrow 0$, while this increase is not continued for the correction estimates less than $E\{d\}$ for $D = 0$. However, no better alternative exists. This causes a bias to greater values. In the second place, all coherence values within one bin of the histogram are mapped onto the coherence value of the centre of the histogram bin. Because the bias works in one direction, this itself introduces a bias, albeit it very small.

As figure 3.4 illustrates, our bias correction algorithm removes the bias in the coherence estimation to a great extent. The corrected histograms for different estimation window sizes have approximately the same position. However, the corrected coherence

estimator window	N	L	coherence estimation	
			biased	corrected
2 × 11	22	14.8	0.406	0.321
3 × 15	45	30.3	0.355	0.306
6 × 30	180	121	0.291	0.275
12 × 60	720	485	0.264	0.256

Table 3.2 Due to the bias in the coherence estimator, the mean coherence estimation is substantially smaller for large estimator window sizes. Due to the higher standard deviation of the estimator for small window sizes, the bias correction for high coherence estimations over small windows will not yield the same coherence distribution as the estimator for larger windows. This results in a histogram broader than that for larger windows and a corrected coherence mean still not similar. However, the mean corrected coherence estimations show much less variation for different window sizes than the mean biased coherence estimations.

estimation histograms are still not similar for all estimator window sizes. Estimations over small windows give a substantially broader coherence value distribution than estimations over large windows. This is because the standard deviation of the coherence estimator is substantially higher for small window sizes than for large windows (Touzi et al., 1999). This causes the histograms over smaller windows to contain more high coherence estimations than the histograms over larger windows. Because the bias for high coherence estimations is very small and almost independent of the estimator window size (figure 3.3), the bias correction algorithm does not correct these high estimates to the values present in the histograms for larger estimation windows. The same holds for the lower coherence estimations. Because of the larger standard deviation, the number of coherence estimations substantially smaller than the theoretical lower limit of equation (3.20) for $D = 0$ for small window sizes is higher than for large window sizes. If these estimates are bias-corrected, a larger number of coherences less than zero results.

The dissimilarity of the coherence estimation histograms due to the standard deviation also appears from the calculated mean coherence, biased and corrected, in table 3.2. However, the mean corrected coherence estimations show much less variation for different window sizes than the mean biased coherence estimations.

Note that if the coherence estimations are calculated using the overlapping-window algorithm (§ 3.4.1), the coherence histograms will contain fewer entries directly above zero than if the the adjacent-window algorithm would have been used. This is because with overlapping windows, the averaging step acts as a smoothing window over the coherence image, whereas the pixels in that coherence image were already calculated over a window with a certain extent.

The correction of the bias we devised is not a necessity for the measurement of the coherence improvement due to spectral filtering, because for the estimator window size $N = 720$ we used, the bias is rather small, as figures 3.3 and 3.4 show. In the tables in § 5.9 the mean biased and corrected coherence estimations show a limited difference. However, the corrected coherence estimations are closer to unbiased and hence show less variation over estimator windows of different sizes. Furthermore, if the goal is calculation of coherence images and a high resolution is requested and hence a small estimator window is used, the bias-correction algorithm will be very useful.

4 Properties of spectra in range and azimuth

In chapter 2, the technique of synthetic aperture radar was discussed; in appendix A the calculation of spectra with the discrete and fast Fourier transform and the representation of spectra are discussed. With this knowledge, the parameters of the SAR system for the imaging in range and azimuth directions will be further examined in this chapter, serving as the foundation for the treatment of spectral filtering in chapter 5.

In § 4.1, the use of weighting functions to reduce sidelobes in range and azimuth spectra will be described, of which Hamming is the best known. They are recognized in § 4.2, where the relation between the spectra in range and azimuth and the SAR parameters will be discussed. Finally, the relation between the spectra in range and azimuth and the SAR resolution will be discussed in § 4.3.

4.1 Spectral weighting functions

4.1.1 Von Hann and Hamming weighting functions

The restriction of the bandwidth of a signal $x(t)$ to B, as necessary for sampling because of the sampling theorem of Shannon (equation A.3), has an unwanted effect. If the Fourier components of a not-bandlimited complex signal are $X(f)$, the bandwidth is restricted to B with

$$X'(f) = X(f)\Pi\left(\frac{f}{B}\right),\tag{4.1}$$

with the rectangular window function

$$\Pi\left(\frac{f}{B}\right) = \begin{cases} 1 & \text{if } |f| \leq B/2 \\ 0 & \text{otherwise} \end{cases},\tag{4.2}$$

plotted in figure 4.1a. According to the convolution theorem (Ziemer et al., 1993), the signal $x'(t)$ resulting from the bandlimited Fourier components $X'(f)$ can be calculated by convolving the original signal $x(t)$ with the inverse Fourier transform of the rectangular window function Π,

$$x'(t) = x(t) * B \operatorname{sinc} Bt,\tag{4.3}$$

where $*$ is the convolution operator. The sinus cardinalis (cf. figure 4.1b) causes the time signal to get 'wrinkles' known as sidelobes. If it changes fast, as in the case of an rectangular pulse, overshoot is visible. This is called the *Gibbs phenomenon* (Ziemer et al., 1993).

The sidelobes of the sinc function in (4.3) can be reduced by choosing a frequency

window function that approaches zero at the edges more smoothly than the rectangular window Π. Such a function is the *Von Hann window* (often called Hann or Hanning window),

$$W_{\text{Von Hann}}(f) = \begin{cases} 0.5 + 0.5 \cos \dfrac{2\pi f}{B} & \text{if } |f| \leq B/2 \\ 0 & \text{otherwise} \end{cases}, \tag{4.4}$$

graphed in figure 4.1c. Its inverse Fourier transform is (Ziemer et al., 1993)

$$w(t) = \frac{B}{2}\left(\text{sinc } Bt + \tfrac{1}{2}\text{sinc}(Bt - 1) + \tfrac{1}{2}\text{sinc}(Bt + 1) \right). \tag{4.5}$$

The first term has half the amplitude of the transform of the rectangular window, as is clear from the first term of (4.4). Two shifted sincs are added in order to reduce the sidelobes of the first sinc, as is depicted in figure 4.1d and e. The first sidelobe of the inverse Fourier transform of the Von Hann window has a level of -31.5 dB, whereas the level of the sidelobe of the rectangular window is -13.3 dB. On the other hand, the width of the main lobe of the transform of the Von Hann window is twice that of the rectangular window (Mitra, 1998).

Curlander and McDonough (1991) follow a more radar oriented approach, starting from the level of the first sidelobe. They arrive at a Taylor expansion and for a sidelobe level of -40 dB,

$$W(f) = 1 + 0.78 \cos \frac{2\pi f}{B}, \tag{4.6}$$

which is normalized

$$W(f) = 0.56 + 0.44 \cos \frac{2\pi f}{B}. \tag{4.7}$$

This is very near the *Hamming window function,*

$$W(f) = 0.54 + 0.46 \cos \frac{2\pi f}{B}. \tag{4.8}$$

The level of the first sidelobe of the Hamming window is -42.7 dB (Mitra, 1998).

Generally, a normalized frequency weighting or windowing function is

$$W(f) = \begin{cases} \alpha + (1 - \alpha) \cos \dfrac{2\pi f}{B} & \text{if } |f| \leq B/2 \\ 0 & \text{otherwise} \end{cases}. \tag{4.9}$$

This windowing function is sometimes also called *Hamming function.* The parameter α is known as the *pedestal level* for the cosine and (4.9) is called *cosine on a pedestal* (ASF, 1995c).
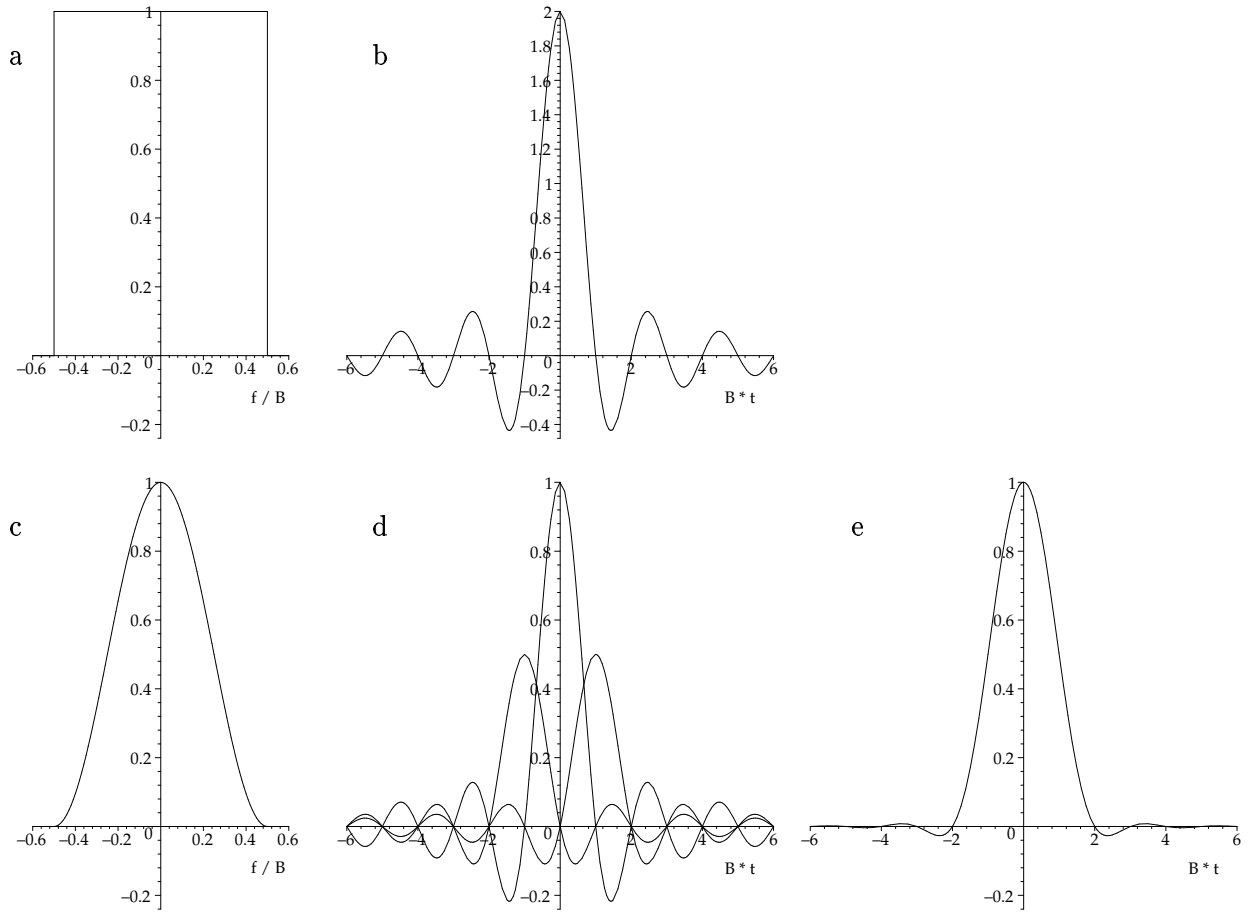
Figure 4.1   The rectangular frequency windowing function (a) and its inverse Fourier transform (b). The signal is convolved with this sinc-function, causing sidelobes and overshoot. This effect can be reduced by choosing a smoother windowing function, like the Von Hann function (c), one cycle of a cosine on a pedestal. The inverse Fourier transform is composed of three sinus cardinalis functions (d), resulting in a broader peak with minor sidelobes (e).

4.1.2 Hamming weighting for the range spectrum

In § 2.2 it was shown that the imaging process in range direction utilizes a linearly frequency modulated pulse, the *chirp* (equation 2.6). This type of signal has a short autocorrelation length as was shown in equation (2.10) and this results in a high range resolution.

In figure 4.2a, a chirped pulse of the synthetic aperture radar is simulated. The bandwidth of the signal is smaller than the sampling frequency and therefore the spectrum does not occupy the complete domain of the graph, as the figure shows. On the other hand, in this simulation the lowest frequencies are missing, resulting in a dip around $f = 0$. In real data this does not happen due to the appropriate intermediate frequency mixing. The wrinkles shown at the edges of the spectrum are due to the steep edges of the signal in time.

The correlation of the pulse with the backscattered signal is used to retrieve the ranges of the backscattering objects. Sidelobes of the autocorrelation function cause objects to appear with 'ghost images'. The sidelobes of the autocorrelation function

must be reduced and this can be done, as we saw in § 4.1.1, with a spectral weighting or windowing function. In figure 4.2b, a Von Hann window is applied (equation 4.4), including the zeroing outside the cosine cycle. The sidelobes of the autocorrelation function are now almost absent, but the resolution is halved because the central peak has doubled in width (Curlander and McDonough, 1991; ASF, 1995c). The wrinkles at the edges of the spectrum are also reduced.

A trade-off is shown in 4.2c, where the general 'Hamming' window (4.9) with $\alpha = 0.75$ is used, as often applied to ERS-data (Solaas and Laur, 1993).

4.1.3 Hamming weighting for the azimuth spectrum

In azimuth, also spectral weighting is applied. The reason is similar to that for range, where a chirp is applied. The phase history of the repeated pulses act as an frequency modulated azimuth chirp. Therefore also in azimuth a weighting function is applied to reduce the sidelobes of the chirp. For ERS-data, often the general 'Hamming' window (4.9) with $\alpha = 0.75$ is applied (ASF, 1995c; Carrara et al., 1995).

4.2 Spectral parameters of ERS in range and azimuth

In this section, we will investigate the spectra of the single look complex (SLC) images of ERS and relate the spectral properties to the radar image processing parameters, described in chapter 2.

We will describe the spectra in both image coordinates, range and azimuth. To illustrate this, we will use the data we processed, described in § 5.1. It is a selection of 2048×2048 pixels of a 'quarter scene' or quadrant of an ERS-SLC image of Groningen in the Netherlands. This image is shown in figure 5.1.

For the spectrum in range, a fast Fourier transform (§ A.1) is calculated for each range line. If the image counts N pixels in range and M lines in azimuth, we have M spectra with N frequency samples X_k each. In figure 4.3, the modulus of the spectrum over $N = 2048$ range pixels was taken for each of the $M = 2048$ azimuth lines. The vertical axis shows the azimuth coordinate, while the horizontal axis shows the range frequency.

For the spectrum in azimuth, the FFT is calculated for each azimuth line. In figure 4.4, in a similar way 2048 azimuth spectra over 2048 azimuth lines are shown.

In the range spectra, we see that the range signal band is smaller than the domain of the graph: the range bandwidth is smaller than the sampling frequency. At the edges, wrinkles appear. Some spectra are very bright due to a highly backscattering object. Also in the azimuth spectra the bandwidth is smaller than the sampling frequency. Most striking feature is that the empty spectral band is not at the edges: the spectrum is not centred. Its location depends on range, as will be discussed in the sequel.

4.2.1 Range spectrum

In figure 4.5 the amplitude of one range spectrum (one line from figure 4.3 for a particular azimuth line) is plotted. By averaging over 128 spectra, the shape of the range spectrum becomes more clear; the resulting amplitude is shown in figure 4.6.

With equations (A.11) and (A.13) we are able to determine the frequencies X_k
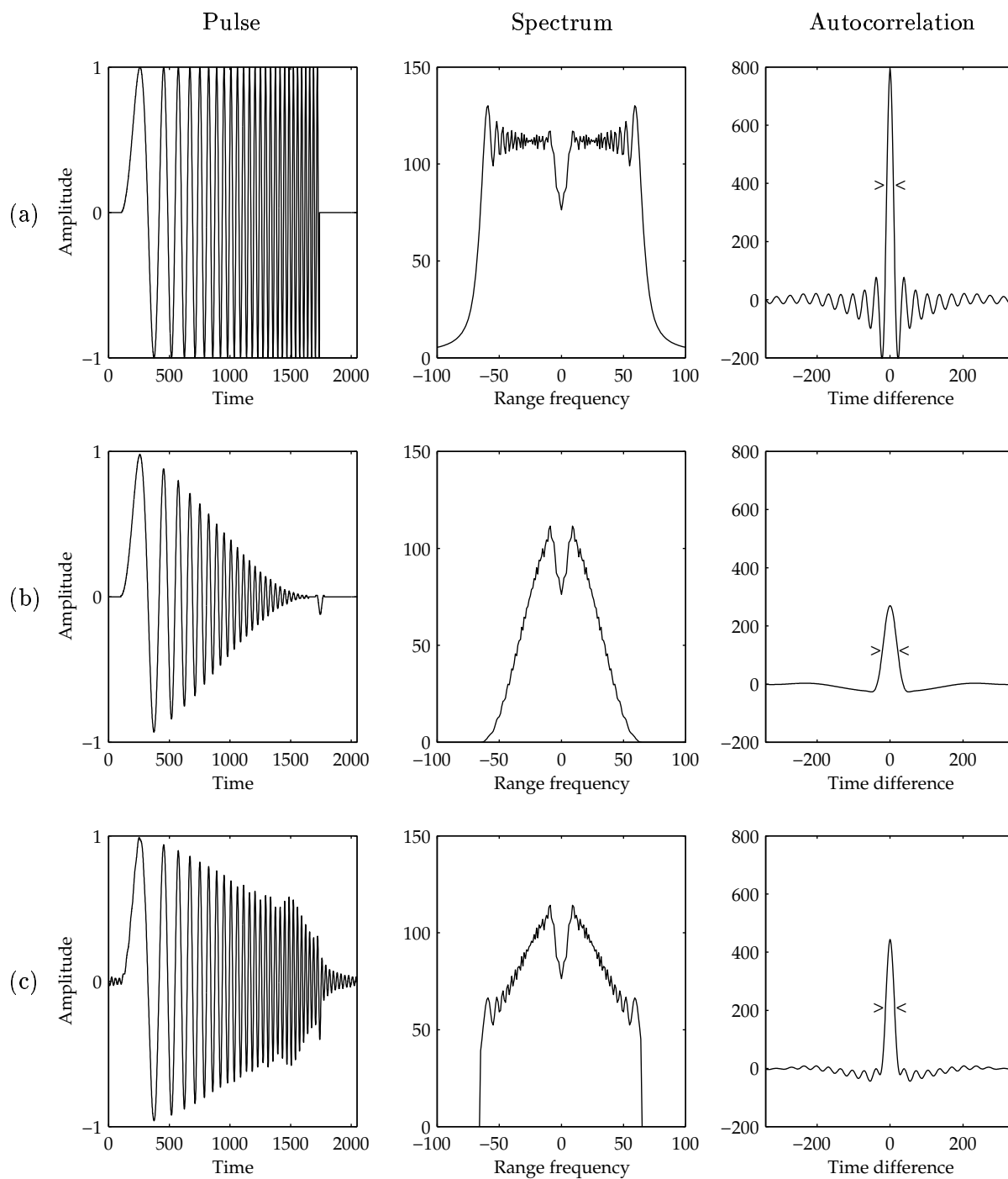
Figure 4.2 In figure (a), a simulation is shown of the unweighted linearly frequency modulated pulse or chirp of the synthetic aperture radar. The sidelobes of the autocorrelation causes objects to appear with 'ghost images' and must be reduced. This is realized by applying a spectral weighting or windowing function. In figure (b) the Von Hann window (equation 4.4) is applied. The sidelobes of the autocorrelation function are now almost absent, but the resolution is halved because the central peak has doubled in width. A trade-off is shown in figure (c), where the general 'Hamming' window (equation 4.9) is used with $\alpha = 0.75$.

azimuth

range frequency
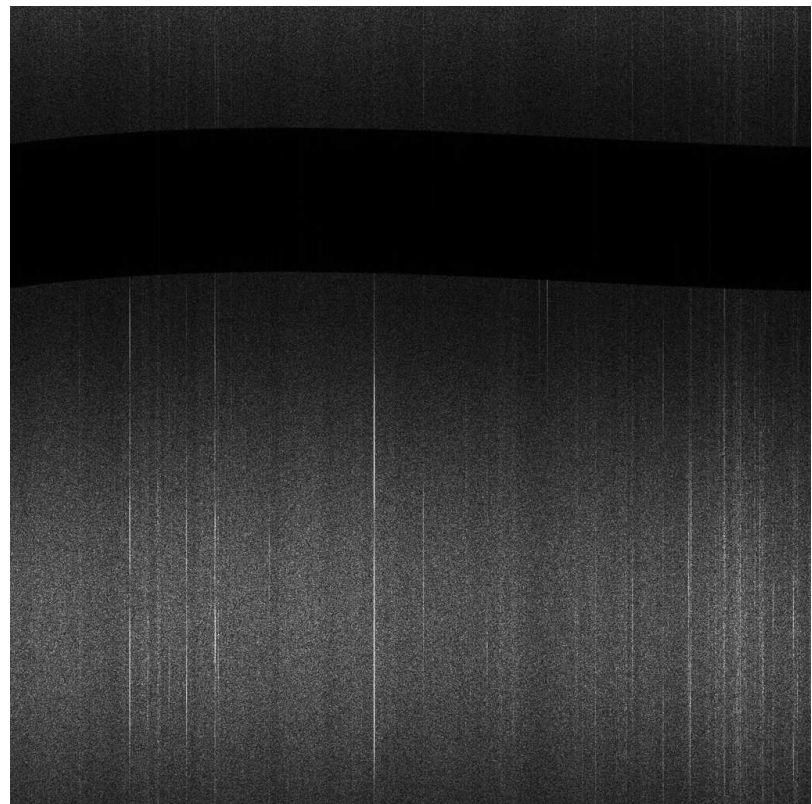
Figure 4.3 Of the selection of 2048 × 2048 pixels of the Groningen image of figure 5.1, the range spectrum is calculated for all azimuth lines. The amplitude is shown, with zero-frequency vertically in the middle.

azimuth frequency

range

Figure 4.4 Of the selection of 2048 × 2048 pixels of the Groningen image of figure 5.1, the azimuth spectrum is calculated for all range lines. The amplitude is shown, with zero-frequency horizontally in the middle.

and annotate the axis. The extent of the domain of the range spectrum is the sampling frequency (equation A.8), which is for ERS (ASF, 1995b; Geudtner, 1995).

$$f_s = 18.96 \text{ MHz}. \tag{4.10}$$

As we see in figure 4.6, the actual bandwidth of the range signal B_r (r for range) is slightly less. The range signal has been oversampled. This bandwidth is equivalent to the bandwidth of the chirp, used to obtain the resolution in range, as described in § 2.2 and equation (2.11). For ERS this is (ASF, 1995b)

$$B_r = aT = 15.55 \text{ MHz}. \tag{4.11}$$

We see that the spectrum resembles that of the simulation depicted in figure 4.2c (except for the dip around $f = 0$ due to the lowest frequencies being absent). The unwanted effects of the chirped range signal described in § 4.1.2 – the sidelobes of the autocorrelation function and the wrinkles at the edges of the spectrum, shown in in figure 4.2a – are reduced by the application of a weighting function.

For the European Remote Sensing satellites ERS, the windowing function used for the processing in range direction is often chosen to be the general Hamming window of equation (4.9) with (Solaas and Laur, 1993; Geudtner, 1995)

$$\alpha = 0.75. \tag{4.12}$$

The applied weighting function is referred to as Hamming, although it is not the original Hamming window of equation (4.8). The width of the Hamming cosine is, as will be clear from § 4.1.1, the bandwidth of the range data B_r.

With this, the amplitude transfer function for the range data of ERS is (Geudtner, 1995[†])

$$W(f_r) = \left(0.75 + 0.25 \cos \frac{2\pi f_r}{B_r} \right) \Pi\left(\frac{f_r}{B_r} \right) \tag{4.13}$$

This transfer function is shown in figure 4.6 as the smooth line through the data.

In some ERS range spectra – like the ones plotted by Geudtner (1995) and some of the data we processed – the actual data show a shift with respect to zero-frequency. This is a result of the squint angle of the antenna, causing a modulation of the chirp. The effect is larger for RADARSAT than for ERS, because of its larger squint angles. However, the effect on range filtering is negligible (Geudtner et al., 1998).

---

† In equation (41) and figure 13 in Geudtner (1995) the width of the cosine of the weighting function is taken to be equal to the range sampling frequency instead of the range bandwidth.
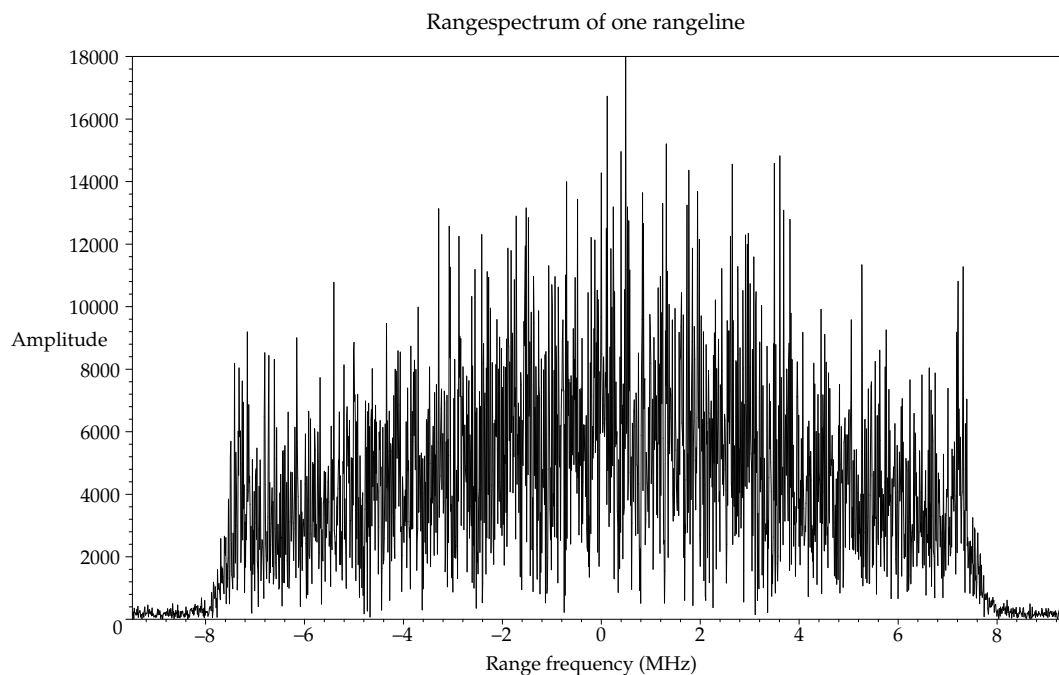
Rangespectrum of one rangeline

Figure 4.5   The amplitude of the spectrum of one range line.

Rangespectrum averaged over 128 rangelines
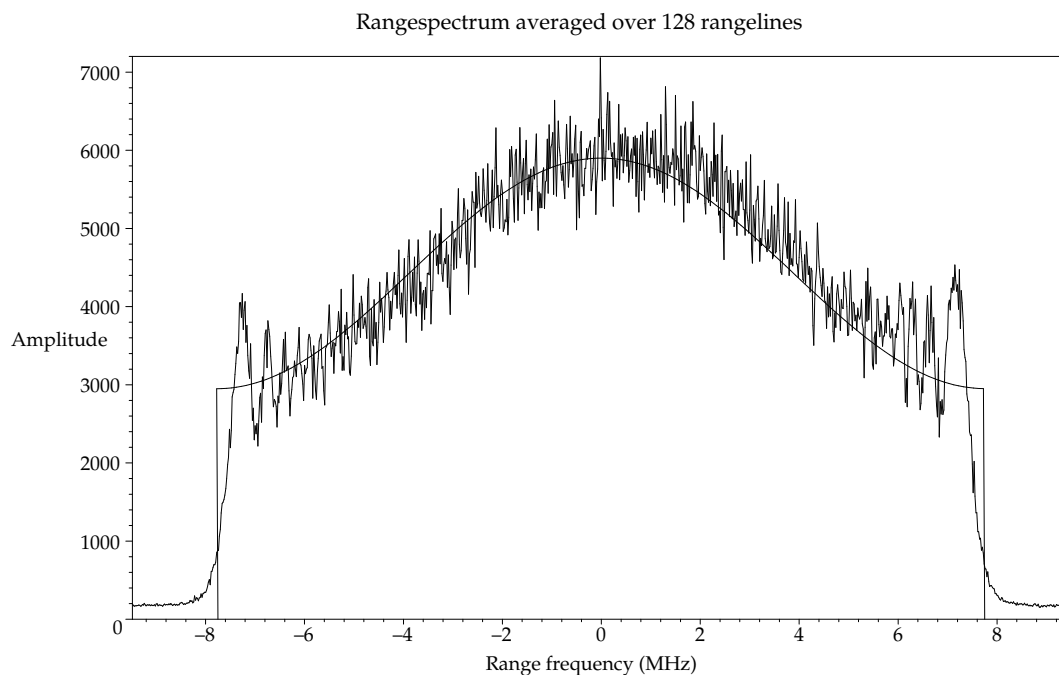
Figure 4.6   The amplitude of the average of the spectra of 128 range lines. The extent of the domain of the graph is the sampling frequency in range, $f_s = 18.96$ MHz. The bandwidth of the range signal is $B_r = 15.55$ MHz. The spectrum is weighted with a 'Hamming' function with $\alpha = 0.75$ in order to reduce the sidelobes of the autocorrelation function and the wrinkles at the edges, as described in § 4.1.2. The theoretical shape of the spectrum (equation 4.13) is shown as the smooth line.

Azimuthspectrum averaged over 128 azimuthlines
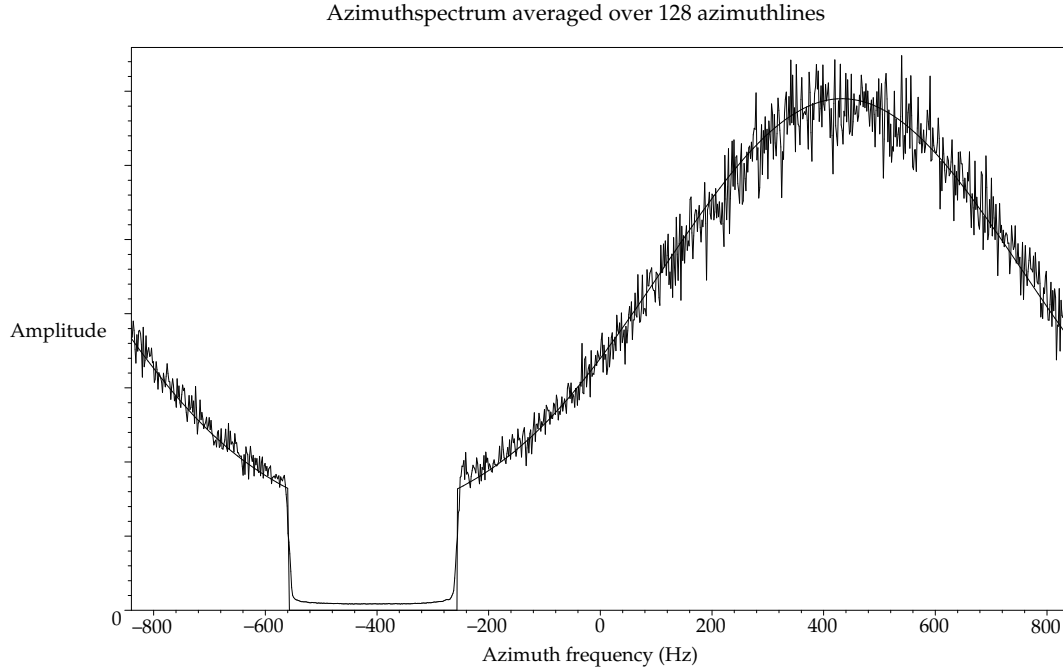
Figure 4.7   The amplitude of the average of the spectra of 128 azimuth lines. The extent of the domain of the graph is the sampling frequency in azimuth, the pulse repetition frequency, $f_{\text{pr}} \approx 1679$ Hz for ERS. The azimuth bandwidth is often chosen to be $B_a \approx 1378$ Hz. The spectrum shows a squared sinus cardinalis due to the antenna pattern and is weighted with a 'Hamming' function with $\alpha = 0.75$ in order to reduce the sidelobes of this antenna pattern, as described in § 4.1.3.   The spectrum is shifted with the Doppler centroid, which differs from zero-frequency due to the squint angle of the antenna. The theoretical shape of the spectrum (equation 4.16) is shown as the smooth line.

4.2.2 Azimuth spectrum

For each range line, a chirped pulse is emitted. After the satellite has moved in its orbit, the next pulse is emitted. A complete range line thus is acquired in the same time as one azimuth pixel of an azimuth line. The time scale for range is therefore often refered to as *fast time* and for azimuth *slow time*, which is illustrated by the frequency orders of their respective sampling frequencies.

The sampling in azimuth is performed by the chirped pulses, so the *pulse repetition frequency* is the sampling frequency in azimuth,

$$f_{s,\text{azimuth}} = f_{\text{pr}} \approx 1679 \text{ Hz} \qquad (4.14)$$

for ERS (theoretically, the instrument is able to sample with $1640 \ldots 1720$ Hz) (ESA, 1997). Similar to range, the azimuth data is slightly oversampled, resulting in the *processed bandwidth* B_a to be smaller than the pulse repetition frequency. In the SAR processing it is often chosen to be

$$B_a \approx 1378 \text{ Hz.} \qquad (4.15)$$

In figure 4.7, the average amplitude of the spectra of 128 azimuth lines is shown. The empty region shows the oversampling because $B_a < f_{\text{pr}}$. As described in § 4.1.3, the sidelobes of the squared sinus cardinalis of the antenna pattern are reduced by the application of a weighting function. For the European Remote Sensing satellites ERS, the
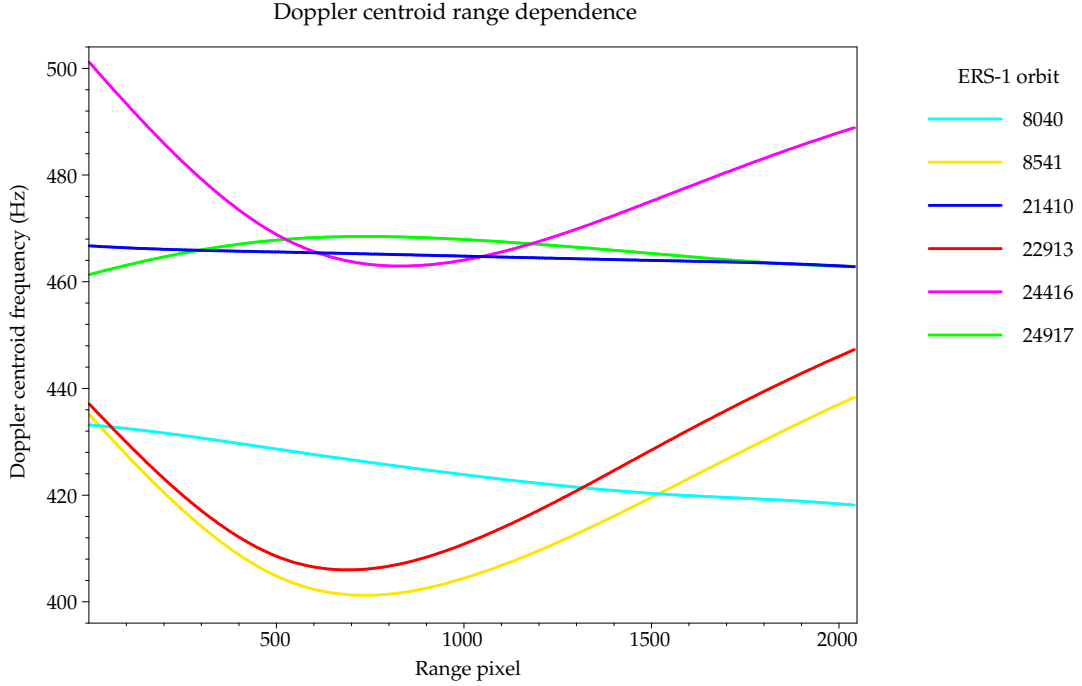
Figure 4.8   The Doppler centroid frequency depends on range, partly due to the dependence of the surface velocity component in the line of sight on the incidence angle. Shown are the Doppler centroids determined in chapter 5 for frame 2529 in six ERS-1 orbits.

weighting function often used for the data processing in azimuth direction is – similar to that in range – the general Hamming window of equation (4.9) with $\alpha = 0.75$ (Solaas and Laur, 1993; Geudtner, 1995). The width of the Hamming cosine is, as discussed in § 4.1.1, the bandwidth of the azimuth data B_a.

With this, the theoretical shape of the amplitude transfer function of the azimuth spectrum of ERS data is

$$W(f_a) = \left(0.75 + 0.25 \cos \frac{2\pi(f_a - f_{\mathrm{Dc}})}{B_a}\right) \left(\mathrm{sinc}\, \frac{f_a - f_{\mathrm{Dc}}}{f_{\mathrm{Dop}}}\right)^2 \Pi\left(\frac{f_a - f_{\mathrm{Dc}}}{B_a}\right), \qquad (4.16)$$

with $\mathrm{sinc}\, x = \sin \pi x/(\pi x)$ and $f_{\mathrm{Dop}} \approx 1505$ Hz, a Doppler bandwidth parameter related to the beam angle of the antenna pattern (Geudtner, 1995). This transfer function is shown in figure 4.7 as the smooth line through the data.

The shift f_{Dc} of the centroid of the azimuth spectrum is treated in the next subsection. If it is large enough, this shift causes the spectrum to fold to the other side: a replica of the spectrum becomes visible, as described in § A.2 and visible in figure 4.7.

4.2.3 Doppler shift of the azimuth spectrum and dependence of range

In equation (4.16), the centroid of the azimuth spectrum is shifted from zero-frequency with f_{Dc}, the *Doppler centroid* of the beam. In § 2.3 was explained that the varying platform velocity components in the line of sight for different parts of the footprint (figure 2.5) cause the backscatter to have a varying Doppler shift.

One would expect the Doppler shift of backscatter originating from a location perpendicular to the flight direction as seen from the satellite to be zero, because there

is no component of the platform velocity in the line of sight. Because the surface has a velocity due to the rotation of the earth, this is not the case. The antenna of ERS is a phased array that can be steered electronically to compensate for this effect. However, the net result of the angle the antenna beam makes with respect to the direction perpendicular to the flight direction, the inclination of the orbit and the rotation of the earth causes the azimuth spectrum to show a shift that depends on the geographic latitude. This central frequency f_{Dc} is called the *Doppler centroid*. The angle between the antenna pointing direction and the zero-Doppler direction is called the *squint angle* (Curlander and McDonough, 1991; Esteban et al., 1999).

As is shown in figures 4.4 and 4.8, the Doppler centroid depends on range. This is mainly caused by the variation of the incidence angle over the range within the footprint. Because the squint angle is not equal to zero, the surface velocity component in the direction of the line of sight depends on the incidence angle (Hanssen, 2000b; Curlander and McDonough, 1991).

4.3 Resolution and bandwidth

In § 2.2 was shown that the range resolution is proportional to the bandwidth of the chirp (equation 2.11). In azimuth, the resolution is proportional to the Doppler bandwidth of the signal (§ 2.3). The application of a weighting function to the spectrum reduces the sidelobes of the autocorrelation function in range (§ 4.1.2) and the sidelobes of the antenna pattern in azimuth (§ 4.1.3). However, application of a weighting function broadens the mainlobe, as we already showed in § 4.1.2. Therefore the resolution decreases (Curlander and McDonough, 1991). Other processes that reduce the bandwidth have the same effect, like the spectral filtering, treated in chapter 5.

5 Filtering in azimuth and range

In this chapter spectral filtering in range and azimuth will be discussed, the main subject of this research. The filtering will be tested and its theory will be illustrated with the data described in § 5.1. In § 5.2 the need for filtering in the spectral domain is showed, both for the azimuth and range direction. In order to judge the results of our experimental work, the theoretical improvement that can be achieved with filtering is discussed in § 5.3. After this, spectral filtering in azimuth is discussed, first the method to filter (§ 5.4) and then its implementation (§ 5.5). The method to filter in range is treated in § 5.6 and its implementation in § 5.8, after filtering in range has been demonstrated with a simulation in § 5.7.

The results of the spectral filtering on the test images with our implementation are presented in § 5.9. After this, the need for spectral filtering is discussed for several platforms in § 5.10. This chapter is concluded with a discussion on the location of spectral filtering in the interferometric processing in § 5.11.

5.1 Data used for experiments and illustrations

The theory of spectral filtering (this chapter) and the properties of spectra in range and azimuth (chapter 4) are illustrated with the data that were also used to test the developed implementation of spectral filtering. The data had to be suitable to test the spectral filtering: the influence of sources of decorrelation other than the geometric decorrelation had to be small. The area had to be flat, because then the influence of topography on the fringe frequency would be negligible for range filtering and the influence on coherence estimation would be negligible as well. The temporal decorrelation should be as small as possible and therefore images of ERS-1 and ERS-2 in tandem – with an interval of one day – have been used. Because these tandem pairs show relatively short baselines and thus are not suitable to demonstrate high baseline decorrelation and range filtering, also ERS-1 image pairs with an interval of one month had to be used, which show a higher temporal decorrelation.

The selected images were of the province of Groningen in the Netherlands. In figure 5.1, the amplitude image of an ERS-SLC image of Groningen is shown. It is a 'quarter scene' or quadrant of the full-size image frame 2529 and counts 2500 range pixels and 14600 azimuth lines. The pixel spacing is

$$\Delta r_{\text{slant range}} = 7.905 \text{ m} \tag{5.1}$$

$$\Delta r_{\text{range}} \approx \frac{\Delta r_{\text{slant range}}}{\sin 21.4°} \approx 21.6 \text{ m} \tag{5.2}$$

$$\Delta r_{\text{azimuth}} = 3.972 \text{ m} \tag{5.3}$$

This is not the physical resolution, as stated in § 2.2 and § 2.3, which is about 25 meter in range and 5 meter in azimuth. The actual width of the quarter scene is thus 54.1 km (half the footprint), its length is 58.0 km. For the amplitude image, we averaged over 3 pixels in range and 15 lines in azimuth. This *multilooking* causes the speckle to diminish and the resulting pixels to be approximately square, i.e., 65 × 60 meter.

Most of our processing was performed on a selection of 2048 × 2048 pixels. Its approximate position is shown in figure 5.1; not all image pairs have exactly this position. The selection is 44 km in range and 8 km in azimuth. The exact orbits, baselines and Doppler centroid frequencies of the data that have been used will be listed in § 5.9.

5.2   The need for spectral filtering

The two SLC images that are used to generate an interferogram must be as similar as possible. In order to be able to derive a digital elevation model, the only difference needed is the phase difference due to the different viewpoints of the satellites (§ 2.5). In practice, several processes cause the phase to deteriorate, leading to *decorrelation* and noise in the interferogram. By reducing this deterioration, the phase unwrapping can be improved and the quality of the produced digital elevation model can be increased.

One of the sources of decorrelation listed in § 3.2 is the imaging geometry during the acquisition, which is different for the master and the slave image. This type of decorrelation is called *geometric decorrelation.* The scattering characteristics of the terrain are dependent of the incidence angle. If the slave imaging geometry is different from the imaging geometry of the master, the recorded backscatter will contain different parts of the terrain or *object spectrum.* A requirement for optimal interferometry is that the spectral features of the object spectrum are reflected in a similar way in the spectrum of the master and slave image. In the next subsections, this requirement will be investigated for azimuth and range.

5.2.1 Spectral misalignment in azimuth

In § 4.2.3 the shift of the azimuth spectrum with the Doppler centroid f_{Dc} was discussed. The Doppler centroid for a certain frame shows a distribution, as is clear from figure 5.44 for ERS-1. If the master and slave image were acquired by the same satellite, they can thus have different Doppler centroid frequencies. If the master image is of another satellite than the slave or of ERS-2 in a different gyroscope phase (§ 4.2.3), a difference in Doppler centroid frequency is very likely to occur, as is clear from figure 5.46.

The difference in Doppler centroid is

$$\Delta f_{\text{Dc}} = f_{\text{Dc}_{\text{m}}} - f_{\text{Dc}_{\text{s}}}, \tag{5.4}$$

with $f_{\text{Dc}_{\text{m}}}$ the Doppler centroid frequency of the master azimuth spectrum as in equation (4.16) and $f_{\text{Dc}_{\text{s}}}$ the Doppler centroid frequency of the slave azimuth spectrum.

The occurrence of a difference in Doppler centroid frequency is illustrated by the spectra of the Groningen frame from two different orbits in figure 5.2. The ERS-1 image from orbit 22913 has a mean Doppler centroid of 421.86 Hz; the ERS-2 image from orbit

Figure 5.1   An amplitude image of the province of Groningen in the north-east of the Netherlands. This is a quadrant ('quarter scene') of single look complex ERS data with original dimensions of 2500 pixels in range (vertical) and 14600 lines in azimuth (vertical), multilooked over 3 pixels in range and 15 in azimuth, yielding a resolution of 65 × 60 meter. The image is 54.1 km wide and 58.0 km high. The indicated rectangle of 2048 × 2048 pixels (44 × 8 km) is used to perform the spectral filtering experiments in this thesis.

Azimuthspectrum of master and slave
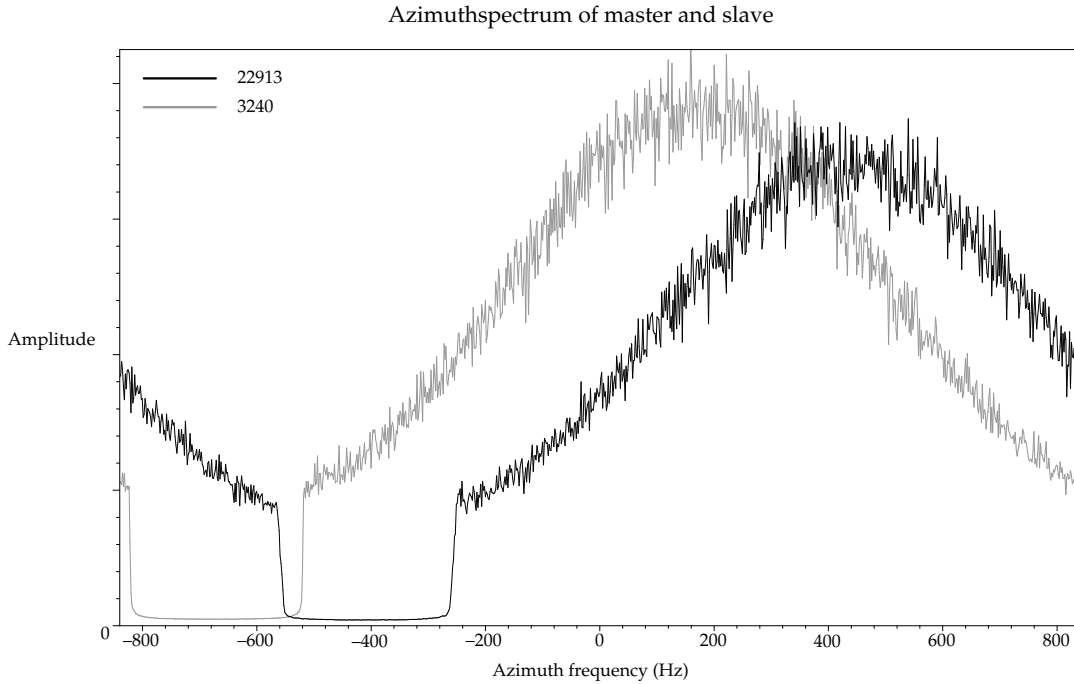
Figure 5.2   The azimuth spectra of the Groningen frame from orbit 22913 (ERS-1) and 3240 (ERS-2) (averaged over 128 lines) show a very different Doppler centroid: 421.86 Hz and 169.23 Hz, respectively. Because the object spectrum is assumed to be the same for master and slave, a certain spectral feature has the same frequency in both spectra. However, its location with respect to the spectral envelope is different for master and slave, leading to decorrelation. This can be reduced by azimuth filtering.

3240 shows a mean Doppler centroid of 169.23 Hz. Because the object spectrum is assumed to be the same for master and slave, a certain spectral feature has the same frequency in both spectra. However, its location with respect to the spectral envelope is different for master and slave. Some frequencies present in one spectrum are not even present in the other spectrum. This can also be explained in terms of a different transfer function (Bamler and Just, 1993; Bamler and Hartl, 1998). This causes decorrelation and shows up as noise in the interferometric phase.

This effect can be reduced by filtering the azimuth spectrum, so that both spectra show the same transfer function, at the expense of the resolution. The method to accomplish this is explained in § 5.4.

5.2.2 Spectral misalignment in range

If the spectra in range (§ 4.2.1) of the master and slave image are examined, the need for spectral filtering in range is not immediately clear, as the spectra show no relative shift nor disjunct frequency bands, in contrast with the azimuth spectra. However, in range also a source of geometric decorrelation is present.

The scattering characteristics of the terrain depend on the incidence angle and are reflected in the object spectrum. Because interferometry is based on the difference in viewpoint from both ends of the baseline, the incidence angle during the acquisition of the master and slave image is different. The 'spatial wavelength' of the terrain is sampled with the projected wavelength of the SAR signal, which is different for master and slave. Therefore the object spectrum is reflected into different range spectra for master and slave.

The ground range frequency f_g can be derived with help of the projection λ_g of the slant range wavelength λ_r onto the terrain (compare this with the geometry in equation (2.3)),

$$\lambda_g = \frac{\lambda_0}{2 \sin \theta}, \tag{5.5}$$

with θ the incidence angle. This can be stated in terms of the range frequency f_r and ground range frequency f_g,

$$f_g = \frac{c}{\lambda_g} = \frac{2c \sin \theta}{\lambda_r} = 2 f_r \sin \theta. \tag{5.6}$$

From the master side of the baseline, assume the incidence angle to a viewed terrain patch to be θ_m. The recorded reflectivity f_r is that of $f_{g,m}$ with $\theta = \theta_m$ in equation (5.6). From the slave side of the baseline, where the incidence angle to the viewed terrain patch is θ_s, the recorded reflectivity on range frequency f_r originates from frequency $f_{g,s}$ of the object spectrum, calculated with $\theta = \theta_s$ in equation (5.6). Thus, different frequencies of the object spectrum have the same range frequency in the master and slave spectrum. Because the envelope of the range spectrum is determined by the SAR processing and similar for master and slave, the difference in object frequency is not visible as a shift in the range spectrum.

The spectrum of the master image contains a band of the object spectrum that is not present in the slave image, and the opposite side of the spectrum of the slave contains a band of the object spectrum that is not present in the master image. This will lead to decorrelation. By removing the frequency bands that are only contained in one of the spectra, this geometric decorrelation can be removed, at the expense of the resolution. The bandwidth of the band that has to be removed depends on the frequency shift in the SAR spectrum.

Range frequency shift analysis

The amount of the shift in the range spectrum of features of the object spectrum due to the baseline separation can be derived in different ways. The derivation that follows uses the wavenumber; alternative derivations use the interferometer geometry (§ 2.4) and the frequency (appendix B).

Gatelli et al. (1994) consider the wavenumber k to derive the shift in the object spectrum, which they call the *wavenumber shift*. The wavenumber is defined as

$$k := \frac{2\pi}{\lambda}. \tag{5.7}$$

Projected onto the terrain with the incidence angle θ, the ground wavenumber becomes

$$k_g = \frac{4\pi f_r}{c} \sin \theta, \tag{5.8}$$

accounting for the round trip the signal makes. Due to the shift of the viewing position to the other end of the baseline, the incidence angle changes. If we denote this change with $\Delta\theta$, the wavenumber shift can be calculated by differentiating equation (5.8) to θ,

$$\Delta k_g = \frac{4\pi f_r \Delta\theta}{c} \cos \theta, \tag{5.9}$$
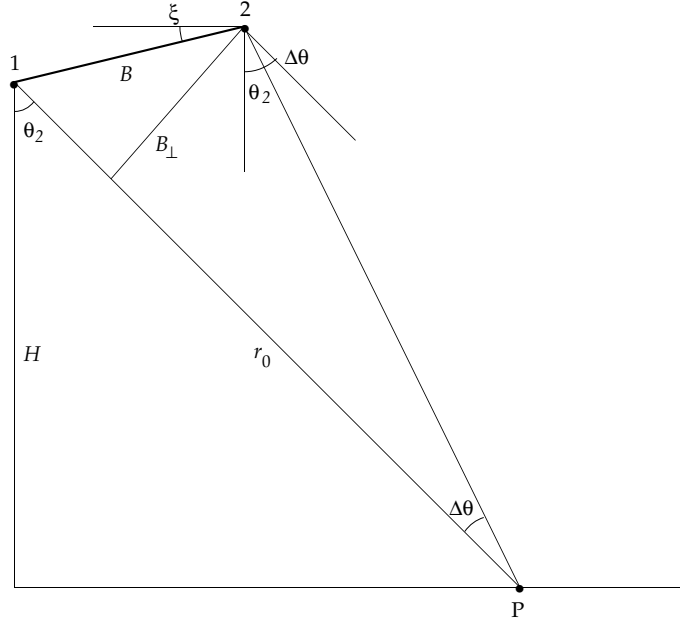
Figure 5.3   The viewing points 1 and 2 are separated by the baseline B. This causes the incidence angle θ_2 of satellite position 2 to be $\Delta\theta$ smaller than that of position 1. The ratio of the perpendicular baseline $B_\perp$ to the slant range r_0 is equal to this incidence angle difference $\Delta\theta$.

where θ can be taken to be the mean incidence angle from both ends of the baseline. Because the bandwidth of the SAR signal is small relative to the carrier frequency, the frequency f_r can be replaced by the central frequency f_0. To get an impression of the severity of the baseline decorrelation, this wavenumber shift is often compared with the SAR bandwidth B_r (equation 4.11); therefore it must be expressed in terms of frequency. Equation (5.8) expressed in terms of frequency and differentiated to θ is

$$f_r = \frac{c}{4\pi} k_g \frac{1}{\sin\theta} ; \tag{5.10}$$

$$\frac{\Delta f_r}{\Delta\theta} = \frac{c}{4\pi} k_g \frac{-1}{\sin^2\theta} \cos\theta = -\frac{f_0}{\tan\theta} , \tag{5.11}$$

where the last term results from substituting equation (5.8) again.

In equation (5.11), some interferometric parameters can be substituted. As is clear from figure 5.3, the ratio of the perpendicular baseline $B_\perp$ to the slant range r_0 is approximately equal to the incidence angle difference $\Delta\theta$ (for a flat earth),

$$\Delta\theta \approx B_\perp / r_0 . \tag{5.12}$$

The frequency shift of equation (5.11) can now be written

$$\Delta f_r = -\frac{f_0}{\tan\theta} \Delta\theta = -\frac{cB_\perp}{r_0 \lambda \tan\theta} . \tag{5.13}$$

The range frequency shift Δf_r of equation (5.13) is equal to the *fringe frequency* of equation (2.31), derived in § 2.4,

$$\Delta f_r = f_{\text{fringe}} . \tag{5.14}$$

As the cause of both phenomena is the same, this is what could be expected.

The fringe frequency can be expressed in megaHertz, which makes comparison with the range signal bandwidth easy. However, often an alternative expression in cycles per pixels is used. Because for spectral filtering in range, the ratio with the range bandwidth is of interest, we will use the range frequency shift of equation (5.13), but we will call it the fringe frequency.

Visualisation of the range frequency shift

Because the object spectrum is projected back in the slant range direction with the same angle, the object frequency shift is not visible as a difference in location of the envelope of the range spectrum of master and slave. If we know the perpendicular baseline $B_\perp$ or the incidence angle difference $\Delta\theta$, we can illustrate the ground range frequency shift by converting the range frequency into ground range frequency for the master and slave range spectrum with equation (5.6).

In figure 5.4 the power spectra of ERS-1 images 8040 and 8541 were converted to the ground range frequency. Master image 8040 is nearest to the ground track and shows the lowest ground range frequency, 8541 the highest. The perpendicular component of the baseline is $|B_\perp| = 376.7$ meter; this results in a range shift of $\Delta f = 6.030$ MHz and a ground range shift of $\Delta f_g = 4.405$ MHz. We see that the master and slave spectrum contain different parts of the object spectrum. The bands that they do not share can be removed by filtering, discussed in § 5.6.

Variation of the fringe frequency due to topography

As shown in § 2.5, the topography of the imaged scene influences the fringe distance and hence the fringe frequency. Parameter θ in equation (5.13) is the incidence angle, which depends on the slope of the terrain. If the terrain slopes towards the satellite, the incidence angle decreases and the range frequency shift increases. If eventually the slope angle equals the incidence angle for flat terrain, which is $23°$ for ERS, the fringe frequency becomes unbounded. On the other hand, if the terrain slope is directed away from the satellite, the fringe frequency decreases, until eventually the slope is $67°$ and the incidence is grazing and the fringe frequency zero. Beyond this limit, shadowing occurs.

If the slope angle of the terrain increases to the incidence angle for flat terrain, foreshortening transits into layover. Because the active microwave instrument on board of ERS was designed in the first place to monitor ocean phenomena, its look angle is relatively small, which is why layover occurs relatively often. Gatelli et al. (1994) show that by determining the locations where the sign of the fringe frequency changes, layover regions can be separated from non-layover regions. In this way decorrelated areas due to layover can be masked out, which can improve phase unwrapping.

Variation of the fringe frequency with range for a flat earth

Because within the interferogram the incidence angle slightly increases with range if the earth's surface would be flat, and the perpendicular component of the baseline projects different, the fringe frequency of equation (5.13) is not constant over the range of the interferogram. Because the orbits are in general not parallel, also a azimuth dependency of the baseline and hence of the fringe frequency occurs.

In figure 5.3 the difference in incidence angle $\Delta\theta$ is

$$\Delta\theta \approx B_\perp/r_0. \tag{5.12}$$
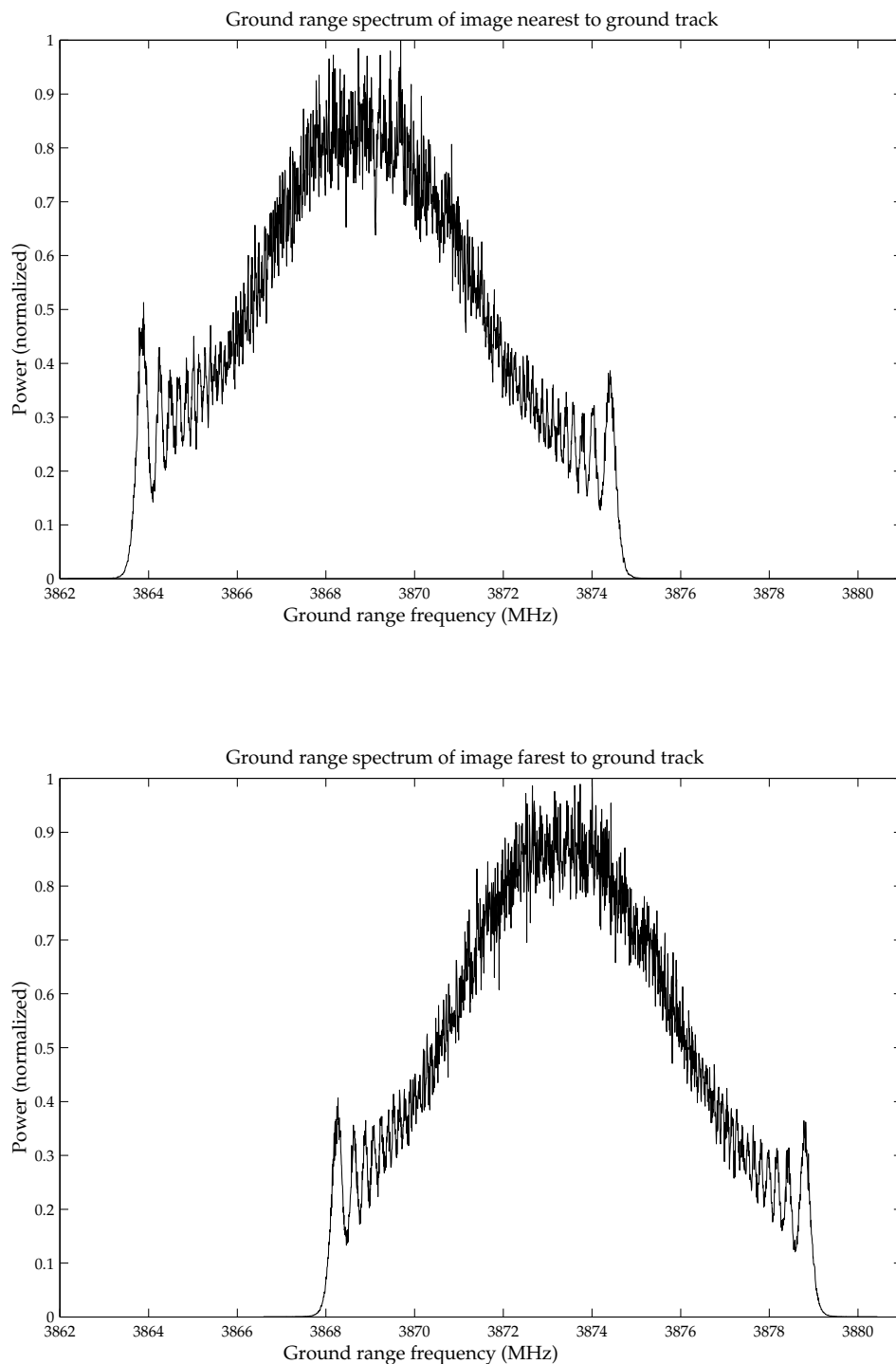
Figure 5.4   The power spectra of ERS-1 images 8040 and 8541, averaged over 128 lines, converted to the ground range frequency with equation (5.6). Master image 8040 is nearest to the ground track and shows the lowest ground range frequency, 8541 the highest. The perpendicular component of the baseline is $|B_\perp| = 376.7$ m; the average incidence angle $\theta = 21.421°$ and the range $r_0 = 844$ km. This results in a range shift of $\Delta f = 6.030$ MHz and a ground range shift of $\Delta f_g = 4.405$ MHz. The range frequency shift is equivalent to 39% of the range bandwidth. We must realize that the band shift due to the different incidence angle from either side of the baseline does not *appear* from this figure, but that this figure is *constructed* to demonstrate this.

As a result of the variation in incidence angle over the swath, also this incidence angle difference, the perpendicular projection of the baseline B and the slant range distance r_0 will vary. The height H, baseline slope angle ξ and length B will not vary. Hence, we can substitute

$$B_\perp = B \cos(\theta - \xi) \tag{2.23}$$

$$r_0 = \frac{H}{\cos \theta} \tag{5.15}$$

into equation (5.13),

$$\Delta f_r(\theta) = -\frac{f_0}{\tan \theta} \Delta \theta \tag{5.13}$$

$$= -\frac{f_0}{\tan \theta} \frac{B}{H} \cos(\theta - \xi) \cos \theta. \tag{5.16}$$

If we want to illustrate this in a straightforward way, without knowledge of the orbits, we can express this in the value of the usually available interferometric parameters for the middle of the scene, θ_0, r_0, and $B_{\perp_0}$. Because the orbits and hence the orientation of the baseline are not used, the baseline slope angle is chosen to be $\xi = 0$. The range-varying parameters are then (Swart, 1999)

$$B_\perp(\theta) = B \cos \theta \frac{\cos \theta_0}{\cos \theta_0} = B_{\perp_0} \frac{\cos \theta}{\cos \theta_0}; \tag{5.17}$$

$$r(\theta) = \frac{H}{\cos \theta} \frac{\cos \theta_0}{\cos \theta_0} = r_0 \frac{\cos \theta_0}{\cos \theta}. \tag{5.18}$$

The range or incidence angle dependent fringe frequency now becomes

$$\Delta f_r(\theta) = -\frac{f_0}{\tan \theta} \frac{B_{\perp_0}}{r_0} \frac{\cos^2 \theta}{\cos^2 \theta_0} = -\frac{cB_{\perp_0}}{r_0 \lambda \tan \theta} \frac{\cos^2 \theta}{\cos^2 \theta_0}. \tag{5.19}$$

The variation of the fringe frequency over the range of an ERS-1 SLC image for a flat earth is shown in figure 5.5 for a baseline of $B_{\perp_0} = 376.7$ m.

5.2.3 Reduction of resolution due to filtering

The decorrelation due to the spectral misalignment in range and azimuth can be removed by filtering the spectra, so that only the band they have in common remains. Because this reduces the bandwidth, the resolution of the interferogram degrades (§ 4.3).

5.2.4 Restrictions to interferometry due to spectral misalignment

If the spectral band the master and slave image have in common is narrow, after spectral filtering little information will be present, reducing the resolution. But if eventually the spectrum of master and slave are disjunct, calculation of an interferogram becomes senseless.

For the azimuth spectrum, this is the case if the difference in Doppler centroid is more than the azimuth bandwidth. For ERS, this does not happen, as is discussed in § 4.2.3.

For the range spectrum, this can happen if the baseline becomes too long. The baseline for which the spectra of master and slave become disjunct is called the *critical*
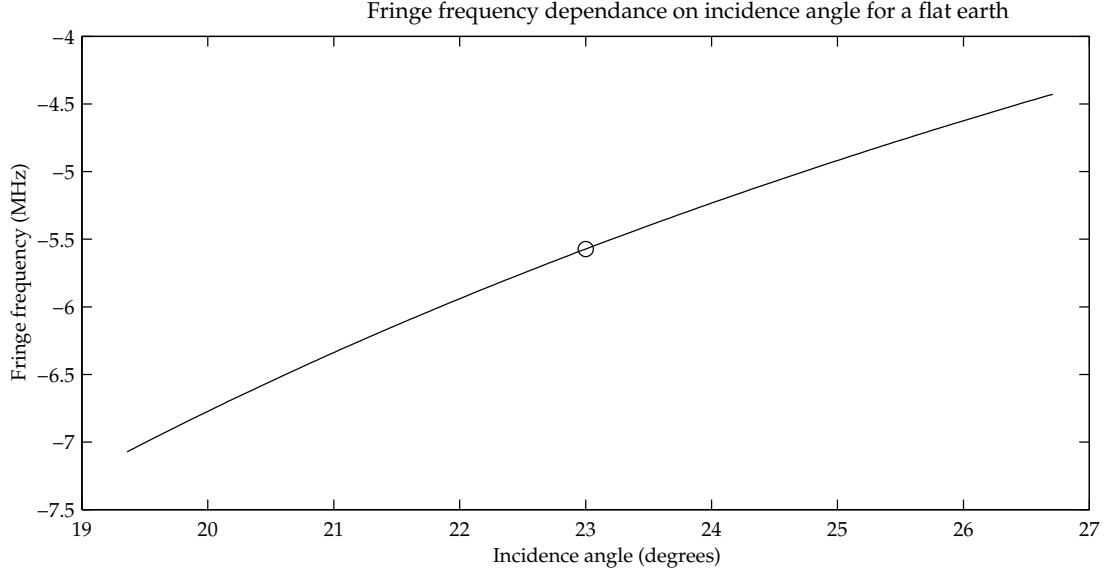
Figure 5.5 The variation of the fringe frequency over range due to the incidence angle dependence for a flat earth. For the swath width of 100 km of ERS, the slant range of 844 km and the incidence angle of the scene centre of 23.00°, the incidence angle of the swath edge near the groundtrack is 19.36° and that of the opposite edge is 26.74°. The baseline is taken to be that of image pair 8040 and 8541: 376.7 meter. This figure leads to the conclusion that range filtering has to be carried out dependent on range.

baseline. For ERS, the critical baseline can be calculated by substituting the range bandwidth, often chosen to be $B_r = 15.55$ MHz, as the range shift frequency in equation (5.6). The critical baseline is (Gatelli et al., 1994; Geudtner, 1995)

$$|B_{\perp,\text{crit}}| = \frac{cB_r r_0 \tan\theta}{\lambda}$$
$$\approx \frac{3 \cdot 10^8 \cdot 15.55 \cdot 10^6 \cdot 850 \cdot 10^3 \cdot \tan 23°}{0.0566} \approx 1060 \text{ m.} \quad (5.20)$$

Parameter θ is the incidence angle, which depends on the slope of the terrain. If the terrain slopes towards the satellite, the incidence angle decreases; if eventually the slope angle equals the incidence angle for flat terrain, which is 23° for ERS, the fringe frequency becomes unbounded and even a zero-baseline yields total decorrelation.

5.2.5 Other filtering processes

Filtering processes can be undertaken in several steps of the interferometric processing. The noise in the interferogram that is corrected for the reference phase can be decreased by filtering in order to improve the phase unwrapping. Mostly this is a smoothing operation along the fringes; because it depends on the fringe frequency and the orientation of the fringes, it is called *adaptive* (Schwäbisch, 1995; Lee et al., 1998). Goldstein and Werner (1998) describe adaptive interferogram filtering using the spectral properties of the interferogram. These adaptive filtering methods have nothing to do with the spectral filtering in this thesis, that in range can also be adaptive because it can be made dependent of the local fringe frequency. The difference is that we discuss spectral filtering of the SLC images, not of the interferogram.
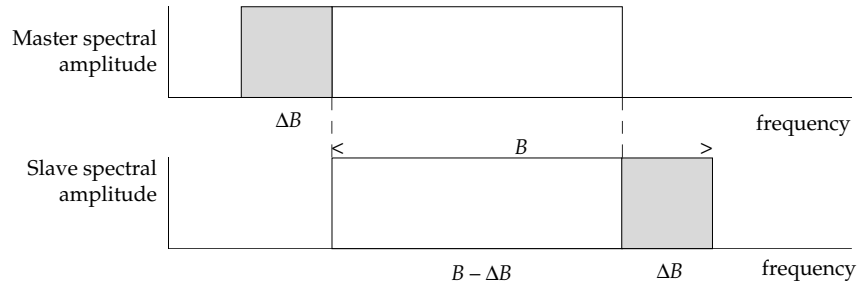
Figure 5.6 The spectra of master and slave with bandwidth B have the shaded band ΔB not in common. The signal-to-noise ratio of the interferogram due to the non-overlapping spectra can be calculated with the ratio of the common and non-common bandwidths.

5.3 Theoretical improvement by spectral filtering

As shown in § 5.2, due to the geometric conditions during acquisition of the images, the spectral bands of the master and slave do not completely overlap. Because the shape of the spectra is known, it is possible to derive the theoretically resulting decorrelation and reduction of the signal-to-noise ratio of the interferogram, given the spectral shift in range or azimuth. This theoretical decorrelation, calculated in this section, can be compared with the decorrelation estimated from the interferograms.

5.3.1 Decorrelation of spectra with rectangular envelope

For the calculation of the theoretical reduction in signal-to-noise ratio, we first assume the envelope of the spectra of master and slave to be rectangular. In figure 5.6, the spectra show a bandwidth B. The spectra have a band ΔB not in common. In the interferogram, this band causes noise. The common bandwidth $B - \Delta B$ of each spectrum contributes to the ideally noise-free interferogram. The signal-to-noise ratio thus is

$$\text{SNR} = \frac{B - \Delta B}{\Delta B}. \tag{5.21}$$

According to equation (3.14) in section § 3.3.1, the correlation is

$$\gamma = \frac{1}{1 + \text{SNR}^{-1}}$$
$$= 1 - \frac{\Delta B}{B}. \tag{5.22}$$

The decorrelation due to the spectral misalignment in range can be characterized by the fringe frequency $\Delta B = |\Delta f_r|$ (equation 5.11) and the signal bandwidth in range is often chosen to be $B_r \approx 15.55$ MHz for ERS (equation 4.11). In azimuth, the spectral shift is the difference in Doppler centroids of both images, $\Delta B = |\Delta F_{\text{Dc}}|$ (equation (5.4) and the azimuth signal is often processed with a bandwidth of $B_a \approx 1378$ Hz for ERS (equation 4.15).

As stated in section § 3.2, the decorrelation appearing in an interferogram is caused by several sources. They can all be characterized by a decorrelation γ_i and as in equation (3.15), the total decorrelation can be written as the product of the decorrelation factors due to the individual sources. If a rectangular envelope of the azimuth and range spectra

is assumed, the geometric decorrelation in azimuth and range can thus be written as (Bamler and Just, 1993; Geudtner, 1995)

$$\gamma_{\text{geometric}} = \gamma_{\text{azimuth}} \cdot \gamma_{\text{range}}$$
$$= \left(1 - \frac{|\Delta f_{\text{Dc}}|}{B_a}\right)\left(1 - \frac{|\Delta f_r|}{B_r}\right). \tag{5.23}$$

If the spectra of azimuth and range have a rectangular shape, the decorrelation is thus linearly dependent of the fringe frequency for range and the Doppler centroid difference in azimuth. This is shown by the diagonal line in figure 5.8 for azimuth and figure 5.9 for range. Apart from the fringe frequency and the Doppler centroid difference, also the spectral overlap $\frac{B - \Delta B}{B}$ is given in these figures. Total decorrelation occurs if $|\Delta f_r| \geq B_r$ in range and $|\Delta f_{\text{Dc}}| \geq B_a$ in azimuth, as discussed in § 5.2.4.

If the spectral bands that the master and slave spectrum do not have in common are removed and the transfer functions are made similar, as will be described in sections 5.4 and 5.6, the geometric decorrelation should theoretically be one. The expected improvement m of the spectral filtering process thus is the reciprocal of the decorrelation,

$$m_{\text{azimuth}} = \frac{1}{\gamma_{\text{azimuth}}} = \frac{B_a}{B_a - \Delta f_{\text{Dc}}}, \tag{5.24}$$

$$m_{\text{range}} = \frac{1}{\gamma_{\text{range}}} = \frac{B_r}{B_r - \Delta f_r}. \tag{5.25}$$

5.3.2 Decorrelation of spectra with weighted envelope

In practice, the envelope of the azimuth and range spectrum are not rectangular. In § 4.2.2, the shape of the azimuth spectrum was shown to consist of a squared sinus cardinalis and a Hamming weighting function,

$$W(f_a, f_{\text{Dc}}) = \left(0.75 + 0.25 \cos \frac{2\pi(f_a - f_{\text{Dc}})}{B_a}\right) \left(\text{sinc} \frac{f_a - f_{\text{Dc}}}{f_{\text{Dop}}}\right)^2 \Pi\left(\frac{f_a - f_{\text{Dc}}}{B_a}\right). \tag{5.26}$$

The Doppler centroid frequency f_{Dc} is the amount the azimuth spectrum is shifted.

The range spectrum is, as discussed in § 4.2.1, weighted with a Hamming function. In the previous section, we showed that the different view angle from either side of the baseline causes no shift in the range spectrum, although the object spectrum does. The shift of the object spectrum can be translated into a shift of spectral features in the range spectrum with the fringe frequency Δf_r (equation 5.13). For the goal of this section, we will express this as a shift of the range spectrum. The shape of the range spectrum then is

$$W(f_r, \Delta f_r) = \left(0.75 + 0.25 \cos \frac{2\pi(f_r - \Delta f_r)}{B_r}\right) \Pi\left(\frac{f_r}{B_r}\right). \tag{5.27}$$

The noise inducing bands ΔB of the not perfectly overlapping spectra are weighted, so that the formula for the decorrelation (5.22) of rectangular spectra does not hold any more. The formula for weighted spectra uses the convolution of the spectra. The calculation of an interferogram is the complex multiplication of the master and slave image, as discussed in § 2.4; this is equivalent with the convolution of the spectra of the master and slave image. The expected decorrelation for the weighted spectra can be brought in a form similar to that of equation (5.22), $\frac{B - \Delta B}{B}$. The nominator is the value
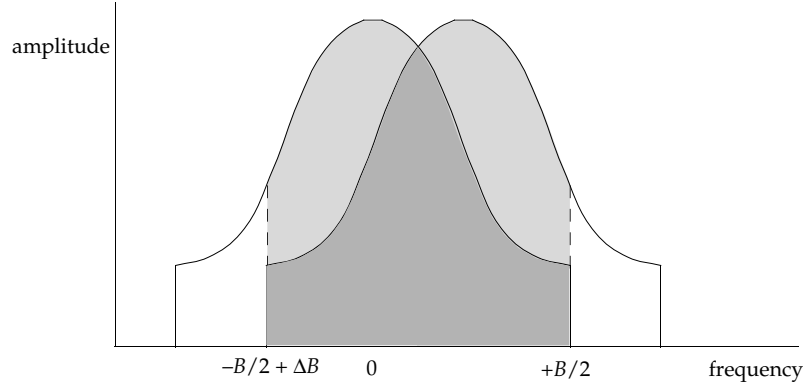
Figure 5.7   The decorrelation due to the spectral shift ΔB can be calculated as the ratio of the autoconvolution value for the shift ΔB (the shaded area) and the total area under the squared spectral envelope.

of the autoconvolution function for the spectral shift ΔB; de denominator is the integral of the square of the spectrum (which is the value of the autoconvolution function with a shift of zero). This is illustrated in figure 5.7.

For the weighted azimuth spectrum,

$$\gamma_{\text{azimuth}}(\Delta f_{\text{Dc}}) = \frac{1}{A_{\text{azimuth}}} \int\limits_{-f_{\text{pr}}/2}^{f_{\text{pr}}/2} W(f_a, 0) W(f_a, \Delta f_{\text{Dc}}) \, df_a, \tag{5.28}$$

with $W(f_a, f_{\text{Dc}})$ from equation (5.26) and

$$A_{\text{azimuth}} = \int\limits_{-f_{\text{pr}}/2}^{f_{\text{pr}}/2} \left(W(f_a, 0) \right)^2 df_a. \tag{5.29}$$

Because of the rectangular function Π in equation (5.26), the integration lower limit in equation (5.28) is effectively $-B_a/2 + |\Delta f_{\text{Dc}}|$ and the upper limit $B_a/2$, as shown in figure 5.7. This theoretical coherence γ_{azimuth}, resulting in a decorrelation of $1 - \gamma_{\text{azimuth}}$ due to the Doppler centroid difference Δf_{Dc} of the azimuth spectrum, is drawn in figure 5.8 as a function of the Doppler centroid difference and the spectral overlap $\frac{B - \Delta B}{B}$. For comparison, also the coherence is drawn if the spectrum would have a rectangular envelope.

For the weighted range spectrum, the theoretical coherence is

$$\gamma_{\text{range}}(\Delta f_r) = \frac{1}{A_{\text{range}}} \int\limits_{-f_s/2}^{f_s/2} W(f_r, 0) W(f_r, \Delta f_r) \, df_r, \tag{5.30}$$

with $W(f_r, \Delta f_r)$ from equation (5.27) and

$$A_{\text{range}} = \int\limits_{-f_s/2}^{f_s/2} \left(W(f_r, 0) \right)^2 df_r. \tag{5.31}$$

Coherence due to Doppler centroid difference
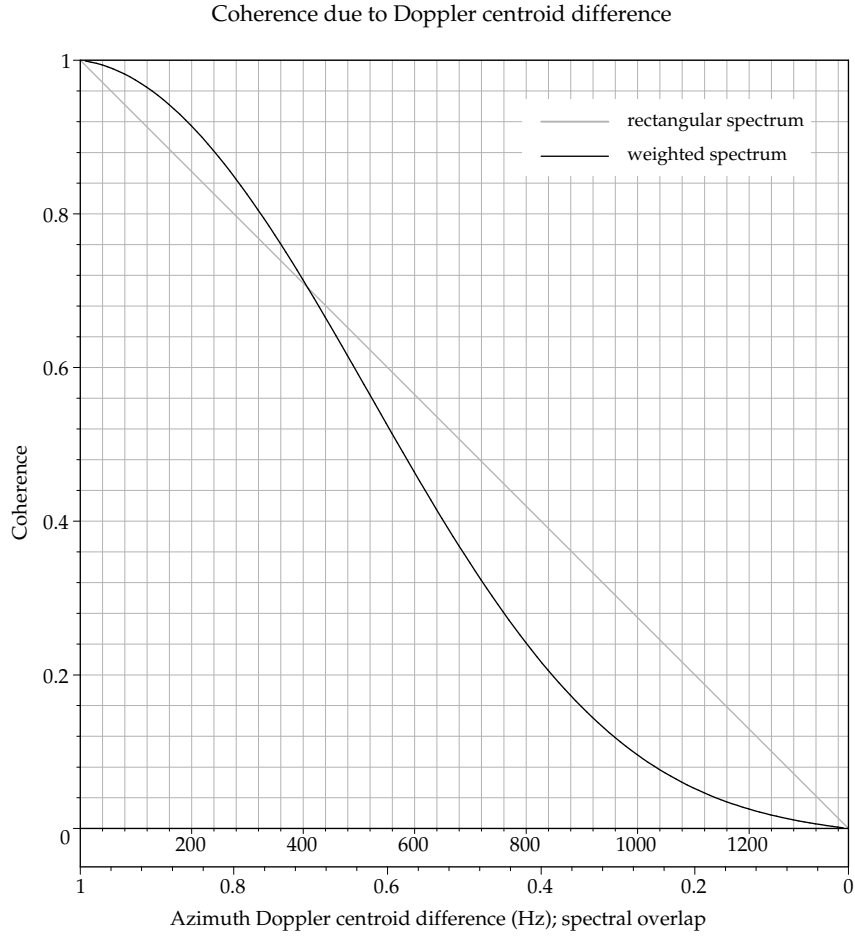
Figure 5.8 The theoretical coherence γ_{azimuth}, resulting in a decorrelation $1 - \gamma_{\text{azimuth}}$, due to the Doppler centroid difference Δf_{Dc} of the weighted azimuth spectrum of equation (5.26) as a function of the Doppler centroid difference and the spectral overlap $\frac{B - \Delta B}{B}$. For comparison, also the coherence is drawn if the spectrum would have a rectangular envelope.

Because of the rectangular function Π in equation (5.27), the integration lower limit in equation (5.30) is effectively $-B_r/2 + |\Delta f_r|$ and the upper limit $B_r/2$. This theoretical coherence γ_{range}, resulting in a decorrelation of $1 - \gamma_{\text{range}}$ due to the range frequency shift or fringe frequency Δf_r of the range spectrum, is drawn in figure 5.9 as a function of the range frequency shift and the spectral overlap $\frac{B - \Delta B}{B}$. Also the coherence is drawn if the spectrum would have a rectangular envelope. These results for azimuth and range are consistent with the graph shown by Askne (1996).

If the spectral bands that the master and slave spectrum do not have in common are removed and the transfer functions are made similar, the geometric decorrelation should theoretically be zero and the coherence one. The expected improvement m of the spectral filtering process thus is the reciprocal of the coherence,

$$m_{\text{azimuth}} = \frac{1}{\gamma_{\text{azimuth}}(\Delta f_{\text{Dc}})}, \qquad (5.32)$$

$$m_{\text{range}} = \frac{1}{\gamma_{\text{range}}(\Delta f_r)}. \qquad (5.33)$$

Coherence due to incidence angle difference
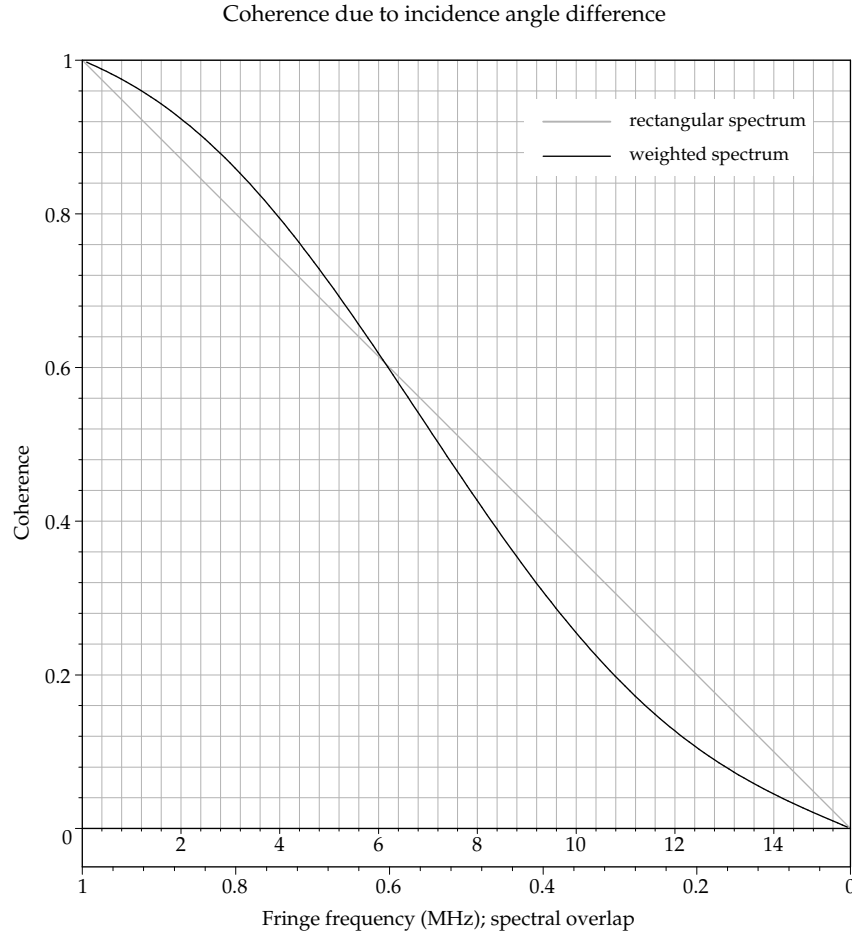
Figure 5.9 The theoretical coherence γ_{range}, resulting in a decorrelation $1 - \gamma_{\text{range}}$ due to the incidence angle difference, which leads to a range frequency shift or fringe frequency Δf_r. The range spectrum is assumed to be weighted according to equation (5.27). The theoretical coherence is drawn as a function of the range frequency shift and the spectral overlap $\frac{B - \Delta B}{B}$. For comparison, also the coherence is drawn if the spectrum would have a rectangular envelope.

5.3.3 Estimation of improvement due to spectral filtering

If the azimuth and range spectra are weighted according to equations (5.26) and (5.27), the expected improvement m of the spectral filtering process was described by equations (5.32) and (5.33). To test the developed algorithms and implementations for azimuth and range filtering, the estimator of the coherence of the filtered images can be calculated, as discussed in § 3.3 and § 3.4. After the coherence is corrected for the bias (§ 3.4.4), the mean coherence of the coherence image can be compared with the theoretically predicted improvement to assess the effectiveness of the implemented spectral filtering.

5.4 Method to filter in azimuth

In § 5.2.1, the need for spectral filtering in azimuth was shown. In this section, the practical approach to accomplish this is treated. Before the approach to spectral filtering is discussed, a few words on a technique that would make spectral filtering in azimuth superfluous, but has other drawbacks.

It is possible to process the raw SAR data with the Doppler centroid frequency

being the average of the individual centroids of the master and slave image. This causes defocusing in both images because the matched filter is different from the filter appropriate to the actual Doppler centroid of the individual images, but on the other hand there is no need to limit the bandwidth, as in the case of spectral filtering. The increase in coherence is comparable (Rosich et al., 2000). However, if a SAR image has to be used in more than one interferometric image pair, for each pair the SAR processing has to be performed with a different average Doppler centroid frequency. Moreover, if the standard SLC-products are used, it is not possible to process the data with a different Doppler centroid (Schwäbisch and Geudtner, 1995). This approach is therefore not treated in this thesis.

The shape of the spectra in azimuth of master and slave image must be as similar as possible. This means that the spectral band they have not in common must be removed and the spectrum must be reweighted. The goal is to achieve the system transfer function $H(f_a)$ to be the same for the master and slave image.

If the shape of the spectrum of the transfer function of the master image is $W(f_a - f_{Dc_1})$ (equation 4.16) and that of the slave image is $W(f_a - f_{Dc_2})$, with f_a the azimuth frequency and f_{Dc_i} the respective Doppler centroids, we want to apply spectral filter functions $F_1(f_a)$ and $F_2(f_a)$ so that (Schwäbisch and Geudtner, 1995)

$$W(f_a - f_{Dc_1}) \cdot F_1(f_a) = W(f_a - f_{Dc_2}) \cdot F_2(f_a) = H(f_a). \tag{5.34}$$

Without having to know $H(f_a)$, we can derive the filter functions. Equation (5.34) is satisfied if

$$F_1(f_a) = \sqrt{\frac{W(f_a - f_{Dc_2})}{W(f_a - f_{Dc_1})}}; \tag{5.35}$$

$$F_2(f_a) = \sqrt{\frac{W(f_a - f_{Dc_1})}{W(f_a - f_{Dc_2})}}. \tag{5.36}$$

Thus equation (5.34) becomes

$$H(f_a) = \sqrt{W(f_a - f_{Dc_1}) \cdot W(f_a - f_{Dc_2})}. \tag{5.37}$$

The filter in fact is the geometrical mean of both spectra. The spectra do now have the same amplitude. However, the filter functions $F_1(f_a)$ and $F_2(f_a)$ do not account for the fact that the spectra show frequency bands that only one of them utilizes. Therefore, these bands are filtered out with a rectangular windowing function, so that the filters eventually become

$$\tilde{F}_1(f_a) = F_1(f_a) \cdot \tilde{\Pi}(f_a) = \sqrt{\frac{W(f_a - f_{Dc_2})}{W(f_a - f_{Dc_1})}} \cdot \tilde{\Pi}(f_a) \tag{5.38}$$

$$\tilde{F}_2(f_a) = F_2(f_a) \cdot \tilde{\Pi}(f_a) = \sqrt{\frac{W(f_a - f_{Dc_1})}{W(f_a - f_{Dc_2})}} \cdot \tilde{\Pi}(f_a) \tag{5.39}$$

with

$$\tilde{\Pi}(f_a) = \begin{cases} 1 & \text{if } f_a \in B_{a_1} \cap B_{a_2} \\ 0 & \text{otherwise} \end{cases} \tag{5.40}$$

the rectangular window function, but different from the definition of Π in equation (4.2)

Azimuth spectra and filters
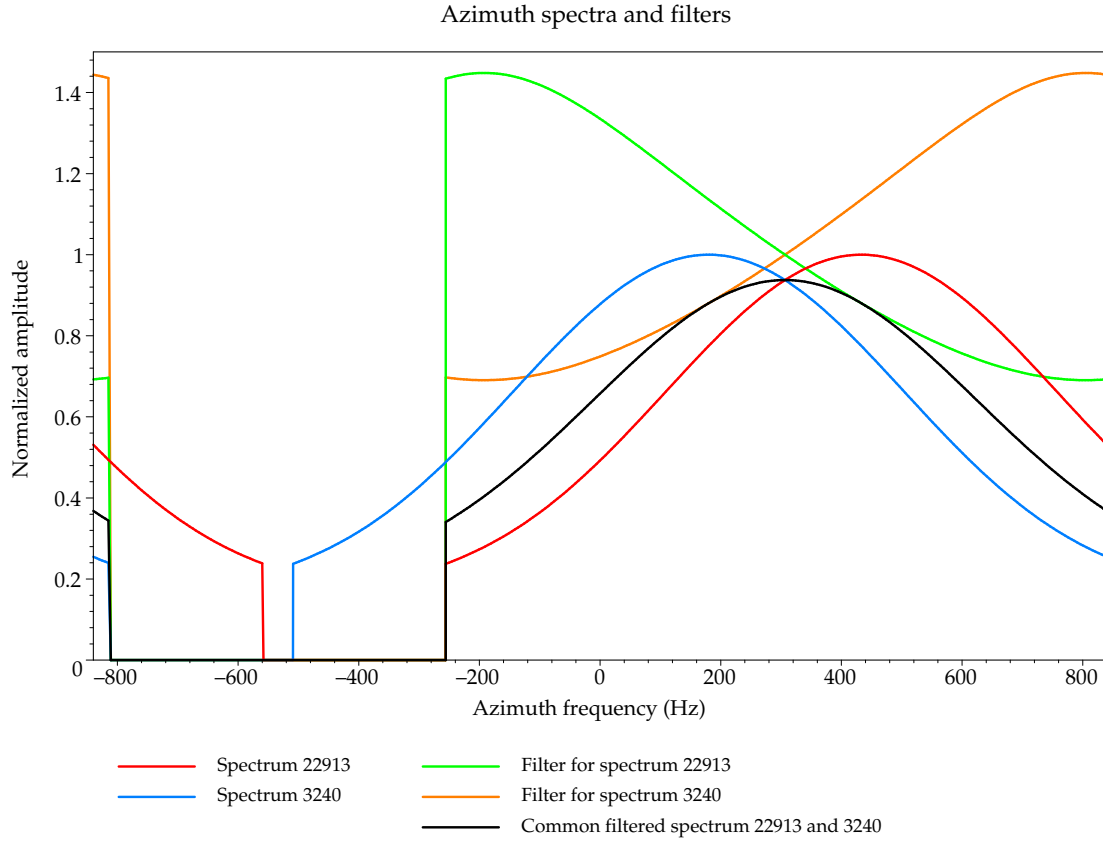
Figure 5.10 From the theoretical shape of the azimuth spectra of the master and the slave, showed in figure 5.2, the azimuth filters can be calculated. The master image from orbit 22913 has a Doppler centroid of 433.1 Hz (i.e., the average over the first 128 lines) and the slave image from orbit 3240 has a Doppler centroid of 169.8 Hz. The result of the application of the azimuth filters is a common spectrum for both master and slave.

in that it only is unequal to zero where the azimuth spectral bands of master and slave overlap.

In figure 5.10, the theoretical shape of the azimuth spectra (equation 4.16) is shown for the case that the Doppler centroid frequency of the master image 22913 (shown in figure 5.2) is $f_{Dc_1} = 433.1$ Hz and that of the slave image 3240 is $f_{Dc_2} = 169.8$ Hz. From the positions of these spectra, the filters (5.38) and (5.39) are calculated and shown. Finally, the resulting common spectral envelope is shown.

The now common transfer function should lead to less geometric decorrelation. In § 5.9 we will show the results of our experiments. To be able to carry out these experiments, the azimuth filtering has to be implemented. This is treated in § 5.5.

As is clear from figure 5.10, the removal of the spectral bands which the master and slave image do not have in common with the application of the rectangular window function $\tilde{\Pi}(f_a)$ of equation (5.40), the bandwidth of the signal decreases. As explained in § 4.3, a limitation of the bandwidth will reduce the resolution.

5.5 Implementation of azimuth filtering

During the research, an implementation of azimuth filtering has been developed. The parameter files and a list of written software can be found in appendix E.

5.5.1 Doppler centroid as central parameter

The main issue with implementing the azimuth filtering method discussed in § 5.4 is the determination of the Doppler frequency centroid of the master and slave image. As discussed in § 4.2.3, the Doppler centroid depends on range. This is demonstrated by figures 4.3 and 4.8. If the interferometric processing is started with the single look complex SAR images, the header files will contain the Doppler centroid averaged over range or an approximation of the range dependence with a polynomial. However, because the headers that we had at our disposal did not contain all necessary information on the Doppler centroid, we derived the Doppler centroid from the spectra of the images.

The Doppler centroid can be determined by locating the azimuth frequency of the maximum of the azimuth spectrum. Figure 4.5 shows that parameters of the shape of the range spectrum are difficult to determine from one range line, because of its 'noisy' character. After averaging over 128 range lines, as is shown in figure 4.6, the shape of the spectral envelope becomes clear and the shape parameters can be determined with less effort. The same holds for the azimuth spectrum. We determined the Doppler centroid f_{Dc} by averaging the spectra of 128 azimuth lines. A plot of such an averaged azimuth spectrum can be found in figure 4.7.

In this way, the Doppler centroid is determined for each block of 128 azimuth lines. The different values demonstrate the dependency of range of the centroid. The smooth range dependency must be derived from these values. This is discussed in § 5.5.3.

5.5.2 Methods used to determine the Doppler centroid

The location of the Doppler centroid of an averaged azimuth spectrum as in figure 4.7 can be determined in different ways.

Determination of the maximum

The location of the maximum could determine the Doppler centroid directly. However, because the still oscillating character of the average over 128 spectra, the maximum can not be determined without a large possible error. Therefore this method was not used.

Determination of the maximum of a best fitting curve through the maximum

By fitting a curve through the maximum of the spectrum, the symmetry axis and the maximum can be determined accurately. This was performed in the following steps.

- After the spectrum is smoothed, a first approximation of the location of the maximum is determined.

- Symmetrically around the determined maximum, n spectrum samples are taken (we used $n = 256$, see the parameter file example in § E.2). These n samples must occupy about half the spectrum in order to be able to determine the curve accurately. On the other hand, n can be limited to simplify the fitting of a curve. If the number of samples in the spectrum $N > 2n$, one out of a power of two spectrum samples are taken, in order to let the selection of n samples occupy about half the spectrum. Depending of the location of the maximum in the spectrum, the selected samples might be taken by cyclically extending the spectrum.
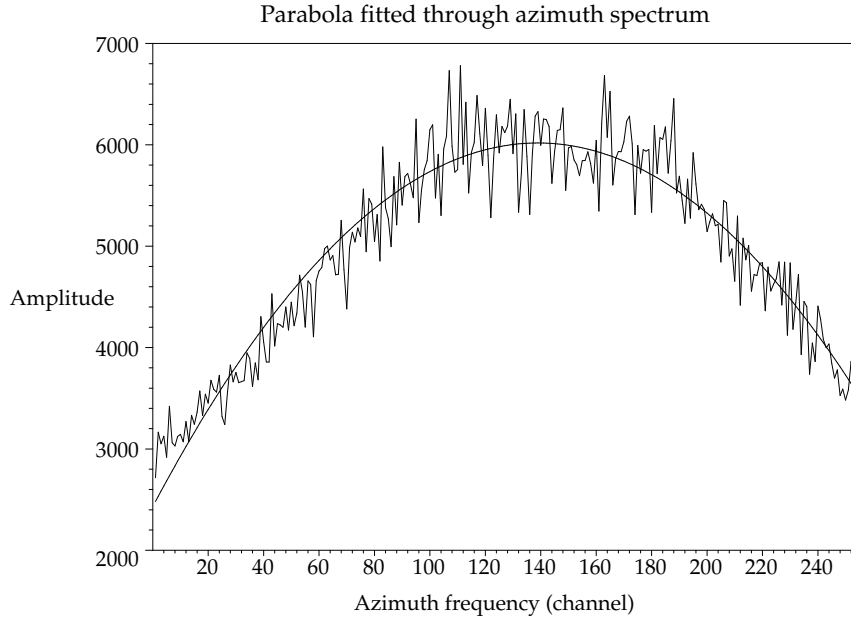
Figure 5.11   The maximum of the azimuth spectrum (actually the average of 128 azimuth spectra) is determined by fitting a parabola to the data of half the bandwidth. This selection was determined by locating the maximum of a smoothed copy of the spectrum.

- Through the selection of the spectrum, the best fitting curve in a least squares sense is determined. A parabola was used instead of the theoretical azimuth spectrum shape of equation (4.16), because this was easier to linearize; moreover, a parabola fits well to the maximum part of the spectrum. The linearization and solution of the linear system was performed in a straightforward way, without optimization of the calculation technique with linear algebra techniques. In our implementation, this causes numerical instability if the systems get larger than $n \approx 400$. An example of a fitted parabola is shown in figure 5.11.

- From the determined parabola coefficients, the location of the maximum can be calculated. Accounting for the selection made of the spectrum and the azimuth sampling frequency, the location of the spectrum sample can be converted to an azimuth frequency, which is the Doppler centroid frequency f_{Dc}.

The determined Doppler centroid frequency will in general not lie exactly in the middle of the azimuth signal band. This implies that the azimuth spectrum envelope described in equation (4.16) is no longer valid, because in the Hamming weighting factor the shift f_{Dc} can be different from the shift f_{Dc} of the rectangular function factor.

Determination of the centre of the empty band with an autoconvolution

In the azimuth spectrum, even if it is averaged over 128 spectra, the location of the maximum is less clear than the location of the empty band, as figure 4.7 shows. This empty band is a result of the sampling frequency being greater than the azimuth signal bandwidth (the pulse repetition frequency). Normally, the shape of the azimuth spectrum is expected to be symmetric around the Doppler centroid. This implies that the centre of the empty band differs exactly half the pulse repetition frequency from the Doppler centroid. In equation (4.16), the shift f_{Dc} of the Hamming weighting factor is equal to

that of the rectangular filter factor. By determining the location of the centre of the empty band, the Doppler centroid can be derived. This was performed with help of the autoconvolution in the following steps.

- After the spectrum is smoothed, a first approximation of the location of the maximum is determined.

- Starting from the left edge of the spectrum, the first spectrum sample with an amplitude lower than 10% of the maximum is flagged to be the left edge of the empty band. This 10% is well below the value of the azimuth transfer function at the edges of the azimuth bandwidth, which is 0.2375 according to equation (4.16). After this, the first spectrum sample is searched with an amplitude higher than 10% of the maximum. Because the signal is not smooth, an additional test is necessary: this sample is only accepted to be the right edge of the empty band if it is more than 10% of the sampling frequency away from the left edge. Because the azimuth bandwidth is often 82% of the sampling frequency, this 10% is a sensible lower limit for this criterion.

- Symmetrically around the determined centre of the empty band, n spectrum samples are taken (we used $n = 256$, see the parameter file example in § E.2). These n samples must occupy about a quarter of the spectrum in order to contain the complete empty band including the edges. On the other hand, n can be limited to simplify the calculation of the autoconvolution. If the number of samples in the spectrum $N > 4n$, one out of a power of two spectrum samples are taken, in order to let the selection of n samples occupy about a quarter of the spectrum. Depending of the location of the maximum in the spectrum, the selected samples might be taken by cyclically extending the spectrum.

- The location of the symmetry axis of the empty band is determined with the *auto-convolution* of the selected spectrum pixels. The inproduct of the selection with its shifted mirrored counterpart shows a maximum if the shift causes the edges of the empty band to coincide. This is exactly what an autoconvolution does: mirror the selection a and calculate the inproduct for each shift i,

$$
\begin{aligned}
A(i) &= \sum_{j=1}^{n} a(j)a(i-j) \\
     &= \sum_{j=1}^{n} a(j)a(i-j+n), \qquad i = 1\ldots n,
\end{aligned}
\tag{5.41}
$$

where the latter holds if the selection a is cyclically extended. If $n \geq 30$, it is more efficient to calculate the cyclic convolution of two signals a and b by using the discrete Fourier transform (Rabiner and Gold, 1975). After signals both have been transformed with the FFT, their spectra can simply be multiplied and the result is transformed back with the inverse FFT. Because for the *auto*convolution $b = a$ (Ziemer et al., 1993),

$$
A = \text{IFFT}\left([\text{FFT}(a)]^2\right).
\tag{5.42}
$$

The location of the maximum of the autoconvolution is determined. Half of this is the shift of the symmetry axis with respect to the centre of the selected band. This implies an ambiguity: a shift with half of the interval has the same autoconvolution. Because the edges of the empty band were already determined very well in the second step, the

Autoconvolution of selection of azimuth spectrum with empty band
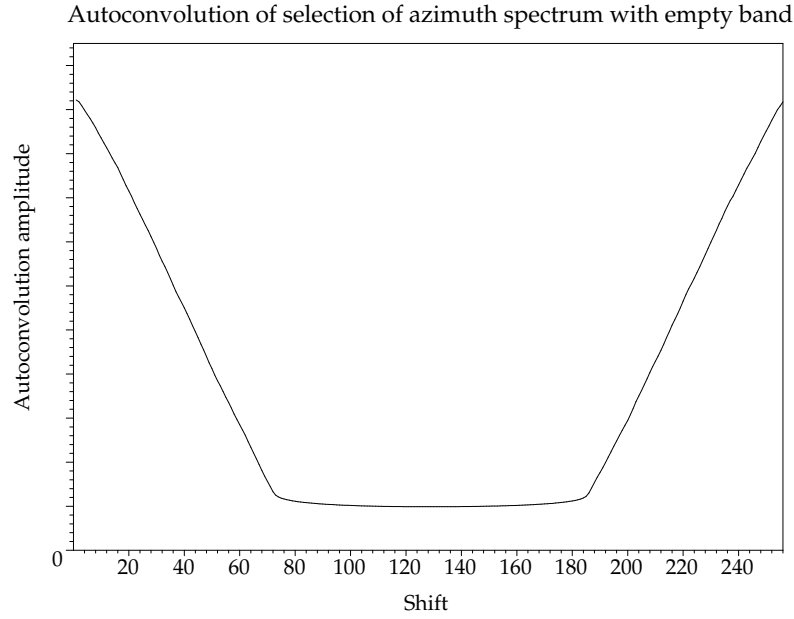
Figure 5.12 The autoconvolution function of the selected part of the azimuth spectrum around the empty band. Because the edges of the empty band were already determined very well in the second step of the algorithm, the location of the maximum of the autocorrelation will be near to zero, which makes the determination of the shift unambiguous. The shift is converted to the original azimuth frequency, of which the Doppler centroid frequency can be derived by adding or subtracting half the pulse repetition frequency.

location of the maximum of the autocorrelation will be near to zero, which makes the determination of the shift unambiguous. This is demonstrated by the experimental autoconvolution function shown in figure 5.12.

- The location of the centre of the empty band is converted to the azimuth frequency, accounting for the selection made of the spectrum. The Doppler centroid frequency f_{Dc} is now the azimuth frequency of the empty band centre plus or minus half of the pulse repetition frequency f_{pr} (which is the azimuth sample frequency).

It is also possible to determine the maximum of the autoconvolution of the empty band by fitting a curve, but this turned out to be unnecessary, as figure 5.12 shows. If this would be done, the autoconvolution can best be cyclically shifted with half of the interval, because the location of the maximum of the autocorrelation will be near to zero due to the well determined maximum in the first step.

It turned out that the location of the centre of the empty band could also be found without help of the autoconvolution with an accuracy only slightly less than with the algorithm described above. This is performed by executing the first two steps. The location of the edges found in this way suffices to derive the Doppler centroid.

5.5.3 Smoothing of the determined Doppler centroids over range

In the previous subsection, the Doppler centroid of blocks of 128 azimuth spectra was determined. As discussed in § 4.2.3, the Doppler centroid depends smoothly on range. This is demonstrated by figures 4.3 and 4.8. Thus, the blockwise determined Doppler centroid values must now be smoothed.

Because in the shown figures, a second or third order polynomial seemed to fit the range dependent Doppler centroids badly, we chose to do the smoothing with *splines*.

Doppler centroids of master and slave spectra with spline-approximation
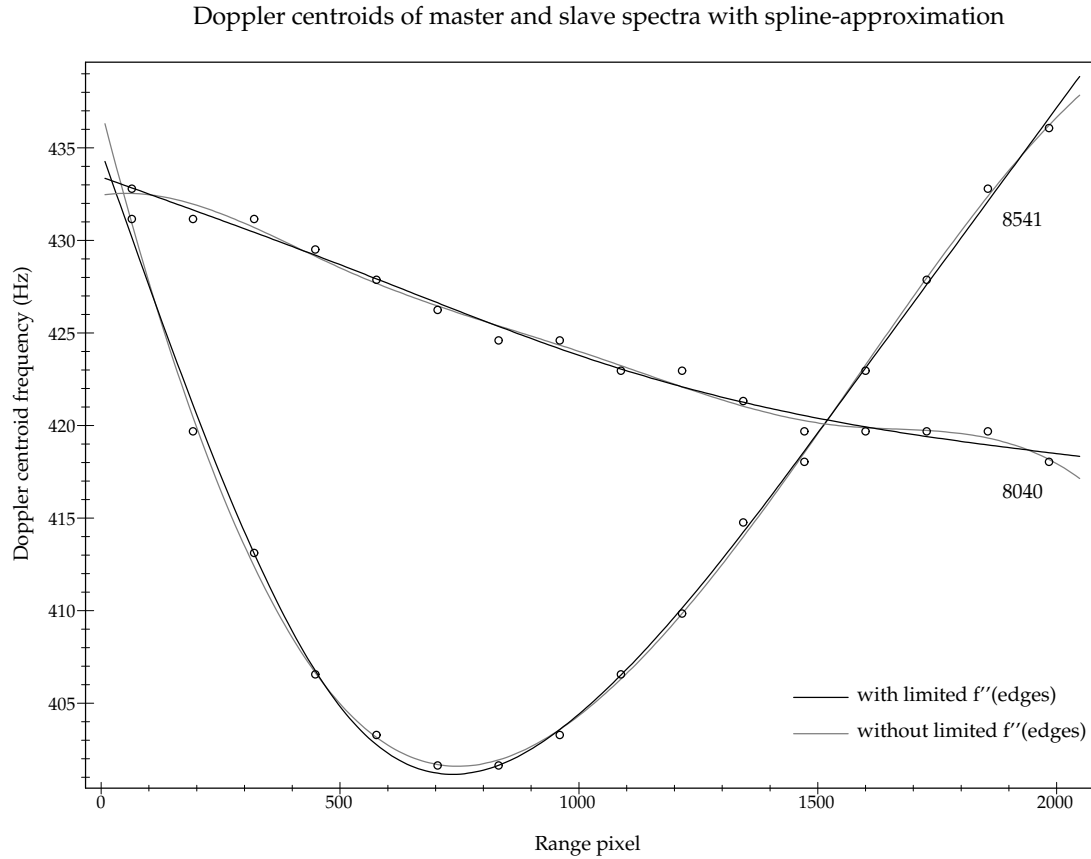
Figure 5.13   Over 16 blocks of 128 averaged azimuth spectra of the master orbit 8040 and slave orbit 8541, the Doppler centroid was determined (circles). With five-point cubic splines these centroids were approximated. If the second derivative on the edges is not limited, as for the black curves, the splines show too much curvature near the edges (grey curves).

The selected data (§ 5.1) consisted of 2048 range pixels. The Doppler centroid was determined over 128 pixels, so that over range 16 values resulted. Approximation with a limited number of knots turned out to behave smoother than interpolation, were the Akima splines were most suitable (Visual Numerics, 1997). Eventually, the values were approximated with a cubic spline with three intermediate knots. To prevent the splines from curving to much, a variant was used were the absolute value of the second derivative on the two end points could be limited. This limited was made dependent of the number of range pixes n (mostly 2048) and azimuth pixels m (mostly 2048); it was shown that it is

$$|f''(x)| < a\frac{m}{n^2},\tag{5.43}$$

with x the pixel number of the end points and $a = 0.05$ the chosen parameter value.

In this way the Doppler centroid was determined for each azimuth spectrum line over range. For the determination of the rectangular windowing function, also the blockwise determined edges of the empty band were approximated with the same sort of splines. In figure 5.13, the range-dependent blockwise Doppler centroids of the master image orbit 8040 and its slave image orbit 8541 are shown with their spline-approximation. In grey, also the spline-approximation is drawn without limitation on the second derivative at the end points.

5.5.4 Execution of azimuth filtering

For each azimuth line of the master and the slave image, each with a different range, a Doppler centroid has been determined in the previous subsection. Now for each range, the azimuth filter is calculated: $\tilde{F}_1(f_a)$ with equation (5.38) for the master image and $\tilde{F}_2(f_a)$ with equation (5.39) for the slave image. The rectangular windowing function $\tilde{\Pi}(f_a)$ of equation (5.40) is not calculated from the determined Doppler centroid and the bandwidth recorded in the header file of the SLC-images, but the spline-approximation of the azimuth frequencies of the edges of the empty band, determined in § 5.5.3 is used.

Each of the stored azimuth spectrum lines of master and slave is now multiplied with the appropriate filter. After this and optionally writing the Doppler centroids, approximations, filters, averaged spectrum lines, and filtered spectrum lines to separate files, the filtered spectra are transformed into images by application of an inverse Fourier transform and written to disk.

An estimation of the expected improvement of the filtering can be calculated from the average of the difference between the Doppler centroids of each master and slave azimuth line. Also the maximum and minimum of the Doppler centroids and their difference is shown during the execution of the program. The actual average bandwidth can also be presented.

5.6 Method to filter in range

In § 5.2.2, the need for spectral filtering in range was shown. In this section, the approach to accomplish this is treated.

The goal of spectral filtering in range is to achieve a system transfer function $H(f_r)$ which is the same for the master and slave image. In that case no geometric decorrelation will occur. In contrast with the azimuth spectra, the range spectra itself show a similar shape, as discussed in § 5.2.2. If the range frequency is translated to ground range, the object spectra show a difference, which was visualized in figure 5.4. The filtering process is performed on the range spectra in order to achieve similar object spectra.

The filtering comprises of the removal of the Hamming weighting, the removal of the band that is only present in one of the object spectra, and the reweighting with a Hamming window adapted to the new bandwidth.

The Hamming weighting of the range spectrum is assumed to be the same for each range spectrum line. On the range spectra of master and slave the *inverse Hamming weighting* is applied,

$$W_{\mathrm{InvHamm}}(f_r) = \frac{1}{0.75 + 0.25\cos\frac{2\pi f_r}{B_r}}\,\Pi\!\left(\frac{f_r}{B_r}\right),\qquad (5.44)$$

the reciprocal of the range amplitude transfer function in equation (4.13), but with the separate application of the rectangular windowing function Π because its reciprocal would be singular. After the inverse Hamming, the range spectra should be approximately block-shaped, as in figure 4.2 (a).

After the determination of the spectrum side to be filtered out, the spectra can be weighted with a new cosine on a pedestal (§ 4.1.1), with the period of the cosine being the new bandwidth and centred in the new band. Let us assume that of the master spectrum negative frequencies must be removed and that the slave spectrum must be filtered at the

Range spectrum and filters
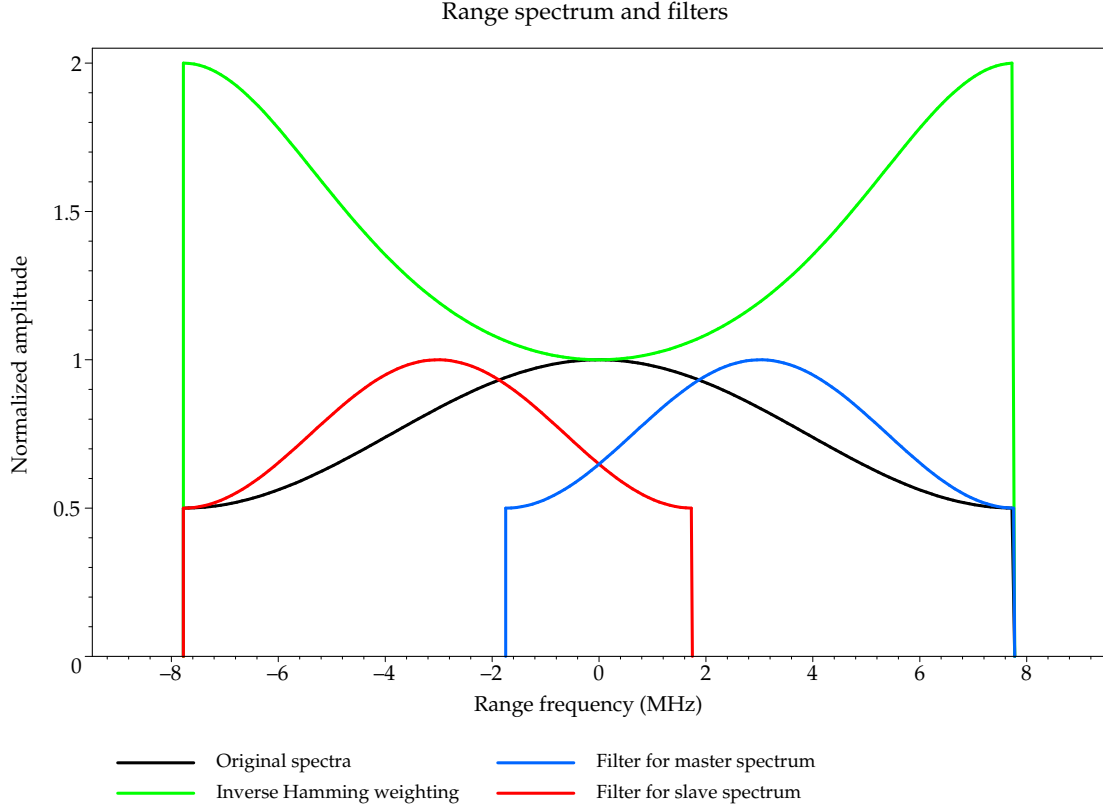
Figure 5.14   For range filtering, the spectra of master and slave image (black) are first multiplied with the inverse of the Hamming weighting function (green). The spectra are now about rectangular. In this example, the interferogram of the master (orbit 8040) and the slave (orbit 8541) shows a fringe frequency of 6.030 MHz. Of the master, at the negative frequency side a band of 6.030 MHz is removed and the remaining band is reweighed with a narrower Hamming function (blue). Of the slave, a similar filter is applied, but to the positive side (red).

positive side (this is what figure 5.4 shows). The band to filter out is the fringe frequency, Δf_r. The new bandwidth of the range spectra becomes

$$B_{\mathrm{rangefilt}} = B_r - |\Delta f_r| \tag{5.45}$$

(the fringe frequency can be positive or negative). The Hamming weighting for the master and slave thus becomes

$$W_{\mathrm{Hamm_m}}(f_r) = \left(0.75 + 0.25 \cos \left(2\pi \frac{f_r - \frac{1}{2}|\Delta f_r|}{B_r - |\Delta f_r|} \right) \right) \Pi \left(\frac{f_r - \frac{1}{2}|\Delta f_r|}{B_r - |\Delta f_r|} \right), \tag{5.46}$$

$$W_{\mathrm{Hamm_s}}(f_r) = \left(0.75 + 0.25 \cos \left(2\pi \frac{f_r + \frac{1}{2}|\Delta f_r|}{B_r - |\Delta f_r|} \right) \right) \Pi \left(\frac{f_r + \frac{1}{2}|\Delta f_r|}{B_r - |\Delta f_r|} \right). \tag{5.47}$$

The inverse Hamming weighting and the new weighting of the master and slave are shown in figure 5.14. The interferogram of the master (orbit 8040) and the slave (orbit 8541) shows a fringe frequency of 6.030 MHz, which is the band to filter out. The filtering of the master and slave spectra $W_m(f_r)$ and $W_s(f_r)$ can be performed by multiplication
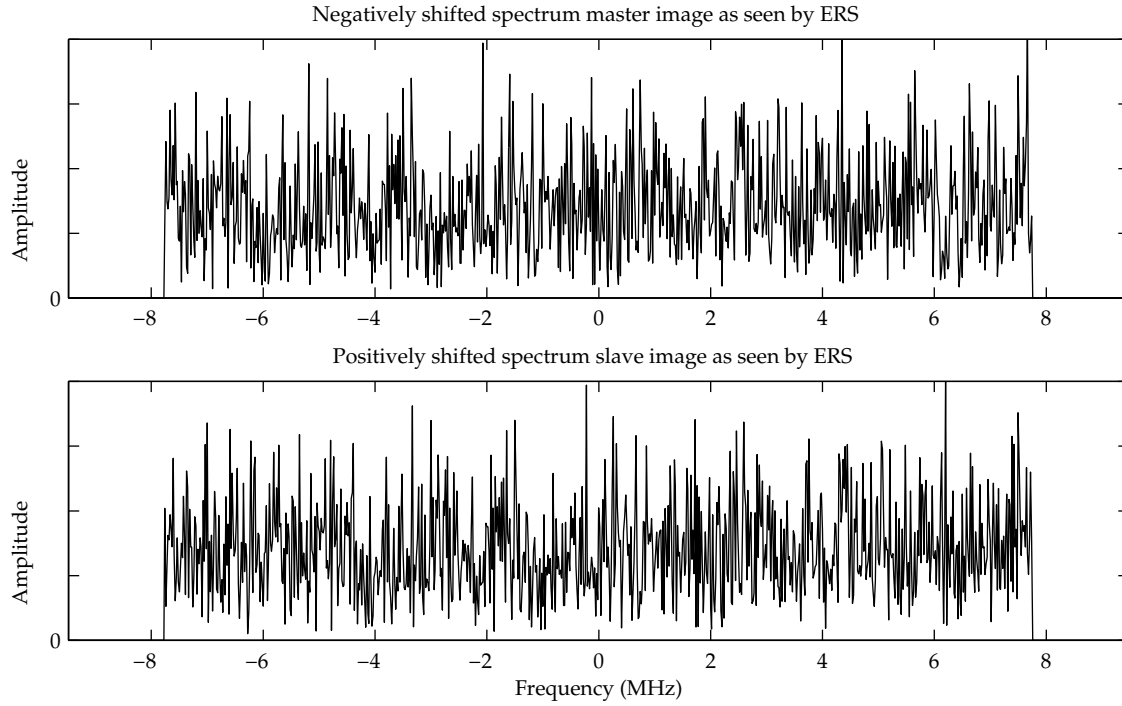
Figure 5.15 A simulated ERS spectrum is shifted to the negative frequency side for the master image and to the positive side for the slave image. The spectra are restricted to the bandwidth of ERS, which is 15.55 MHz; the oversampling of ERS is shown by taking the frequency domain to be 18.96 MHz, the sampling frequency of ERS. The relative shift is equal to the fringe frequency of 1.85 MHz. The range spectrum of the master image shows features not visible in the slave spectrum and vice versa. The relative shift of the object spectrum features is recognizable.

of the inverse Hamming weighting function (equation 5.44) and new filtering Hamming weighting function (equations 5.46) and 5.47),

$$W_{\mathrm{rangefilt}_m}(f_r) = W_m(f_r) \cdot W_{\mathrm{InvHamm}}(f_r) \cdot W_{\mathrm{Hamm}_m}(f_r); \qquad (5.48)$$

$$W_{\mathrm{rangefilt}_s}(f_r) = W_s(f_r) \cdot W_{\mathrm{InvHamm}}(f_r) \cdot W_{\mathrm{Hamm}_s}(f_r). \qquad (5.49)$$

After this range filtering, the now common transfer function should lead to the elimination of geometric decorrelation. In § 5.9 we will show the results of our experiments. To be able to carry out these experiments, the range filtering has to be implemented. This is treated in § 5.8.

5.7   Simulation of range filtering

In order to demonstrate the baseline decorrelation and range filtering, a simulation was performed. With this simulation we had the ability to consider baseline decorrelation without any disturbance due to other sources of decorrelation.

The simulated complex signal is one-dimensional circular Gaussian, which means that its phase is random and the amplitude of its real and imaginary parts is Gaussian distributed (Hanssen and Bamler, 1999). Of this signal, the spectrum is calculated. To limit the complexity, no Hamming weighting is applied. For the master image, this spectrum is shifted to the negative frequency side with a fringe frequency of 1.85 MHz; the slave spectrum is shifted the same amount to the positive side. In this way, the shift

Range filtered master spectrum

Range filtered slave spectrum
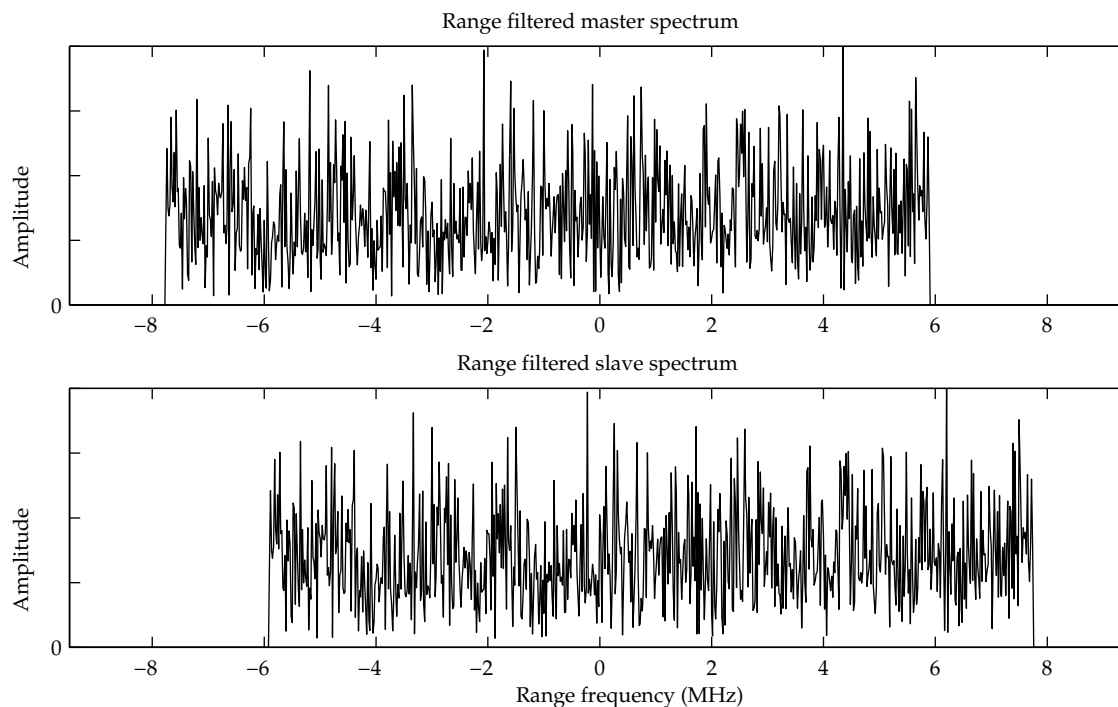
Figure 5.16   From the master spectrum, a band with a width equal to the fringe frequency is removed: the negative frequency band that contains features of the object spectrum not present in the slave spectrum. From the slave spectrum the positive side is filtered in a similar way. Both spectra are now similar and show only a shift with the fringe frequency.

of the object spectrum due to the baseline separation is simulated, similar to figure 5.4.

These master and slave object spectra are restricted to the bandwidth of ERS, which is 15.55 MHz; the oversampling of ERS is shown by taking the frequency domain to be 18.96 MHz, the sampling frequency of ERS. As is shown in figure 5.15, the range spectrum of the master image shows features not visible in the slave spectrum and vice versa. In this figure, the relative shift of the object spectrum features is recognizable.

In order to filter these signals in range, from the master spectrum a band with a width equal to the fringe frequency is removed: the negative frequency band that contains features of the object spectrum not present in the slave spectrum. From the slave spectrum the positive side is filtered in a similar way. The result is shown in figure 5.16. Both spectra are now similar and show only a shift with the fringe frequency.

From the constructed original bandlimited spectra, the images are calculated; from them the interferogram is calculated. The phase of the interferogram is shown in figure 5.17 (a). The spectral information the master and slave have not in common leads to phase noise. In order to make this figure as clear as possible, the interferometric phase was calculated from a master and slave spectrum that only show a relative shift of 16 pixels (which is equivalent to a fringe frequency of 0.30 MHz). In that case, the interferogram shows only 16 fringes. The phase of the interferogram calculated from the range filtered spectra is shown in figure 5.17 (b). It shows a perfect phase ramp: exactly what is expected from two mutually shifted but equal spectra.

The interferometric noise due to the baseline decorrelation can be shown by subtracting the noise-free from the noisy interferogram, but a more elegant method is to shift the unfiltered spectra back, each with half the fringe frequency. This is equivalent

Interferometric phase of unfiltered spectra

Interferometric phase of filtered spectra

Interferometric phase of backshifted unfiltered spectra: phase noise
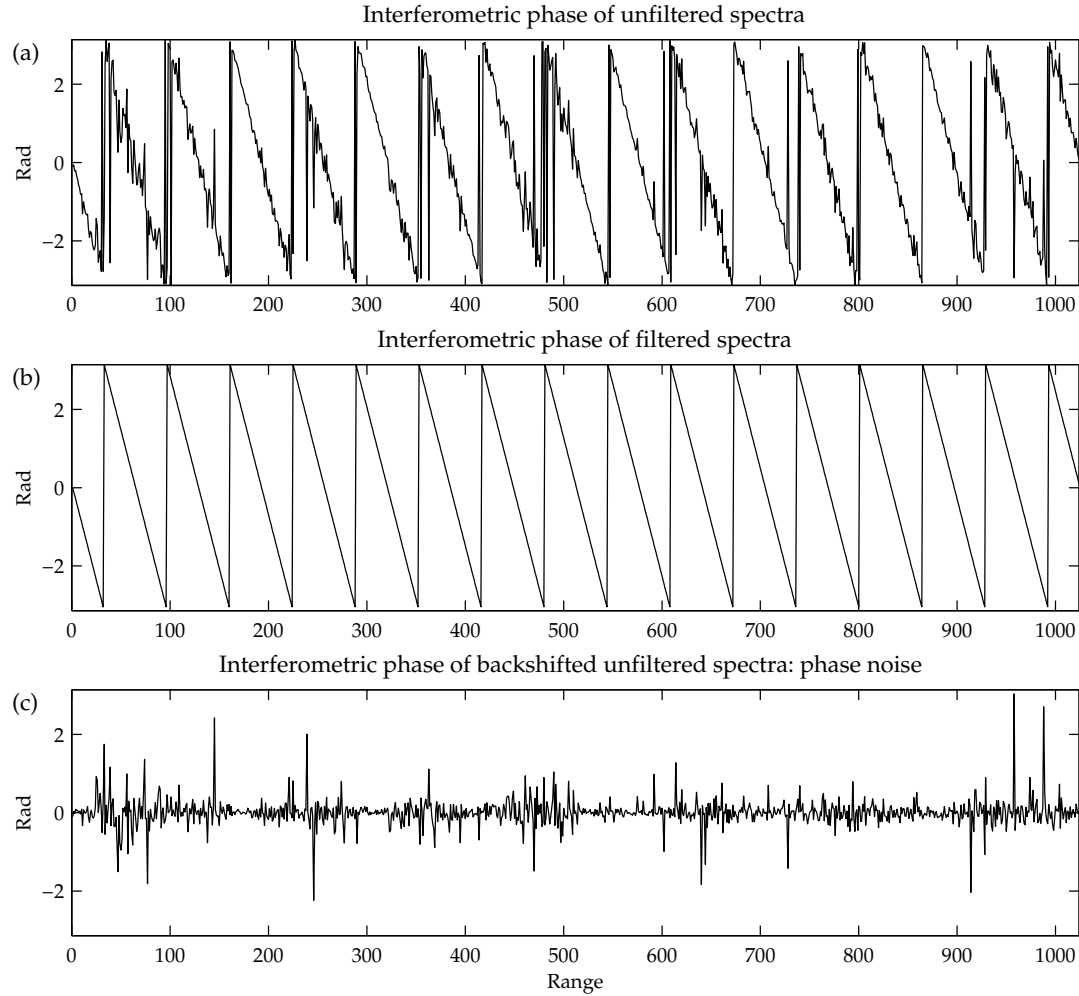
Figure 5.17   The phase from the interferogram of the unfiltered simulated images is shown in (a). The spectral information the master and slave have not in common leads to phase noise. The interferogram shows 16 fringes because, in this example, a relative shift of 16 spectrum pixels was used, equivalent to a fringe frequency of 0.30 MHz. In (b) the interferometric phase is shown from the range filtered images. It shows a perfect phase ramp. By shifting the unfiltered spectra back, each with half the fringe frequency, the 'flat earth' fringes are removed and the interferometric phase noise is shown (c).

to removing the phase ramp induced by the 'flat earth'. The interferometric phase noise is shown in figure 5.17 (c).

From the shift or fringe frequency, the theoretical signal-to-noise-ratio (SNR) can be calculated, as shown in equation (5.21) in § 5.3.1. Also the theoretical correlation can be calculated with equation (5.22). These figures are given for several shifts in table 5.3.

With the theory of § 3.3.2, we are able to estimate the coherence for the simulated complex unfiltered images with the correlation equation (3.17). As discussed there, the baseline-induced phase should be corrected for, as in equation (3.19); as an alternative the correlation can be calculated for the images of which the spectra have been shifted back, as just described. From this correlation estimation coefficient, the signal-to-noise-ratio of the simulated unfiltered images can be calculated with equation (3.14).

In table 5.3 the mean correlation and signal-to-noise-ratio of several simulations are listed for several fringe frequencies or shifts. The results of the simulation do well agree

shift (pix)	Δf_r (MHz)	$\Delta f_r / B_r$	coherence theor.	simul.	signal-to-noise theor.	simul.
2	0.037	0.002	0.998	0.997	418.92	507.21
4	0.074	0.005	0.995	0.995	208.96	255.37
8	0.148	0.010	0.990	0.991	103.98	123.58
20	0.370	0.024	0.976	0.976	40.99	41.55
40	0.741	0.048	0.952	0.954	20.00	20.92
100	1.852	0.119	0.881	0.882	7.40	7.47
200	3.703	0.238	0.762	0.775	3.20	3.46

Table 5.3   The coherence and signal-to-noise-ratio for different spectral shifts of the simulated range spectra

with the theoretical values derived from the fringe frequency.

5.8   Implementation of range filtering

During the research, an implementation of range filtering has been developed. As an illustration, the parameter files are listed in appendix E. In this section the topics with implementation will be discussed.

5.8.1   Determination of the fringe frequency from interferometric parameters

The main issue with implementing the approach to range filtering discussed in § 5.6 is the determination of the width of the band that has to be removed from one side of the master image spectrum and from the opposite side of the slave image spectrum. This width is the fringe frequency Δf_r, that according to equation (5.13) can be calculated from the interferometric parameters perpendicular baseline length $B_\perp$, slant range distance r_0, and incidence angle θ. The wavelength $\lambda_0 = 5.66$ cm is fixed for ERS, with its carrier frequency of $f_0 = 5.3$ GHz. Hence, if the orbits are known, the fringe frequency can be calculated. The most important interferometric parameter with respect to baseline decorrelation and range filtering is the perpendicular baseline length; other parameters show less variation.

However, the incidence angle θ depends on the terrain slope, as discussed in § 5.2.2. If it is not possible to estimate the fringe frequency from the interferogram and no digital terrain model is available to approximate the slope (§ 5.8.2), the fringe frequency can be calculated from the interferometric parameters and the incidence angle for a flat or ellipsoidal earth with equation (5.13).

Because within the interferogram the incidence angle slightly increases with range if the earth's surface would be flat, and the perpendicular component of the baseline projects different, the fringe frequency depends of the range, as shown in figure 5.5. Therefore if the fringe frequency can not be estimated from the interferogram, the spectrum can be divided into strips parallel to the ground track and the fringe frequency can be calculated for the average incidence angle of each strip with the interferometric parameters calculated from the orbits or with equation (5.19).

Because the orbits are in general not parallel, also an azimuth dependency of the

Figure 5.18   The average over 32 spectra of the interferogram of a strip of 256 range pixels of the images 8040 and 8541. Because the imaged region is almost flat, the fringe frequency is very well determined. The peak is equivalent with a fringe frequency of −6.60 MHz.

baseline and hence of the fringe frequency occurs. Apart from strips in range, the spectra can therefore be process for patches with different azimuth, each with a different fringe frequency.

5.8.2 Determination of the fringe frequency from the interferogram

If the range filtering is performed without taking the variations in fringe frequency due to topography into account, this leads – depending on the direction of the slope – to removal of valid spectral information or to non-removal of invalid spectral information. Therefore, the fringe frequency should be determined dependent on the topography. This can be performed by determining the fringe frequency from the interferogram (§ 5.8.2). This kind of spectral filtering is called *adaptive range filtering* (Gatelli et al., 1994; Geudtner, 1995; Davidson and Bamler, 1999).

The fringe frequency can be determined from strips or patches of the interferogram. The smaller the patches, the better the fringe frequency is adapted to the local fringe frequency variations due to topography and the smaller the decorrelation. However, dividing the images too much will lead to spectra that are based on too little information to be able to carry out the filtering with a certain precision. A trade-off must be made between fine determination of the topography-dependent fringe frequency and the number of pixels to calculate a spectrum from. A number of 64 range pixels seems to fit well (Kampes, 2000).

The fringe frequency due to the 'flat earth' will be dominant in the spectrum that can be calculated from the interferogram in range direction. On a local level, the topography will modulate this fringe frequency. Adaptive range filtering therefore determines the local fringe frequency from the spectrum of the interferogram.

The bandwidth of the spectrum of the interferogram is twice that of the individual images (chapter 6). In order to prevent aliasing, the spectra of the master and slave image must be oversampled, as described in § 6.2. From the interferogram, the peak is deter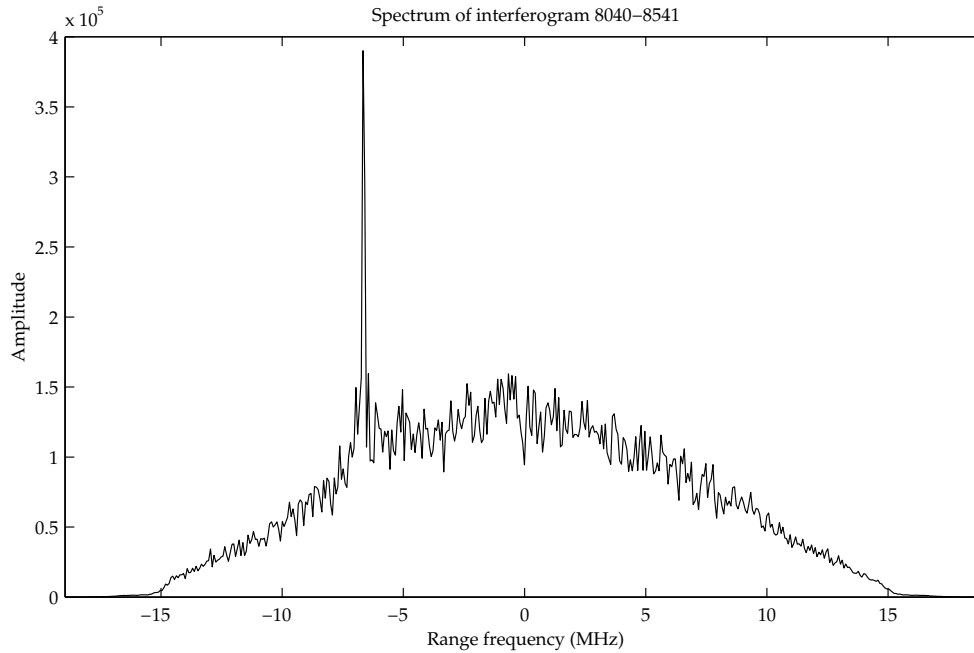mined and converted to the fringe frequency. In figure 5.18, the average over 32 spectra of the interferogram of a strip of 256 range pixels of the images 8040 and 8541 is shown. Because the imaged region is almost flat, the fringe frequency is very well determined. If the interferogram spectrum is calculated over a smaller area, the peak becomes less distinct and the overall shape of the interferogram spectrum (the convolution of the Hamming weighted range spectra) must be removed first.

If the baseline is very long, the baseline decorrelation will make the calculation of an interferogram rather senseless, especially if additionally temporal decorrelation occurs. The determination of a fringe frequency from the interferometric spectrum can then be impossible. In this case the fringe frequency must be determined from the interferometric parameters (§ 5.8.1).

5.8.3 Prefiltering in range for fine coregistration

Because some coregistration algorithms utilize the coherence between the images, in case of a very long baseline the coregistration can be badly determined, yielding a bad interferogram. If the coregistration is bad, the master and slave images must be range filtered with the fringe frequency determined from the interferometric parameters (§ 5.8.1), because it can not be determined from the interferogram. The resulting images will have a higher coherence and the fine registration can be better determined (Geudtner, 1995).

The original, unfiltered master and slave image are then fine coregistered with the determined parameters. After this, these images can again be range filtered with adaptive determination of the fringe frequency, as described in § 5.8.2.

5.8.4 Execution of range filtering

In our implementation of range filtering, both master and slave images are read and the spectrum of each range line is determined and stored. For the adaptive determination of the fringe frequency the range is divided into 8 strips of 256 pixels. The spectra of 32 of these range lines (see the parameter file sample in § E.2) are taken and oversampled; the now oversampled image lines are calculated with the inverse Fourier transform and for each line the interferogram is calculated. In the end, the 32 interferograms are averaged.

The average interferogram spectrum is smoothed with a 5-pixel window, the location of the maximum is determined and this is converted to a range frequency. This is the fringe frequency.

A test can be performed: if the determined fringe frequency differs more than 0.5 MHz (parameter) from the fringe frequency in the parameter file – stemming from the interferometric parameters (§ 5.8.1) or from other sources – then the parameter file version of the fringe frequency might be used. This helps if (parts of) the interferogram are bad because of high decorrelation due to long baselines in combination with temporal decorrelation and possibly bad coregistration. The test can not be performed if the area is not rather flat, because the topography induced fringe frequency shows larger variations. Alternatively, the filtering of the whole interferogram can be optionally performed with a fringe frequency calculated with equation (5.19) and the fringe frequency from the parameter file. After this the fringe frequency of the next 32 range lines is determined and the range strips are processed, until the fringe frequencies of the whole image pair

are stored.

Then for each 32 range lines one range filter is calculated and the filtering is performed. For the master spectrum, filter equation (5.48) is applied and for the slave spectrum equation (5.49). After this, the filtered spectra are transformed back to images and written to disk.

5.9 Results of spectral filtering

5.9.1 Introduction to the presentation of the results

In § 5.1 the selected data were described: tandem images of ERS-1 and ERS-2 with a time interval of one day but with a rather small baseline, and ERS-1 pairs with a longer baseline and an interval of 35 days. The Groningen area (ERS frame 2529) of 44 km in range and 8 km in azimuth is almost flat. Azimuth and range filtering was performed separately and in combination.

For azimuth filtering, the Doppler centroid frequency was determined based on the location of the empty bands with help of the autoconvolution (§ 5.5.2). Additionally, as an experiment the Doppler centroid frequency was for two pairs in a separate run based on the determined maximum of the spectrum; the goal was to conclude whether the more difficult to determine spectrum maximum gives a better description of the spectrum and hence a better azimuth filtering result.

Range filtering was performed with the fringe frequency determined from the interferogram of the average over 32 azimuth lines of 256 range pixels; the range was thus divided into 8 strips, as described in § 5.8.4. If the determined fringe frequency differed more than 0.5 MHz from the fringe frequency calculated with the baseline and incidence angle for the centre of the range strip in equation (5.19), the calculated fringe frequency was replaced by this strip fringe frequency. Our implementation was not extended to the calculation of the perpendicular component of the baseline from the orbits and imaged scene expressed in Cartesian coordinates. For long baselines, due to the limited coherence this replacement scheme was very useful.

In the tables hereafter we present for all interferograms the parameters that the software determined. For each interferometric image pair, in the first table the parameters of the individual images are presented: the average Doppler centroid frequency f_{Dc} and its minimum and maximum and the average azimuth bandwidth B_a. In the left figure, the approximation over range for the determined 16 discrete Doppler centroid values is graphed for both images. In the second table the interferometric parameters are listed. The listed Doppler centroid frequency difference Δf_{Dc} is the average of the difference over range (not the difference of the average Doppler centroid frequencies over range). The listed range frequency shift Δf_r, equal to the fringe frequency f_{fringe}, is the average of the determined fringe frequencies of the separate blocks. The listed perpendicular component of the baseline $B_\perp$ is calculated from this average fringe frequency.

In order to assess the improvement due to the filtering, the quality of the filtered and unfiltered interferograms was measured with the coherence estimator of equation (3.19). The reference phase, needed for the correction in this equation, was calculated using the fifth-order polynomial coefficients supplied by the interferometric software we used to produce the coregistered image selections. The estimator window size was chosen to be 12 pixels in range (260 metre) and 60 in azimuth (240 metre) so that $N = 720$, for reasons described in § 3.4.1, leading to square coherence pixels and a coherence image

of 170 × 34 pixels. The calculation of the coherence image was performed over adjacent windows, as described in § 3.4.1.

The coherence estimator is biased (§ 3.3.3). We corrected for this bias with the algorithm we devised in § 3.4.4, although not all bias is removed in this way, which will influence low coherence images in particular. The bias correction was performed with $L = 485$ in equation (3.20), because the window size $N = 720$ and the resolution of ERS is such that $N = 1.485L$ (equation 3.21). The estimation of the quality of the interferogram is presented in a bias-corrected coherence histogram and in the tables with the average coherence estimation γ_{estim} (biased and corrected). To illustrate the spatial distribution and the coherence improvement, also the most interesting coherence images are presented.

From the determined parameters Δf_{Dc} for azimuth or Δf_r for range, the software calculated the theoretical decorrelation with the azimuth or range factor in equation (5.23), based on the assumption that the spectra are rectangular. This decorrelation is presented in the tables as $\Delta B / B$. Also the coherence factor γ_{rect} is listed, which is $\Delta B / B = 1 - \gamma_{\text{rect}}$. As described in § 5.3.2, γ_{rect} can be transformed into the decorrelation and improvement for *weighted* spectra. Therefore we used our tables with evaluations of equations (5.28) and (5.30). The theoretical coherence factor for weighted spectra is listed as γ_{weight} and its reciprocal, the improvement (equations 5.32 and 5.33), in the column denoted m_{weight} (converted to an improvement percentage).

The images were also filtered in range after the azimuth filtering was performed. According to equation (5.23), the total decorrelation due to spectral misalignment in range and azimuth is the product of the individual decorrelations. This theoretical decorrelation and the expected improvement are also listed and can be compared with the experimental decorrelation, estimated from the coherence estimation of the images filtered in range as well as azimuth. To be able to compare this with the product of the decorrelation of the range and that of the azimuth filtered images, this product is also listed in some tables.

According to equation (3.15), the decorrelation is multiplicative. If the estimated coherence of the interferogram of the unfiltered images is $\gamma_{\text{estim,none}}$ and that of the azimuth filtered images is $\gamma_{\text{estim,azim}}$, then the measured decorrelation $1 - \gamma$ that the azimuth filtering removed should be such that the coherence factor is

$$\gamma = \frac{\gamma_{\text{estim,none}}}{\gamma_{\text{estim,azim}}} \tag{5.50}$$

and the measured improvement due to the azimuth filtering is the reciprocal

$$m = \frac{\gamma_{\text{estim,azim}}}{\gamma_{\text{estim,none}}}. \tag{5.51}$$

These values are listed in the tables in the 'experimental' column. They can be compared with the theoretical γ_{weight} and m_{weight}.

The filtering removes noise from the interferometric phase. To demonstrate this, of some interferograms the interferometric phase image is shown with and without filtering. To be able to assess the real noise level, no multilooking is applied to those images and hence the pixels are not square. Most interferometric phase images are a selection of 200 pixels in azimuth (800 metre) and 400 in range (8600 metre), so that the individual pixels can be seen. Of one interferogram, also the complete phase image is shown, to illustrate the phase features present.

5.9.2 Analysis of the results of spectral filtering

The four ERS-1-ERS-2 tandem pairs

The first four ERS pairs listed on the following pages are tandem pairs: ERS-1 and ERS-2 with an interval of one day. This results in the temporal decorrelation to be limited compared with that for the three ERS-1 pairs, which were acquired with a 35-day interval. On the other hand, the tandem pairs show a considerable Doppler centroid frequency difference, because the Doppler centroid frequency for ERS-2 is substantially lower than the Doppler centroid for ERS-1. The tandem pairs are thus very suitable to test azimuth filtering.

The Doppler centroid difference ranges from 253 Hz for the pair 22913-3240 to 341 Hz for 24416-4743; the expected improvement of azimuth filtering ranges from 15% to 28%. For all four tandem pairs, the realised improvement in the coherence, as calculated with equation (5.50) was only slightly less than predicted.

This difference is for all pairs very similar. It might be caused by the correction of the expected theoretical coherence for a rectangular spectrum γ_{rect}, which can easily be calculated from the azimuth Doppler centroid frequency difference, to the expected theoretical coherence for the weighted spectrum γ_{weight}. In this correction, calculated with equation (5.28), a Hamming weighting only slightly different from equation (5.26) already results in a difference. For example, if the theoretical coherence for a rectangular spectrum would have been used for pair 22913-3240, the predicted coherence improvement would have been 22.4 % instead of 14.9%, while the measured coherence improvement is 14.2%. After all, the improvement is so constantly near the predicted improvement for all four pairs, that we can conclude that azimuth filtering has the expected result and that the correction for the weighting of the spectrum works almost perfect.

The Doppler centroid frequency was determined from the location of the centre of the empty azimuth spectral band. For the pairs 22913-3240 and 24917-5244 the Doppler centroid was also determined from the location of the maximum of the spectral envelope, as listed in tables 5.6 and 5.10. Because the maximum is more difficult to determine due to the fluctuations of the spectrum, the expected error is larger. However, figures 5.23 and 5.29 show that the Doppler centroid determined from the spectrum maximum differs significantly from the centroid determined from the empty band. As figures of the azimuth spectra show, this effect is really present in the spectra and not a result of a bad determination of the spectrum maximum. Because the azimuth filtering is based on the assumed spectral envelope of equation (4.16), a better determination of the location of the Doppler centroid is expected to result in a higher coherence. However, tables 5.7 and 5.11 show that the coherence of the azimuth filtered images with the Doppler centroid determined from the maximum is nearly identical to the coherence of the filtering results with the Doppler centroid determined from the location of the empty band.

As the baseline for the four considered tandem pairs ranges from 18 to 83 metre and the equivalent fringe frequency from 0.29 to 1.33 MHz, range filtering is not crucial for these pairs, but not completely negligible. The maximum improvement for the tandem pairs was 4.3% for 21410-1737. In the (normalized) coherence histogram in figure 5.20 the improvement due to both range and azimuth filtering is clear. As for azimuth, also for range the measured improvement was slightly less than predicted, probably due to a spectral envelope slightly different from that used for the calculation of equation (5.27).

For the tandem pairs, the correction of the bias in the coherence estimation is almost negligible because of the high coherences of the images. These pairs thus cannot

serve to determine whether the bias correction algorithm is well devised and whether the number of independent looks L was determined right.

Due to the one-day interval between the acquisition of the tandem pair images the temporal decorrelation is limited. However, as figure 5.21 shows, the coherence of the pair 21410-1737 is lower than that of the other tandem pairs. This is probably the temporal decorrelation caused by crop growth and harvesting on the fields: the images were taken in August. As the coherence images are compared with the amplitude image, indeed the fields show the lowest coherence.

Because the reduction of phase noise in the interferogram is an important goal to spectral filtering, interferometric phase images were calculated. The most interesting images are shown in this thesis. To be able to assess the noise, no multilooking is applied to those images and hence the pixels are not square and only a selection of 200 pixels in azimuth (800 metre) and 400 in range (8600 metre) can be displayed. To understand these pictures, also the phase image of a complete processed interferogram is shown. In figure 5.31, the interferometric phase image of the tandem pair 24917 and 5244 is shown. As for all phase images, the reference phase is subtracted because the fringes would make the noise less visible. The image is 2048 × 2048 pixels or 44 (range) × 8 (azimuth) km. As the baseline of this pair is 66 metre and the corresponding height difference that would cause the phase to shift 2π is 131 metre (equation 2.32), the coloured phase differences are not caused by topography of the almost flat Groningen scene. They are primarily due to atmospheric delay: a 2.8 cm delay causes a phase shift of 2π, according to equation (2.38). The phase gradient over range is probably due to the subtraction of a non-perfect reference phase, but can also be due to an atmospheric delay gradient. Water is noisy because of the total decorrelation.

The coloured interferometric phase differences for pair 21410-1737 in figure 5.22 also show the atmospheric delay. The red and blue colours stem from the ends of the phase scale: the average interferometric phase happens to be about π and transitions to the other end of the scale cause the image to look rather coloured. This phase image show the 20% improvement due to azimuth filtering as a reduction in phase noise. Range filtering with its improvement of 4% is not crucial, but the phase noise of the azimuth and range filtered images is the lowest.

The tandem pair 24416 and 4743 with their Doppler centroid frequency difference of 341 Hz profit the most from azimuth filtering. The interferometric phase images of this pair in figure 5.28 show the 27% improvement due to azimuth filtering as a reduction in phase noise. Range filtering has a negligible effect, because the perpendicular component of the baseline is only 17.95 metre. The yellowish coloured feature in the image will thus not be topography: according to equation (2.32), a baseline of 17.95 metre causes the phase to shift 2π for a height difference of 486 metre. That the feature is due to atmosphere is also unlikely because of its clear borders. The phase difference feature is probably due to a deformation: the soil may have swelled due to a moisture difference between master and slave (Bamler and Hartl, 1998).

Range and azimuth filtering reduce the bandwidth and hence the resolution will be reduced. In the tandem pair interferometric phase images this is not visible, because the reduction is rather small. For the pair with the highest Doppler centroid difference, the resolution will drop from 1.2 to 1.5 pixel. However, for the long baseline pairs, the resolution reduction is visible, as will be shown.

Orbits 21410 and 1737

orbit	platform	date	f_{Dc} mean	f_{Dc} min	f_{Dc} max	B_a mean
21410	ERS-1	19 aug 1995	464.76	462.79	466.73	1378.61
1737	ERS-2	20 aug 1995	168.03	166.90	168.76	1378.20

Table 5.4

Figure 5.19

21410 (ERS–1)
1737 (ERS–2)

Figure 5.20

unfiltered   azimuth filtered
range filtered   azimuth and range filtered

filter operation	Δf_{Dc} (Hz)	Δf_r (MHz)	$B_\perp$ (m)	$\dfrac{\Delta B}{B}$	theoretical			γ_{estim}		experimental	
					γ_{rect}	γ_{weight}	m_{weight}	biased	correct.	γ	m
none	296.73							0.479	0.478		
azimuth				0.215	0.785	0.829	20.7%	0.574	0.573	0.834	19.9%
range		1.332	−83.35	0.086	0.914	0.955	4.7%	0.500	0.499	0.959	4.3%
az&ra				0.282	0.718	0.791	26.4%	0.598	0.598	0.800	25.0%
– multi[†]										0.800	25.1%

† Experimental coherence $\gamma_{\mathrm{az\&ra}}$ calculated from $\gamma_{\mathrm{az\&ra}} = \gamma_{\mathrm{azimuth}} \cdot \gamma_{\mathrm{range}}$ instead of from γ_{estim}

Table 5.5

Amplitude of image 21410

Coherence of unfiltered image pair 21410–1737

Coherence of azimuth filtered image pair 21410–1737

Coherence of range filtered image pair 21410–1737

Coherence of azimuth and range filtered image pair 21410–1737
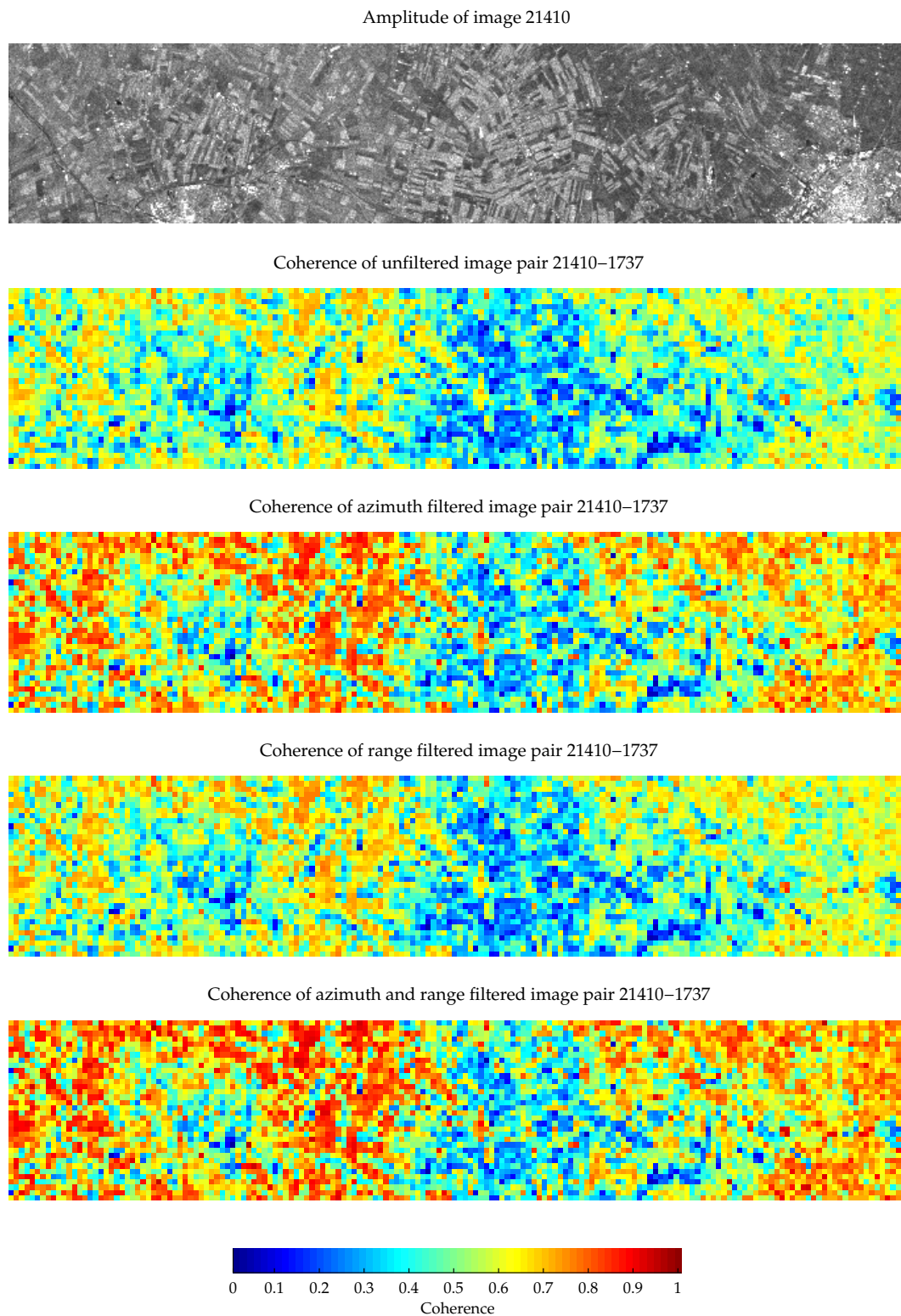
Coherence

Figure 5.21 The coherence images of the interferometric pair 21410 and 1737 show the 20% improvement due to azimuth filtering. Range filtering with its improvement of 4% is not crucial. Although the pair is a tandem pair with a one day interval, the decorrelation is higher than that of other tandem pairs, probably caused by crop growth and harvesting on the fields: the images were taken in August. Coherence pixels are 12 (range) × 60 (azimuth) SLC pixels or 260 × 240 metre; amplitude pixels are 3 × 15 SLC pixels or 65 × 60 metre.

Interferometric phase of unfiltered image pair 21410–1737
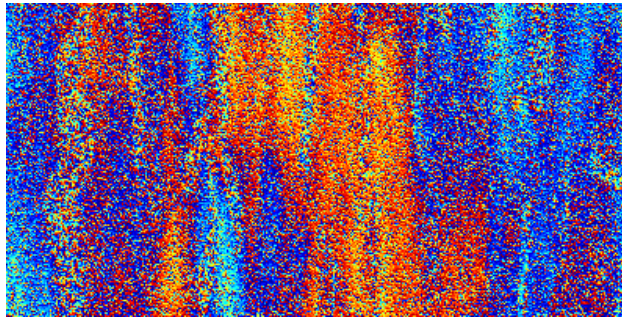
Interferometric phase of azimuth filtered image pair 21410–1737
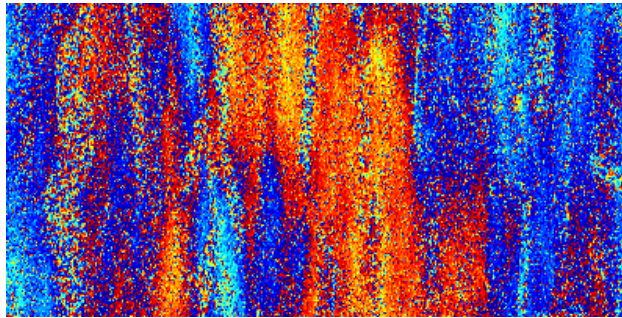
Interferometric phase of range filtered image pair 21410–1737
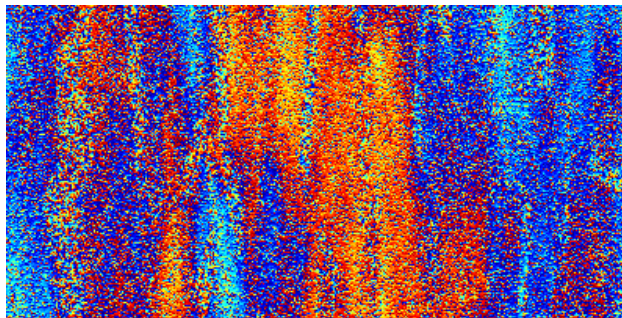
Interferometric phase of azimuth and range filtered image pair 21410–1737
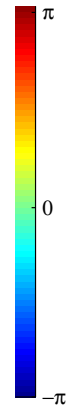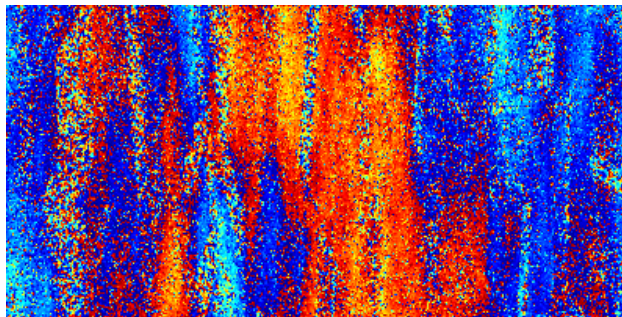
Figure 5.22   The interferometric phase images of the tandem pair 21410 and 1737 show the 20% improvement due to azimuth filtering as a reduction in phase noise. Range filtering with its improvement of 4% is not crucial. The phase noise of the azimuth and range filtered images is the lowest. To show the noise, no multilooking was applied and hence the pixels are not square. The coloured phase differences are primarily due to atmospheric delay. The images are 400 (range) × 200 (azimuth) pixels or 8600 × 800 m.

Orbits 22913 and 3240

orbit	platform	date	f_{Dc} mean	f_{Dc} min	f_{Dc} max	B_a mean
22913	ERS-1	2 dec 1995	421.86	405.99	447.49	1380.56
– max[†]			434.01	425.38	451.81	1380.56
3240	ERS-2	3 dec 1995	169.23	166.41	172.47	1379.48
– max[†]			174.04	170.24	177.79	1379.48

† Doppler centroid f_{Dc} determined from location of maximum of azimuth spectrum instead of empty band

Table 5.6

Doppler centroids 22913 and 3240

Coherence histograms pair 22913–3240
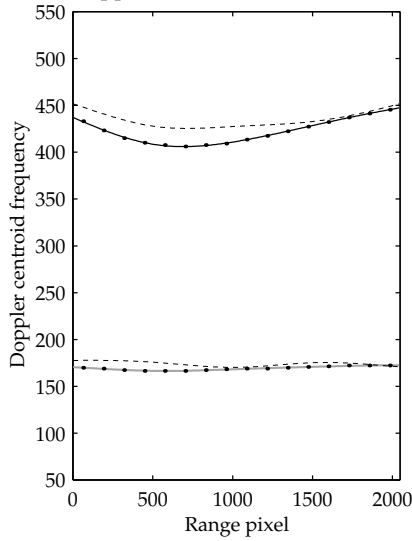
Figure 5.23

22913 (ERS–1)
3240 (ERS–2)
fDc from maximum

unfiltered   azimuth filtered
range filtered   azimuth and range filtered

Figure 5.24

filter operation	Δf_{Dc} (Hz)	Δf_r (MHz)	$B_\perp$ (m)	$\dfrac{\Delta B}{B}$	theoretical			γ_{estim}		experimental	
					γ_{rect}	γ_{weight}	m_{weight}	biased	correct.	γ	m
none								0.715	0.715		
azimuth	252.62			0.183	0.817	0.871	14.9%	0.817	0.817	0.876	14.2%
– max[†]	259.96			0.188	0.812	0.864	15.8%	0.816	0.815	0.876	14.0%
range		0.743	−46.42	0.048	0.952	0.977	2.3%	0.729	0.729	0.981	1.9%
az&ra				0.222	0.778	0.851	17.5%	0.834	0.833	0.858	16.6%
– multi[‡]										0.860	16.3%

† Doppler centroid f_{Dc} determined from location of maximum of azimuth spectrum instead of empty band
‡ Experimental coherence $\gamma_{\mathrm{az\&ra}}$ calculated from $\gamma_{\mathrm{az\&ra}} = \gamma_{\mathrm{azimuth}} \cdot \gamma_{\mathrm{range}}$ instead of from γ_{estim}

Table 5.7

Orbits 24416 and 4743

orbit	platform	date	f_{Dc} mean	f_{Dc} min	f_{Dc} max	B_a mean
24416	ERS-1	16 mar 1996	474.91	462.94	501.13	1380.51
4743	ERS-2	17 mar 1996	134.26	126.90	142.26	1394.75

Table 5.8

Figure 5.25 — 24416 (ERS–1) / 4743 (ERS–2)

Figure 5.26 — unfiltered / range filtered / azimuth filtered / azimuth and range filtered

filter operation	Δf_{Dc} (Hz)	Δf_r (MHz)	$B_\perp$ (m)	$\dfrac{\Delta B}{B}$	theoretical			γ_{estim}		experimental	
					γ_{rect}	γ_{weight}	m_{weight}	biased	correct.	γ	m
none								0.651	0.651		
azimuth	340.65			0.246	0.754	0.785	27.4%	0.825	0.824	0.78	26.7%
range		−0.287	17.95	0.018	0.982	0.992	0.8%	0.651	0.651	1.000	0.0%
az&ra				0.261	0.739	0.776	28.9%	0.825	0.825	0.789	26.8%
– multi†										0.789	26.7%

† Experimental coherence $\gamma_{az\&ra}$ calculated from $\gamma_{az\&ra} = \gamma_{azimuth} \cdot \gamma_{range}$ instead of from γ_{estim}

Table 5.9

Amplitude of image 24416

Coherence of unfiltered image pair 24416–4743

Coherence of azimuth filtered image pair 24416–4743

Coherence of range filtered image pair 24416–4743

Coherence of azimuth and range filtered image pair 24416–4743
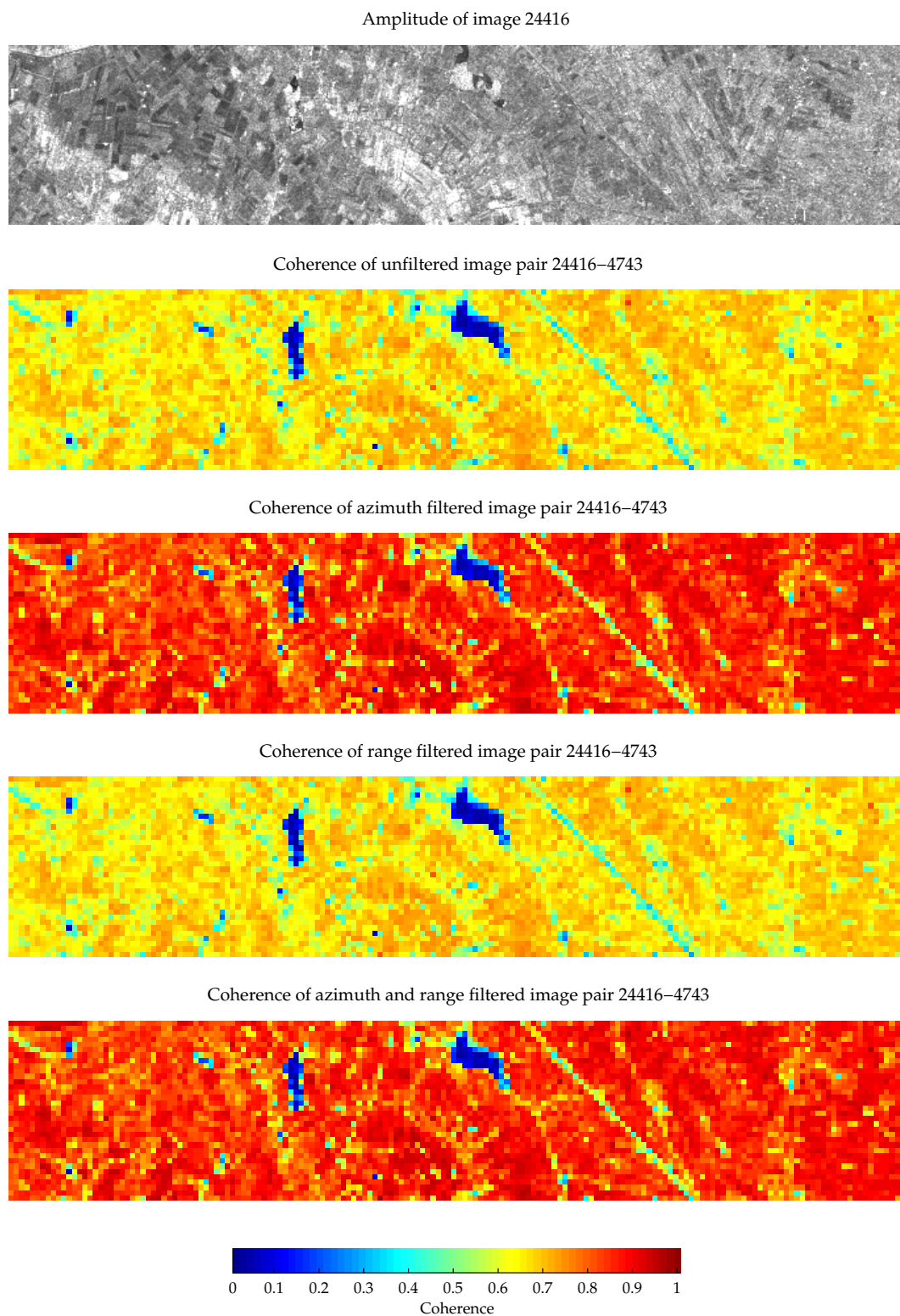
Figure 5.27 The coherence images of the interferometric pair 24416 and 4743 show the 27% improvement due to azimuth filtering. Range filtering has a negligible effect, in accordance with the prediction. The temporal decorrelation is low because the images were taken in March. Lakes show no coherence at all. Coherence pixels are 12 (range) × 60 (azimuth) SLC pixels or 260 × 240 metre; amplitude pixels are 3 × 15 SLC pixels or 65 × 60 metre.

Interferometric phase of unfiltered image pair 24416–4743
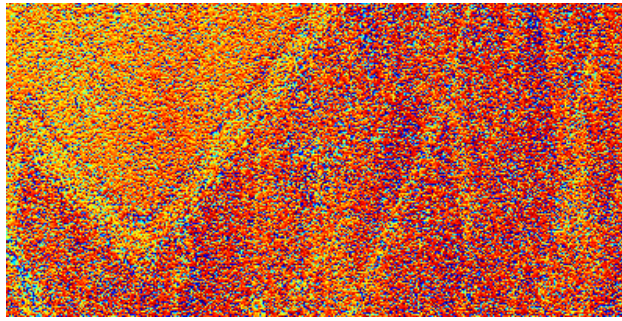
Interferometric phase of azimuth filtered image pair 24416–4743
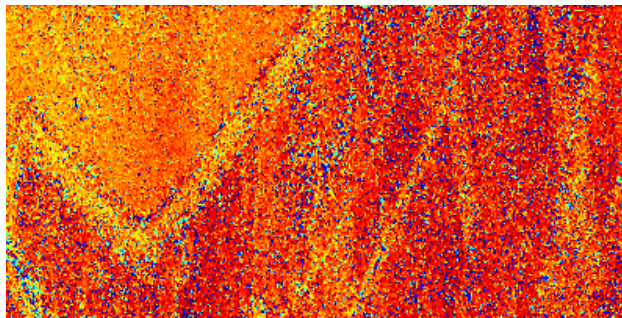
Interferometric phase of range filtered image pair 24416–4743
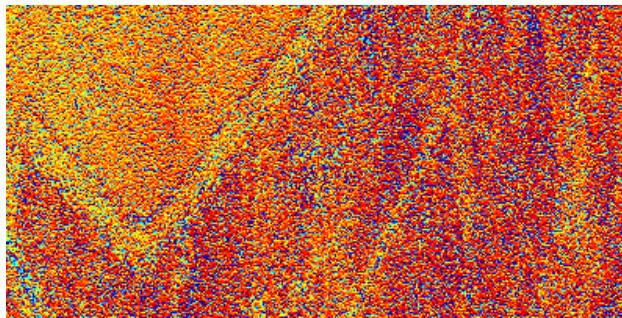
Interferometric phase of azimuth and range filtered image pair 24416–4743
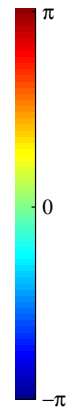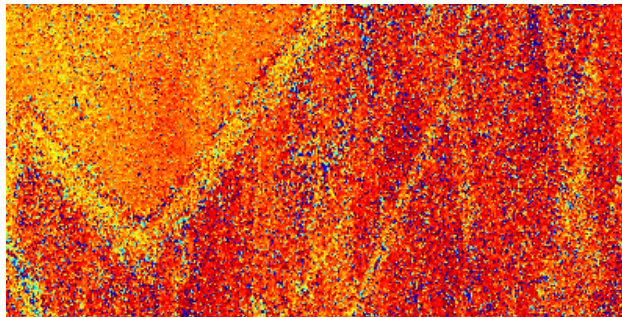
Figure 5.28 The interferometric phase images of the tandem pair 24416 and 4743 show the 27% improvement due to azimuth filtering as a reduction in phase noise. Range filtering has a negligible effect. To show the noise, no multilooking was applied and hence the pixels are not square. The yellowish coloured feature is probably due to a swell of the soil due to a moisture difference between master and slave. The images are 400 (range) × 200 (azimuth) pixels or 8600 × 800 m.

Orbits 24917 and 5244

orbit	platform	date	f_{Dc} mean	f_{Dc} min	f_{Dc} max	B_a mean
24917	ERS-1	20 apr 1996	465.93	461.33	468.49	1378.40
– max†			473.90	468.77	480.10	1378.40
5244	ERS-2	21 apr 1996	205.23	198.42	213.81	1392.24
– max†			206.56	203.61	217.14	1392.24

† Doppler centroid f_{Dc} determined from location of maximum of azimuth spectrum instead of empty band

Table 5.10

Doppler centroids 24917 and 5244   Coherence histograms pair 24917–5244

24917 (ERS–1)
5244 (ERS–2)
fDc from maximum

unfiltered   azimuth filtered
range filtered   azimuth and range filtered
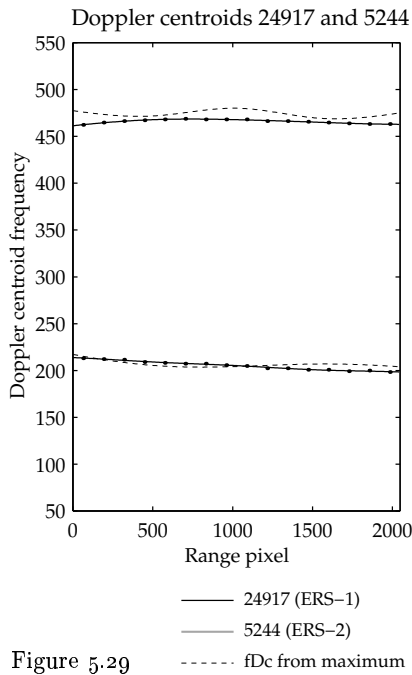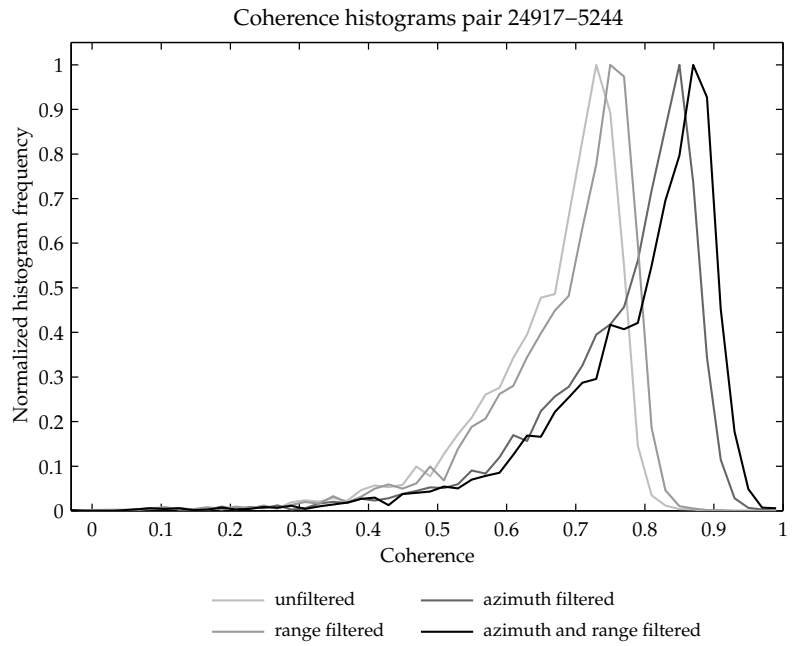
Figure 5.29   Figure 5.30

filter operation	Δf_{Dc} (Hz)	Δf_r (MHz)	$B_\perp$ (m)	$\dfrac{\Delta B}{B}$	theoretical γ_{rect}	γ_{weight}	m_{weight}	γ_{estim} biased	correct.	experimental γ	m
none								0.661	0.661		
azimuth	260.71			0.189	0.811	0.863	15.8%	0.760	0.760	0.870	15.0%
– max†	267.33			0.194	0.806	0.857	16.7%	0.759	0.759	0.871	14.8%
range		1.06	−66.30	0.068	0.932	0.966	3.6%	0.682	0.682	0.970	3.1%
az&ra				0.244	0.756	0.834	19.9%	0.784	0.784	0.843	18.6%
– multi‡										0.844	18.5%

† Doppler centroid f_{Dc} determined from location of maximum of azimuth spectrum instead of empty band
‡ Experimental coherence $\gamma_{\mathrm{az\&ra}}$ calculated from $\gamma_{\mathrm{az\&ra}} = \gamma_{\mathrm{azimuth}} \cdot \gamma_{\mathrm{range}}$ instead of from γ_{estim}

Table 5.11

Interferometric phase 24917–5244 with reference phase subtracted

$-\pi$ 0 π
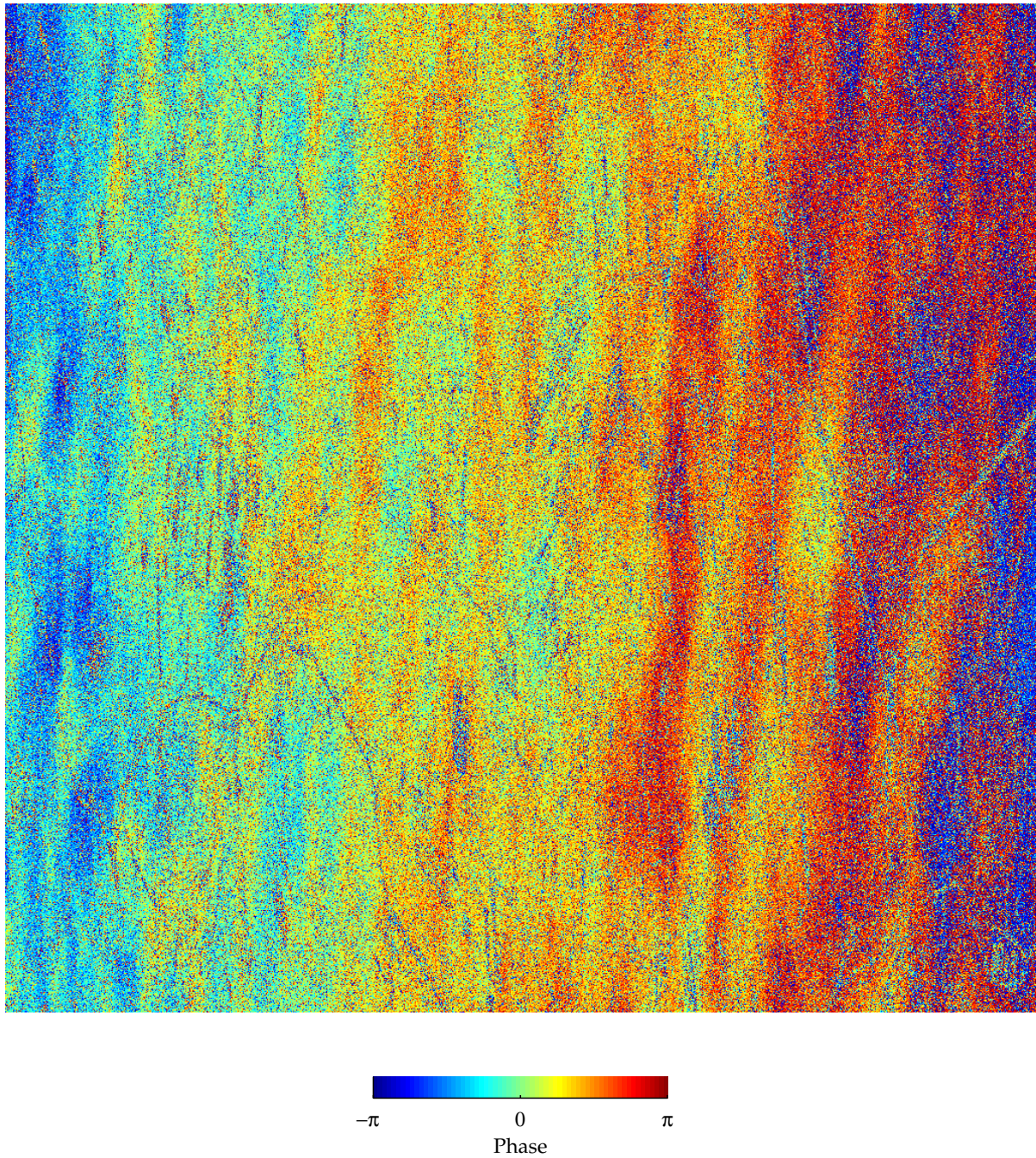
Phase

Figure 5.31   The interferometric phase image of the tandem pair 24917 and 5244 with the reference phase subtracted. As the baseline of this pair is 66 metre and the corresponding height difference that would cause the phase to shift 2π is 131 metre, the coloured phase differences are not caused by topography of the almost flat Groningen scene. They are primarily due to atmospheric delay: a 2.8 cm delay causes a phase shift of 2π. The phase gradient over range is probably due to the subtraction of a non-perfect reference phase, but can also be due to an atmospheric delay gradient. Water is noisy because of the total decorrelation. To show the noise, no multilooking was applied and hence the pixels are not square. The image is 2048 × 2048 pixels or 44 (range) × 8 (azimuth) km.

Continued from page 86

The images were also filtered in range after the azimuth filtering was performed to test whether the multiplicity of equation (5.23) holds. According to this equation, the total decorrelation due to spectral misalignment in range and azimuth is the product of the individual decorrelations. In the tables, the experimental improvement is slightly less than the predicted improvement. However, the improvement of the azimuth and range filtering was also slightly less. Therefore, the measured coherence of the twice filtered image was also compared with the predicted coherence calculated from the measured coherence of the range and of the azimuth filtered image. The listed results show that this yields a perfect multiplicity.

The three long baseline ERS-1 pairs

After the four ERS tandem pairs with a one-day interval, three ERS-1 pairs were processed with an interval of 35 days. This results in the temporal decorrelation to be high compared with that of the tandem pairs. Furthermore, the three ERS-1 pairs were selected to have a long baseline in order to demonstrate range filtering. Hence also a high geometric decorrelation was expected for the unfiltered images.

Because these long baseline interferometric pairs were acquired with the same satellite, the Doppler centroid frequency differs only a little and azimuth filtering is far less important than range filtering. This is clear from the range dependent Doppler centroid figures 5.34, 5.38 and 5.41. The average Doppler centroid difference ranges from 5 Hz for the pair 5535-6036 to 53 Hz for 7539-8040; the expected improvement of azimuth filtering ranges from 0.1% to 1.0%.

8040 has a larger azimuth bandwidth than the other images and the bandwidth of 8541 was determined to show a remarkable variation between 1348.16 and 1432.75 Hz (not depicted). In the azimuth weighting functions equation (5.26) and the filter functions equations (5.35) and (5.36) this was not accounted for. This can be a reason for the slightly greater improvement in azimuth than expected: the spectra were given a shape too narrow. The bandwidth of the filtered signal is right, because the rectangular function of equation (5.40) processes the actual range dependent azimuth bandwidths, which are spline-approximated like the Doppler centroids. The calculation of the expected improvement does however not account for this.

Because the mean coherence for the pair 8040-8541 is only 0.154 and for the other pairs it is still lower, the fine coregistration was expected to suffer. Because the determination of the fine coregistration parameters in the used PCI package is performed by coherence estimation, it is more sensitive to low coherences than a determination from the correlation, which only uses the similarity of the speckle pattern and not the interferometric phase (Zebker et al., 1994). Therefore the coregistration was performed independently with the Doris software package for the image pair 8040-8541. Indeed the coherence increased with 6%.

Additionally, the image pairs 8040-8541 and 5535-6036 were range filtered before the coregistration parameters were determined. Because the coregistration utilizes the coherence or correlation, it is expected that the coregistration parameters are better determined from an image pair with the geometrical decorrelation removed by range filtering (Geudtner, 1995). After the determination of the coregistration parameters, the processing starts with the unfiltered images: the prefiltering in range serves only to improve the coregistration. However, the coherence of the unfiltered images that were coregistered with the parameters determined from the range filtered

Fine registration after range filtering above coherence 0.24

a

Pair 8040–8541 fine registration above coherence 0.24

b

Pair 8040–8541 fine registration above coherence 0.3

c
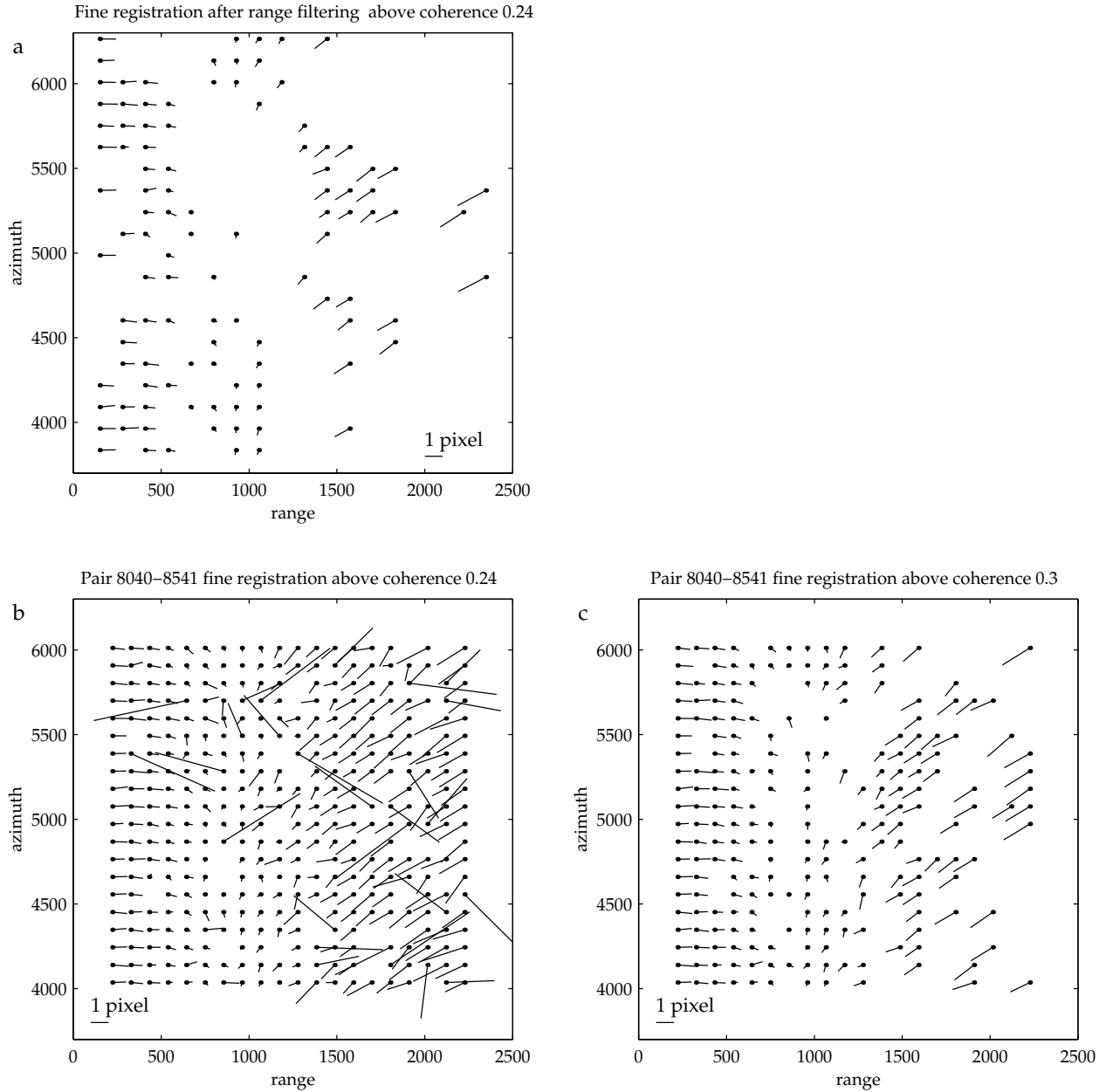
Figure 5.32   Of the pair 8040-8541 in figure a the fine registration vectors with a coherence higher than 0.24 are shown. The length of the vectors is magnified hundred times. The stretch of the slave compared with the master due to its greater incidence angle is clearly visible. The right-hand part of the image suffers from a low coherence and is badly determined. After the images were range filtered, the coherence increases, but because the resolution decreased, the standard deviation of the coherence estimator increases, leading to several badly determined registration vectors which nevertheless have a coherence greater than 0.24 (figure b). Therefore for the eventual fineregistration, the coherence limit is set to 0.30 (c).

pair was only 7% higher.

In figure 5.32 a, the fine registration vectors with a coherence higher than 0.24 are shown. The length of the vectors is magnified hundred times. The stretch of the slave compared with the master due to its greater incidence angle is clearly visible. The right-hand part of the image suffers from a low coherence and is badly determined. If a selection of 2048 × 2048

Pair 5535–6036 fine registration above coherence 0.13

Pair 5535–6036 fine registration above coherence 0.14

Fine registration after range filtering above coherence 0.28

Fine registration after range filtering above coherence 0.32
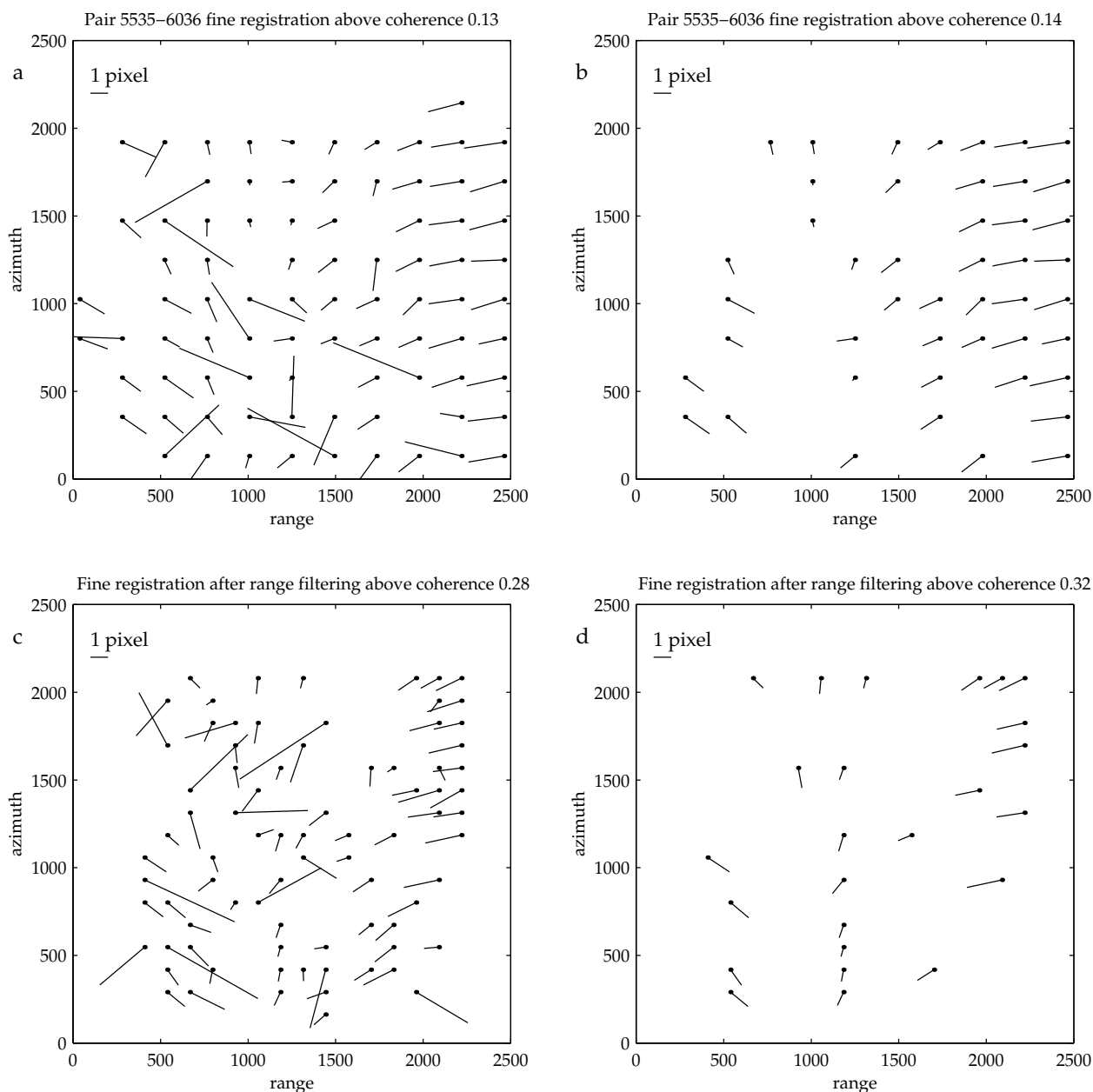
Figure 5.33 Of the pair 5535-6036 in figure a the fine registration vectors with a coherence higher than 0.13 are shown. The length of the vectors is magnified hundred times. The coherence lower limit of 0.13 yields some bad vectors (figure a), but with the limit set to 0.14 only a few vectors remain (b). After the images were range filtered, the coherence increases, but because the resolution decreased, the standard deviation of the coherence estimator increases. If the limit is set to 0.28, many bad vectors are selected (figure c). Only if the limit is set to 0.32, no bad vectors remain, but the number of useful vectors is very limited (d).

of the original 2500 × 2500 image is range filtered and the fine coregistration parameters are again determined from the coherence, the number of vectors above a coherence limit of 0.24 is substantially increased, as is shown in figure 5.32 b. However, because the images are filtered and the resolution drops, the number of independent looks L in the estimator window also decreases. This leads to a higher standard deviation of the coherence estimator. Furthermore,

the fine coregistration is performed to align the master and slave to an accuracy of about one tenth of a pixel; if the resolution drops to for example 2.0 pixels due to range filtering, this is more difficult to realize.

In 5.32 b several badly determined registration vectors are visible, which nevertheless have a coherence greater than 0.24. Therefore for the eventual fineregistration, the coherence limit is set to 0.30. As depicted in figure 5.32 c, this yields a higher number of vectors than the limit of 0.24 in the unfiltered case. Therefore, the determination of the fine registration parameters is expected to be better.

For the image pair 5535-6036, with a coherence of 0.059 due to the baseline of 505 metre, a similar procedure was performed. If the coregistration parameters are determined from the unfiltered images, a coherence lower limit of 0.13 yields some bad vectors (figure 5.33 a). With 0.14 only a few vectors remain (b). If the coregistration is determined after range filtering, the coherence increases, but the coregistration suffers from the reduced resolution and the increased standard deviation due to the decreases number of independent looks. If the limit is set to 0.28, many bad vectors are selected (figure c). Only if the limit is set to 0.32, no bad vectors remain, but the number of useful vectors is very limited (d) and indeed the coregistration based on range filtered images increases the coherence of the unfiltered images only with 1.9%. Therefore this procedure was not followed for pair 7539-8040.

The experimentally estimated coherence improvement after range filtering is in accordance with the predicted improvement for the pair 8040-8541. Range filtering is very effective for this pair, with a perpendicular baseline of 390 metre. This is also reflected in the coherence images in figure 5.36. This pair shows a lower coherence after range filtering than the other two long-baseline pairs. This is probably due to a higher temporal decorrelation.

The coherence is increased at the expense of resolution, because range filtering reduces the range bandwidth. This is clear from figure 5.37: the reduction of interferometric phase noise is impressive, but the range resolution drops significantly. Unfiltered images have a range resolution of 1.2 pixels; filtering this pair in range with a fringe frequency of 6.2 MHz reduces the resolution to 2.0 pixels. For the 684 metre baseline of pair 7539-8040, the resolution drops even further, as shown in figure 5.45: from 1.2 to 4.1 pixels in range.

In this figure, a line is visible in the phase. It is a discontinuity due to the strip-wise range filtering: the two adjacent strips were filtered with a slightly different fringe frequency. Because the fringe frequency for long baselines is high, this effect will primarily appear in long-baseline interferograms. Filtering with overlapping strips would be better.

In general, a reduction in resolution will lead to a higher coherence. However, this does not mean that all reductions of the range bandwidth lead to a higher coherence. If the spectra of master and slave are range filtered by removing a band with a width equal to the fringe frequency at the wrong side, the coherence drops further, as experiments show.

For the pairs 5535-6036 and 7539-8040 the experimental improvement after filtering is less than predicted. However, the realized improvement in coherence is still vast, as the histograms and the coherence images 5.40 and 5.43 show. Because the coherence of the unfiltered images of these pairs is very low, the influence of the bias reduction algorithm on the coherence estimation increases. In the tables, the coherence improvement after filtering is also listed calculated from the coherence estimation of the images without bias correction. These improvement figures are lower than predicted.

As indicated in § 3.4.4, the bias correction algorithm cannot completely remove the bias. This is one reason for the deviation of the estimated improvement. However, a more important reason will be the reduced resolution of the filtered images. This causes the number of independent looks L in the coherence estimator window to decrease; the bias correction algorithm must

then be adapted to the lower L. The bias is then larger and the correction will be higher, yielding an improvement that is lower. Probably in this way the improvement calculated from the bias-corrected coherence estimations will be more comparable with the predicted improvement.

Furthermore, as indicated before for azimuth filtering of the tandem pairs, the predicted coherence estimation can be slightly different from that listed in the tables if the range spectral envelope is different from that in equation (5.27). This results in a deviation in the theoretical coherence calculated with equation (5.30) and will also be a reason for the difference between the predicted and experimentally estimated improvement.

Orbits 8040 and 8541

orbit	platform	date	f_{Dc} mean	f_{Dc} min	f_{Dc} max	B_a mean
8040	ERS-1	28 jan 1993	423.72	418.30	433.17	1411.98
8541	ERS-1	4 mar 1993	416.01	401.68	440.88	1396.57

Table 5.12
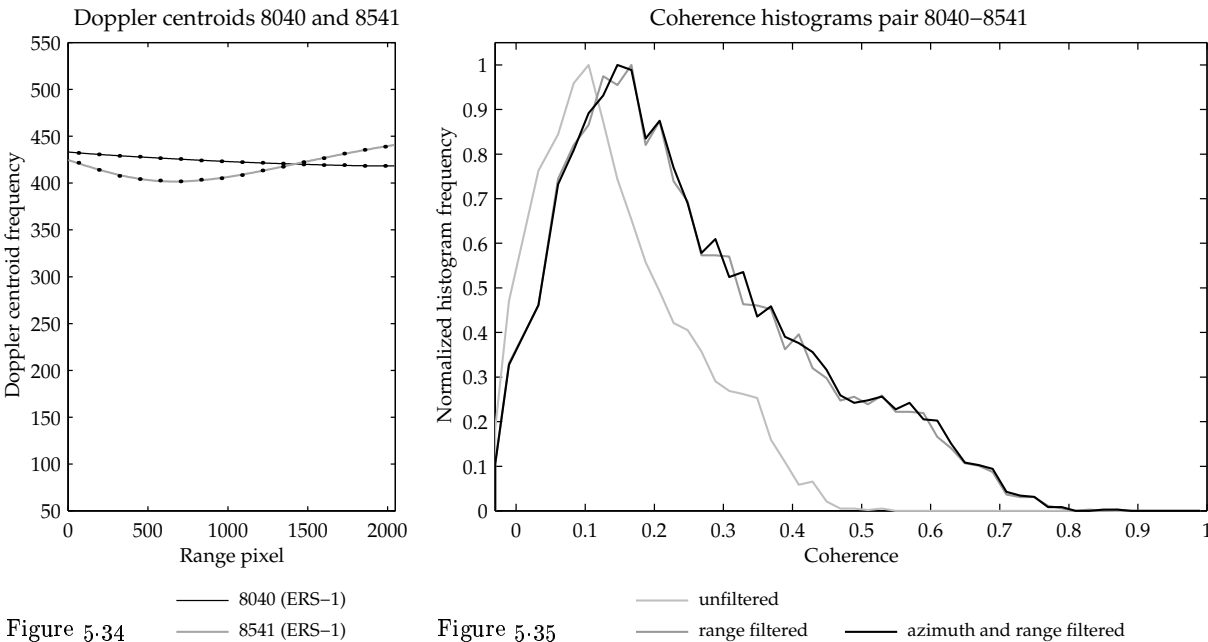
Figure 5.34

Figure 5.35

filter operation	Δf_{Dc} (Hz)	Δf_r (MHz)	$B_\perp$ (m)	$\dfrac{\Delta B}{B}$	theoretical γ_{rect}	γ_{weight}	m_{weight}	γ_{estim} biased	correct.	experimental γ	m
none								0.154	0.146		
– Doris[†]								0.162	0.154	0.944	6.0%
– filter[‡]								0.163	0.155	0.938	6.6%
azimuth	15.17			0.011	0.989	0.998	0.2%	0.164	0.157	0.989	1.1%
range		−6.244	390.38	0.402	0.598	0.595	68.0%	0.264	0.260	0.598	67.2%
az&ra				0.408	0.592	0.594	68.3%	0.267	0.263	0.592	68.9%
– multi*										0.592	69.0%

† After coregistration with Doris software instead of PCI
‡ After coregistration with parameters determined from range filtered images
* Experimental coherence $\gamma_{\text{az\&ra}}$ calculated from $\gamma_{\text{az\&ra}} = \gamma_{\text{azimuth}} \cdot \gamma_{\text{range}}$ instead of from γ_{estim}

Table 5.13

Amplitude of image 8040

Coherence of unfiltered image pair 8040–8541

Coherence of unfiltered image pair 8040–8541 with fine registration from filtered pair

Coherence of range filtered image pair 8040–8541

Coherence of azimuth and range filtered image pair 8040–8541

0   0.1   0.2   0.3   0.4   0.5   0.6   0.7   0.8   0.9   1
Coherence

Figure 5.36   The ERS-1 pair 8040 and 8541 show the low coherence due to the 35-day interval and the perpendicular baseline of 390 meter. Coherence is even lower than for pairs with longer baseline, probably due to a high temporal decorrelation. Determination of the fine coregistration parameters from a range filtered pair hardly shows improvement. Because the image pair was acquired with the same satellite, the Doppler centroid differs a little and azimuth filtering is far less important than range filtering, necessary because of the long baseline.

Interferometric phase of unfiltered image pair 8040–8541

Interferometric phase of unfiltered filtered image pair 8040–8541 with fine registration from filtered pair

Interferometric phase of range filtered image pair 8040–8541
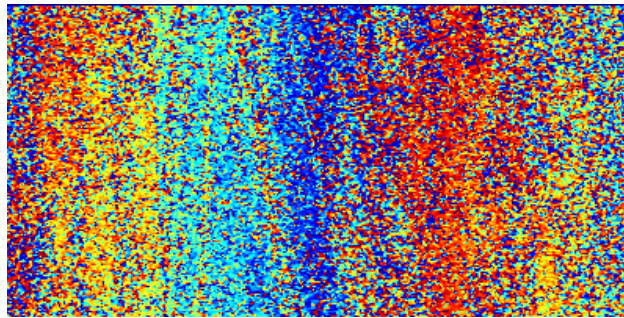
Interferometric phase of azimuth and range filtered image pair 8040–8541
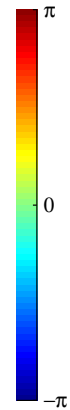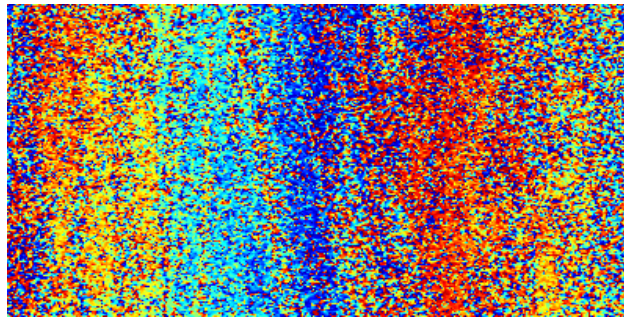
Figure 5.37   The interferometric phase images of the ERS-1 pair 8040 and 8541 show that due to the large baseline and the temporal decorrelation, the phase is rather noisy, but the improvement after range filtering is clear. The effect of azimuth filtering is negligible. Because the range filtering reduces the bandwidth, the range resolution drops from 1.2 pixels to 2.0 pixels. To show the noise, no multilooking was applied and hence the pixels are not square. The images are 400 (range) × 200 (azimuth) pixels or 8600 × 800 m.

Orbits 5535 and 6036

orbit	platform	date	f_{Dc} mean	f_{Dc} min	f_{Dc} max	B_a mean
5535	ERS-1	6 aug 1992	453.02	447.28	456.53	1411.24
6036	ERS-1	10 sep 1992	448.06	444.88	449.24	1378.25

Table 5.14

Figure 5.38   5535 (ERS–1)   6036 (ERS–1)

Figure 5.39   unfiltered   range filtered   azimuth and range filtered

filter operation	Δf_{Dc} (Hz)	Δf_r (MHz)	$B_\perp$ (m)	$\dfrac{\Delta B}{B}$	theoretical γ_{rect}	theoretical γ_{weight}	theoretical m_{weight}	γ_{estim} biased	γ_{estim} correct.	experimental γ	experimental m
none								0.059	0.037		
– filt[†]								0.060	0.038	0.981	1.9%
azimuth	4.96			0.004	0.996	0.999	0.1%	0.061	0.038	0.995	0.5%
– biased[‡]								0.061		0.998	0.2%
range		−8.067	504.77	0.519	0.481	0.4203	138%	0.133	0.123	0.310	223%
– biased[‡]								0.133		0.455	120%
az&ra				0.521	0.479	0.420	138%	0.133	0.123	0.309	224%
– biased[‡]								0.133		0.454	120%

† After coregistration with parameters determined from range filtered images

‡ Experimental coherence $\gamma_{\text{az\&ra}}$ calculated from $\gamma_{\text{estim,biased}}$

Table 5.15

Amplitude of image 5535

Coherence of unfiltered image pair 5535–6036

Coherence of unfiltered image pair 5535–6036 with fine registration from filtered pair

Coherence of range filtered image pair 5535–6036

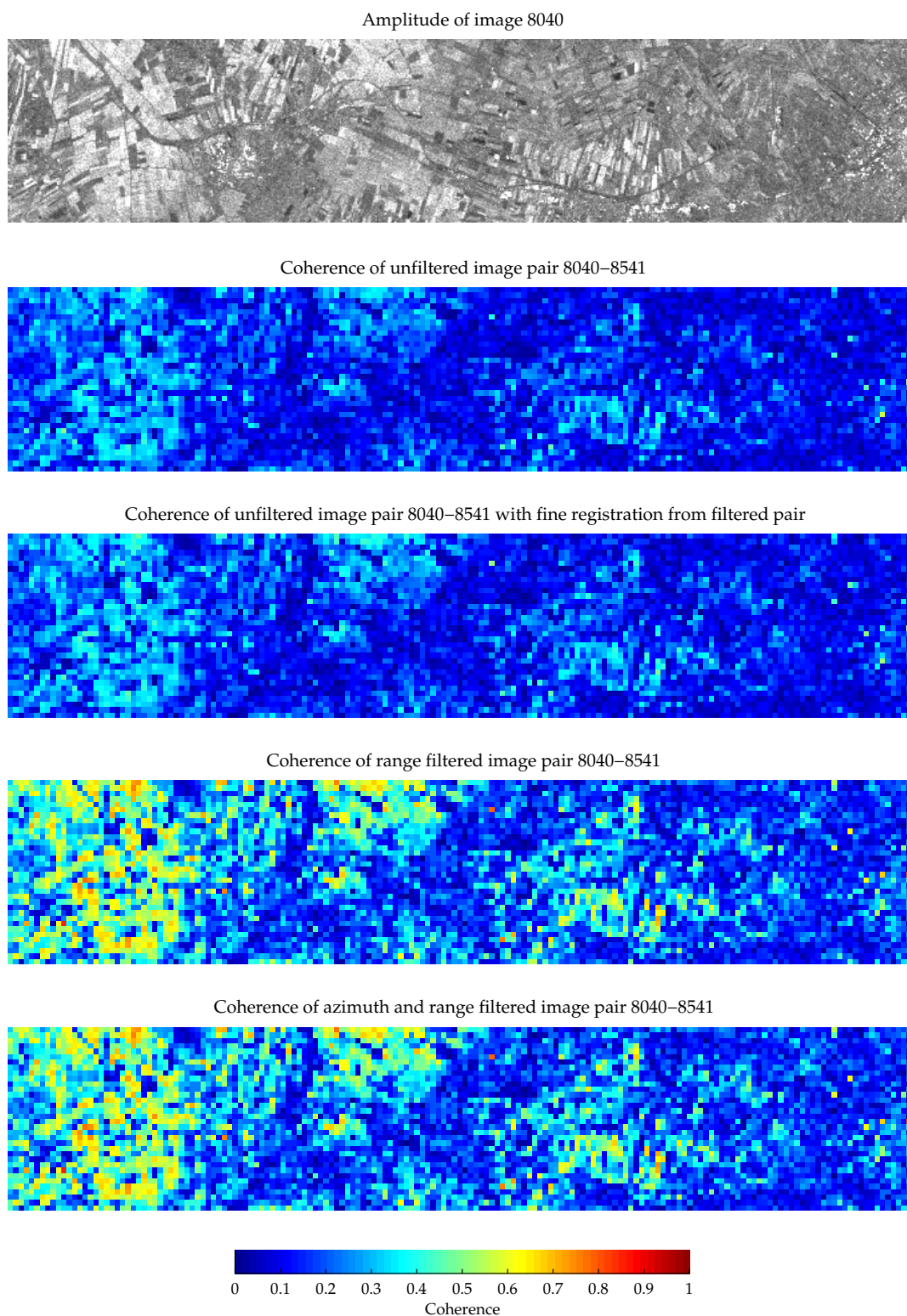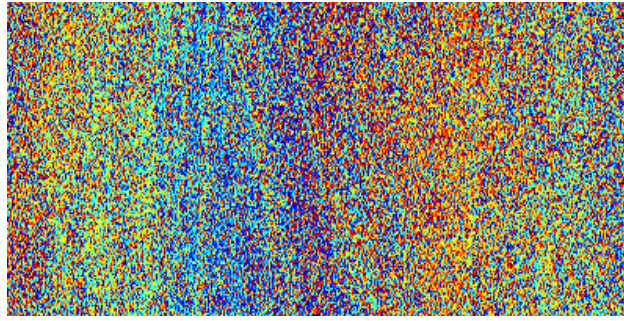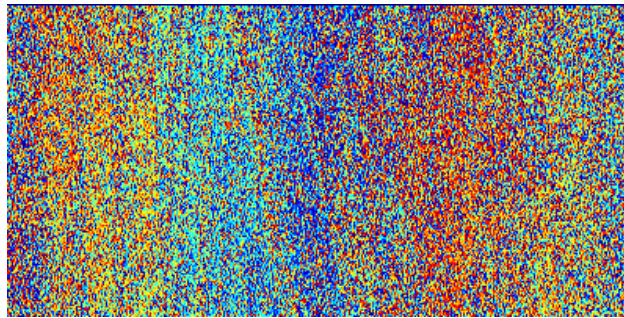Coherence of azimuth and range filtered image pair 5535–6036

Coherence

Figure 5.40   The ERS-1 pair 5535 and 6036 show the low coherence due to the 35-day interval and the perpendicular baseline of 505 meter. Determination of the fine coregistration parameters from a range filtered pair hardly shows improvement. Because the image pair was acquired with the same satellite, the Doppler centroid differs a little and azimuth filtering is far less important than range filtering, necessary because of the long baseline. However, even after range filtering the coherence is still low, probably due to a high temporal decorrelation.

Orbits 7539 and 8040

orbit	platform	date	f_{Dc} mean	f_{Dc} min	f_{Dc} max	B_a mean
7539	ERS-1	24 dec 1992	476.11	469.02	483.03	1379.38
8040	ERS-1	28 jan 1993	423.10	418.27	430.99	1412.09

Table 5.16

Figure 5.41

7539 (ERS–1)
8040 (ERS–1)

Figure 5.42

unfiltered
range filtered
azimuth and range filtered

filter operation	Δf_{Dc} (Hz)	Δf_r (MHz)	$B_\perp$ (m)	$\dfrac{\Delta B}{B}$	theoretical			γ_{estim}		experimental	
					γ_{rect}	γ_{weight}	m_{weight}	biased	correct.	γ	m
none								0.068	0.051		
azimuth	53.01			0.038	0.962	0.991	1.0%	0.069	0.051	0.990	1.0%
– biased†								0.069		0.993	0.7%
range		−10.95	683.51	0.704	0.296	0.188	432%	0.333	0.329	0.154	550%
– biased†								0.333		0.206	386%
az&ra				0.715	0.285	0.186	437%	0.335	0.331	0.155	547%
– biased†								0.335		0.204	389%

† Experimental coherence $\gamma_{\mathrm{az\&ra}}$ calculated from $\gamma_{\mathrm{estim,biased}}$

Table 5.17

Amplitude of image 7539

Coherence of unfiltered image pair 7539–8040

Coherence of azimuth filtered image pair 7539–8040

Coherence of range filtered image pair 7539–8040

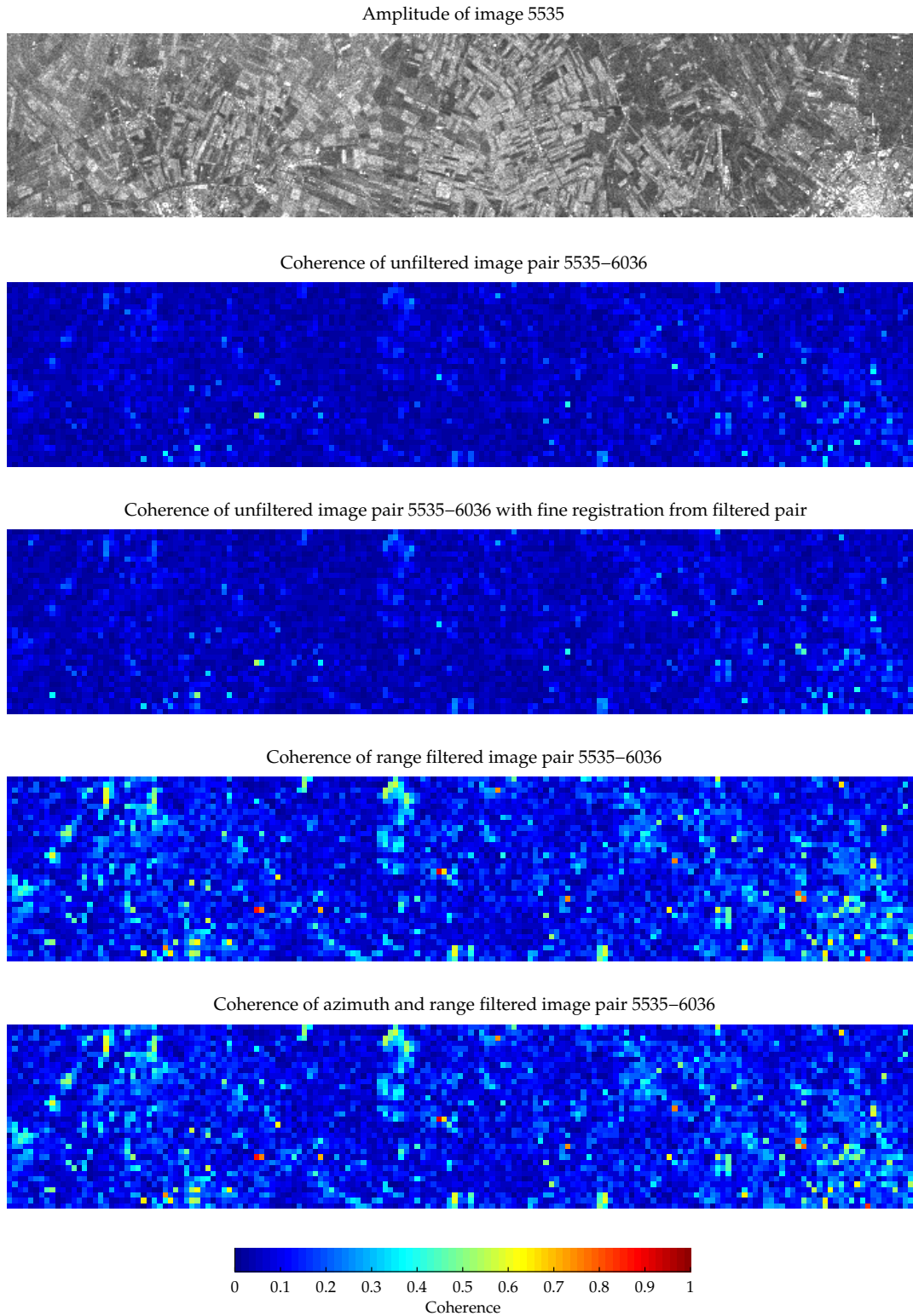Coherence of azimuth and range filtered image pair 7539–8040
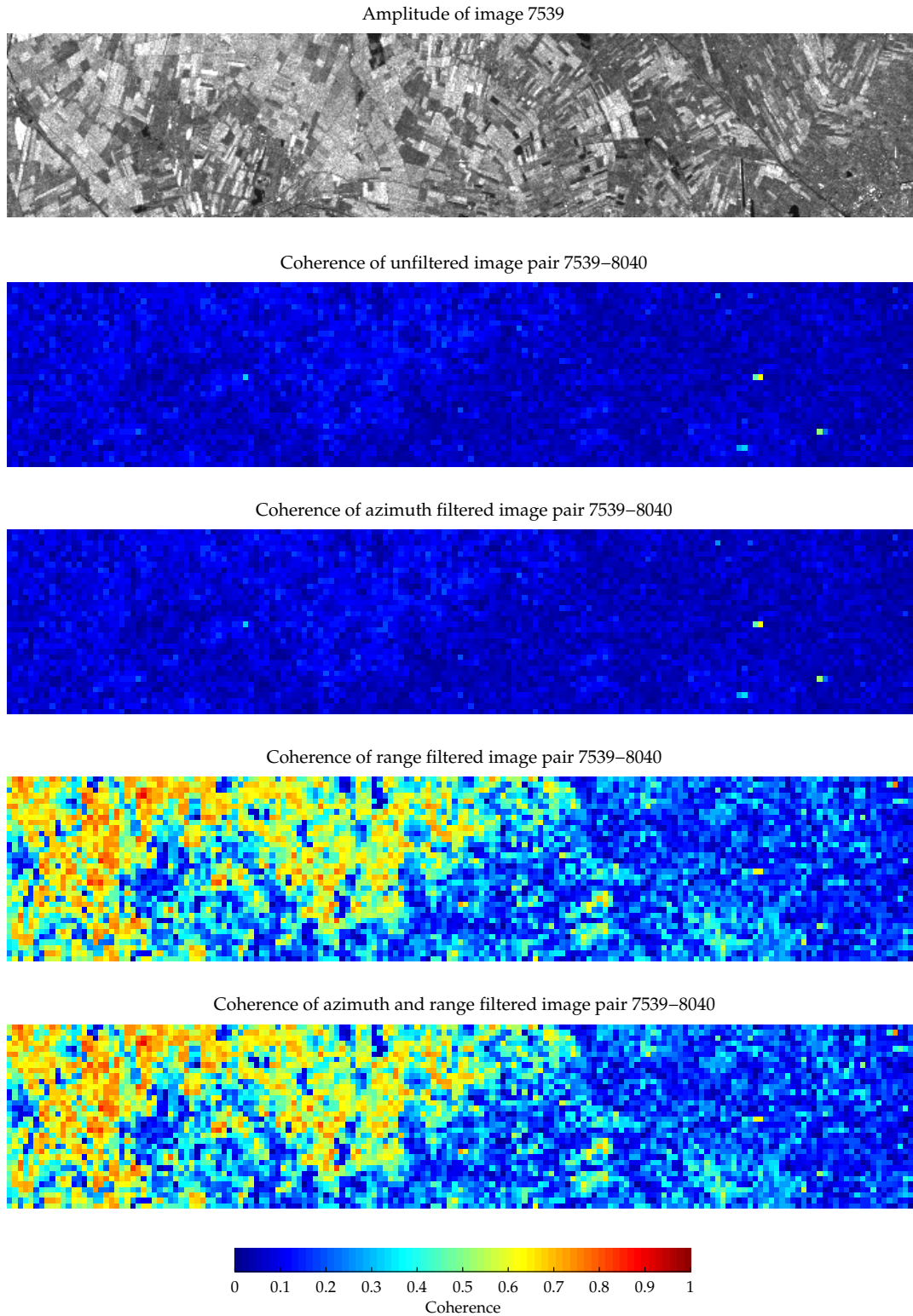
Figure 5.43 The ERS-1 pair 7539 and 8040 show a very low coherence due to the 35-day interval and the perpendicular baseline of 684 meter. Because the Doppler centroid differs only a little, azimuth filtering results in a negligible improvement. Due to the very long baseline range filtering results in a vast improvement of the coherence, which is even higher than for the other two ERS-1 pairs, probably due to a very low temporal decorrelation.

Figure 5.44   The Doppler centroid frequency distribution of ERS-1 as a function of the time in seconds since the passage of the ascending node. This pattern is similar among all orbits. Due to the inclination of the orbit and the rotation of the earth the Doppler centroid is n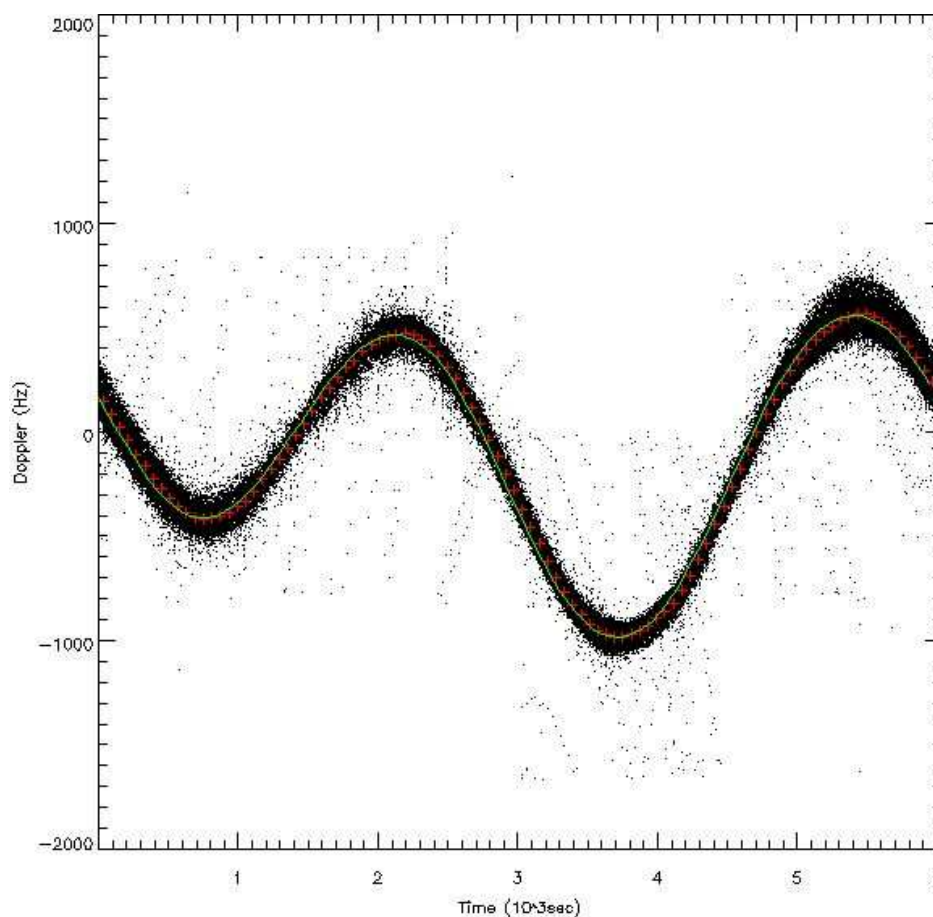ot constant. The few points with deviating centroids are due to satellite manoeuvres (Rosich et al., 2000). (Figure from ESA.)

5.10   The need for spectral filtering for ERS-1 and -2

Azimuth filtering

In § 4.2.3 the cause of the shift of the azimuth spectrum with the Doppler centroid frequency f_{Dc} was discussed. In this subsection the difference in the Doppler centroid frequency for interferometric pairs of ERS-1 and ERS-2, that gives cause to azimuth filtering, is discussed.

For the European Remote Sensing satellites, the steering of the beam and the attitude of the satellite is controlled with help of three gyroscopes. For ERS-1, all three were operational till the end of its lifetime on 10 March 2000; the attitude of the satellite could be controlled within 0.11° in pitch and roll and within 0.21° in yaw (ASF, 1995b). The Doppler centroid frequency therefore shows a similar pattern among all orbits. This is shown in figure 5.44, were the Doppler centroid distribution is shown as a function of the time in seconds since the passage of the ascending node; due to the inclination of the orbit and the rotation of the earth the Doppler centroid is not constant. The few points with deviating centroids are due to satellite manoeuvres (ESA, 1997; Rosich et al., 2000). The orbital period of ERS is $P = 6035.93$ seconds; the more commonly used

Interferometric phase of unfiltered image pair 7539–8040

Interferometric phase of azimuth filtered image pair 7539–8040

Interferometric phase of range filtered image pair 7539–8040

Interferometric phase of azimuth and range filtered image pair 7539–8040
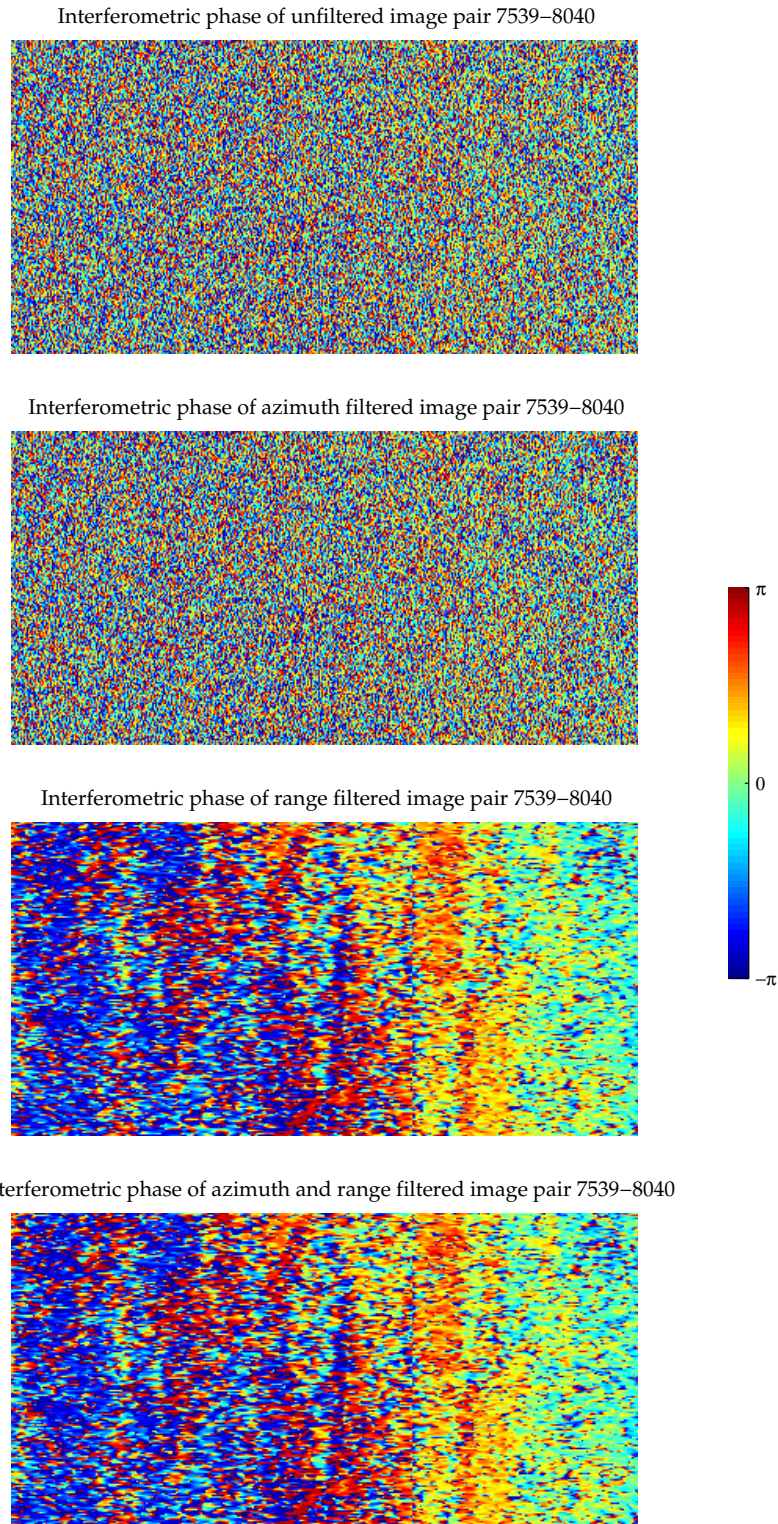
Figure 5.45   The interferometric phase images of the ERS-1 pair 7539 and 8040 show that due to the very large baseline the phase is very noisy. The effect of azimuth filtering is negligible, but the improvement after range filtering is vast. However, because the range filtering reduces the bandwidth, the range resolution drops from 1.2 pixels to 4.1 pixels. The visible line in the phase is due to the strip-wise range filtering; filtering with overlapping strips would be better. To show the noise, no multilooking was applied and hence the pixels are not square.

framenumber of ERS can be derived from the time since the passage of the ascending node t in milliseconds from (Scarpino, 2000)

$$\text{frameno} = \text{int}\left(\frac{9 + 7182 * t}{6020838}\right) \qquad (5.52)$$

For the Groningen scene, the time 2113 s gives the framenumber 2529.

During the first part of its lifetime, the Doppler centroid of ERS-2 showed a distribution very similar to that of ERS-1 and as stable, but with a Doppler centroid approximately 250 Hz lower. Later on, the stability of the platform suffered from problems with two of the three gyroscopes. From 7 February 2000, new software has been uploaded to optimize the attitude operations with one gyroscope. After an experimental period, ERS-2 now operates with one gyroscope.

The stability reduction due to its mono-gyroscope operation causes the Doppler centroid of ERS-2 to show a behaviour during its orbits different from that of ERS-1 graphed in figure 5.44 (ESA, 1997; Esteban et al., 1999; Rosich et al., 2000). The average Doppler centroid as a function of the time since passage of the ascending node is graphed in figure 5.46 for ERS-1, ERS-2 operating with three gyroscopes and ERS-2 in monogyro mode. ESA publishes Fourier coefficients of the Doppler centroid each two weeks.

Sometimes the Doppler centroid of ERS-2 in monogyro mode falls outside the baseband of azimuth sampling of about 1680 Hz (equation 4.14). In the SAR-processing, the resulting ambiguity has to be solved. This can be a problem to the few SAR-processors that assume the spectrum to fall in the baseband (Rosich et al., 2000).

Interferograms can be calculated using pairs of ERS-1 images, pairs of ERS-2 images and mixed pairs of ERS-1 and ERS-2 images. The use of mixed pairs acquired in the tandem mission phase is attractive for geodetic applications because of the time interval of one day, which limits temporal decorrelation. However, the average Doppler centroid of ERS-2 can be very different from that of ERS-1, depending on geographical latitude, as figure 5.46 shows. Azimuth filtering hence is almost always profitable for tandem pairs.

If ERS-1 pairs are used, the time interval between images of the same scene is 35 days, except for the two 'ice phases' with an interval of 3 days and two 'geodetic phases' with an interval of 168 days (ASF, 1995). Temporal decorrelation will hence be higher than for tandem pairs and spectral filtering can help to improve the coherence. As figure 5.44 and our experiments show, the Doppler centroid frequency of ERS-1 pairs show a certain distribution, but the difference will never be as great as for the ERS-1-ERS-2 tandem pairs, as is clear from figure 5.46. The highest of the Doppler centroid differences in our three ERS-1 pairs was 53 Hz, the smallest 5 Hz. According to figure 5.44, the difference depends on the time since the passage of the ascending node and hence of the geographical latitude and will not exceed 300 Hz. In general, azimuth filtering will not be as necessary as range filtering, but if the Doppler centroid difference is more than 85 Hz, the improvement according to equation (5.28) will be 2% and if it is more than 143 Hz, the improvement will be 5% and one can choose to apply azimuth filtering.

For interferometric image pairs of ERS-2, the same holds as for ERS-1. In the first phase, ERS-2 pairs show a spectral overlap of almost 100% (Rosich et al., 2000). However, if the images were acquired after 7 February 2000, due to the reduced stability of ERS-2 operating in single gyroscope mode, the Doppler centroid frequency differences increased irregularly but substantial (figure 5.46). Azimuth filtering is then certainly recommended.
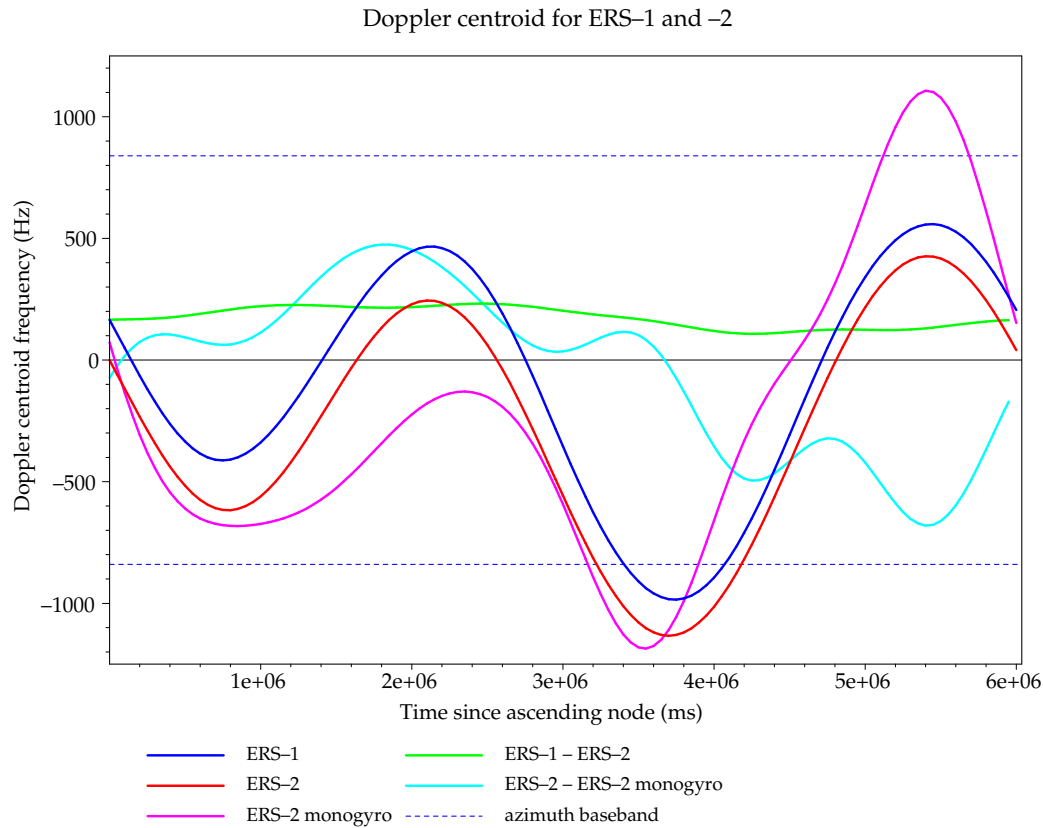
Figure 5.46   The Doppler centroid of ERS-1 and ERS-2 as a function of the time in milliseconds since the passage of the ascending node. Since February 2000, ERS-2 operates with a single gyroscope instead of three. Shown is its reduced stability in the second half of May 2000. Also shown are the differences between the Doppler centroids of ERS-1 and ERS-2 and of ERS-2 in three- and one-gyroscope mode, of interest to interferometric processing especially for spectral filtering. Sometimes the Doppler centroid falls outside the baseband, hampering the SAR-processing. The figure has been calculated from Fourier coefficients supplied by ESA.

Range filtering

The baseline of the four tandem ERS-1-ERS-2 pairs we used in our experiments was small. The maximum baseline was 83 meter, leading to a theoretical improvement after range filtering of 4.7%. Moreover, because in the Groningen scene topography is almost absent, range filtering is not really necessary. However, because tandem baselines are in general between 200 and 300 metre and topography is present, range filtering for tandem pairs can be profitable.

As noted above, if ERS-1 pairs are used, the time interval between images of the same scene is – depending on the phase – 35 days. Temporal decorrelation will hence be higher than for tandem pairs and all possible improvement of the coherence will be needed to improve the phase unwrapping. The perpendicular component of the baselines for these pairs show a large variation, from several tenths of meters to more than the critical baseline of 1060 meter. For ERS-1 pairs range filtering is in general necessary, as well as for ERS-2 pairs.

5.11 Spectral filtering in the interferometric processing

In § 2.7, the processing steps for interferometry were discussed. In this section, the location of spectral filtering in this process is discussed. It is illustrated in figure 2.14.

To apply filtering in range and azimuth, the shift of the slave image relative to the master image must be known more or less accurate. On the subpixel level, it is calculated in the fine coregistration processing step.

If the baseline is very long, due to the baseline decorrelation the fine coregistration is difficult to apply, because it relies on the correlation between master and slave image. This was probably the reason for the bad coherence of the ERS-1 pairs we processed. In that case the images can be range filtered before the fine coregistration can take place. After the determination of the fine coregistration, the original images are filtered. This is depicted in 2.14. However, as was shown in § 5.9.2, the increase of the coherence after prefiltering in range leads to a reduction in resolution and an increase in the standard deviation of the coherence estimator due to the reduced number of independent looks in the estimator window. In our experiments the increase in coherence of the unfiltered image after determination of the registration parameters from the filtered pair was low, but not negligible.

If the baseline is long and the terrain shows a lot of topography, this coregistration process is complicated. In the case of topography, the fringe frequency varies to a great extent with the local terrain slope. Range filtering must be performed with the fringe frequency estimated from the interferogram, but because of the bad coregistration this is often impossible. The range filtering must then be applied with the range frequency shift calculated from the baseline for adjacent range strips.

After the fine coregistration – now improved because of the range filtering – range filtering can be applied again, based on the fringe frequency measured in the local interferogram spectrum.

For interferometric image pairs with a large Doppler centroid difference and hence a large decorrelation – which is less likely to occur than large baseline correlation, as discussed in § 5.10 – the fine coregistration can also be difficult to determine (Usai and Klees, 1999, Geudtner et al., 1998). The azimuth filter is calculated for each azimuth line, depending on the Doppler centroid frequency of the master and slave image for that line. The Doppler centroid depends on range. This means that for azimuth filtering at least the coarse coregistration must have been applied. Because this can be difficult for large Doppler centroid differences, a prefiltering in azimuth for coregistration can be performed with an azimuth and range independent filter, based on the average Doppler centroids of both images. After the determination of the coregistration parameters and the coregistration of the unfiltered images, the usual range-dependent azimuth filter can be applied to these unfiltered images.

6 Oversampling

The principles of aliasing, oversampling and downsampling are discussed in appendix C and demonstrated with cosine signals. In this chapter these principles are applied to radar interferometry. In § 6.1, the occurrence of aliasing in the interferogram due to undersampling of the master and slave signal is discussed and demonstrated with a simulated signal. It can be prevented by oversampling the master and slave signals (§ 6.2), after which the original size of the interferogram can be restored by downsampling, discussed in § 6.3. The improvement reported in the literature and the conditions for oversampling to be necessary are discussed in § 6.4.

6.1 Aliasing in the interferogram

The calculation of an interferogram consists essentially of a complex multiplication of a master radar image with an aligned slave radar image. As known from signal processing, a multiplication of two signals is equivalent to the convolution of their respective spectra (Ziemer et al., 1993). If the spectra of both signals have the same bandwidth, the bandwidth of the interferometric spectrum will be twice as wide. In § C.1 is shown that is the highest frequency in the master image is f_1 and f_2 in the slave image, the highest frequency in the interferogram is $f_1 + f_2$.

As known from the sampling theorem of Shannon, the highest frequency in a signal that can be reconstructed after sampling the signal, is half the sampling frequency f_s. This frequency is called the *Nyquist frequency*. Because the Nyquist frequency for the interferogram is equal to that of the master and slave image, the spectrum of the interferogram thus can only contain the sum frequency $f_1 + f_2$ if the sampling frequency of the master and slave is twice as high. In general this is not the case for radar interferometry. As is shown in § C.1, if this Nyquist criterion is not fulfilled, the frequency band above the Nyquist frequency is folded to the other side of the spectrum, an effect known as aliasing.

In this paragraph, the aliasing effect in the interferogram of two undersampled simulated signals is shown. The signal is a one-dimensional circular Gaussian series, as used and explained in the section on the simulation of a range signal and range filtering, § 5.7. The signal is oversampled with the same rate as the ERS range signal, the ratio of the sampling frequency and the range bandwidth, $r = 18.96/15.55 = 1.219$. For this simulation, the starting point was an identical master and slave signal. This leads to a zero fringe frequency, visible in the interferogram as a strong peak for $f_r = 0$; the interferometric phase is zero everywhere in the interferogram. To the slave signal, noise
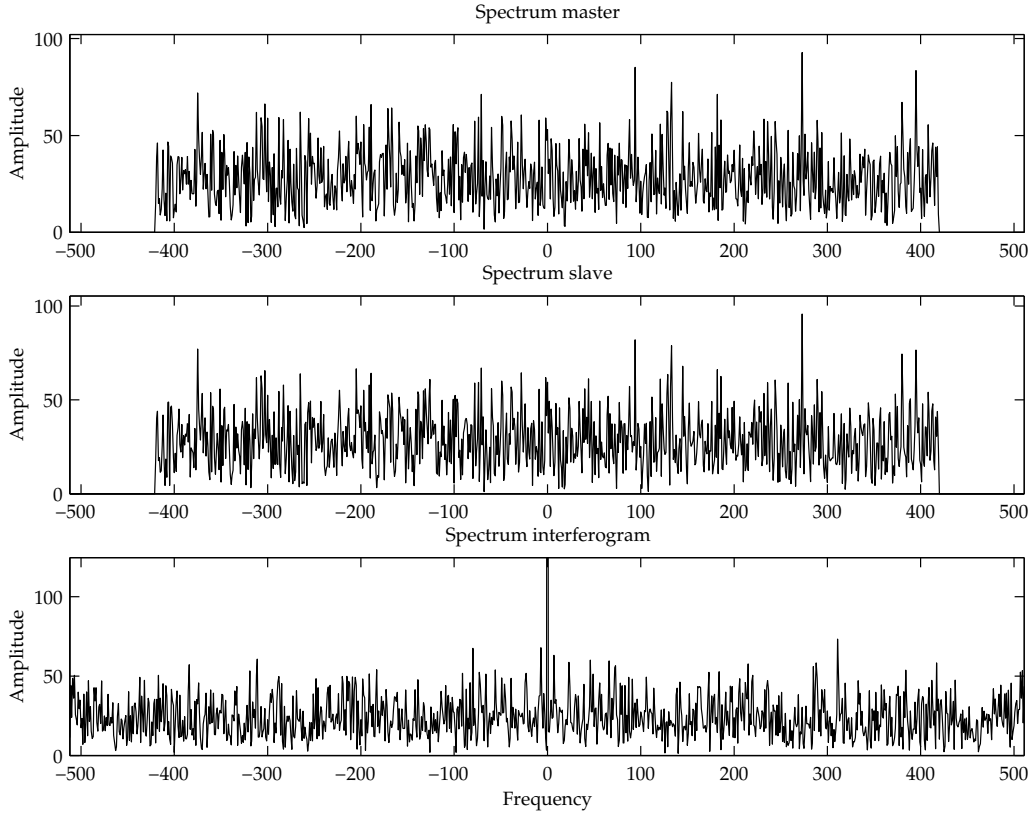
Figure 6.1   The spectra of the slave signal is that of the master signal with noise added. The oversampling factor 1.219 is visible as the empty high-frequency bands. The interferogram spectrum shows the fringe frequency peak at zero, because the similar master and slave image are not relatively shifted. The spectrum was scaled to one sixth of the peak amplitude. The spectrum of the interferogram fills the band; it can not occupy the doubled bandwidth that is a result of the convolution of the master and slave spectrum. The tails of the interferometric spectrum are folded to the other side of the spectrum and aliasing occurs.

was added, leading to a interferometric phase without a phase ramp, but with noise.

In figure 6.1, the spectra of the master and slave signal is shown. The oversampling factor 1.219 is visible as the empty high-frequency bands. Also the similarity of the signals except for some noise is visible. The interferogram spectrum shows the zero-fringe frequency peak; the spectrum was scaled to one sixth of the peak amplitude. The spectrum of the interferogram fills the band; it can not be twice as wide as the bandwidth of the master and slave image. The tails of the interferometric spectrum are folded to the other side of the spectrum and aliasing occurs. Where individual frequencies are folded to can be clearly demonstrated for cosine signals; this is discussed in § C.1.

6.2   Oversampling of the master and slave spectra

The calculation of the interferogram of the master and slave image is performed by the pointwise multiplication of both images. Because both images and both spectra are known at n sampling points, the complex multiplication also yields n sampling points. By extending the spectrum of master and slave to $2n$ points by insertion of zeros (*zero padding*), the interferogram and its spectrum also occupy $2n$ points and the doubled bandwidth fits in the spectral range. This is called *oversampling*; in § C.3 the way it is
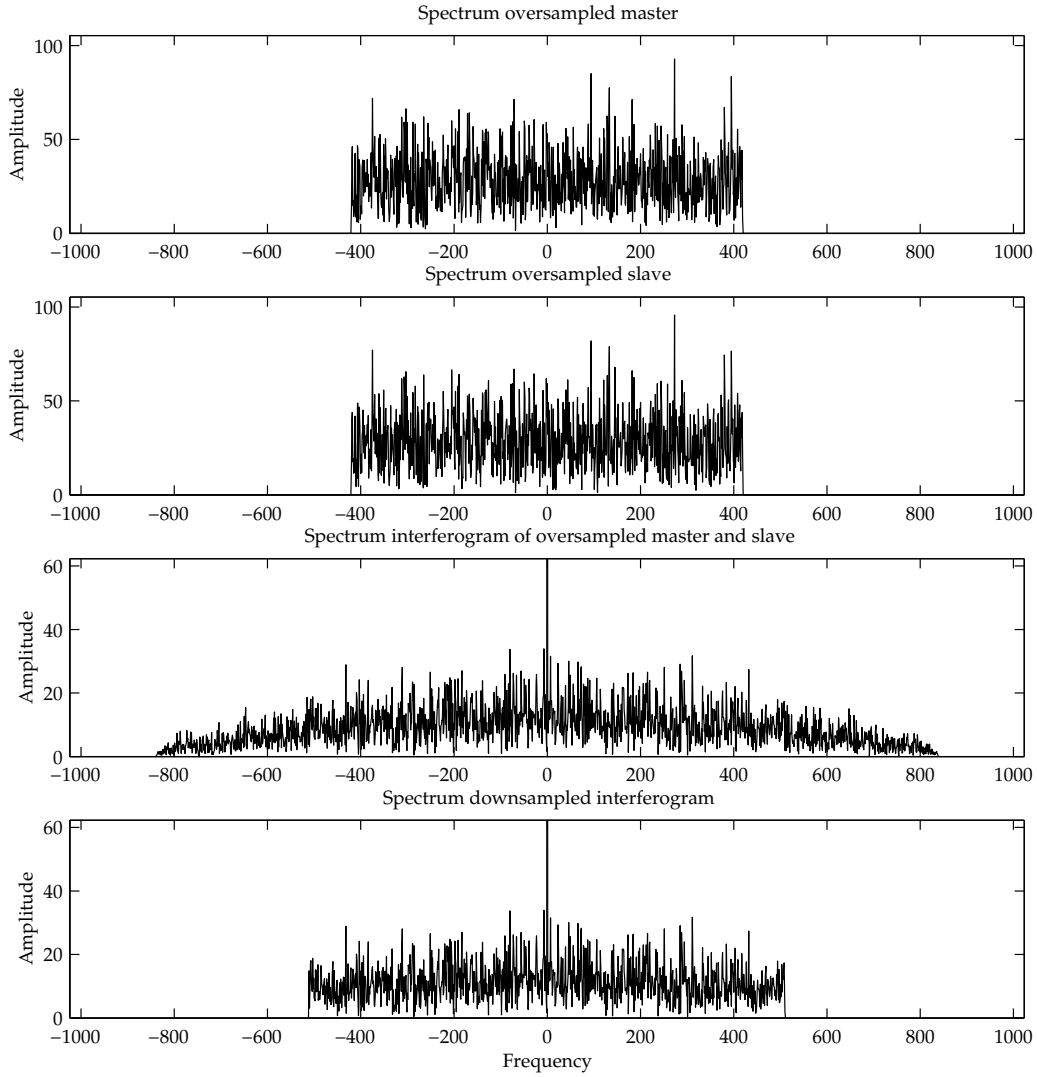
Figure 6.2   The spectra of master and slave are oversampled by extending the $n = 1024$ point spectrum of figure 6.1 to $2n = 2048$ points: on either side 512 zeros are added. Now the interferogram and its spectrum also contain $2n = 2048$ samples. The Nyquist frequency is doubled and the sum frequencies fit in the interferogram band. The tails that were aliased to the other side of the spectrum in figure 6.1 are now visible. As is expected from the convolution, the interferogram spectrum shows a tapered envelope. If the interferogram must be limited to $n = 1024$ samples, its spectrum is lowpass filtered by limiting it to the central n points.

performed is discussed.

In figure 6.2, the spectra of master and slave were oversampled by extending the $n = 1024$ point spectrum to $2n = 2048$ points: on either side 512 zeros are added. Now the interferogram and its spectrum also contain $2n = 2048$ samples. The Nyquist frequency is doubled and the sum frequencies fit in the interferogram band.

The tails that were aliased to the other side of the spectrum in figure 6.1 are now visible. As is expected from the convolution, the interferogram spectrum shows a tapered envelope.

6.3   Downsampling of the interferogram

Often the interferogram is required to contain the same number of samples as the master and slave image, in order to limit processing time and space requirements and because the high-frequency information is not needed in the end (§ 6.4). To prevent aliasing, the master and slave must be oversampled; after this, the interferogram can be *downsampled* (§ C.5). This is accomplished by limiting the interferogram spectrum to the original n samples. Effectively, this is a lowpass filter.

In figure 6.2 this is shown for the simulated signal. The tails are cut off and the resulting spectrum is limited to $n = 1024$ points. Because the tails are not folded to the other side, the envelope shows still some tapering, in contrast with the aliased interferogram spectrum in figure 6.1. The aliasing is prevented.

6.4   Improvement due to oversampling and necessity for ERS

Aliasing results in noise in the interferogram. By applying oversampling of the master and slave image before the interferogram is calculated, the number of phase residues can be reduced with 15% (Geudtner, 1995). This improvement is not dependent of the baseline and Doppler centroid frequency difference.

Because the range spectrum of ERS is centred around zero, oversampling is straightforward. For oversampling in azimuth, the spectrum must be split in the empty band, which for ERS in general is not situated at the edges of the spectrum. For oversampling in azimuth, the Doppler centroid frequency, which slightly depends on range (§ 4.2.3) must thus be known. (Schwäbisch, 1995; Geudtner, 1995.)

In order to limit processing time and space requirements, in general the interferogram of the oversampled images is lowpass filtered. The high-frequency information filtered away is not needed in general; on the contrary, often the interferogram is averaged over for example 2×11 pixels, reducing the high-frequency information. This *multilooking* limits the noise in the phase. According to Zebker et al. (1994) this multilooking already reduces the noise induced by aliasing to such an extent that oversampling is not worth the effort.

Because the bandwidth of the ERS signals is smaller than the Nyquist frequency permits, oversampling with a factor two is not necessary. However, because most implementations of the fast Fourier transform (appendix A) are restricted to a power of two, while other implementations can handle multiples of 2, 3 and 5, oversampling is in general performed by extending the number of sampling with a factor two.

Range and azimuth filtering limit the bandwidth of the ERS signals. If the azimuth spectrum is limited from the usual $B_a = 1379$ Hz to half the pulse repetition frequency $f_{pr}/2 = 840$ Hz, it occupies only half the spectrum and oversampling in azimuth is not necessary because the interferogram in azimuth direction fulfils the Nyquist criterion. This is equivalent to a Doppler centroid frequency difference $\Delta f_{Dc} = 539$ Hz, which can sometimes occur. In range, oversampling is not necessary if the bandwidth is limited from the usual 15.55 MHz to $f_s/2 = 9.48$ MHz. This is equivalent with a fringe frequency of $\Delta f_r = 6.07$ MHz and according to equation (5.13) this is a perpendicular baseline of $B_\perp = 410$ metre. For non-tandem ERS pairs, baselines longer than this occur often. Two of our ERS-1 pairs had a longer baseline and the third had almost this baseline.

Because the spectra of ERS are usually weighted with a Hamming weighting function in azimuth and range, the amplitude of the high-frequency components of the spectrum is reduced and the influence of aliasing is further reduced. Even for slightly higher

Doppler centroid frequency differences or slightly longer baselines, oversampling will not be necessary.

7 Conclusions

The research in this thesis leads to the following conclusions.

7.1 Coherence estimation

- The coherence of an interferogram can be calculated with the coherence estimator of equation (3.19). The reference phase (the phase due to a flat or ellipsoidal earth) might be subtracted from the interferometric phase in order to remove the non-stationarity due to the geometry.

- The coherence estimator is biased. The higher the coherence and the greater the number of independent pixels in the estimator window, the smaller the bias.

- Choosing a large coherence estimator window decreases the bias, but the influence of local topography increases: this reduces the similarity of the phase of the pixels in the window, reducing the estimated coherence.

- The method to calculate the coherence estimator over windows that shift one pixel and averaging the results afterwards is, if the coherence has to be estimated as an interferogram quality measure, unnecessarily complicated and time consuming. Moreover, at the edges of the interferogram it does not give the expected results and calculating one coherence value by taking the estimator window to be equal to the interferogram gives an erroneous result. However, if a coherence estimation has to be calculated for each interferogram pixel, this method is suitable. The coherence estimation over adjacent windows gives a result better suited to serve as an interferogram quality measure and is more efficient to calculate.

- The bias of the coherence estimator can be removed to a great extent. From the estimation, the bias for that particular estimated coherence is subtracted. If the estimation is less than the bias for a zero coherence, then this bias is subtracted, leading to a negative coherence. The coherence histogram can be corrected for the bias by subtracting the bias from the coordinate of the histogram bins. The corrected mean can be calculated from the histogram frequencies and bin coordinates. However, the bias cannot be removed completely. For all estimations less than the bias for a zero coherence, the same correction is performed: the bias for a zero coherence is subtracted. Furthermore, because the standard deviation for smaller numbers of independent pixels in the estimation window is higher, the distribution of the biased coherence is broader; the bias correction algorithm can not correct for this. Additionally, if the mean corrected coherence is calculated, the unbiasing algorithm does not account for the

variable width of the corrected histogram bins.

- The mean (corrected) coherence of an interferogram is a suitable interferogram qua-lity measure to assess the effectiveness of interferogram improvement algorithms, like spectral filtering. Coherence histograms can be used for the coherence distribution; coherence images give information on the spatial distribution.

7.2 Spectral properties of ERS

- Although the attitude of ERS is kept very accurately, the net result of the angle the antenna beam makes with respect to the direction perpendicular to the flight direction, the inclination of the orbit and the rotation of the earth causes the azimuth spectrum to show a shift with respect to zero-frequency. This is the Doppler centroid frequency. It depends on the geographic latitude.

- Within one image, the Doppler centroid frequency depends on range, due to the variation of the incidence angle over range.

7.3 Filtering in azimuth and range

Spectral misalignment

- The azimuth spectra of master and slave image are misaligned because in general they have a different Doppler centroid frequency. This causes decorrelation and shows up as noise in the interferogram.

- The shift of the azimuth spectra with respect to each other is equal to the Doppler centroid frequency difference.

- The envelopes of the range spectra of master and slave are not misaligned; however, the ground range or object spectra (in which the characteristics of the terrain are reflected) are misaligned due to the different incidence angle from either side of the baseline.

- The shift of the object spectrum features in the range spectrum is equal to the fringe frequency, which is linearly dependent on the perpendicular component of the baseline. It decreases with the incidence angle.

- For a flat terrain, the fringe frequency equals the range bandwidth for a perpendicular baseline of 1060 meter. This results in total decorrelation.

- The spectral misalignment in azimuth and range can be removed by filtering the spectra in order to achieve a common system transfer function.

Azimuth filtering

- The spectral filtering in azimuth is performed by multiplying the spectra of master and slave with a filter that is the geometrical mean of the theoretical spectra with the respective Doppler centroids of the master and slave. The bandwidth of master and slave is limited to the overlap of the original spectra; it decreases with the Doppler centroid frequency difference.

- Because of the range dependency, the Doppler centroid must be determined for the

azimuth spectrum of each range line. However, because the spectra show fluctuations, several azimuth spectra must be averaged. After the blockwise determination of the Doppler centroid, it can be smoothed, leading to Doppler centroid values for all range lines. The smoothing can be performed by a cubic spline with a limit imposed to the second derivative at the end points.

- The Doppler centroid can be determined from the location of the maximum of the spectrum. To accomplish this, the average spectrum is smoothed and a first approximation of the maximum is determined. The accuracy of the location of this maximum is poor. After this, a parabola can be fitted through a spectrum interval around this maximum. The maximum of the parabola is the Doppler centroid.

- Alternatively, the Doppler centroid can be determined from the location of the empty band, which is supposed to differ half the sampling frequency from the Doppler centroid. From an interval around the empty band, the symmetry axis can be determined accurately with the autoconvolution. However, the location of the empty band can be determined with an accuracy almost as high by finding the edges of the empty band and determining the centre from them.

- The Doppler centroid determined from the spectrum maximum differs significantly from the centroid determined from the empty spectrum band. Performing the azimuth filtering with the Doppler centroid determined from the spectrum maximum was expected to give a better coherence as the azimuth filtering is based on the location of the spectral envelope, but it turns out to be nearly identical.

Range filtering

- The bandwidth of the range filtered spectra is equal to the original bandwidth minus the fringe frequency.

- The range filtering is performed by removing the original Hamming weighting of the spectra and reweighting the spectra with a Hamming function over the new bandwidth. In the master spectrum, a spectral band is removed from the side opposite to the band removed from the slave spectrum.

- A simulation of a range spectrum and range filtering has the advantage that the only decorrelation present is due to the spectral misalignment. The simulation shows that the range filtering algorithm is valid.

- The fringe frequency is the dominant frequency in the spectrum of the interferogram. To prevent aliasing, the range spectra must be oversampled before calculating the interferogram. After this, the fringe frequency can be determined from the interferogram spectrum.

- The terrain slope and the range cause the incidence angle to vary and therefore the fringe frequency varies. The fringe frequency should be determined from the interferogram spectrum for small terrain patches individually. If the terrain shows a lot of topography, the patches must be as small as possible, but the ability to determine the maximum of the interferogram spectrum imposes a limit to the size of the patches.

- If the interferogram shows a very low correlation, due to a long baseline or a bad coregistration, the fringe frequency cannot be determined from the interferogram spectrum. The fringe frequency must then be determined from the perpendicular

component of the baseline and the incidence angle, as if the terrain would be flat or ellipsoidal. Because both parameters vary over range, the range filtering should be performed dependent on range. Because the orbits are in general not parallel, the baseline is not constant over azimuth and the range filtering should be performed dependent on azimuth too. Alternatively, the fringe frequency can be determined from the orbits and a digital elevation model.

- If the terrain slope equals the ERS incidence angle of $23°$, foreshortening becomes layover. Layover regions can be traced by determining locations where the sign of the fringe frequency changes.

Theoretical and experimental coherence improvement

- The theoretical decorrelation due to spectral misalignment for spectra with a rectangular envelope can be converted to the theoretical decorrelation for (Hamming) weighted spectra. Because the correction is based on the theoretical envelope of the spectra, a slight deviation in the envelope parameters will cause a difference between predicted and estimated coherence improvement.

- The experimental improvement of the estimated coherence after filtering in azimuth and range agrees very well with the predicted improvement.

- The decorrelation due to spectral misalignment in azimuth and range and other sources is theoretically multiplicative. The experimental decorrelation and coherence factor can be derived from the estimated coherence before and after filtering.

- Because decorrelation is theoretically multiplicative, the improvement after filtering in azimuth as well as range should be the product of the improvement due to the filtering in azimuth and that in range. The experiments show that this is true.

- The coherence of three interferometric pairs with very long baseline was extremely bad, due to baseline decorrelation, a bad coregistration and temporal decorrelation. Determination of the fringe frequency from the interferogram spectrum was not possible. Range filtering improved the coherence considerably. However, for two pairs the measured improvement was greater than predicted, probably due to deviations in the number of independent looks in the coherence bias correction algorithm and in the spectral envelope parameters.

- The reduction of interferometric phase noise by spectral filtering can be visualized by interferometric phase images with the reference phase subtracted and without multilooking. The phase features visible in these images are not primarily due to topography for the almost flat Groningen, but to atmospheric delay and, to a limited extent, to deformation, probably due to a moisture difference between master and slave.

- The interferometric phase images show that spectral filtering reduces the resolution in range or azimuth.

The necessity of spectral filtering for ERS-1 and ERS-2

- For ERS-1 pairs, azimuth filtering is in general not necessary, but often profitable. Range filtering is necessary depending on the baseline.

- For tandem ERS-1-ERS-2 pairs, azimuth filtering is often advantageous; range filtering is often profitable.

- For ERS-2 pairs, azimuth filtering is in general not necessary, but often profitable. Since the operation of ERS-2 with one gyroscope (7 February 2000), azimuth filtering is more often necessary. Range filtering is necessary depending on the baseline.

Spectral filtering in the interferometric processing

- For exact azimuth and range filtering, the shift of the slave with respect to the master image must be known. In general, coarse and fine coregistration is therefore performed before spectral filtering.

- If the interferogram shows a very low correlation, e.g., due to a long baseline or a high Doppler centroid difference, the fine coregistration can be bad or impossible. The coherence can be improved by prefiltering the images, after which the coregistration parameters are determined. The original unfiltered images are then coregistered and filtered. However, because the prefiltering reduces the bandwidth and hence the resolution, the standard deviation of the coherence estimator increases, leading to badly determined fine registration vectors which nevertheless have a high coherence and hence are selected for the determination of the coregistration parameters. Prefiltering for coregistration not always results in a better coregistration; if it is better, the increase of the coherence of the coregistered images is only moderate.

- A fine coregistration performed by means of coherence estimation suffers from a low coherence. The correlation operation utilizes the similarity of the speckle pattern and is not sensitive to noise in the interferometric phase. Therefore the determination of the fine coregistration parameters for low coherence images should be performed with a correlation instead of a coherence estimation.

7.4 Oversampling

- If the spectra of master and slave are not oversampled before calculating the interferogram, the spectrum of the interferogram may show aliasing because its sampling frequency is too small to fulfil the Nyquist criterion. This increases the noise in the interferogram.

- To oversample, the spectra are split at the empty band and zeros are inserted to double the number of samples. For the range spectrum, the empty band is always at the edges. For the azimuth spectrum, knowledge about the Doppler centroid frequency is necessary to locate the empty band.

- If the interferogram must be restricted to the number of samples of the original images, lowpass filtering is performed by removing the high-frequency bands.

- Oversampling is not necessary if the spectra have a maximum bandwidth equal to half the sampling frequency, for example after spectral filtering. If the azimuth spectra have the usual 1379 Hz bandwidth, filtering for a Doppler centroid frequency difference of 539 Hz reduces the bandwidth to half the sampling frequency, making oversampling superfluous. In range, oversampling is not necessary if the bandwidth is limited from the usual 15.55 MHz to 9.48 MHz. This is equivalent with a fringe frequency of 6.07 MHz and a perpendicular baseline of 410 metre. Because the spectra are usually weighted, even for slightly higher Doppler centroid frequency differences or slightly longer baselines, oversampling will not be necessary.

- Because the limited bandwidth after spectral filtering and the application of multi-looking after the calculation of the interferogram, the noise due to aliasing will be very limited, making oversampling in general not necessary.

References

Absoft, *Pro Fortran for Power Macintosh. User Guide for Fortran 90, FORTRAN 77, and C/C++.* Paper and PDF version, Rochester Hills, 1999

ASF (Alaska SAR Facility), *European Remote Sensing Satellite, ERS-1.* ASF internet document www.asf.alaska.edu/source_documents/ers1_source.html, 1995a

ASF (Alaska SAR Facility), *Active Microwave Instrumentation, AMI.* ASF internet document www.asf.alaska.edu/sensor_documents/ami_sensor.html, 1995b

ASF (Alaska SAR Facility), *ASF SAR processing algorithm.* ASF internet document www.asf.alaska.edu/reference_documents/datacenters_references/sar_processing.html, 1995c

ASF (Alaska SAR Facility), *ERS-1 satellite's orbit repeat cycle phases.* ASF internet document www.asf.alaska.edu/reference_documents/source_references/ers1_phases.html, 1995d

ASF (Alaska SAR Facility), *ERS-1 and ERS-2 SAR images.* ASF internet document www.asf.alaska.edu/dataset_documents/ers1_and_ers2_sar_images.html, 1996

ASF (Alaska SAR Facility), *SAR theory/interpreting images.* ASF internet document www.asf.alaska.edu/reference_documents/sensor_references/sar_theory.html, 1998

ASF (Alaska SAR Facility), *SAR FAQ – Frequently asked questions.* ASF internet document www.asf.alaska.edu/user_serv/sar_faq.html, 1999

Askne, Jan, Patrik Dammert and Gary Smith, *Report on ERS-1/2 tandem demonstration.* ESA internet document earth.esa.int/l2/11/0xc1cce41c_0x0000240d, 1996

Bamler, Richard and Dieter Just, 'Phase statistics and decorrelation in SAR interferograms'. In: *Proceedings International Geoscience and Remote Sensing Symposium, Tokyo, Japan, 18–21 August 1993*, 980–984

Bamler, Richard and Philipp Hartl, 'Synthetic aperture radar interferometry'. *Inverse problems*, 14 (1998), R1–R54

Bracewell, Ronald N., *The Fourier transform and its applications.* Second edition, McGraw-Hill, New York, 1978

Brigham, E. Oran, *The fast Fourier transform.* Prentice-Hall, Englewood Cliffs, 1974

Carrara, Walter G., Ron S. Goodman and Ronald M. Majewski, *Spotlight synthetic aperture radar. Signal processing algorithms.* Artech House, Boston, 1995

Cattabeni, M., A. Monti Guarnieri and F. Rocca, 'Estimation and improvement of coherence in SAR-interferograms'. In: *Proceedings International Geoscience and Remote Sensing Symposium, Pasadena, California, USA, 8–12 August 1994*, 720–722

Curlander, John C. and Robert N. McDonough, *Synthetic aperture radar: systems and signal processing.* John Wiley & Sons Inc., New York, 1991

Davidson, Gordon W., and Richard Bamler, 'Multiresolution phase unwrapping for SAR interferometry'. *IEEE Transactions on Geoscience and Remote Sensing*, 37 no. 1 (1999), 163–174

ESA (European Space Agency), *SAR design: AMI image mode.* Internet document earth1.esrin.esa.it/ERS1.3.2, 1997

Esteban Fernández, D., P.J. Meadows, B. Schättler and P. Mancini, *ERS attitude errors and its impact on the processing of SAR data.* PDF-document on ESA internet site and on
131.176.49.1/ceos99/papers/p027.pdf, 1999

Feynman, Richard P., Robert B. Leighton and Matthew Sands, *The Feynman lectures on physics.* Addison Wesley, Reading, Massachusetts, 1963

Fitch, J. Patrick, *Synthetic Aperture Radar.* 1988

Gatelli, Fabio, Andrea Monti Guarinieri, Francesco Parizzi, Paolo Pasquali, Claudio Prati and Fabio Rocca, 'The wavenumber shift in SAR interferometry'. *IEEE Transactions on Geoscience and Remote Sensing*, 32 no. 4 (July 1994), 855–865

Gens, R. and J.L. van Genderen, 'Analysis of the geometric parameters of SAR interferometry for spaceborne systems'. *International Archives of Photogrammetry and Remote Sensing*, 31 (B2) (1996), 107–110, 1996a

Gens, Rüdiger and John L. van Genderen, 'SAR Interferometry – Issues, techniques, applications'. *International Journal of Remote Sensing*, 17 (1996), 1803–1835, 1996b

Geudtner, Dirk, *Die interferometrische Verarbeitung von SAR-Daten des ERS-1*, English translation *The interferometric processing of ERS-1 SAR data.* Deutsche Forschungsanstalt für Luft- und Raumfahrt, Oberpfaffenhofen, August 1995

Geudtner, D., P.W. Vachon, K.E. Mattar and A.L. Gray, 'RADARSAT repeat-pass SAR interferometry'. In: *Proceedings International Geoscience and Remote Sensing Symposium*, 1998, 1635–1637

Goldstein, Richard M., Howard A. Zebker and Charles L. Werner, 'Satellite Radar Interferometry: Two-dimensional Phase Unwrapping'. *Radio Science* 23 no. 4 (1988), 713–720

Goldstein, Richard M. and Charles L. Werner, 'Radar interferogram filtering for geophysical applications', *Geophysical research letters*, 25 no. 21 (1 November 1998), 4035–4038

Hanssen, Ramon F., and Roland Klees, 'Applications of SAR interferometry in terrestrial

and atmospheric mapping'. In: *Workshop proceedings of the 28th European Microwave conference. Remote sensing technology: the sensor to application chain. Amsterdam, 9 October 1998* (ISBN 90-804551-1-3), Amsterdam, 1998

Hanssen, Ramon and Richard Bamler, 'Evaulation of interpolation kernels for SAR interferometry'. *IEEE Transactions on Geoscience and Remote Sensing*, 37 no. 1 (January 1999), 318–321

Hanssen, Ramon F., Tammy M. Weckwerth, Howard A. Zebker and Roland Klees, 'High-resolution water vapor mapping from interferometric radar measurements'. *Science*, 283 (26 February 1999), 1297–1299

Hanssen, Ramon, Ilona Weinreich, Susanne Lehner and Ad Stoffelen, 'Tropospheric wind and humidity derived from spaceborne radar intensity and phase observations'. *Geophysical research letters*, 27 no. 12 (15 June 2000), 1699–1702, 2000a

Hanssen, Ramon, *Radar interferometry: Data interpretation and error analysis.* PhD thesis, Delft University of Technology, 2000b (in preparation)

Hartl, P., S. Usai and R.F. Hanssen, *SAR interferometry.* Lecture notes, Delft, April 1996

Hecht, Eugene and Alfred Zajac, *Optics.* Addison-Wesley, Reading, 1974

Jakowatz jr., Charles V, Daniel E. Wahl, Paul H. Eichel, Dannis C. Ghiglia and Paul A. Thompson, *Spotlight-mode synthetic aperture radar: a signal processing approach.* Kluwer, Dordrecht, 1996

Just, Dieter and Richard Bamler, 'Phase statistics of interferograms with applications to synthetic aperture radar'. *Applied Optics*, 33 no. 20 (1994), 4361–4368

Kampes, B.M, personal communication, 2000

Lee, Jong-Sen, Konstantino P. Papathanassiou, Thomas L. Ainsworth, Mitchell R. Grunes en Andreas Reigber, 'A new technique for noise filtering of SAR interferometric phase images. *IEEE Transactions on Geoscience and Remote Sensing*, 36 no. 5 (September 1998), 1456–1465

Li, Fuk K. and R.M. Goldstein, 'Studies of multibaseline spaceborne interferometric synthetic aperture radars'. *IEEE Transactions on Geoscience and Remote Sensing*, 28 (1990), 88–97

Lillesand, Th.M. and R.W. Kiefer, *Remote Sensing and Image Interpretation.* John Wiley & Sons Inc., New York, 1994

Massonnet, D., M. Rossi and F. Adragna, 'CNES general purpose SAR correlator'. *IEEE Transactions on Geoscience and Remote Sensing*, 32 (1994), 636–643

Massonnet, Didier and Kurt L. Feigl, 'Radar interferometry and its application to changes in the earth's surface'. *Reviews of geophysics*, 36 no. 4 (November 1998), 441–500

Mitra, Sanjit K., *Digital signal processing. A computer based approach.* McGraw-Hill Series in Electrical and Computer Engineering, New York, 1998

Monti Guarnieri, A. and Claudio Prati, 'SAR interferometry: A "quick and dirty" coherence estimator for data browsing'. *IEEE Transactions on Geoscience and Remote Sensing*, 35 no. 3 (May 1997), 660–669

Otten, M.P.G., 'Review of SAR processing techniques'. In: *Workshop proceedings of the 28th European Microwave conference. Remote sensing technology: the sensor to application chain. Amsterdam, 9 October 1998* (ISBN 90-804551-1-3), Amsterdam, 1998

PCI Geomatics, Canada, *Manual PCI Works, Version 6.2, Release date November 1, 1997*. Manual on paper and on-line

Prati, C. and F. Rocca, 'Use of spectral shift in SAR interferometry'. In: *Proceedings second ERS-1 symposium – Space at the service of our environment, Hamburg, Germany, 11–14 october 1993* (January 1994), 691–696

Prati, C. and F. Rocca, 'Improving slant-range resolution with multiple SAR surveys'. *IEEE Transactions on Aerospace and Electronic Systems*, 29 no. 1 (January 1993), 135–144

Rabiner, Lawrence R. and Bernard Gold, *Theory and applications of digital signal processing*. Prentice Hall, Englewood Cliffs, 1975

Rodriquez, E. and J.M. Martin, 'Theory and design of interferometric synthetic aperture radars'. In: *IEE Proceedings, part F (Radar and signal processing)*, 139 no. 2 (1992), 147–159

Rosich, B., D. Esteban, G. Emiliani, P. Meadows, B. Schättler and R. Viggiano, *ERS-2 mono-gyro piloting. Impact on ERS-2 SAR data quality and ERS-2 SAR application performance*. ESA-esrin PDF-document earth.esa.int/ers2_1gp_tn.pdf, 22 June 2000

Scarpino, Gabriella (ESA helpdesk), personal communication, 2000

Schwäbisch, M. and D. Geudtner, 'Improvement of phase and coherence map quality using azimuth prefiltering: examples from ERS-1 and X-SAR'. *IEEE Transactions on Geoscience and Remote Sensing*, 33 (1995), 205–207

Schwäbisch, Marcus, *Die SAR-Interferometrie zur Erzeugung digitaler Geländemodelle*. Deutsche Forschungsanstalt für Luft- und Raumfahrt, Oberpfaffenhofen, 1995

Small, David, Charles Werner en Daniel Nüesch, 'Baseline modelling for ERS-1 SAR interferometry'. In: *Proceedings International Geoscience and Remote Sensing Symposium*, 1993, 1204–1206

Solaas, G. and H. Laur, *An assessment of ERS SAR low resolution imagery*. ESA internet document earth1.esrin.esa.it/lori, 1993

Spivak, Michael, *Calculus*. Second edition, Publish or Perish, Inc., Berkeley, 1980

Swart, L.M.Th., *Filtering voor SAR-interferometrie en voorbereidingen voor dijkdeformatiebepaling. Stage bij het Fysisch en Elektronisch Laboratorium van TNO*. Alphen aan den Rijn, February 1999

Touzi, Ridha, Armand Lopes, Jérôme Bruniquel and Paris W. Vachon, 'Coherence estimation for SAR imagery'. *IEEE Transactions on Geoscience and Remote Sensing*, 37 no. 1 (January 1999), 135–149

Usai, Stefania, and Roland Klees, 'SAR interferometry on a very long timescale: a study of the interferomtric characteristics of man-made features'. *IEEE Transactions on Geoscience and Remote Sensing*, 37 no. 4 (July 1999), 2118–2123

Visual Numerics, *IMSL Fortran 90 MP Library*. PDF documentation, 1996; *Math/Library* (Fortran 77). PDF documentation, 1997

Xu, Wei, and Ian Cumming, 'A region-growing algorithm for InSAR phase unwrapping'. *IEEE Transactions on Geoscience and Remote Sensing*, 37 no. 1 (January 1999), 124–134

Zebker, H.A. and J. Villasenor, 'Decorrelation in interferometric radar echoes'. *IEEE Transactions on Geoscience and Remote Sensing*, 3 no. 30 (September 1992), 950–959

Zebker, Howard A., Charles L. Werner, Paul A. Rosen and Scott Hensley, 'Accuracy of topographic maps derived from ERS-1 interferometric radar'. *IEEE Transactions on Geoscience and Remote Sensing*, 32 no. 4 (July 1994), 823–836

Ziemer, Rodger E., William H. Tranter and D. Ronald Fannin, *Signals and systems: continuous and discrete*. Third edition, Macmillan Publishing Company, New York, 1993

A Calculation and representation of spectra

This appendix serves as a basis for the examination of the spectra in range and azimuth in chapter 4. In § A.1 the calculation of spectra with the discrete and fast Fourier transform is discussed. In § A.2 the different ways spectra can be represented are described.

A.1 The discrete and fast Fourier transform

Information on the frequency distribution of a signal in time or space $x(t)$ can be presented in the *spectrum*. A spectrum can be calculated with the *Fourier transform*, resulting in the frequency distribution $X(f)$, of which in turn the time distribution of the signal can be reconstructed. The Fourier transform is the pair

$$X(f) = \int_{-\infty}^{\infty} x(t)e^{-2\pi ift} \, dt, \tag{A.1}$$

$$x(t) = \int_{-\infty}^{\infty} X(f)e^{2\pi ift} \, df. \tag{A.2}$$

In practice, signals continuous in time are sampled with the sampling frequency f_s, resulting in a time series x_n. The *sampling theorem of Shannon* states that a bandlimited signal $x(t)$, that contains no frequency components above f_h Hertz, is completely specified by samples that are taken at a uniform rate greater than $2f_h$ Hertz,

$$f_s > 2f_h. \tag{A.3}$$

The frequency $2f_h$ is known as the *Nyquist rate* (Ziemer et al., 1993). If the sampling frequency is chosen too low ($f_s < 2f_h$), this *undersampling* has the effect of *aliasing*, treated in § C.2.

The Fourier transform for discrete-time signals is

$$X_k = \sum_{n=0}^{N-1} x_n e^{-2\pi ink/N}, \qquad k = 0, 1, \ldots, N-1, \tag{A.4}$$

$$x_n = \frac{1}{N} \sum_{k=0}^{N-1} X_k e^{2\pi ink/N}, \qquad n = 0, 1, \ldots, N-1. \tag{A.5}$$

Equation (A.4) is known as the *discrete Fourier transform* or DFT and equation (A.5) is known as the *inverse discrete Fourier transform*. For the calculation of the DFT, we write equation (A.4) as

$$X_k = \sum_{n=0}^{N-1} x_n W_N^{nk}, \qquad k = 0, 1, \ldots, N-1, \tag{A.6}$$

with

$$W_N = e^{-2\pi i/N}. \tag{A.7}$$

For an N-point DFT, the value of W_N^k is calculated for $k = 1 \ldots N$. These values are calculated prior to the calculation of the DFT. For example, for $N = 4$ we calculate $W_N^{N/4} = -i$, $W_N^{N/2} = -1$ and $W_N^{3N/4} = i$. For the calculation of equation (A.6), these are taken to the power n for $n = 0, \ldots, N-1$ and the sum can be calculated.

The calculation of the DFT for large sums can be very time consuming. By calculating sums that several terms have in common first, a much faster algorithm can be developed. In the DFT, the terms can be reordered, so that in the first step only W_2^k is needed and in the second step W_4^k is needed. The 4-point DFT starts with two 2-point DFTs and the second step contains only one fourth of the steps of a full 4-point DFT. In this way, by reordering terms and recursion, a very efficient algorithm can be developed, that is known as the *fast Fourier transform* or FFT (Ziemer et al., 1993; Brigham, 1974; Bracewell, 1978).

The greater the number N, the faster the FFT-algorithm compared to the DFT. For a fast Fourier transform over 2048 points (the number we used), the number of real multiplications is 372 times less than needed for the discrete Fourier transform (Ziemer et al., 1993).

Numerical libraries are available with very efficient implementations of the FFT and its inverse counterpart, the IFFT. In most implementations, use is not restricted to N being powers of two, but to al numbers that can be written as multiples of two, three and five (see for example for Power Macintosh: Visual Numerics, 1996).

A.2   Graphical representation of spectra

If the number of samples of the signal $x(t)$ is N, i.e., we have $x_n, n = 0, \ldots, N-1$, the number of points of the spectrum is also N, in this case $X_k, k = 0, \ldots, N-1$, according to equation (A.4). In this equation, the frequency is $f_k = k/N$. The lowest frequency contained in the series is $f_0 = 0$ with amplitude $X_0 = \sum_{n=0}^{N-1} x_n$ and that is the total amplitude of the samples. The highest frequency is $f_{N-1} = (N-1)/N$ with amplitude X_{N-1} and $W_N^{N-1} = e^{-2\pi i(N-1)/N}$. These frequencies are with respect to the time series with unspecified, i.e., unit interval.

In practice, the sampling rate is f_s instead of one; the frequencies mentioned above must be multiplied with f_s. This can also be stated in terms of the bandwidth of the signal. Because the Fourier transform of the sampling time interval $t_s = 1/f_s$ is the bandwidth B_s of the sampled signal, this bandwidth is the sampling frequency,

$$B_s = f_s. \tag{A.8}$$

(Often the actual bandwidth of the signal is less than the sampling frequency allows. The signal is then slightly oversampled.) The highest frequency occurring in the spectrum is

thus $f_{N-1} = \frac{N-1}{N} f_s$. Indeed, most implementation of the fast Fourier transform present a spectrum with frequencies $f = 0, \frac{1}{N} f_s, \ldots, \frac{N-1}{N} f_s$, as in (A.4).

Other representations of the spectrum are possible. For W_N (equation A.7), because

$$e^{-2\pi i m} = 1, \qquad m \in \mathbb{Z}, \tag{A.9}$$

the following holds:

$$W_N^k = e^{-2\pi i k/N} = e^{-2\pi i(k+mN)/N} = W_N^{k+mN}, \qquad m \in \mathbb{Z}. \tag{A.10}$$

The spectrum therefore is not unique, but is replicated to both positive and negative frequencies; each *replica* has the width of the sampling frequency f_s. Therefore, the DFT in equation (A.4) can equivalently be written as

$$X_k = \sum_{n=0}^{N-1} x_n W_N^{nk}, \qquad k = -N/2, -N/2 + 1, \ldots, N/2 - 1. \tag{A.11}$$

In this representation of the DFT, the frequency runs from $f_{-N/2}$ to $f_{N/2-1}$ or for signals with sampling frequency f_s,

$$-\tfrac{1}{2} f_s < f < (\tfrac{1}{2} - \tfrac{1}{N}) f_s, \tag{A.12}$$

mostly approximated as

$$-\tfrac{1}{2} f_s < f < \tfrac{1}{2} f_s. \tag{A.13}$$

A drawing of a spectrum ranging from $-f_s/2 < f < f_s/2$ thus is equivalent with a drawing with $0 < f < f_s$. We will use the first, with positive and negative frequencies, although most of the numerical libraries we had to our disposal calculate the latter.

Both representations of a spectrum seem to violate the sampling theorem of Shannon (§ A.1), which stated that to prevent aliasing, the highest frequency in the signal f_h must be less or equal to half the sampling frequency f_s (equation A.3). If this condition is fulfilled, one would expect half the bandwidth of the spectrum to remain empty, but this is not the case.

As stated in § C.1, a real signal with frequency f can be thought of as the resultant of two complex phasors with frequencies f and $-f$ (equation C.1). Because the radar signal contains amplitude and phase information, it is represented in complex form in the single look complex (SLC) images. It thus contains positive and negative frequencies as in equation (A.13), so that the Nyquist condition of equation (A.3) is met. The bandwidth is indeed $B_s = f_s$.

The spectra of the complex SLC data are complex (equation A.11). To draw them, in this thesis we take their amplitude or modulus $|X_k|$,

$$X_k = |X_k| e^{2\pi i \angle(X_k)}. \tag{A.14}$$

B Alternative derivations of the fringe frequency

In this appendix two alternative derivations of the range frequency shift Δf_r or fringe frequency are given for the derivation in § 5.2.2, that considers the wavenumber k. In § 2.4, a fourth derivation is presented, that uses the interferometer geometry.

The first derivation presented here is a variant of Geudtners (1995) derivation. We use (figure 5.3)

$$\theta_2 = \theta_1 - \Delta\theta \tag{B.1}$$

and approximate the sine,

$$\begin{aligned}
\sin\theta_2 &= \sin(\theta_1 - \Delta\theta) \\
&= \sin\theta_1 \cos\Delta\theta - \cos\theta_1 \sin\Delta\theta \\
&\approx \sin\theta_1 - \Delta\theta\cos\theta_1.
\end{aligned} \tag{B.2}$$

Consider the frequency shift of the object spectrum as the difference in ground frequency, and use the approximation equation (B.2),

$$\begin{aligned}
\Delta f_g = f_{g_2} - f_{g_1} &= \frac{2c}{\lambda_0}(\sin\theta_2 - \sin\theta_1) \\
&\approx -2f_0\Delta\theta\cos\theta_1.
\end{aligned} \tag{B.3}$$

This object frequency shift has to be projected back into the viewing direction of the satellite, so that the range frequency shift becomes with equation (5.6)

$$\Delta f_r = \frac{\Delta f_g}{2\sin\theta_1} = -\frac{f_0}{\tan\theta_1}\Delta\theta, \tag{B.4}$$

which is equivalent to equation (5.11), derived in § 5.2.2.

In an alternative derivation, the change in range frequency f_r due to a change in incidence angle θ is considered. Because the relations between ground range and slant range is a geometrical one, the derivation uses wavelength rather than frequency; if frequency would be used, the sign would be opposite. We also use equation (5.6). We write

$$\begin{aligned}
\frac{\Delta f_r}{\Delta\theta} &= \frac{d}{d\theta}\frac{c}{\lambda_r} = \frac{d}{d\theta}\frac{c}{2\lambda_g\sin\theta} \\
&= \frac{c}{2\lambda_g}\cdot -\frac{\cos\theta}{\sin^2\theta} = -\frac{c\cos\theta}{\lambda_r\sin\theta} \\
&= -\frac{f_0}{\tan\theta},
\end{aligned} \tag{B.5}$$

where the monochromatic approximation of f_r by f_0 was substituted. This is equivalent to equations (B.4), (5.11) and (2.31), derived before.

C Sampling and oversampling experiments

In this appendix, sampling and oversampling is demonstrated for cosine signals. It serves as a basis for the discussion on oversampling for interferometry in chapter 6.

In § C.1, the spectrum of two cosines and their product is discussed. If the sampling frequency is too low, aliasing and undersampling occurs; this is demonstrated in § C.2. Aliasing can be eliminated by oversampling the original signals, discussed in § C.3. The result of oversampling and undersampling in the time domain shows that if the signals must be interpolated, oversampling is necessary (§ C.4). Also the effect of filtering the resulting spectrum, so that it can be downsampled to the original sampling density, will be demonstrated (§ C.5).

C.1 Complex spectrum of two cosines and their product

A cosine is a real function, but this does not complicate the demonstration of aliasing and oversampling for complex signals, like single look complex (SLC) SAR images. A cosine can be thought of as the resultant of two phasors of equal length but rotating in the complex plane in opposite direction (Ziemer et al., 1993). (A *phasor* is a complex vector considered as an arrow with certain length and phase.) The resultant always projects on the real axis. A cosine with amplitude A and frequency f consists of two phasors with amplitude $A/2$ and frequency f and $-f$, which is also shown by

$$A\cos(2\pi f t) = \frac{A}{2}\Big(e^{2\pi i f t} + e^{-2\pi i f t}\Big). \qquad (\text{C.1})$$

(Spivak, 1980). The complex spectrum of equation (C.1) can be calculated with the Fourier transform (§ A.1). If the spectrum is presented with positive and negative frequencies, as discussed in § A.2, the spectrum shows peaks on frequencies f and $-f$. This is illustrated in figure C.1a, where the amplitude of the complex spectrum of a cosine with a frequency of $f = 16$ Hertz is plotted by taking the modulus.

In a simulation, during one second we take samples of two cosine signals with a frequency of 16 and 24 Hertz, respectively. The signals are sampled with a sampling frequency $f_s = 128$ Hz. Now we calculate the interferogram of both cosines by multiplication of the samples of the 'master' with the complex conjugate of the samples of the 'slave'. Because

$$A\cos(2\pi f_1 t)\cos(2\pi f_2 t) = \frac{A}{2}\Big(\cos\{2\pi(f_1 - f_2)t\} + \cos\{2\pi(f_1 + f_2)t\}\Big), \qquad (\text{C.2})$$
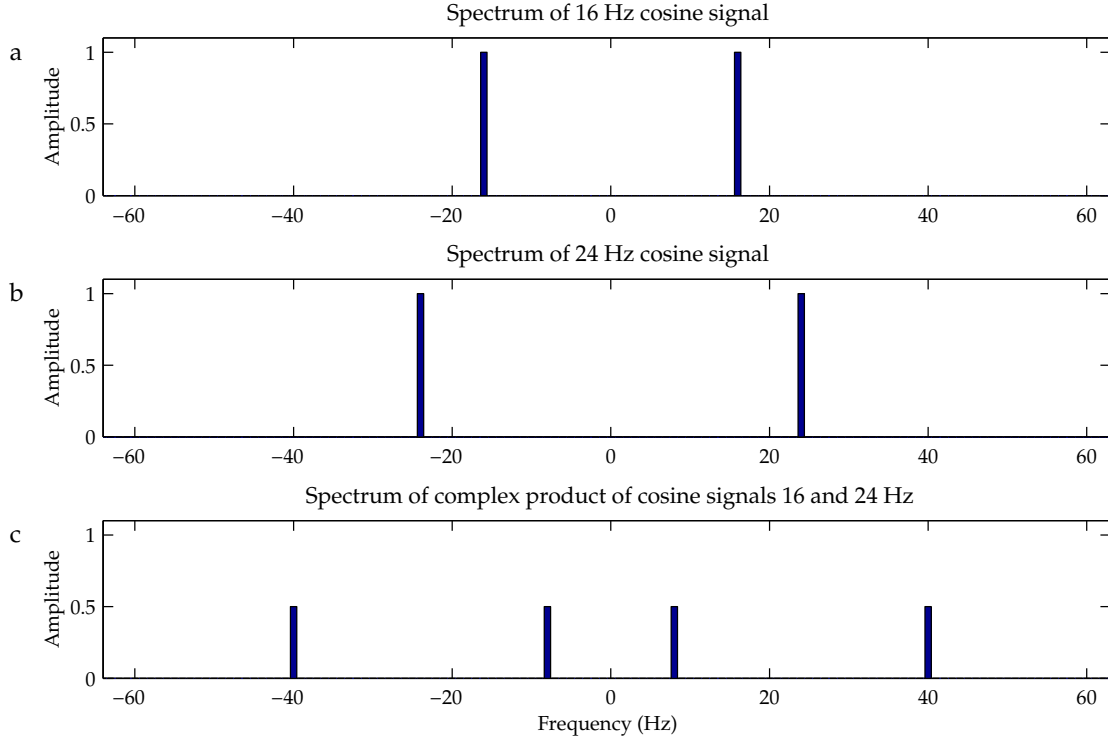
Figure C.1   The complex spectrum of a cosine of 16 Hz consists of two components: one on 16 and one on −16 Hz (figure a). Here the modulus of the complex spectrum is shown. The product of cosine signals of 16 (a) and 24 (b) Hz contains the difference and sum frequency, according to equation (C.2): 8 and 40 Hz (figure c). The amplitude of the spectral components is halved, because the power is distributed over twice as much channels.

in the interferogram the difference and the sum of the frequencies in the individual signals are present. In figure C.1a and b, the amplitude of the spectrum of the 16- and 24-Hertz cosines is shown. Figure C.1c shows the spectrum of the interferogram; indeed only frequencies of 8 and 40 Hz are present. The amplitude of the spectral components of the original signals is halved, as the above formula shows but also can be shown by realising that the power, which must be conserved, is now distributed over twice as much channels.

Figure C.1 also shows that multiplication in the time domain is equivalent to convolution in the spectral domain (Ziemer et al., 1993). Convolution of figure C.1a with b results in c.

Figure C.2 shows the original and resulting signals in the time domain; figure C.3 shows what an amplitude map would look like. In the product signal indeed a high frequency oscillation is visible superposed on a low frequency.

C.2   Aliasing and undersampling

As known from the sampling theorem of Shannon, the highest frequency in a signal that can be reconstructed after sampling the signal, is half the sampling frequency f_s. This frequency is called the *Nyquist frequency*,

$$f_{\text{Nyq}} = f_s/2. \tag{C.3}$$

This can be made clear by considering a cosine: its oscillating character can only be
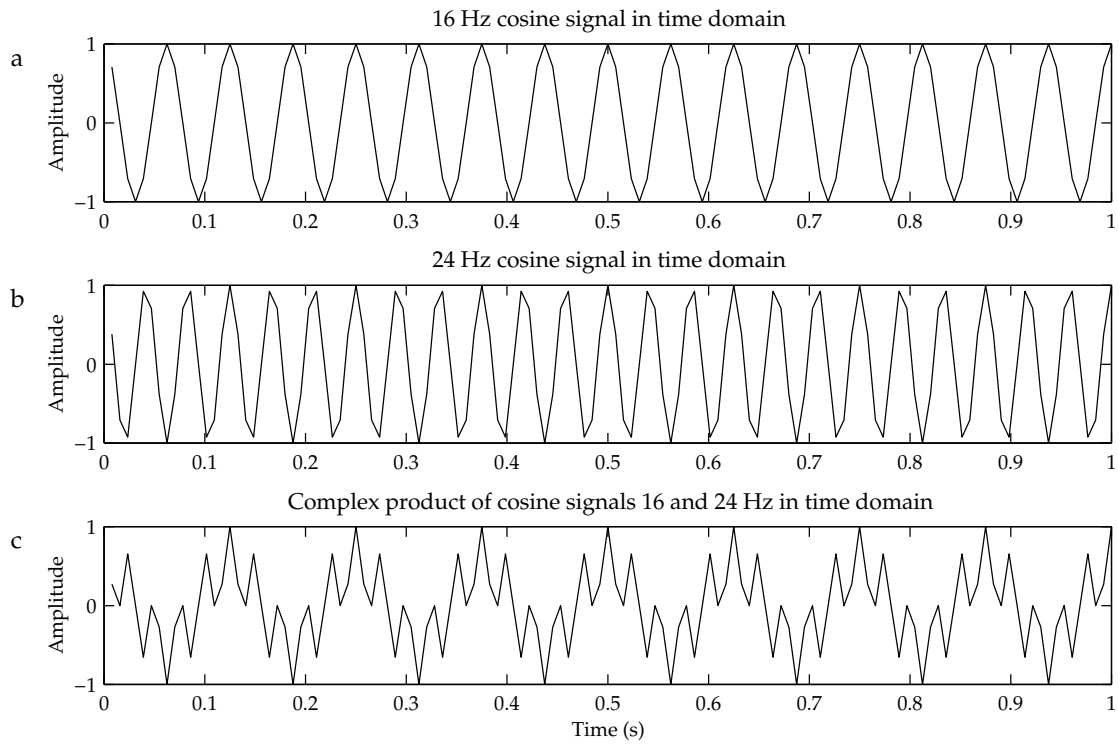
Figure C.2   The cosine signals of 16 (a) and 24 (b) Hz in the time domain and their product (c), showing the difference and sum frequencies.
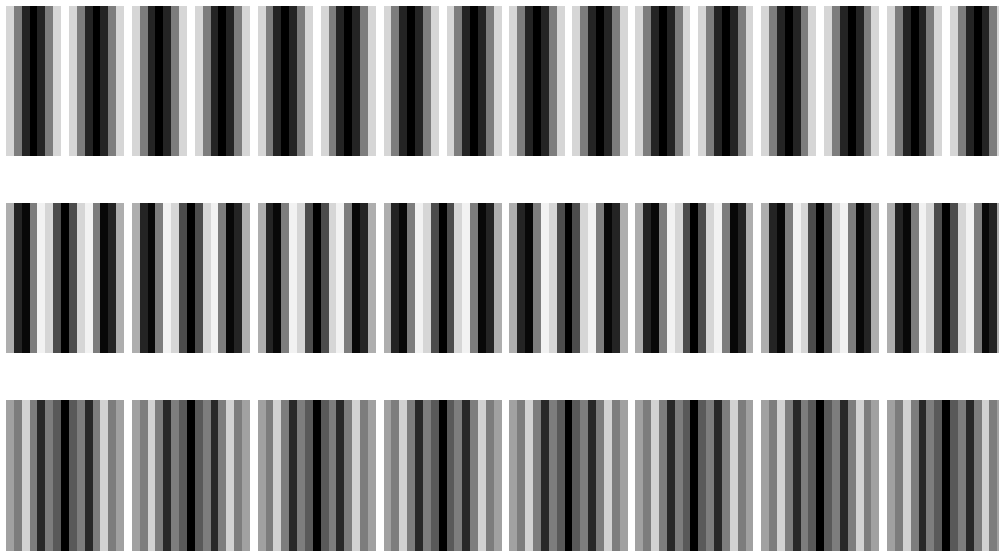

Figure C.3   The cosine signals of 16 (a) and 24 (b) Hz in the time domain and their product (c), visualised as an amplitude image.

reconstructed if at least two samples per cycle are taken. In the simulation, the sampling frequency was 128 Hz, so that the Nyquist frequency is 64 Hz.

Now we take two cosines with frequencies almost as high as the Nyquist frequency, 50 and 52 Hz. Both signals can thus be reconstructed from their samples. Their spectrum is shown in figure C.4a and b. According to equation (C.2), the interferogram should show the difference component on 2 Hz and the sum component on 102 Hz. This is not what happens, as figure C.4c shows.

Before we can understand what happens, we need some extra knowledge. Samples taken with rate f_s can be used to reconstruct the original signal with frequency f_0, with $f_0 < f_{\mathrm{Nyq}}$. However, if a signal with frequency $f_1 = f_0 + k f_s$ ($k \in \mathbb{Z}$) is sampled with frequency f_s, the same samples result, as a simple drawing can show. Therefore a discrete spectrum is not unique, but has replicas on multiples of the sampling frequency f_s. This is discussed in § A.2.

In our example, the sum frequency of 102 Hz is higher than the Nyquist frequency and can not be contained in the central spectrum. Instead, this frequency falls into the next replica of the spectrum. Because the spectrum is not unique, the frequency of $f_0 = 102$ Hz is also folded in the frequency band of the central spectrum on a frequency of $f_0 - f_s = 102 - 128 = -26$ Hz. Because a cosine has an even spectrum, also a component on +26 Hz occurs, as figure C.4c shows. This process is called *aliasing*.

In short, aliasing occurs because the sampling frequency is too low to let the spectrum contain a certain high frequency. Aliasing is a result of *undersampling*.

C.3   Oversampling

Aliasing can be avoided by increasing the sampling frequency to fulfil te Nyquist criterion: it must be twice as high as the highest frequency contained in the signal.

Because the interferogram can theoretically contain frequencies twice as high as present in the master and slave radar image, the frequency with which the images have been sampled, must be doubled in order to prevent aliasing from happening while calculating the complex product of the images. However, the sampling rate of the radar images has already been chosen by the radar signal processing facility. How can we double the sampling frequency?

The original master and slave radar image consist in a certain direction of, say, n sampling points. The Fourier transform yields the spectrum, that also has n points or *channels*. The increasing of the sampling frequency, or *oversampling*, can be performed by taking the spectrum and adding zeros to the high frequency bands. This is called *zero padding*. Because we want to double the sampling frequency, we add $n/2$ zeros to the left of the negative frequencies and $n/2$ zeros to the right of the positive frequencies. If we Fourier transform the spectrum back to the time domain, we have an image of $2n$ points that is called to be *harmonically interpolated*. Oversampling is indeed a way of interpolation.

There is however a complication. A complex spectrum of n samples contains negative frequencies in channels $-n/2$ to -1 and positive frequencies in channels 0 to $n/2 - 1$. For a real signal like a cosine, channel i is equal to channel $-i$. However, frequency $-n/2$ exists, but $n/2$ does not. The amplitude of channel $-n/2$ therefore turns out to be twice what it would be if $n/2$ would be present. If oversampling is performed, after expanding the number of samples to $2n$, the amplitude of channel $-n/2$ should halved and the amplitude of the newly added channel $n/2$ should be set to the same value.
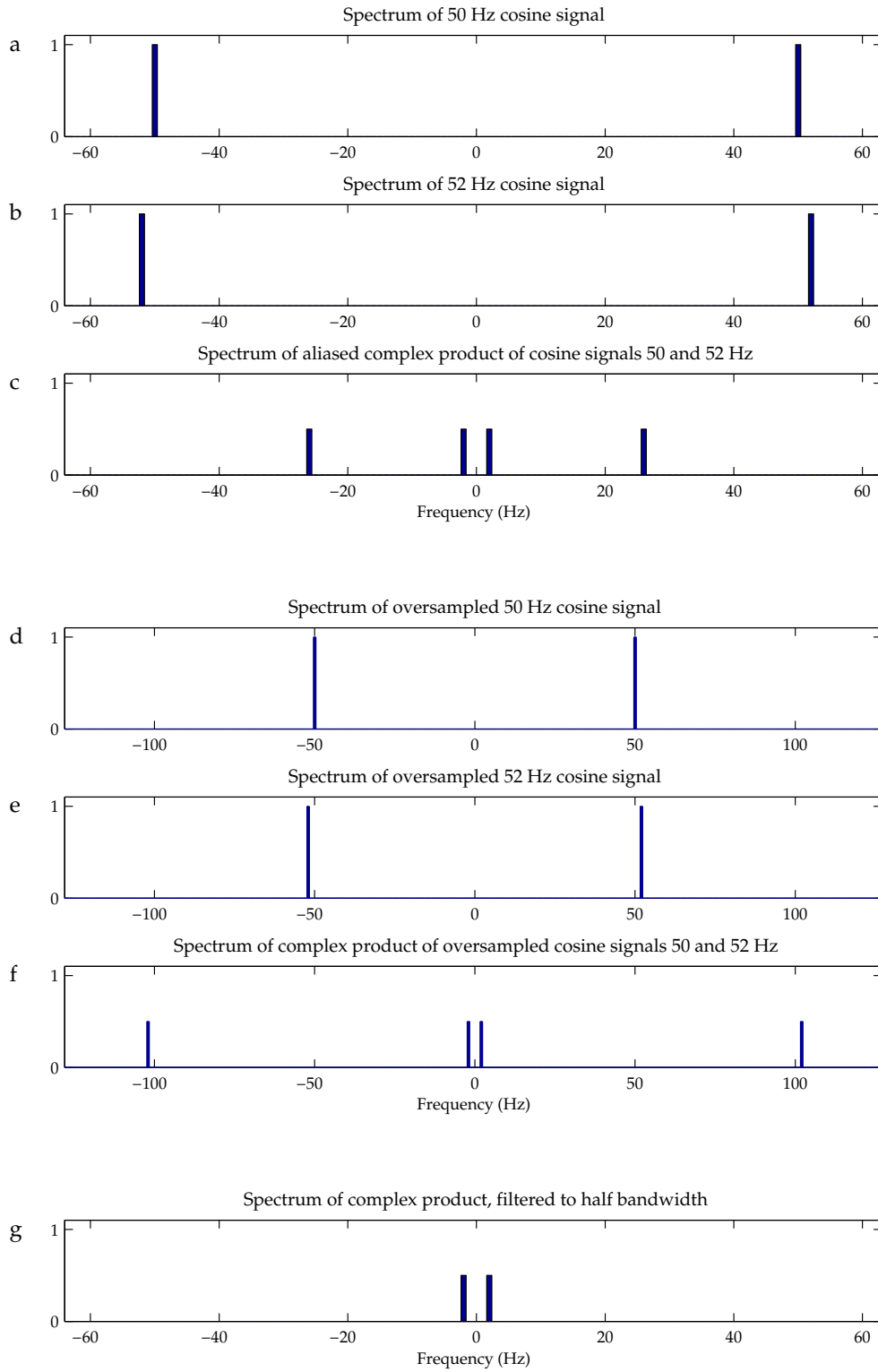
Figure C.4 The interferometric spectrum (c) of the cosine signals of 50 and 52 Hz (a, b) shows the difference frequency of 2 Hz, but not the sum frequency of 102 Hz. Instead, an aliased frequency of $102 - 128 = -26$ Hz (and 26 Hz) is shown. If the original signals are oversampled (d, e), the spectrum of the product does show the sum frequency of 102 Hz (f). If the bandwidth has to be limited to that of the original signals, the sum frequency can now be filtered out (g) and the spectrum can be downsampled.

In figure C.4 the second triple of plots shows the results of oversampling. The original sampling frequency of 128 Hz is doubled to 256 Hz, thereby increasing the maximum frequency that can be contained in the spectral band to the new Nyquist frequency of 128 Hz. The multiplication of the first image with the complex conjugate of the second image yields an interferogram with $2n$ points with a spectrum of $2n$ points. Now the sum frequency of 102 Hz can be contained in the spectrum and aliasing does not occur.

Figure C.5a shows the aliased product of the cosines of 50 and 52 Hz in the time domain. The sum frequency of 102 Hz is aliased to 26 Hz and is superposed on the difference frequency of 2 Hz. If we oversample, the aliasing frequency of 26 Hz has disappeared and the much higher difference frequency of 102 Hz now becomes visible (figure C.5b).

C.4   Oversampling in the time domain and interpolation

In the previous section, the need for oversampling in the spectral domain was discussed. In this section, the time domain is considered.

In figure C.6, the first 0.25 seconds of the interferogram of the 50 and 52 Hz cosines is plotted in the time domain, both for the original and oversampled signals. The interferogram signals coincide on the original n sampling points. This comes to no surprise, as the calculation of the interferogram consists of the pointwise product of the two signals, which does not introduce errors. Therefore, if the interferogram is only needed on the original n sampling points, oversampling is not necessary. The interferogram contains too few points to show errors due to the aliasing that is present in the spectrum.

As figure C.6 shows, the product of the oversampled signals – consisting of $2n$ points – does not coincide with the product of the not-oversampled signals on the n points between the n original points. As soon as the product (the interferogram) must be evaluated on other points than the original n points, as is the case with *interpolation*, the signals must be oversampled. Aliasing would otherwise result in erroneous results.

Indeed, as discussed in § C.3, the product of the not-oversampled signals is not showing the high frequency present in the product of the oversampled signals, because the sampling rate is too low to follow this high frequency signal.

C.5   Downsampling

For one reason or another, one could want an interferogram only with frequencies limited to the original bandwidth of the input signals. In paragraph C.2 was shown that processing the not-oversampled images yields aliasing and is not the way to go to limit the product bandwidth and image size.

Instead, master and slave image should be oversampled and after calculation of the interferogram, an interferogram can be obtained with the same sampling frequency as the constituent images. Therefore a lowpass filter is applied on the spectrum of the product that filters all frequencies above the original Nyquist frequency out.

In figure C.4f the spectrum of the interferogram of the oversampled master and slave images are shown. With the lowpass filter all frequencies above 64 Hz are filtered out. The resulting bandwidth now is so small that we are able to remove the high frequency bands, which do not contain signal any more due to the lowpass filtering. In figure C.4f
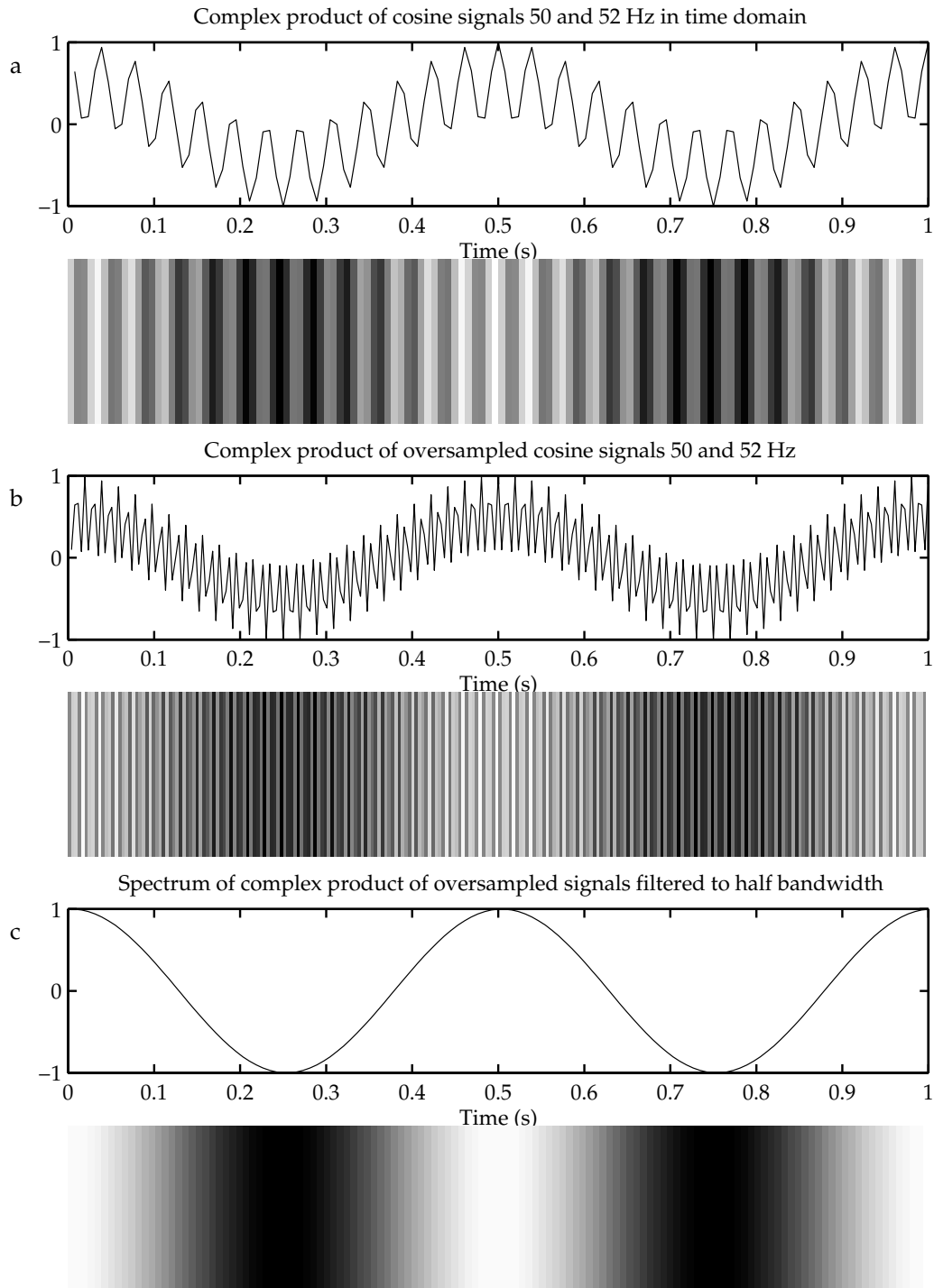
Figure C.5   In figure a, the aliased product of the cosines of 50 and 52 Hz during 1 second in the time domain is drawn. The sum frequency of 102 Hz is aliased to 26 Hz and is superposed on the difference frequency of 2 Hz. If the original 50 and 52 Hz signals are oversampled, in the product signal (figure b) the aliasing frequency of 26 Hz has disappeared and the much higher difference frequency of 102 Hz now becomes visible. After filtering the high sum frequency out, the product signal can be downsampled, leaving only the difference frequency of 2 Hz, without aliased components, as shown in c. If the filtering would be performed on the aliased signal, the 26 Hz signal would still be present.

Product of oversampled and not oversampled signal and filtered product

Figure C.6   The first 0.25 seconds of the products of the original and oversampled signals of figure C.5 are shown here in the time domain. Both product signals (interferograms) coincide on the original n sampling points. If no interpolation is necessary, oversampling is not necessary. If the interferogram is considered with more detail than on the original n points, the undersampling results in the development of a low frequency (drawn dashed) because the sampling rate 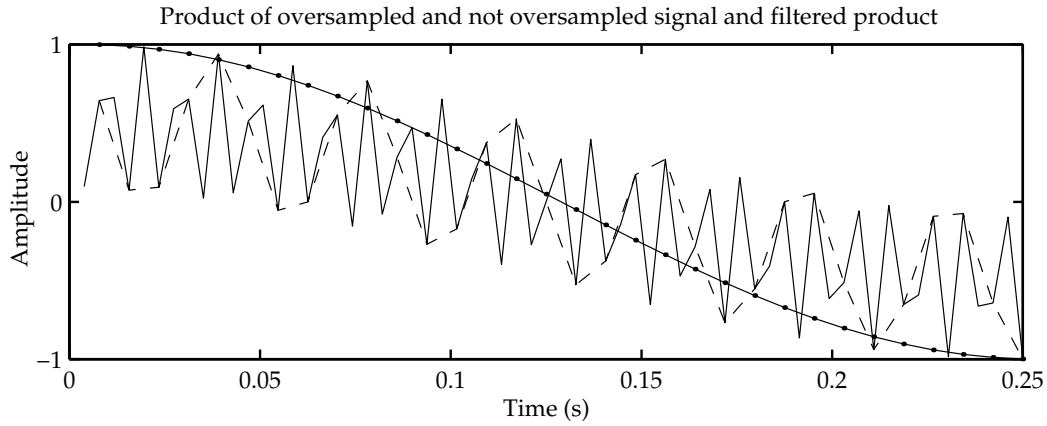is too low to follow the high frequency signal (drawn solid). After filtering the high frequency band from the oversampled spectrum, only the low frequency remains and this can be downsampled to the original n points (drawn solid with evaluation points).

the interferometric spectrum consists of $2n$ points with $n = 128$, because the sampling frequency of the constituent images was 256 Hz, due to the oversampling. After filtering the high frequency bands still exist but do not contain any signal. We now remove n channels, $n/2$ both at positive and negative frequency side. The result is shown in figure C.4g, were the bandwidth is limited and only the 2 Hz spectral components are present.

This process is essentially the opposite of zero padding, described in § C.3. It is called *downsampling*, because if the spectrum is inverse Fourier transformed to the time domain, a signal results that is sampled with half the sampling frequency of the interferogram. Figure C.5c now shows in the time domain a low frequency signal with only the 2 Hz difference frequency.

D Dutch terminology for radar interferometry

Many people in the Netherlands are involved in radar interferometry. As all Dutch scientists, they speak Dutch, whether they are discussing radar interferometry topics or not. However, more than often scientific discussions sound like a strange mixture of Dutch and English. Most scientists appear to restrict their creativity to science and do not extend it to their language skills. To keep it on the expected academic level, discussions on scientific subjects should be in Dutch. So, *if you speak Dutch, please speak Dutch.* This list of radar interferometry and signal processing terminology may serve as a help. The Dutch language rules for the concatenation of words – which provide no choices – are applied.

synthetic aperture radar	apertuursyntheseradar (beter dan synthetische-apertuurradar)
synthetic aperture radar interferometry	apertuursyntheseradarinterferometrie
baseline	basislijn
perpendicular	loodrecht
range	afstand
azimuth	azimuth
slant range	zichtlijn, schuine afstand
ground range	grondafstand, grondrichting
footprint	voetafdruk
ground track	grondspoor
swath	zwad
side-looking	opzij kijkend
attitude maintenance	standregeling
corner reflector	hoekreflector
processing	verwerking
chirp	tsjilp
pulse repetition frequency	pulsherhalingsfrequentie
bandwidth	bandbreedte
transfer function	overdrachtsfunctie
Doppler centroid frequency	Dopplercentroïdefrequentie
sidelobes	zijlussen
tapered	aflopend
lowpass filter	laagdoorlaatfilter
power	vermogen

power spectral density	spectrale vermogensdichtheid
fringe	band, faseband, letterlijk: franje
phase unwrapping	fase uitpakken, oplossen van de fasemeerduidigheid
phase ambiguity	fasemeerduidigheid
scattering	verstrooiing
speckle noise	spikkelruis
windowing	(venster)weging
pedestal (level)	voetstuk(niveau)
shift	verschuiving
bias	onzuiverheid
estimator	schatter
sample	monster
sampling	bemonsteren
resampling	herbemonsteren
undersampling	onderbemonsteren
downsampling	omlaagbemonsteren
aliasing	vouweffect
smooth	versmeren
proceedings	handelingen

E Developed software

In this appendix, the developed software for spectral filtering, coherence calculation and some of its properties are listed in § E.1. Also the main auxiliary software is listed. The way the software operates is illustrated by its parameter files, that are listed in § E.2.

E.1 Developed spectral filtering, coherence calculation and auxiliary software

In Fortran 90, software for the spectral filtering in range and azimuth and for the coherence calculation was developed, plus some auxiliary software. This was done on an Apple Power Macintosh with Absoft's Pro Fortran 6.0 (Absoft, 1999), a package that also permits to use Fortran 90, Fortran 77, C and C++ in one program. As a numerical library IMSL from Visual Numerics was used (Visual Numerics, 1996, 1997). The software was also compiled on a HP-UX workstation.

Several programs contain similar source code, in particular for the Fourier transforms, the listing of sections of the images or spectra on screen, and the writing to disk of sections of the images or spectra or of the complete averaged spectra. Options for writing this and other information to disk were built in in order to monitor the correct performance of the program during its development and to provide data for graphical display.

As the software was developed to devise algorithms and not as production tool, all implemented algorithms are kept in the eventual code. In this way, for example several spline interpolation or approximation schemes can be compared.

Program	lines	description
FilterAzimuth.f90	2088	Determination of the Doppler centroid frequencies of master and slave, calculation of the centroids over range with different approximation schemes and execution of the azimuth filtering. Additionally, a selection of the images or the original or filtered spectra can be showed on screen or written to disk. Spectra of individual azimuth lines or averaged over azimuth can be written to disk, just like the determined Doppler centroids and their different spline approximations. See parameter file in § E.2

FilterRange.f90	1341	Determination of the fringe frequency from the interferogram spectrum, calculated from the oversampled range spectra. As an option, these fringe frequencies can be replaced by a predefined fringe frequency. After this, the range filtering is performed. The program has similar choices as the FilterAzimuth program. See parameter file in § E.2
Coherentie.f90	1087	Calculation of the coherence image and statistics. Coherence can be calculated over shifting or adjacent windows; reference phase can be subtracted. Of the coherence image, a histogram and mean coherence is calculated and a histogram and mean corrected for the coherence estimator bias. See parameter file in § E.2
Referentiefase.f90	339	Calculation of a reference phase image from the parameters supplied by the interferometry software
Berekenspectrum.f90	864	Display a selection of the images or the spectra in range or azimuth on screen or write them to disk. The spectra can be averaged, they can be written complex or as the modulus
ConverteernaarPhotoshop.f90	288	Conversion of real or signed integer single look complex images to an 8-bit integer image with user-defined scaling, for use in Photoshop and as an exercise

E.2   Examples of parameter files

FilterAzimuth

Parameterbestand voor FilterAzimuth.
De naam en het regelnummer zijn cruciaal. Bestandsnamen mogen de gehele
regel innemen; achter andere parameters is ruimte voor toelichting.
Rens Swart * 30 september 1999

1679.902	Pulsherhalingsfrequentie (A-PRF) oftewel totale bandbreedte azimuth in Hz
1378.0	Totale verwerkte bandbreedte azimuth (A-BWA) in Hz
1505	Dopplerfrequentie i.v.m. antennepatroon (Geudtner, f_DOP) in Hz
492.918	Dopplerfrequentie constante term volgens PCI-Works (A-DF1) in Hz (beeld 1)
182.187	Idem, beeld 2
	Bestand met complexe beeld, respectievelijk beeld 1 en beeld 2:
22913	
3240	
g	Bestaat uit vierbyte reële (r) getallen of uit tweebyte gehele (g) getallen zoals SLC-beelden?
r	Idem, beeld 2
2048	Aantal azimuthlijnen
2048	Aantal rangepixels
n	Schrijf deel van beeld naar scherm (j of n)?
n	Schrijf deel van spectrum naar scherm (j of n)?
1092	Zo ja: eerste af te drukken kolom
10	Zo ja: aantal af te drukken kolommen
156	Zo ja: eerste af te drukken rij
10	Zo ja: aantal af te drukken rijen
n	Schrijf bestand met complexe azimuthspectrum? Zo ja, naam:
22913.azimspec.cmplx	
3240.azimspec.cmplx	
n	Schrijf bestand met modulus van azimuthspectrum? Zo ja, naam:
22913.azimspec.intens	

3240.azimspec.intens
n   Schrijf bestand met modulus van DEEL van azimuthspectrum? Zo ja, naam:
22913.azimspec.deel
3240.azimspec.deel
j   Schrijf bestand met gemiddelden van modulus van azimuthspectrum? Zo ja, naam:
22913.azimspec.gemidd
3240.azimspec.gemidd
k   Schrijf deel spectrumlijnen als rijen (r) of als kolommen (k)?
f   Schrijf deel spectrumlijnen geformatteerd (f) of ongeformatteerd/binair (o)?
1   Eerste te schrijven spectrumlijn
64   Aantal te schrijven spectrumlijnen
128   Aantal spectrumlijnen te middelen voor wegschrijven
9999   Aantal stukken spectrum die moeten worden gemiddeld voor wegschrijven
128   Aantal spectrumlijnen te middelen voor bepaling Dopplercentroïde
256   Aantal punten voor bepaling autoconvolutie en paraboolpassing
j   Schrijf bestand met resultaat autoconvolutie? Zo ja, naam:
22913.azimspec.autoconvol
3240.azimspec.autoconvol
j   Schrijf bestand met door autoconvolutie gepaste parabool? Zo ja, naam:
22913.azimspec.pasparabool
3240.azimspec.pasparabool
a   Bepaal positie signaalloze band met maximum autoconvolutie (a) of parabool daardoor (p)?
n   Bepaal centrale Dopplerfrequentie uit bepaalde maximum (j) of uit positie signaalloze band (n)?
n   Schrijf kanaalinformatie waarop berekening Dopplerfrequenties gebaseerd is?
j   Schrijf bestand met bepaalde kanalen Dopplercentroïde en signaalloze band? Zo ja, naam:
22913.azimspec.dopkan
3240.azimspec.dopkan
4   Orde van splines voor Dopplercentroïdeapproximatie (4 = kubisch)
3   Aantal tussenpunten voor Dopplercentroïdeapproximatie
j   Schrijf bestand met geëvalueerde splines voor later gebruik (ongeformatteerd)? Zo ja, naam:
22913.azimspec.splines
3240.azimspec.splines
j   Schrijf bestand met geëvalueerde splines voor grafiek? Zo ja, naam:
22913.azimspec.splinesx
3240.azimspec.splinesx
8   Stap in rangepixels voor wegschrijven evaluatie splines ten behoeve van grafieken tekenen
0.05   Randvoorwaarden spline-approximatie: factor maximale tweede afgeleide op begin en eind
j   Schrijf bestand met de weegfunctie die het filteren voor zijn rekening neemt? Zo ja, naam:
22913_3240.filter
700   Zo ja, van welke kolom moeten de theoretische spectra en de filterfunctie worden afgedrukt?
             De bestanden waarnaar de gefilterde beelden moeten worden weggeschreven
22913.azimgefilterd
3240.azimgefilterd

FilterRange

Parameterbestand voor FilterRange.
De naam en het regelnummer zijn cruciaal. Bestandsnamen mogen de gehele
regel innemen; achter andere parameters is ruimte voor toelichting.
Rens Swart * 26 september 2000

18.96   Bemonsteringsfrequentie f_s oftewel totale bandbreedte range in MHz
15.55   Totale tsjilp-bandbreedte range B_r in MHz
21.422   Kijkhoek beeldmidden (aux-rapport)
19.343   Kijkhoek eerste rangepixel
23.264   Kijkhoek laatste rangepixel
843984   Rangeafstand van referentiepunt 1 in meter (orbcal)
376.590   Loodrechte component basislijn in meter (orbcal)
             Bestand met complexe beeld, respectievelijk beeld 1 en beeld 2:
8040.8
8541.8
g   Bestaat uit vierbyte reële (r) getallen of uit tweebyte gehele (g) getallen zoals SLC-beelden?
r   Idem, beeld 2
2048   Aantal azimuthlijnen
2048   Aantal rangepixels
n   Schrijf deel van beeld naar scherm (j of n)?
n   Schrijf deel van spectrum naar scherm (j of n)?
1   Zo ja: eerste af te drukken kolom
10   Zo ja: aantal af te drukken kolommen

1	Zo ja: eerste af te drukken rij
10	Zo ja: aantal af te drukken rijen
n	Schrijf bestand met complexe rangespectrum? Zo ja, naam:

8040.8.rangespec.cmplx
8541.8.rangespec.cmplx

n	Schrijf bestand met modulus van rangespectrum? Zo ja, naam:

8040.8.rangespec.intens
8541.8.rangespec.intens

n	Schrijf bestand met modulus van DEEL van rangespectrum? Zo ja, naam:

8040.8.rangespec.deel
8541.8.rangespec.deel

j	Schrijf bestand met gemiddelden van modulus van rangespectrum? Zo ja, naam:

8040.8.rangespec.gemidd
8541.8.rangespec.gemidd

f	Schrijf deel spectrumlijnen geformatteerd (f) of ongeformatteerd/binair (o)?
1	Eerste te schrijven spectrumlijn
16	Aantal te schrijven spectrumlijnen
128	Aantal spectrumlijnen te middelen voor wegschrijven
9999	Aantal stukken spectrum die moeten worden gemiddeld voor wegschrijven
32	Aantal interferogramspectrumlijnen te middelen voor bepaling fringefrequentie
8	Aantal blokken in range waarvoor filtering apart moet worden uitgevoerd
5	Aantal spectrumpixels dat moet worden versmeerd voor bepaling maximum
j	Modulus interferogramspectrum per blok gemiddelde lijnen wegschrijven? Zo ja, naam:

8040_8541.8.interfspec

n	Schrijf enkele lijnen van overbemonsterde spectra en interferogramspectrum? Zo ja,
2	aantal te schrijven lijnen per spectrum; bestandsnaam:

8040_8541.8.overbemspectra

n	Schrijf inverse Hammingfilter en nieuwe Hammingfilter (alleen eerste blok)? Zo ja, naam:

8040_8541.8.Hamming

n	Filteren met vaste fringefrequentie i.p.v. bepalen uit interferogram? Zo ja:
-5.96942	Fringefrequentie in MHz (incl. teken), ook ter vergelijking met uit spectrum bepaalde.
j	Als gemeten fringefrequentie te sterk afwijkt, vervangen door vaste? Zo ja:
0.5	Verschil gemeten en gegeven fringefrequentie: daarboven vervangen
j	Filter spectrum meesterbeeld aan negatieve zijde als fringefrequentie positief is?
	De bestanden waarnaar de gefilterde beelden moeten worden weggeschreven:

8040.8.rangegefilterd
8541.8.rangegefilterd

Coherentie

Parameterbestand voor Coherentie
De naam en het regelnummer zijn cruciaal. Bestandsnamen mogen de gehele
regel innemen; achter andere parameters is ruimte voor toelichting.
Rens Swart * 30 september 1999

0	Testparameter: hoe hoger, hoe meer uitvoer
a	Coherentie berekenen over verschuivende (v) of aangrenzende blokken (a)?
	Bestand met complexe beeld, respectievelijk beeld 1 en beeld 2:

24416
4743

g	Bestaat uit vierbyte reële (r) getallen of uit tweebyte gehele (g) getallen zoals SLC-beelden?
r	Idem, beeld 2
2048	Aantal azimuthlijnen
2048	Aantal rangepixels
n	Schrijf deel van beeld naar scherm (j of n)?
j	Schrijf deel van coherentiebeeld naar scherm (j of n)?
j	Schrijf deel van schuivende coherentiebeeld naar scherm (j of n)?
1	Zo ja: eerste af te drukken kolom
15	Zo ja: aantal af te drukken kolommen
1	Zo ja: eerste af te drukken rij
15	Zo ja: aantal af te drukken rijen
j	Schrijf intensiteit originele beelden naar bestand (j of n)? Zo ja, namen:

24416.intens
4743.intens

15	Aantal azimuthlijnen waarover intensiteit bepaald moet worden
3	Aantal rangepixels waarover intensiteit bepaald moet worden
j	Schrijf beeld met interferometrische fase naar bestand (j of n)? Zo ja, naam:

24416_4743.fase

j	Referentiefase aftrekken van interferometrische fase (j of n)?

1	Aantal azimuthlijnen waarover interferometrische fase bepaald moet worden
1	Aantal rangepixels waarover interferometrische fase bepaald moet worden
j	Van interferometrische fase deel van beeld schrijven i.p.v. geheel? Zo ja:
200	Aantal te schrijven fasepixels in azimuth
400	Aantal te schrijven fasepixels in range
n	Schrijf beeld met referentiefase naar bestand (pix=1,1) (j of n)? Zo ja, naam:

24416_4743.reffase
j   Schrijf coherentiebeeld naar bestand (j of n)? Zo ja, naam:
24416_4743.coh
f   Schrijf coherentiebeeld ruw (r) of geformatteerd (f)?
      Bestand met histogram coherentie
24416_4743.coh.his
      Bestand met voor zuiverheid gecorrigeerde coherentie (1 waarde voor elk histograminterval)
Coherentieonzuiverheid73

60	Aantal azimuthlijnen waarover coherentie bepaald moet worden
12	Aantal rangepixels waarover coherentie bepaald moet worden
3	Indien testparameter /= 0: aantal coherentieblokken in azimuth
15	Indien testparameter /= 0: aantal coherentieblokken in range
100	Aantal intervallen histogram
j	Minimum op 0 en maximum op 1 zetten bij maken histogram?
j	Ellipsoïdefase (referentiefase) aftrekken voor berekening coherentie?
5	Zo ja: orde. Aantal coëfficiënten moet (orde + 1) * (orde + 2) / 2
1400	Polynoom is t.o.v. (0,0). Verschuiving dit deelbeeld over azimuthlijnen
400	Idem: verschuiving dit deelbeeld over rangepixels
j	Fase negatief nemen? (PCI: neg)

5.78753055131E-05	c_0
0.111311796745	c_1
-0.015231760934	c_2
-4.555653147E-06	c_3
-9.56490929276E-07	c_4
7.71841066571E-09	c_5
3.69159861388E-10	c_6
5.69655000732E-11	c_7
3.35980648864E-13	c_8
-3.19646960832E-13	c_9
-3.53364218702E-14	c_{10}
-4.68922797075E-15	c_{11}
-2.80146891764E-17	c_{12}
-1.01330242075E-17	c_{13}
-2.2768560766E-19	c_{14}
2.23276839097E-18	c_{15}
3.01230419015E-19	c_{16}
1.96753864364E-21	c_{17}
5.83987396889E-22	c_{18}
-1.93436181181E-22	c_{19}
5.692002406E-23	c_{20}